

NATIONAL UNIVERSITY OF IRELAND MAYNOOTH



NUI MAYNOOTH

Ollscoil na hÉireann Má Nuad

Evanescent Wave Reduction Using a Segmented Wavemaker in a Two Dimensional Wave Tank

Iain Keaney

A thesis submitted in partial fulfillment for the degree of
Doctor of Philosophy

in the
Faculty of Science and Engineering
Electronic Engineering Department

Supervisor: Prof. John Ringwood
Head of Department: Dr. Ronan Farrell

October 2015

Declaration of Authorship

I, Iain Keaney, declare that this thesis titled ‘Evanescence Wave Reduction Using a Segmented Wavemaker in a Two Dimensional Wave Tank’ and the work presented in it are my own. I confirm that:

- This work was done wholly or mainly while in candidature for a research degree at this University.
- Where any part of this thesis has previously been submitted for a degree or any other qualification at this University or any other institution, this has been clearly stated.
- Where I have consulted the published work of others, this is always clearly attributed.
- Where I have quoted from the work of others, the source is always given. With the exception of such quotations, this thesis is entirely my own work.
- I have acknowledged all main sources of help.
- Where the thesis is based on work done by myself jointly with others, I have made clear exactly what was done by others and what I have contributed myself.

Signed:

Date:

ABSTRACT

Evanescent waves are created by the wavemaking process during tank testing. They have long been a nuisance for engineers as they contaminate the wave field in the tank and result in additional inertial force experienced by a wavemaker. Evanescent waves are created by the mismatch between the motion of the wavemaker and the motion of the fluid particles in a progressive wave. To avoid contamination of test results, often a considerable distance must be left between the wavemaker and the test area. This space requirement may be costly for small research groups or companies who wish to have a facility to perform some basic proof-of-concept tests in-house, but are restricted for space. The initial aim of this project was to develop a wavemaker which minimised this space requirement over a large range of frequencies. The exploration into the behaviour of evanescent waves from the point of view of the fundamentals of hydrodynamics has been very enlightening. It became clear with the discovery of an interference pattern between the evanescent waves, that this pattern can be optimised to effectively cancel out the evanescent wave field. This interference pattern arises from a phase shift of π radians experienced by some of the evanescent waves, with respect to the others. The significance of this in hydrodynamics is that it explains the existence of negative added mass. The application for this knowledge far out reaches the topic of reducing the distortion in a wave tank. The ability to minimise the added mass of a wavemaker has a great deal of potential in both active absorbing wavemakers and wave energy conversion. For active absorbing wavemakers, the minimisation of added mass may be useful in the absorption of unwanted waves which can be particularly troublesome at high frequencies.

The concept of designing the geometry of a wavemaker to simply match the motion of the fluid particles has long been proposed; however, the difficulty with designing such a wavemaker is that the ideal geometry is frequency dependent. Hence, a design that eliminates the evanescent waves at one particular frequency will not be able to do so for other frequencies. An investigation into the design of a segmented wavemaker is presented here, as its geometry can easily be adjusted to suit different frequencies.

The wavemaker theory for the multi-body problem of the segmented wavemaker is developed, and a new aspect of wavemaker theory that predicts a phase

shift of π radians in some of the evanescent waves is presented for the first time. A hypothesis is put forward, and then investigated, proposing that this phase shift can be exploited to create an interference pattern that can effectively cancel out the evanescent waves. The hydrodynamics of the segmented wavemaker were constrained using the Newton-Euler equations of motion with Eliminated Constraints (NE-EC). This approach facilitated a comparison between wavemakers with multiple degrees of freedom and traditional wavemakers with a single degree of freedom.

The lengths and strokes of each segment in the wavemaker are optimised to reduce the distortion caused by the evanescent waves using two approaches. Approach one follows the traditional ideas and optimises the lengths and strokes of the segments to best approximate the motion of the fluid particles in a progressive wave. Approach two optimises the lengths and strokes of the segments in order to minimise the distance between the wavemaker and the testable area in the tank. Approach two exploits the phase shift in the evanescent waves by finding the optimal interference pattern that effectively cancels out the evanescent waves. A comparison between both approaches shows that effectively eliminating the distortion caused by the evanescent waves is much more achievable by optimising the interference pattern between the evanescent waves, rather than trying to approximate a progressive wave.

The results for the segmented wavemakers optimised using approach two predicted that the distortion can be effectively eliminated for a wide range of frequencies using a segment wavemaker consisting of three flaps. A sensitivity analysis indicates that the performance of the wavemaker is somewhat effected by errors in the segments strokes, but the overall performance is still better than what has been developed to date.

Acknowledgements

I would like to thank my supervisor, Prof. John Ringwood, and co-supervisor, Dr. Ronan Costello, for their time and efforts on this project. The journey my education has taken me on has certainly presented its share of challenges and I am forever indebted to my parents for their constant support and encouragement over the years, and to my partner, Anita, for her endless patience and understanding. I would like to express my gratitude for the support of the rest of my family, Corinna, Michael and Ciaran. I would also like to thank Harvey Appelbe for the opportunities he's given me and for his support of my work. Finally, I am grateful to Tue Vu, Francesco Fusco, Giorgio Bacelli, Boris Teillant, Tom Kelly, Josh Davidson and the rest of my colleagues at COER for their friendship and assistance over the years.

Contents

1	Introduction	1
1.1	Contributions of the thesis	3
1.2	Thesis layout	4
2	Wave field in a tank	6
2.1	Potential flow theory	8
2.2	Fluid-structure interaction: Wavemaker theory	10
2.2.1	Boundary value problem	12
2.2.2	The general solution to the wavemaker problem	16
2.3	Unique solutions to the dispersion relation	18
2.4	Evanescent waves	20
2.4.1	The effect of evanescent waves on the wave field	21
2.4.2	Phase of evanescent waves	23
2.5	Validation of code	30
3	Designs of wavemakers: A literature survey	32
3.1	Introduction	32
3.2	History of wavemaker theory	33
3.3	Vertical paddle wavemakers	34
3.3.1	Design parameters	35
3.3.2	Consideration of evanescent waves	36
3.3.3	Design curves	37
3.3.4	Rolling seal design	38
3.3.5	Double articulated paddles	39
3.4	Double-flap wavemaker	40
3.4.1	Effect on the evanescent wave field	41
3.5	Plunger wavemaker	41
3.5.1	Performance	43
3.5.2	Exponentially shaped plunger wavemaker	45
3.6	Flexible wavemakers	46
3.6.1	Evaluation of the evanescent wave field	47

3.6.2	Construction of a flexible design	48
3.7	Pneumatic wavemakers	48
3.8	Inclined flap wavemaker	49
3.9	Duck wavemaker	50
3.10	Porous wavemakers	51
3.11	Sloped Piston	51
3.12	Spiral wavemaker	52
3.13	Numerical wave tanks	53
3.13.1	Spinning dipole wavemaker	53
3.13.2	Boundary element method	54
3.13.3	Boundary collocation method	55
3.13.4	Conformal mapping	55
3.13.5	Computational fluid dynamics	56
3.14	Second order theories	56
3.15	Control systems and wave basins	58
3.15.1	First and second-order control	58
3.15.2	Comparison of force vs. position control	59
3.15.3	Active absorbers in NWTs	59
3.15.4	Directional wavemaking in wave basins	60
3.16	Conclusion	60
4	Segmented wavemaker design: A multi-body problem	61
4.1	Introduction	61
4.2	Defining a segmented wavemaker	63
4.3	Hydrodynamics of the segmented wavemaker	64
4.4	Radiation impedance	66
4.4.1	Radiation damping	69
4.4.2	Added mass	74
4.5	Validation of code	79
4.6	Constrained dynamics of a segmented wavemaker	80
4.6.1	Modes of motion of a wavemaker	81
4.6.2	Newton-Euler equations of motion with eliminated constraints	83
4.6.3	Constrained hydrodynamics	85
4.7	Control parameter	92
4.8	Conclusion	92
5	Optimisation of segment length	94
5.1	Introduction	94
5.2	Setting up the optimisation problem	97

5.2.1	Optimisation algorithms	98
5.2.2	Wavemaker constraints	99
5.2.3	Differential evolution algorithm	100
5.2.4	Finding a global minimum	101
5.3	Approach 1: Matching the progressive wave kinematics	101
5.3.1	Tuning the scale factor and crossover probability	102
5.4	Approach 2: Minimising the wave field distortion	104
5.4.1	Objective function: position of 1% distortion away from the wavemaker	104
5.4.2	Tuning the scale factor and the crossover probability	105
5.5	Optimisation results: kinematics matching	107
5.6	Optimisation results: minimisation of distortion	111
5.7	Comparison of results	115
5.8	Conclusion	116
6	Optimisation of segment stroke	117
6.1	Introduction	117
6.2	Tuning the optimisation parameters	119
6.3	Case (1): Optimisation of strokes for segments of equal lengths	122
6.4	Case (2): Optimisation of strokes for optimised segment lengths	125
6.5	Analysis of the evanescent wave field (sample results)	130
6.6	Sensitivity Analysis	135
6.6.1	Sensitivity of the distortion level	136
6.6.2	Sensitivity analysis: progressive wave height	148
6.7	Conclusion	161
7	Conclusion	162
7.1	Suggestions for future work	165
7.2	Closing remarks	165
	Appendix A Results of complete optimised wavemakers	166

*Dedicated to my parents,
Michael and Mary Keaney*

*and to my wife,
Dr. Anita Keaney,*

the world will be a better place because of your work.

Chapter 1

Introduction

The objective of this thesis is to investigate the nature of evanescent waves created by a wavemaker in a wave tank. Evanescent waves arise from a mismatch between the kinematics of a wavemaker and that of the fluid particles in the progressive wave. This results in the existence of added mass and additional inertial force, experienced by the wavemaker, due to the fluid it displaces. At high frequencies the inertial force on a wavemaker due to added mass can be very large in comparison to the force required to radiate a wave away from the wavemaker, leading to difficulties in absorbing high frequency waves. This issue is also relevant to the topic of wave energy conversion.

The existence of negative added mass has long been known [1], yet to the best of the authors knowledge no adequate explanation has been provided as to why it occurs. Presented in this thesis is a clear explanation as to how negative added mass is a result of evanescent waves undergoing a phase shift of π radians, relative to the motion of the wavemaker. It is demonstrated that this phase shift is dependent on the geometry of the wavemaker. Furthermore, the thesis discusses how only some of the evanescent waves experience a phase shift and how this phase difference leads to an interference pattern. It is proposed and subsequently demonstrated that, by optimising the design of the wavemaker's geometry, the phase difference between the evanescent waves can be optimised to create a destructive interference pattern, ultimately minimising the strength of the evanescent wave field. This knowledge can have a significant impact on the absorption of waves by wavemakers or wave energy converters. The presented investigation helps to deepen our understanding of hydrodynamics by providing an explanation as to why negative added mass exists and how it can be utilised by optimising the wavemaker's geometry.

The work presented in this thesis is primarily focused around reducing the distortion caused to the wave field by evanescent waves. Evanescent waves contaminate the region in the wave tank near the wavemaker making test results

unreliable. This leads to the forces experienced by a device tested in a wave tank being different from that intended, leading to unreliable predictions of the power output of the device if deployed at sea. The distortion due to the evanescent waves decreases with distance away from the wavemaker. As a rule of thumb, to avoid the accuracy of test results being compromised, devices are generally tested a distance of two to three times the still water depth away from the wavemaker.

At the far-end of the tank, space must be provided for absorbing waves to prevent reflections back towards the test area. Often an active absorbing wavemaker can be the most space efficient way of preventing reflected waves travelling back upstream to the test area. However, active absorbers create the same evanescent waves as wavemakers do, hence, the same provisions must be provided to avoid contamination. For large testing facilities this space allowance may not be a problem, but with the rising interest in wave energy, many smaller research groups and companies simply cannot afford to house such large wave tanks. Thus, reducing the evanescent wave distortion can be useful in allowing smaller facilities to house their own wave tanks, ultimately speeding up the development of wave energy converters.

Tank testing is an invaluable tool for testing how devices will perform and survive in the ocean environment. Installing and maintaining devices in the ocean is incredibly expensive, in some cases costing up to €100,000 per day for installation. Hence, when a device is being installed in the ocean it is vital that we know how it's going to behave and that it will be able to survive the abuse of storms. Tank testing allows us to predict how devices will behave in the ocean. An extensive knowledge of how a device behaves in various sea conditions can be developed by performing numerous tank tests on scaled models for a fraction of the cost. This has allowed companies to not only test the performance of their device, but also optimise the installation process, helping to drive the cost of installation and operation down. Furthermore, by proving that a device works well under tank testing conditions, companies can find it easier to secure grants or investment to assist with the financial burden of going to sea.

The motivation for this project originated in ITT Dublin, with a need to build a wave tank in a very space restricted area. The space required to be able to take meaningful measurements of the wave field without them being contaminated by the evanescent waves was out of the question, so focus shifted to designing a wavemaker that would permit testing in shorter wave tanks. The tank was limited to being 0.6 m deep and 2.5 m long, which meant that tests could not be performed within a distance of 1.2 m from either the wavemaker or the active absorber, hence, useful tests were impossible. It should be noted that the use for such a short tank would be very limited, but it could certainly play a role in the

very early concept development of off-shore devices in the same manner as the AMOEBA tank discussed by [2]. At the same time Omey Labs Ltd., a company who develops low-end wave tanks for rapid and frequent early stage testing of wave energy converters, were concerned that some clients may not be able to house a large wave tank and were interested in finding space saving solutions. A collaboration was established to design a wavemaker that would reduce the distortion in the wave tank, for which a segmented wavemaker that consisted of a number of paddles stacked on top of each other was chosen. The segmented wavemaker design proposed in [3] and illustrated in Figure 4.1, was picked as it offers a greater level of control over the wavemaker's geometry.

1.1 Contributions of the thesis

Previous to this thesis the literature surrounding segmented wavemakers [3, 4, 5, 6] was limited to two segment flap wavemakers and did not provide a detailed analysis into their ability to reduce distortion. To-date there has been no attempts, to the author's knowledge, to understand how adding more segments to the wavemaker will affect its performance, nor have attempts to optimise the geometry of the wavemaker in order to minimise the distortion directly been published. Clark and Menken [5] did use a linear regression method to find the strokes of the wavemaker that would best approximate the progressive wave. Hyun [4] also presented an elementary investigation into how the lengths of the segments affect the inertial pressure on the wavemaker. Neither [4] or [5] focused on minimising the distortion of the wave field caused by the evanescent waves. As well as studying the performance of the segmented wavemaker, this thesis presents a new aspect of the well known linear wavemaker theory which predicts a phase shift in some of the evanescent waves with respect to the other evanescent waves. The novel contributions to the topics of wavemaker theory and wavemakers presented in this thesis can be broken down as:

1. The phase shift experienced by some of the evanescent waves is presented for the first time in Chapter 2, along with a discussion of why this behaviour occurs, what affect it can have on the wave field and how it can be used to help minimise the distortion.
2. Presented for the first time in Chapter 4, are the hydrodynamics coefficients of piston and flap wavemakers with two to ten segments, where the segments

are all equal in length. The hydrodynamic coefficients for single segment piston and flap wavemakers are also presented for comparison.

3. The optimisation of the theoretical segment lengths in both the piston and flap wavemakers with three to six segments in order to best approximate the kinematics of a progressive wave is discussed, and the results are presented for the first time in Chapter 5. The optimisation results of the geometries of both the piston and flap wavemakers with two segments are also presented.
4. The optimisation of the theoretical segment lengths in piston and flap wavemakers in order to best reduce the distance between the wavemaker and the test area in the tank is presented for the first time in Chapter 5.
5. The optimisation of the theoretical segment strokes in piston and flap wavemakers in order to best reduce the distance between the wavemaker and the test area in the tank is presented in Chapter 6 and the results of the fully optimised segmented wavemakers are also presented for the first time.

Contributions (1) and (2) have already been discussed in the publication:

- [7] I. Keaney, R. Costello, and J. V. Ringwood, *Evanescant Wave Reduction Using a Segmented Wavemaker in a Two Dimensional Wave Tank, ASME 2014 33rd International Conference on Ocean, Offshore and Arctic Engineering*, 2014.

1.2 Thesis layout

In Chapter 2, the well-known linear wavemaker theory is developed by solving the wavemaker boundary value problem. The wavemaker problem is formulated using complex amplitude notation, the dispersion relation is also derived and the unique solutions to the dispersion relation are discussed. The behaviour of the evanescent waves is discussed and the novel concept that some of the evanescent waves undergo a phase shift is introduced and investigated.

A survey of the wavemaker designs and techniques that have been developed and used to-date by researchers is presented in Chapter 3, along with their advantages and limitations. Chapter 3 also discusses other areas related to wavemakers, such as numerical wave tanks, second-order theory and control systems.

Chapter 4 describes the concept of both the piston and flap segmented wavemakers, where all the segments are equal in length. The hydrodynamics for the

multi-body problem of the segmented wavemaker are then developed. The degrees of freedom of the multi-body system are reduced by applying a programmed constraint on the motion of the individual segments, specifically describing the motion of all the segments in relation to the segment closest to the free surface. The hydrodynamics of the constrained multi-body system are derived and presented as functions of the normalised wavenumber k .

In Chapter 5 the lengths of the segments are optimised using two approaches: to best approximate the kinematics of a progressive wave and to minimise the distance between the wavemaker and the testable area in the wave tank. The optimisation is carried out using the Differential Evolution (DE) optimisation algorithm which is described in Chapter 5. The DE algorithm's control parameters are tuned in Chapter 5.

In Chapter 6, the strokes of the segments are also optimised by minimising the distance between the wavemaker and the testable area in the wave tank. Again the optimisation in Chapter 6 is carried out using the DE algorithm, for which the control parameters are again tuned. The interference pattern between the evanescent waves which helps to minimise the distortion is investigated. A sensitivity analysis is also presented in Chapter 6 to investigate how sensitive the performance of the segmented wavemaker in reducing the distortion is to errors in the strokes of the segments. Finally, the findings of the thesis are concluded in Chapter 7 and some future work is suggested.

Chapter 2

Wave field in a tank

The ocean is one of the most chaotic and inaccessible environments on earth, thus, carrying out any kind of construction in the ocean can be extremely expensive. As a result when designing offshore structures, such as coastal defences, telecommunication cables, oil rigs and offshore renewable energy devices, engineers and scientists try to model the interaction between the structures and their environments as extensively as possible before installation. Numerous theoretical and physical modelling techniques have advanced greatly over the past 100 years for studying such interactions and loads experienced by these structures. These modelling techniques have made testing the performance and survivability, as well as designing the installation process of offshore structures, more accessible. Ultimately, these modelling techniques enabled the growth of industries around utilities that the world is heavily dependent on today, such as energy and global telecommunication networks.

Many theoretical models, which will be discussed in Chapter 3, have been developed that have proven to be very useful when predicting the behaviour of devices in various sea states. Theoretical models have the advantage over physical modelling of not requiring a large space for experimenting or the construction of various test rigs, removing a large financial and time expense. The most commonly used model in predicting such behaviour of devices in ocean waves is linear potential flow theory; this has proven to be remarkably successful in accurately predicting the behaviour of devices for a practical range of conditions. Potential flow theory can be used to describe the fluid's flow within the domain by the conditions that exist on the boundaries of the fluid domain. This is a significantly more efficient approach than attempting to solve the entire fluid domain. The problem of describing wave generation using potential flow theory is referred to as wavemaker theory and was first presented by Havelock [8].

Havelock [8] presented a solution to the wavemaker problem by solving the Laplace equation for the potential flow problem of wave generation. To satisfy

the boundary condition of the wavemaker problem, Havelock's boundary value solution is the summation of an infinite number of solutions to the Laplace equation. Of this infinite series, only one solution represents a wave which radiates to infinity while the rest represent local standing waves. Biesel and Suquet [9] extended Havelock's wavemaker theory further by explicitly deriving analytical models for the traditional piston and flap wavemakers, illustrated in Parts (a) and (b) of Figure 2.1 respectively. In Figure 2.1 the coordinate system is defined

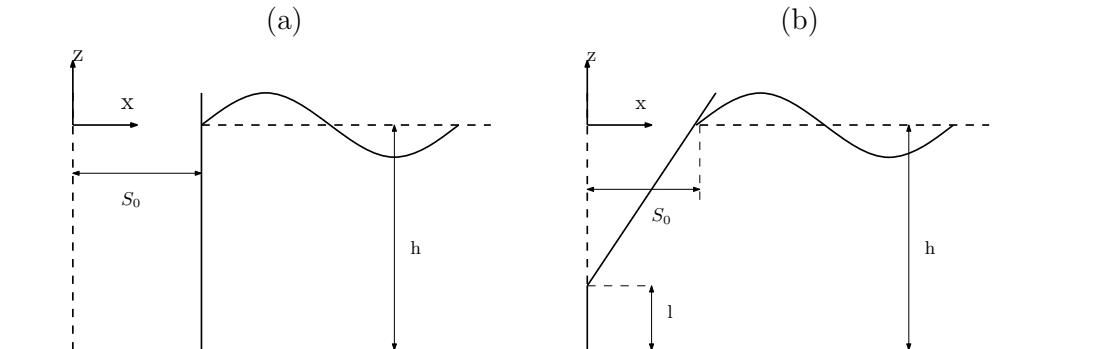


Figure 2.1: (a) Traditional full draft piston wavemaker. (b) Traditional variable draft flap wavemaker.

with x and z denoting the horizontal and vertical axes respectively, S_0 is the stroke of the wavemaker at the still free surface level, h is the depth of the tank and l is the height of the flap's hinge above the tank floor. Further advances in Havelock's wavemaker theory were presented by Suh and Dalrymple [10] who predicted the multi-directional wave field generated by a number of wavemakers side-by-side in a wave basin. The second-order irregular wavemaker theory was developed by Schaffer [11]. More recently, Spinneken [12] derived the force transfer functions for Schaffer's [11] second order irregular wavemaker theory. In this chapter the potential wavemaker theory of Havelock [8] is developed following the convenient notation of Falnes [13]. This chapter takes a deeper look at Havelock's [8] solutions than has been presented in other sources and an investigation into the behaviour of the infinite summation is presented, particularly the possible phases for the summation terms representing the local standing waves, which is a novel contribution.

The first objective of this chapter is to present a concise and clear development of wavemaker theory in order to describe the frequency domain wave field in terms of the wave amplitude. This is achieved in three parts:

- Section 2.1 defines the gravity wave problem by introducing the concept of linear potential flow theory, and discussing the assumptions it makes.
- Section 2.2 establishes the conditions at the boundaries of the fluid domain,

in order to develop the wavemaker model essential for the work carried out and presented in this thesis.

- Section 2.3 studies the dispersion relation, the nature of its unique solutions¹, how these solutions behave and their consequence to the wave field.

The second and third objectives are dealt with in Section 2.4, which are to develop a convention for quantifying the distortion caused to the wave field from the wavemaking process, and to identify a novel approach to minimising this distortion. Finally, Section 2.5 presents a validation of the in-house code developed to generate the results presented in this thesis.

2.1 Potential flow theory

When considering waves on water, the fluid is usually assumed to be incompressible and irrotational. Applying the law of conservation of mass and the Laplace equation,

$$\nabla \vec{v} = \frac{\partial \vec{v}}{\partial \vec{x}} + \frac{\partial \vec{v}}{\partial z} = 0, \quad (2.1)$$

on to the fluid enforces the assumption of incompressibility while stating that the volume of fluid flowing into the domain must equal that flowing out, where v is the velocity of the fluid in a water wave and a vector is indicated by $\vec{\cdot}$. Laplace's equation is commonly used for the water wave problem as it has been shown to hold for a wide range of conditions and allows for the problem to be solved from the conditions imposed on the fluid at its boundaries, making it computationally efficient. Potential theory has also shown extensively to be reliable for nonlinear waves [14] including up to 5th order Stoke waves [15]. The assumption of irrotationality permits the simplification of expressing the flow velocity as the gradient of a scalar potential, ϕ , referred to as the velocity potential [13],

$$\vec{v} = \nabla \phi(x, z, t). \quad (2.2)$$

Thus, the Laplace equation, Equation (2.1), requires that,

$$\nabla^2 \phi = 0 \quad (2.3)$$

¹The term unique solution refers to any solution of the Laplace equation for a unique value of k .

As this thesis is only concerned with the waves radiating from a wavemaker, henceforth, only the radiated wave field will be considered. Following the methodology presented by [13], a further simplification is made by assuming that the radiated wave field can be described as the superposition of waves created by each of the six Degrees Of Freedom (DOF) of an oscillating body,

$$\phi = \sum_{j=1}^6 u_j \varphi_j. \quad (2.4)$$

In Equation (2.4), the index, j , indicates the DOF the body is moving in and u is defined as

$$u(z, t) = u_0 c(z) e^{i\omega t}, \quad (2.5)$$

where u_0 is the amplitude of the body's velocity oscillating in the fluid and φ is a complex coefficient of proportionality. The DOFs of floating bodies will be discussed in greater detail in the next section. The complex coefficient of proportionality, φ_j , in Equation (2.4) can be thought of as the velocity potential generated by a device oscillating in the j^{th} DOF and normalised by the device's velocity in the j^{th} DOF.

To find a solution that satisfies Equation (2.1), the principle of separation of variables is employed [13],

$$\varphi(x, z) = X(x)Z(z). \quad (2.6)$$

Applying the Laplace Equation, Equation (2.1), to Equation (2.6) gives the partial differential problem:

$$\frac{1}{X(x)} \frac{\partial^2 X(x)}{\partial x^2} = -\frac{1}{Z(z)} \frac{\partial^2 Z(z)}{\partial z^2}. \quad (2.7)$$

For this to hold true, both sides of Equation (2.7) must be equal to the same separation constant with opposite signs [13],

$$\begin{aligned} \frac{\partial^2 X(x)}{\partial x^2} &= -k^2 X(x), \\ \frac{\partial^2 Z(z)}{\partial z^2} &= k^2 Z(z). \end{aligned} \quad (2.8)$$

The solutions to Equations (2.8) is given by [13] as,

$$X(x) = c_x e^{ikx} + c_{-x} e^{-ikx}, \quad (2.9)$$

$$Z(z) = c_+ e^{kz} + c_- e^{-kz}. \quad (2.10)$$

It should be noted at this point that if k were to be imaginary, then $Z(z)$ would become harmonic and $X(x)$ would be hyperbolic. This is a property that will be of great importance later in this chapter.

2.2 Fluid-structure interaction: Wavemaker theory

Wavemaker theory deals with some of the fundamental aspects of marine hydrodynamics and has lent itself to the development of wave energy converters,

“a good wave absorber, must be a good wavemaker”, (Falnes and Budal, 1978).

In marine hydrodynamics a floating body can undergo motion in six DOFs (also referred to as modes of motion), three translational: surge, heave and sway, and three rotational: roll, pitch and yaw, all of which are illustrated in Figure 2.2. For the purpose of simplicity in this study we restrict our consideration to a two

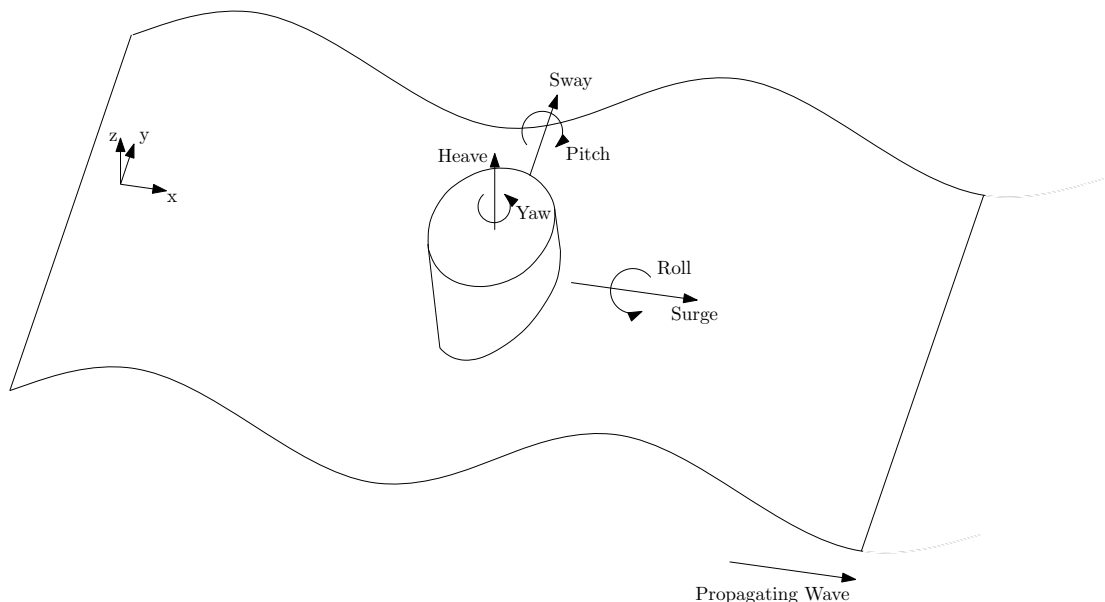


Figure 2.2: Modes of motion of a free body experiencing incident waves.

dimensional wave tank, as described in Figure 2.3. We define a coordinate system where the vertical z -axis points positively upwards, with $z = 0$ set to the mean free

surface elevation, and the horizontal x -axis is defined as pointing positively along the fluid domain, with $x = 0$ set at the wavemaker's mean position, (Figure 2.3). The 2-D wavemaker operates in surge, i.e., a piston wavemaker in Figure 2.3 Part(b), or pitch, i.e., a flap wavemaker in Figure 2.3 Part(a). The horizontal

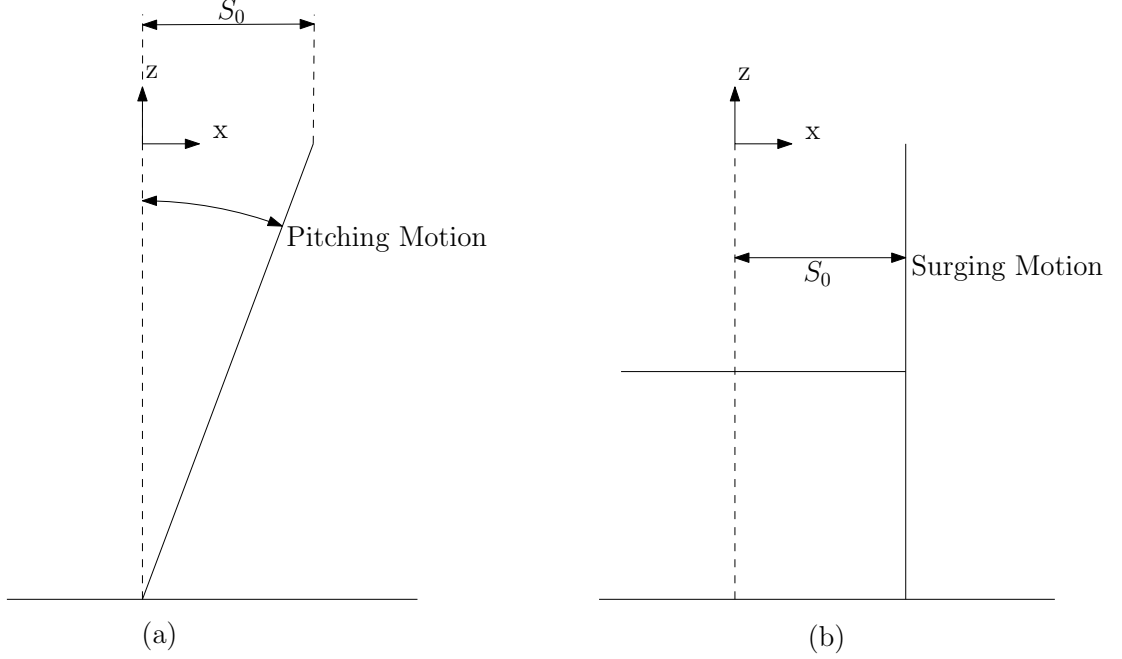


Figure 2.3: Illustration of the modes of motion of (a) a bottom hinged flap wavemaker and (b) a piston wavemaker.

displacement of the wavemaker along the vertical axis is:

$$S(z, t) = S_0 c(z) e^{i\omega t}, \quad (2.11)$$

where S_0 is the wavemaker's stroke at $z = 0$. The wavemaker's depth profile, $c(z)$, is the displacement of the wavemaker over z normalised by the wavemaker's stroke, S_0 . For a piston, the horizontal displacement is constant over depth, so the profile function is given as:

$$c(z) = \begin{cases} 1 & \text{for } -(h-l) < z < 0 \\ 0 & \text{for } z < -(h-l). \end{cases} \quad (2.12)$$

For a piston wavemaker l is the vertical distance between the bottom of the wavemaker and the tank floor. For a flap wavemaker the horizontal displacement decreases linearly towards the pivot point, at which the displacement is zero,

$$c(z) = \begin{cases} 1 + \frac{z}{(h-l)} & \text{for } -(h-l) < z < 0 \\ 0 & \text{for } z < -(h-l), \end{cases} \quad (2.13)$$

In the case of the flap wavemaker l is the vertical distance between the tank floor and the pivot point. When the hinge is above the tank floor l is positive and in the case where the wavemaker has a “virtual” hinge below the tank’s floor l is negative. A wavemaker with a virtual hinge requires a second point of articulation, this wavemaker design will be discussed further in Section 3.3.

2.2.1 Boundary value problem

Laplace equation theory is a boundary value problem for which the solutions depend on the properties of the boundary conditions. The boundaries at the fluid’s interfaces in the presented wave tank problem enforce the condition that the fluid cannot flow through those boundaries. The changes in the pressure distribution on the free surface, caused by the fluctuating elevation of the free surface, impose a condition that must be applied to the fluid at the boundary so as to maintain a balance between the fluid pressure on the free surface and the atmospheric pressure [16].

Dynamic free surface boundary condition

The pressure fluctuation on the free surface, $\eta(x, t)$, due to its oscillating elevation can be described by Bernoulli’s equation [16],

$$\left(gz - \frac{\partial \phi}{\partial t} + \frac{\bar{v}^2}{2} \right)_{z=\eta(x,t)} = C(t), \quad (2.14)$$

where g is the acceleration due to gravity, t represents the time variable and, on the free surface, $C(t)$ equals the atmospheric pressure which we can set to zero. At this point however, we do not know the value for $\eta(x, t)$, so we approximate Equation (2.14) with the Taylor expansion about the point $z = 0$. The truncated form of Equation (2.14) expanded about $z = 0$ is,

$$\left(gz - \frac{\partial \phi}{\partial t} + \frac{\bar{v}^2}{2} \right)_{z=0} + \left(g - \frac{\partial^2 \phi}{\partial z \partial t} + \frac{1}{2} \frac{\partial \bar{v}^2}{\partial z} \right)_{z=0} = 0. \quad (2.15)$$

Assuming small amplitude waves allows us to linearise Equation (2.15) by ignoring all the non-linear terms, thus the first order dynamic free surface boundary condition [16] on $z = 0$ can then be expressed as:

$$\left[\frac{\partial \phi}{\partial t} \right]_{z=0} + g\eta = 0. \quad (2.16)$$

Kinematic boundary condition

A kinematic boundary condition applies at the surface of the wavemaker, where $x = S(z, t)$, the floor of the wave tank, where $z = -h$, and the free surface, where $z = \eta(x, t)$. We can define an arbitrary function, $G(x, z, t) = 0$, to describe the surface of the boundary [16]. By setting $G(x, z, t)$ to zero, [16], we can conveniently describe the boundaries as,

$$G(x) = z + h(x) = 0 \quad (2.17)$$

on the tank floor,

$$G(x, t) = z - \eta(x, t) = 0 \quad (2.18)$$

on the free surface and

$$G(z, t) = x - S(z, t) = 0 \quad (2.19)$$

on the wavemaker's surface. Since the fluid on the boundary moves with the boundary, the material derivative of the boundary's surfaces with respect to time is zero, i.e., if we move with the surface, the surface does not change [16],

$$\frac{DG(x, z, t)}{Dt} = \frac{\partial G}{\partial t} + \frac{\partial \phi}{\partial x} \frac{\partial G}{\partial x} + \frac{\partial \phi}{\partial z} \frac{\partial G}{\partial z} = 0 \Big|_{G(x, z, t)=0}. \quad (2.20)$$

Defining a normal vector, \vec{n} , as a unit vector on the boundary's surface and pointing normally into the fluid domain,

$$\vec{n} = \frac{\nabla G}{|\nabla G|}, \quad (2.21)$$

Equation (2.20) can be simplified to:

$$-\frac{\partial G}{\partial t} = \vec{v} \cdot \nabla G = \vec{v} \cdot \vec{n} |\nabla G| \Big|_{G(x, z, t)=0}, \quad (2.22)$$

and rewritten as,

$$\vec{v} \cdot \vec{n} = \frac{-\frac{\partial G}{\partial t}}{|\nabla G|} \Big|_{G(x, z, t)=0}, \quad (2.23)$$

Following [16], by applying Equation (2.23) separately to Equations (2.17), (2.18) and (2.19) the kinematic boundary conditions on each surface can be derived.

Bottom boundary condition

To derive the bottom boundary condition we start by substituting Equation (2.17) into Equation (2.23). Given that Equation (2.17) is independent of time, the right hand side of Equation (2.23) goes to zero. Inserting Equation (2.17) into Equation (2.21), the normal vector is given as,

$$\vec{n} = \frac{\frac{\partial h(x)}{\partial x} \vec{i} + \vec{k}}{\sqrt{\left(\frac{\partial h(x)}{\partial x}\right)^2 + 1}}. \quad (2.24)$$

Recalling Equation(2.2) and inserting Equation (2.24) into Equation (2.23) gives,

$$\vec{v} \cdot \left[\frac{\frac{\partial h(x)}{\partial x} \vec{i} + \vec{k}}{\sqrt{\left(\frac{\partial h(x)}{\partial x}\right)^2 + 1}} \right] = \left[\frac{\partial \phi}{\partial x} \vec{i} + \frac{\partial \phi}{\partial z} \vec{k} \right] \cdot \left[\frac{\partial h(x)}{\partial x} \vec{i} + \vec{k} \right] = 0, \quad (2.25)$$

which can be rewritten as a general bottom boundary condition [16],

$$\frac{\partial \phi}{\partial z} = - \frac{\partial \phi}{\partial x} \frac{\partial h(x)}{\partial x} \Big|_{z=-h}. \quad (2.26)$$

If $h(x)$ is constant the bottom boundary condition, Equation (2.26), becomes,

$$\frac{\partial \phi}{\partial z} = 0 \Big|_{z=-h}. \quad (2.27)$$

Kinematic Free Surface Boundary Condition

In order to derive the kinematic free surface boundary condition the normal vector to the free surface is given by inserting Equation (2.18) into Equation (2.21),

$$\vec{n} = \frac{-\frac{\partial \eta}{\partial x} \vec{i} + \vec{k}}{\sqrt{\left(\frac{\partial \eta}{\partial x}\right)^2 + 1}}. \quad (2.28)$$

Inserting Equations (2.18) and (2.28) into Equation (2.23) and using Equation (2.2) we can write,

$$\vec{v} \cdot \left[\frac{-\frac{\partial \eta}{\partial x} \vec{i} + 1 \vec{k}}{\sqrt{\left(\frac{\partial h(x)}{\partial x}\right)^2 + 1}} \right] = \frac{-\frac{\partial \phi}{\partial x} \frac{\partial \eta}{\partial x} + \frac{\partial \phi}{\partial z}}{\sqrt{\left(\frac{\partial h(x)}{\partial x}\right)^2 + 1}} = \frac{\frac{\partial \eta}{\partial t}}{\sqrt{\left(\frac{\partial h(x)}{\partial x}\right)^2 + 1}} \Bigg|_{z=\eta(x,t)}. \quad (2.29)$$

Then multiplying through provides the kinematic free surface boundary condition [16],

$$\frac{\partial \phi}{\partial z} = \frac{\partial \eta}{\partial t} + \frac{\partial \phi}{\partial x} \frac{\partial \eta}{\partial x} \Bigg|_{z=\eta(x,t)}. \quad (2.30)$$

As we are only interested in the first order solution, Equation (2.30) is linearised in the same manner as the dynamic free surface boundary condition, Equation (2.16). By expanding Equation (2.30), using Taylor expansion, about the position $z = 0$ and ignoring all non-linear terms, the linear kinematic free surface boundary condition is,

$$\frac{\partial \eta}{\partial t} = \frac{\partial \phi}{\partial z} \Bigg|_{z=0}. \quad (2.31)$$

For convenience, the dynamic and the kinematic free surface boundary conditions, Equations (2.16) and (2.31) respectively, can be combined by differentiating Equation (2.16) with respects of time and substituting into Equation (2.31), giving a combined free surface boundary condition independent of $\eta(x, t)$ [13],

$$\left[\frac{\partial^2 \phi}{\partial t^2} + g \frac{\partial \phi}{\partial z} \right]_{z=0} = \left[-\omega^2 \phi + g \frac{\partial \phi}{\partial z} \right]_{z=0} = 0. \quad (2.32)$$

Wavemaker boundary condition

To derive the boundary condition on the surface of the wavemaker we first find the normal vector to the wavemaker's surface by inserting Equation (2.19) into Equation (2.21) giving,

$$\vec{n} = \frac{1 \vec{i} - \frac{\partial S}{\partial z} \vec{k}}{\sqrt{1 + \frac{\partial S}{\partial z}}}. \quad (2.33)$$

Substituting Equations (2.19) and (2.33) into Equation (2.23) and multiplying through, as we did for the kinematic free surface boundary condition in Equa-

tion (2.30), gives the boundary condition [16],

$$\frac{\partial \phi}{\partial x} = \frac{\partial S}{\partial t} - \frac{\partial \phi}{\partial z} \frac{\partial S}{\partial z} \Big|_{x=S(z,t)}. \quad (2.34)$$

Again, expanding Equation (2.34) about the point $x = 0$ and ignoring all the nonlinear terms provides the linear wavemaker boundary condition,

$$\frac{\partial \phi}{\partial x} = \frac{\partial S}{\partial t} \Big|_{x=0}. \quad (2.35)$$

By substituting Equation (2.11) and (2.4) Equation (2.35) can be written more simply as [13],

$$c(z) = \frac{\partial \phi}{\partial x} \quad (2.36)$$

2.2.2 The general solution to the wavemaker problem

The complete solution to the Laplace equation, Equation (2.1), is a superposition of all the unique solutions φ_n ,

$$\varphi = \sum_{n=0}^N X_n(x) Z_n(z), \quad (2.37)$$

where N is the number of unique solutions. To find the coefficients of $Z(z)$ and $X(x)$, we follow the methodology used by [13] and apply the bottom boundary condition, Equation (2.27), to the depth function Equation (2.10), at $z = -h$,

$$\frac{\partial Z(-h)}{\partial z} = kc_+e^{-kh} - kc_-e^{kh} = 0. \quad (2.38)$$

This allows us to eliminate one of the coefficients of $Z(z)$,

$$c_+ = c_-e^{2kh}. \quad (2.39)$$

Substituting Equation (2.39) into Equation (2.10) gives,

$$Z(z) = c_-[e^{2kh}e^{kz} + e^{-kz}] = c_-e^{kh}[e^{k(h+z)} + e^{-k(h+z)}]. \quad (2.40)$$

Using the identity, $\cosh x = \frac{e^x + e^{-x}}{2}$, we have the hyperbolic function:

$$\Rightarrow Z(z) = 2c_-e^{kh} \cosh[k(h+z)]. \quad (2.41)$$

With a certain amount of foresight and following [13] convention, the coefficient will be denoted as $N^{-1/2}$,

$$\Rightarrow Z(z) = N^{-\frac{1}{2}} \cosh[k(h+z)]. \quad (2.42)$$

The coefficient N can be found by normalising Equation (2.42)

$$\frac{1}{h} \int_{-h}^0 |Z(z)|^2 dz = 1, \quad (2.43)$$

$$\Rightarrow N = \left[\frac{2kh + \sinh 2kh}{4kh} \right]. \quad (2.44)$$

It should be noted that since Equation (2.44) is independent of the wavemaker's depth profile, $c(z)$, it applies to all wave geometries. Since we are only concerned with waves radiating in the positive direction away from the wavemaker, waves incident on, or travelling behind, the wavemaker are ignored satisfying the radiation condition discussed by [13, 16]. Then by dropping the subscript Equation (2.9) becomes,

$$X(x) = ce^{-ikx}. \quad (2.45)$$

The coefficient c , sometimes referred to as the Biesel coefficient, after F. Biesel who first derived it for a piston and flap wavemaker [13], can now be found by applying the wavemaker boundary condition, Equation (2.36), to Equation (2.6)

$$c(z) = \left. \frac{\partial \varphi}{\partial x} \right|_{x=0} = \sum_{n=0}^{\infty} \frac{\partial X_n(0)}{\partial x} Z_n(z). \quad (2.46)$$

Multiplying across by $Z_m^*(z)$, where the index m indicates the relevant solution φ_m , and $*$ denotes the complex conjugate, then integrating over the depth of the wave tank gives:

$$\int_{-h}^0 c(z) Z_m^*(z) dz = \sum_{n=0}^{\infty} \frac{\partial X_n(0)}{\partial x} \int_{-h}^0 Z_m^*(z) Z_n(z) dz = \frac{\partial X_m(0)}{\partial x} h, \quad (2.47)$$

where the integral on the right hand side is the orthogonal condition, [13], and remembering that $\frac{\partial X_n(0)}{\partial x} = -ikc$, the Biesel coefficient, c , is found as a function

of the wavemaker's depth profile,

$$c = \frac{1}{ikh} \int_{-(h-l)}^0 c(z)Z(z)dz. \quad (2.48)$$

2.3 Unique solutions to the dispersion relation

For the purpose of deriving the dispersion relation, the depth function, Equation (2.10), is normalised by setting $Z(0) = 1$. This leads to the depth function, Equation (2.10), being expressed as [13],

$$Z(z) = \frac{\cosh[k(h+z)]}{\cosh(kh)}, \quad (2.49)$$

then applying the free surface boundary condition, Equation (2.32) gives,

$$\omega^2 Z(0) = g \frac{\partial Z(0)}{\partial z} \Rightarrow \omega^2 = gk \frac{\sinh(kh)}{\cosh(kh)} = gk \tanh(kh), \quad (2.50)$$

$$\Rightarrow \frac{\omega^2}{gk} = \tanh(kh). \quad (2.51)$$

Equation (2.51) is referred to as the dispersion relation as it links the wave's angular frequency, ω , to the wavenumber which, as it turns out, is the separation constant k . Previously, in Section 2.1, we discussed the possibility of the wavenumber being imaginary, in which case the dispersion relation becomes [13]:

$$\frac{\omega^2}{gm_n} = -\tan(m_n h), \quad (2.52)$$

where $k = -im$ is the imaginary wavenumber. Plotting both Equations (2.51) and (2.52) against the normalised wavenumber kh in Figure 2.4, it is evident from the intersection of the blue and green lines that only one solution for Equation (2.51) and hence only one real value for k can exist. However, the red lines intersect the blue line in Figure 2.4 at three different points; in fact, if we were to extend kh to infinity we would see that there is an infinite number of solutions to Equation (2.52), and therefore an infinite number of imaginary wavenumbers [16].

Referring back to Equations (2.9) and (2.10) it can be seen that a real value for

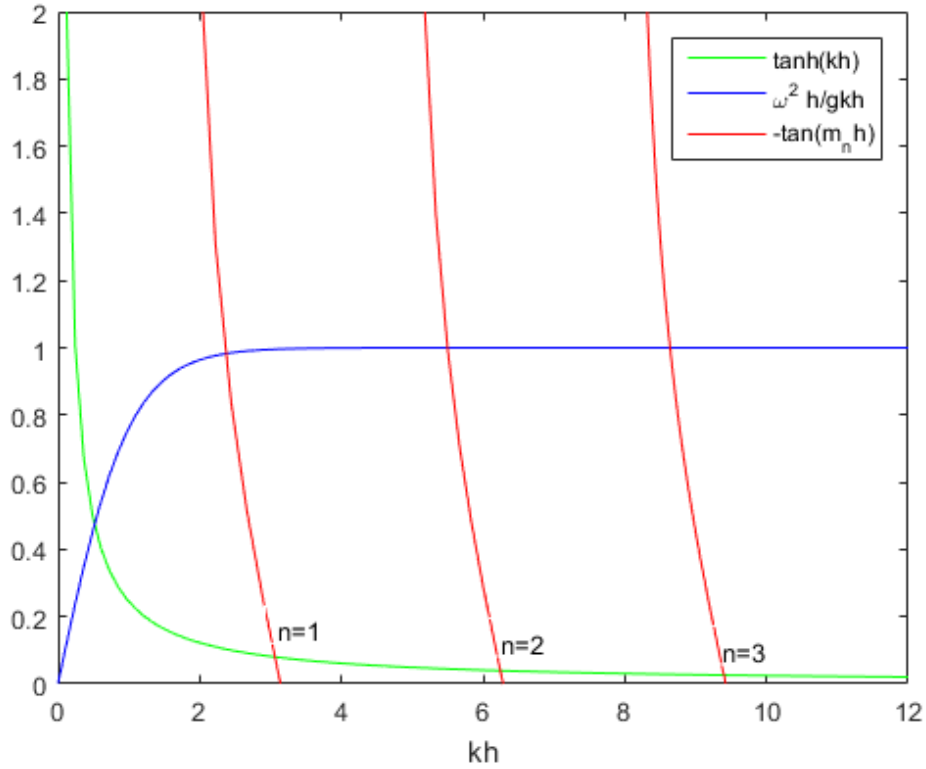


Figure 2.4: Solutions to the dispersion relation.

k represents a wave which is a sine function of x , this is called a progressive wave as it propagates along the x -axis. However, when the wavenumber is imaginary, the sine function is dependent on z instead, shown by Equation (2.53). At this point it is convenient to adapt the notation m_n for the n^{th} wavenumber, where $m_0 = ik_0$ represents the progressive wave. With this in mind the functions describing the solution φ are written in a more general form. The depth function becomes [13],

$$Z_n(z) = N_n^{-\frac{1}{2}} \cos[m_n(h+z)], \quad (2.53)$$

where

$$N_n = \left[\frac{2m_n h + \sin 2m_n h}{4m_n h} \right]^{\frac{1}{2}}. \quad (2.54)$$

The Biesel coefficients proportional to the amplitudes of the waves, Equation (2.48), can be written as [13],

$$c_n = \frac{1}{m_n h} \int_{-(h-l)}^0 c(z) Z_n(z) dz. \quad (2.55)$$

Finally, inserting Equations (2.45) into Equation (2.37) and superimposing

all possible solutions gives the core equation that describes the behaviour of the waves, [13]:

$$\varphi = \sum_{n=0}^{\infty} c_n Z_n(z) e^{-m_n x}. \quad (2.56)$$

The first term of the infinite sum in Equation (2.56) is the progressive wave. All subsequent terms, $n \geq 1$, correspond to the imaginary wavenumbers, which appear on the surface as standing waves and decay in amplitude exponentially with distance away from the wavemaker, and are hence called evanescent waves.

2.4 Evanescent waves

Evanescent waves can contaminate the test area in a wave tank distorting the wave field from the intended sea state; however, this is generally avoided by leaving a distance of two to three times the still water depth between the wavemaker and the test area since we know that the evanescent waves decay over distance away from the wavemaker (Equation (2.56)). In theory, evanescent waves could be eliminated by designing a wavemaker so that the depth profile equates the depth function of the progressive wave [17],

$$c(z) = \frac{\cosh[k(h+z)]}{\cosh(kh)}. \quad (2.57)$$

This would cause the Biesel coefficients in Equation (2.55) of all the evanescent waves to vanish. This technique has been successful in removing the evanescent waves in a numerical wave tank [18], however, building such a physical wavemaker to eliminate evanescent waves for a range of frequencies has not been possible to date. This brings us to the first hypothesis being investigated in this thesis which was proposed by [5]:

Hypothesis 1:

The closer the depth profile of the wavemaker, $c(z)$, matches that of the progressive wave, the smaller the amplitude of the evanescent waves, and hence the lesser the distortion caused by evanescent waves.

It should be noted that the wavemaker depth profile in Equation (2.57) is dependent on the wavenumber of the progressive wave, hence, it would only be

capable of eliminating evanescent waves when generating progressive waves at the wavenumber the wavemaker is tuned for.

2.4.1 The effect of evanescent waves on the wave field

The wavemaker's surface

When the evanescent waves are superimposed to the progressive wave, Equation (2.56), the resultant fluid motion approximates the motion of the wavemaker's surface. This can be seen in Figure 2.5, where the horizontal velocity component of the fluid produced by a piston wavemaker at $x = 0$ is plotted over the depth of the tank. What is evident from Figure 2.5 is that, as more evanes-

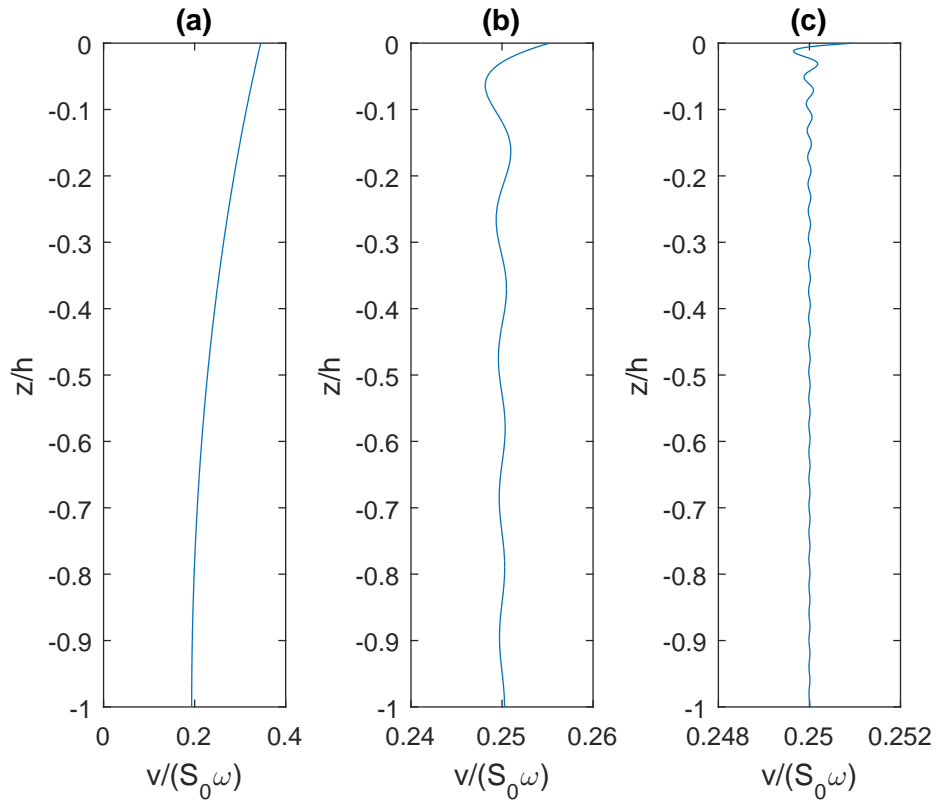


Figure 2.5: Horizontal fluid velocity at $x = 0$ including; (a) only the progressive wave term, (b) the first ten terms and (c) the first fifty terms of the truncated velocity potential generated by a single piston system with a unit stroke, *i.e.*, $S_0 = 1$ m. [$\omega = 4$ rad/sec, $h = 0.6$ m and $kh = 1.1818$]

cent waves are included in the truncated series in Equation (2.56), the closer the motion of the fluid matches that of the wavemaker. Maguire [17] demonstrated numerically that if the wavemaker's motion matched that of the fluid in a progressive wave, shown in Figure 2.5 Part (a), the evanescent wave field vanishes.

Free surface elevation

The main focus of this thesis is how much the evanescent waves distort the free surface. Rearranging Equation (2.16) and carrying out the derivative, the free surface can be expressed as [13],

$$\eta(x, t) = -\frac{1}{g} \left[\frac{\partial \phi}{\partial t} \right]_{z=0} = -\frac{i\omega}{g} [\phi]_{z=0}. \quad (2.58)$$

For convenience the results in this thesis have been evaluated in terms of the complex amplitude of the free surface elevation, $\hat{\eta}$, which is defined so that,

$$\eta(x, t) = \hat{\eta} e^{i\omega t}. \quad (2.59)$$

For a wave generated by a piston wavemaker, the free surface elevation normalised by the wavemaker's stroke S_0 , at phases of 0 and π , is plotted in Figure 2.6 against the distance x away from the wavemaker; the velocity potential has been truncated to include only the first fifty terms. What is highlighted in Figure 2.6

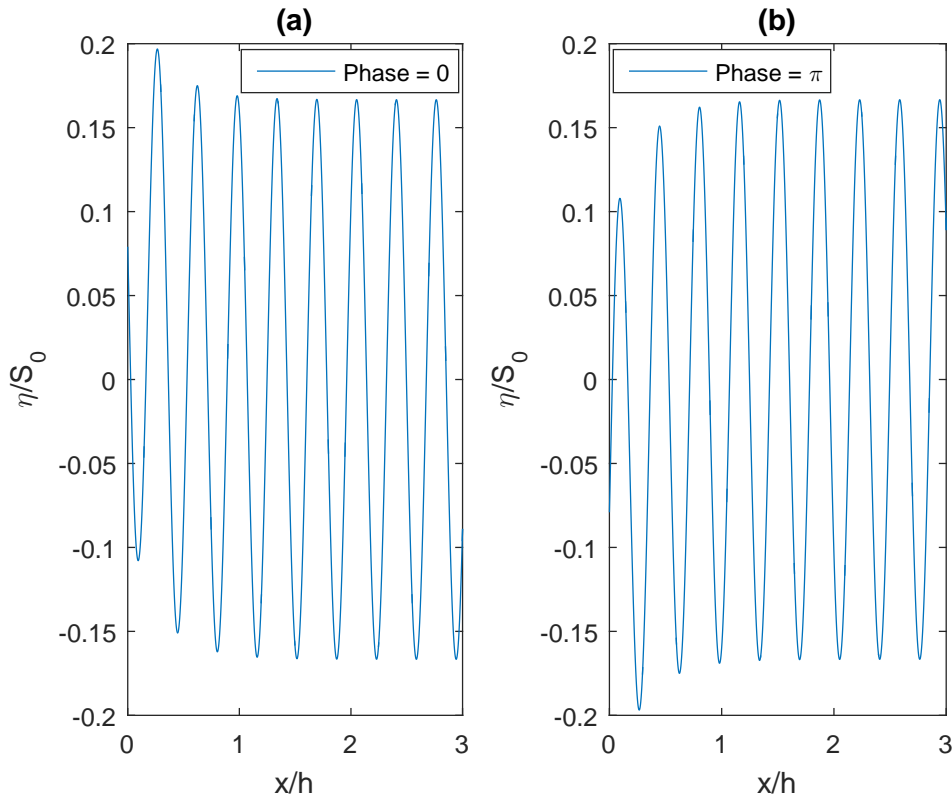


Figure 2.6: Free surface elevation created by a piston wavemaker with a phase of (a) 0 and (b) π , calculated including the first 50 terms of the velocity potential. [$\omega = 12$ rad/sec, $h = 1.2$ m and $kh = 17.6147$]

is the nature of the evanescent waves as standing waves rather than transverse

waves, which they can be misconceived as. The evanescent waves result in the mean position, over a wavelength, of the free surface to be off-set from $z = 0$. An extreme wave was chosen for Figure 2.6 as it best demonstrated the nature of how evanescent waves affect the free surface.

Distortion to the free surface elevation

We can assess the affect of the evanescent waves on the wave field by the distortion caused to the free surface elevation. This is defined as the amplitude of the free surface elevation due to the evanescent waves, $\hat{\eta}_{evan}$, as a percentage of the free surface elevation amplitude due to the progressive wave, $\hat{\eta}_0$,

$$Distortion = \frac{|\hat{\eta}_{evan}|}{|\hat{\eta}_0|} \times \frac{100}{1}. \quad (2.60)$$

The free surface elevation due to the evanescent waves, $\hat{\eta}_{evan}$, is found by evaluating Equation (2.58) for only the summation terms in Equation (2.56) that represent evanescent waves, i.e., where

$$\varphi_{evan} = \sum_{n=1}^{\infty} c_n Z_n(z) e^{-m_n x}. \quad (2.61)$$

Again, the complex amplitude notation is defined so that,

$$\eta_{evan} = \hat{\eta}_{evan} e^{i\omega t}. \quad (2.62)$$

The level of distortion caused to the wave field presented in Figure 2.6 by the evanescent wave field, is plotted against the normalised distance, x/h , away from the wavemaker in Figure 2.7. The distortion at $x = 0$ caused by a piston wavemaker is shown as a function of kh in Figure 2.8.

2.4.2 Phase of evanescent waves

Each evanescent wave has a wavelength λ_n , which corresponds to the imaginary wavenumber, m_n , of the evanescent waves,

$$\lambda_n = \frac{2\pi}{m_n}. \quad (2.63)$$

The dispersion relation, Equation (2.52), imposes the condition

$$(\xi + 0.5)\lambda < h < (\xi + 1)\lambda, \quad (2.64)$$

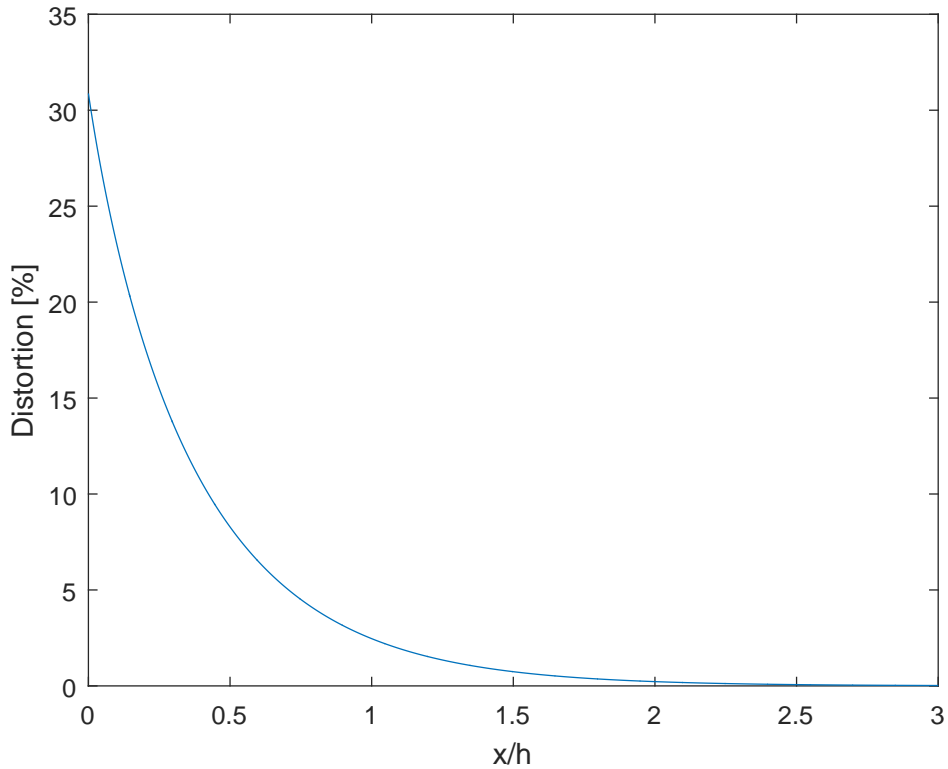


Figure 2.7: Distortion of the free surface from a piston wavemaker, including the first 50 terms of the velocity potential [$\omega = 6\text{rad/sec}$, $h = 0.6\text{ m}$ and $kh = 2.2512$].

on the imaginary wavelength λ_n , where ξ is some positive integer. It can be seen from Figure 2.4 that if this was not the case, the value $\frac{\omega^2}{m_n g}$ would be zero or negative, which is not possible. Subsequently, integrating the function $Z_n(z)$ over the depth of the tank will always give a positive value for any value of n . The Biesel coefficients, c_n , for a wave field generated by a single piston wavemaker, i.e., $c(z) = 1$, is an example of this,

$$c_n = \frac{1}{m_n h} \int_b^a Z_n(z) dz, \quad (2.65)$$

where $a = 0$ and $b = -h$. The limits $z = a$ and $z = b$ are the top and bottom of the wavemaker. However, this does not hold for wavemakers with different depth profiles. The reason for this is, as the amplitude of the evanescent wave changes over depth, it can cause the Biesel coefficient to be either positive or negative. This results in the phase of the evanescent wave being shifted by π radians. An example of this is the flap wavemaker, where the horizontal velocity components due to a selected few evanescent waves are plotted in Figure 2.9 over the depth of the wave tank. Comparing the results shown in Figure 2.9 to the corresponding results for a piston wavemaker in Figure 2.10, the evanescent wave's phase

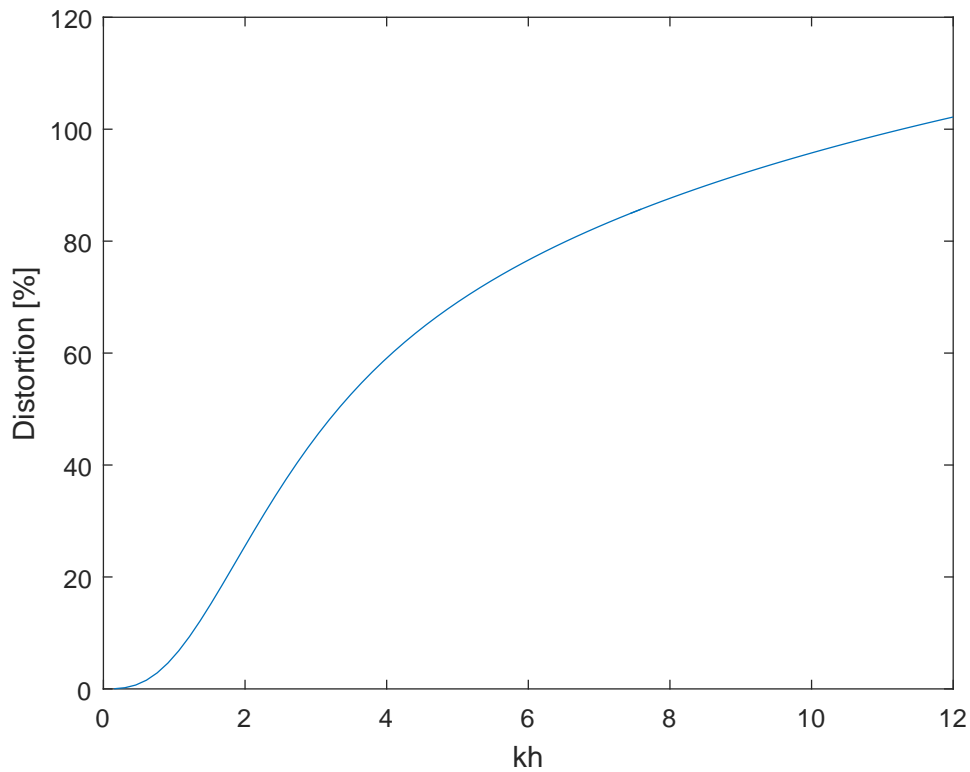


Figure 2.8: Distortion at $x = 0$ of the free surface caused by a piston wavemaker, including the first 50 terms of the velocity potential, where $h = 0.6$ m.

shift can be identified in Parts (a), (c), (e) and (g). It is the superposition of the waves in Figure 2.10 that provide the approximation of the piston profile in Figure 2.5. Not all evanescent waves experience this phase shift, as evident from Parts (b), (d), (f) and (h) in Figure 2.9. Superimposing the first fifty terms of the velocity potential, Equation (2.56), generated by a flap wavemaker and evaluating the distortion to the wave field, Equation (2.60), with $h = 0.6$ m and $kh = 2.2512$, in Figure 2.11 it is clear that the distortion is not a monotonic function of x . The interference pattern causes the distortion in Figure 2.11 to vanish at approximately $x/h = 0.1$ away from the wavemaker and then immediately increases again with x . Similarly, Figure 2.12 shows that the distortion is also not a monotonic function of frequency or relative depth, kh . This behaviour is due to an interference pattern occurring from superimposing the natural exponential functions in Equation (2.56) which have different exponents and both positive and negative coefficients. These findings are in agreement with those of [19] and [11], whose results show the summation of the evanescent waves' Biesel coefficients, Equation (2.55), change from negative to positive over frequency for flap wavemakers. Though both [19] and [11]'s results show this behaviour, neither offer an explanation as to why this behaviour occurs or the affect it can have on the

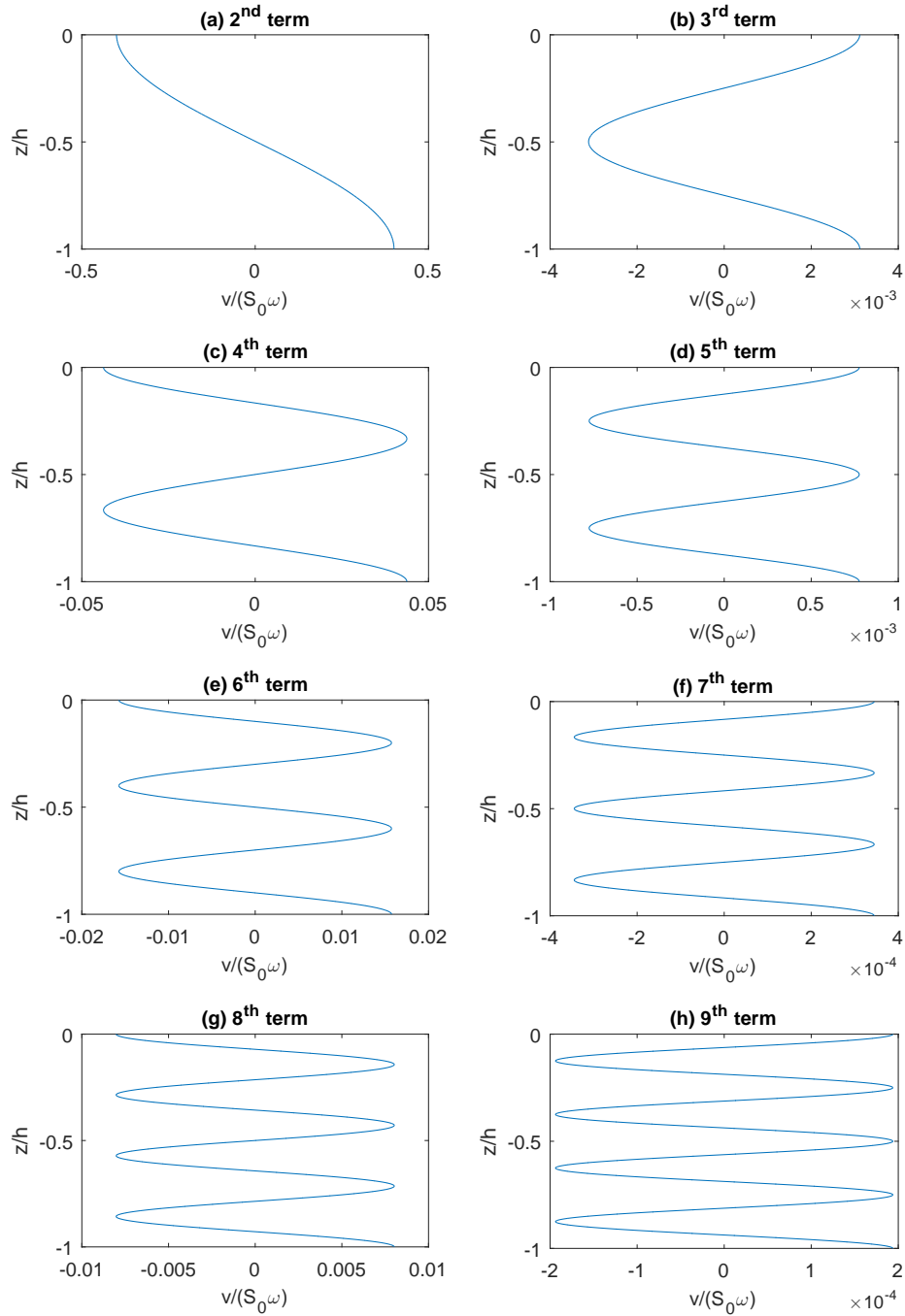


Figure 2.9: The horizontal velocity component of the fluid due to the (a) 2nd, (b) 3rd, (c) 4th, (d) 5th, (e) 6th, (f) 7th, (g) 8th and (h) 9th terms of the velocity potential generated by a flap wavemaker hinged at the wave tank's floor with a unit stroke, *i.e.*, $S_0 = 1$ m [$h = 0.6$ m, $\omega = 1$ rad/sec and $kh = 0.2499$].

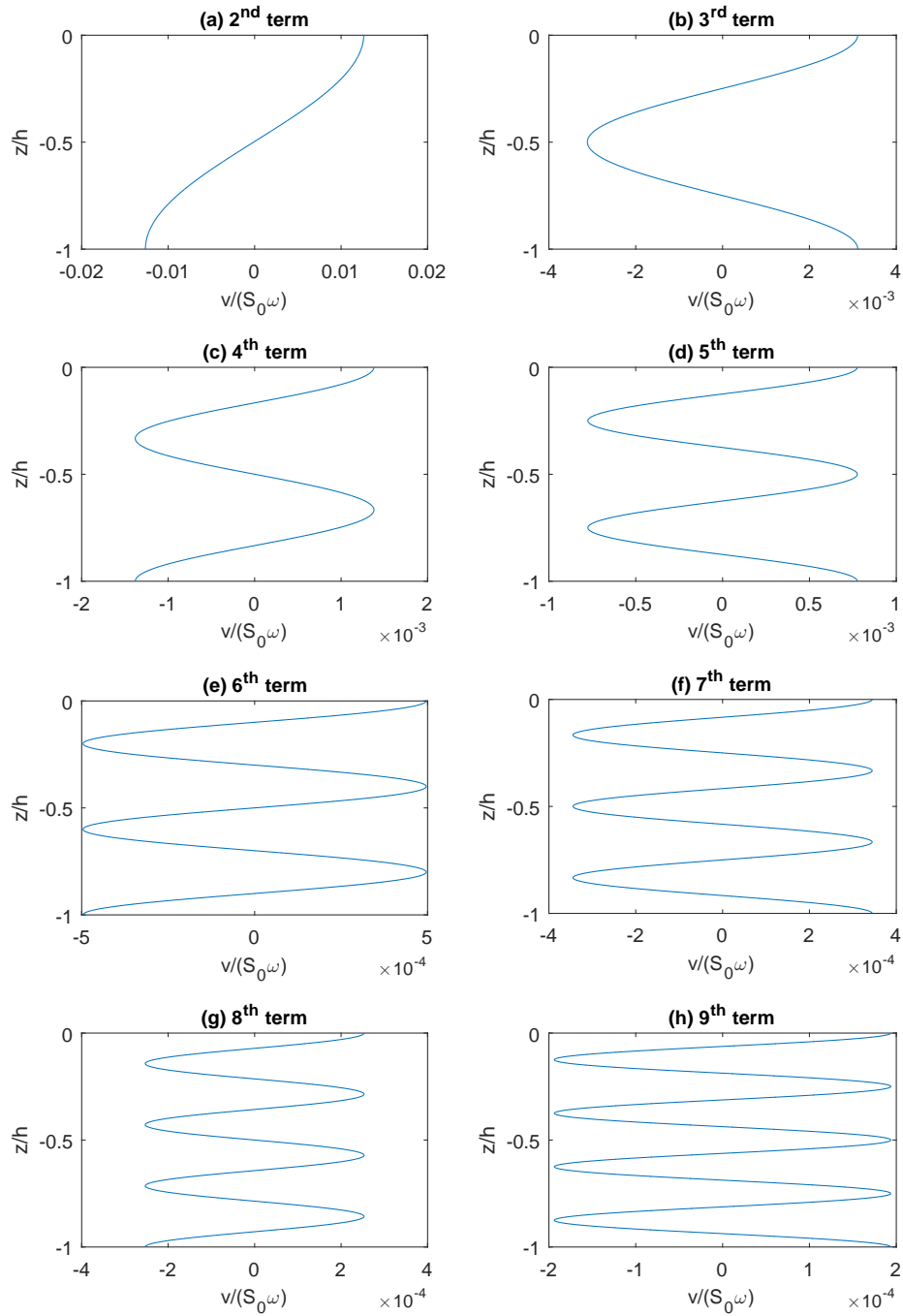


Figure 2.10: The horizontal velocity component of the fluid due to the (a) 2nd, (b) 3rd, (c) 4th, (d) 5th, (e) 6th, (f) 7th, (g) 8th and (h) 9th terms of the velocity potential generated by a piston wavemaker with a unit stroke, *i.e.*, $S_0 = 1$ m [$h = 0.6$ m, $\omega = 1$ rad/sec and $kh = 0.2499$].

wave field, probably because it was not the focus of either study. Consequently,

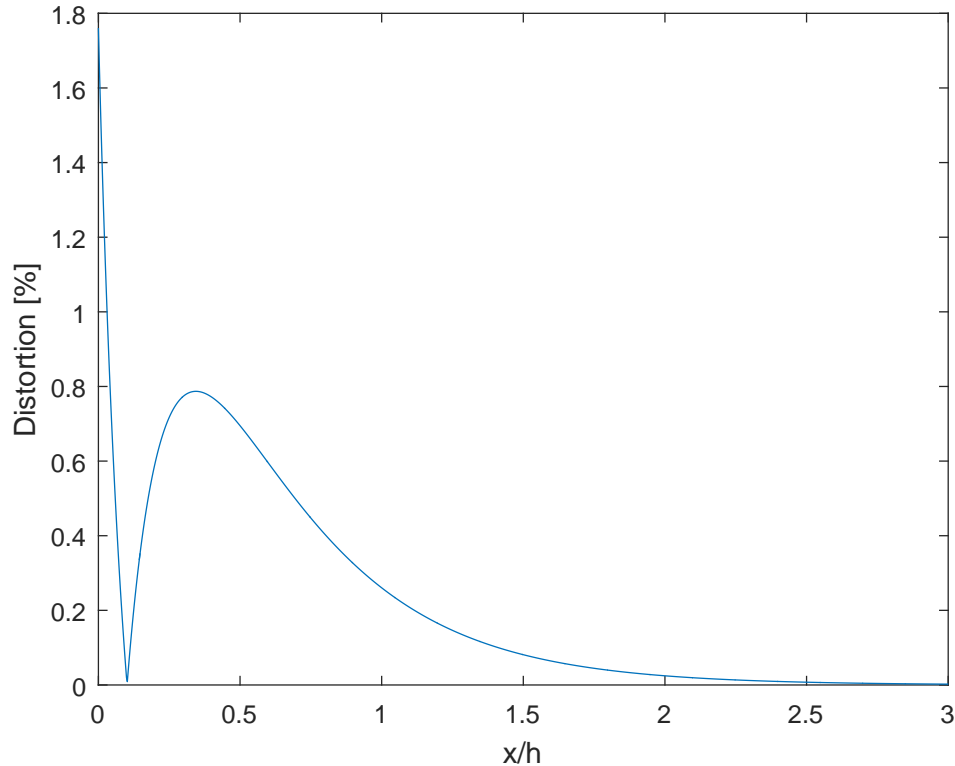


Figure 2.11: Distortion to the free surface against distance, x , away from the wavemaker, generated by a flap wavemaker hinged at the wave tank's floor, with $h = 0.6$ m, $\omega = 6$ rad/sec and $kh = 2.2512$.

reducing the distortion in the tank due to the evanescent waves is not necessarily a matter of trying to create a wavemaker that imitates a progressive wave, which is not practically possible. Instead we can propose the novel hypothesis:

Hypothesis 2:

The distortion of the wave field, and more specifically the distance of 1% distortion from the wavemaker, can be minimised by developing a multi-body wavemaker, which is designed to maximise the destructive interference between the evanescent waves.

The distance of 1% distortion is defined as the distance from the wavemaker to the point at which the distortion has decreased to 1% and does not increase above 1% for further increases in x and is denoted in the rest of the thesis as $X_{1\%}$. The concept of a multi-body wavemaker will be described in detail in Chapter 4. We aim to achieve this in two ways:

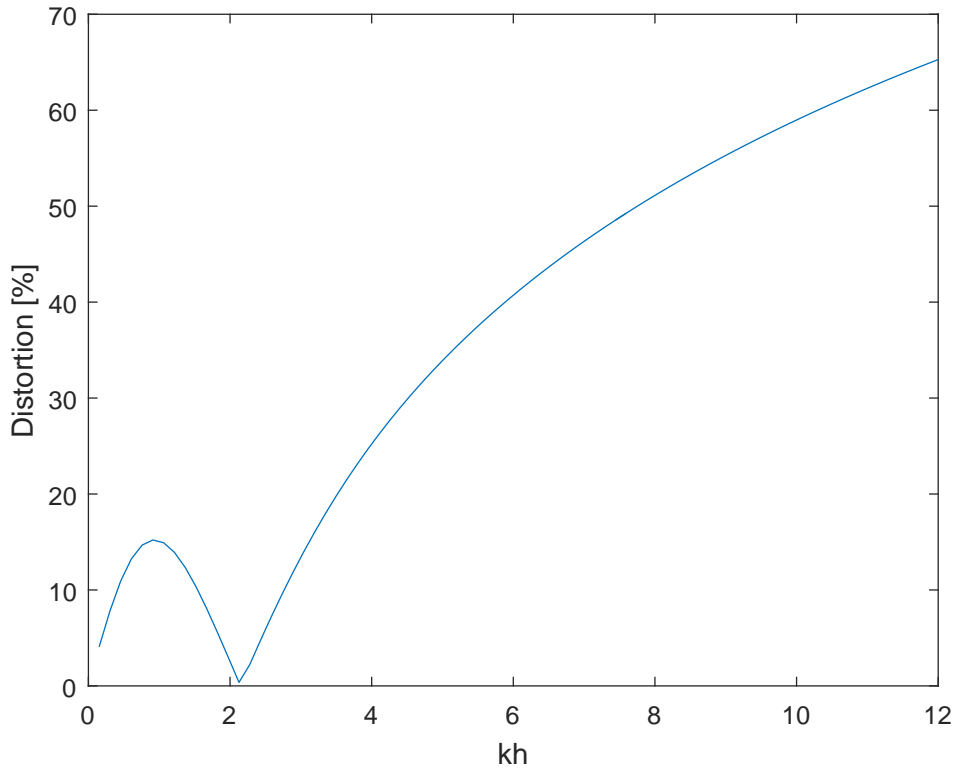


Figure 2.12: Distortion at $x = 0$ of the free surface caused by a flap wavemaker hinged at the wave tank's floor, including the first 50 terms of the velocity potential, where $h = 0.6$ m.

1. Optimising the upper and lower edges of each body in the wavemaker which are given as limits of the integral in Equation (2.65). This study is presented in Chapter 5.
2. Optimising the stroke amplitude of each individual body in the wavemaker system to achieve a depth profile, $c(z)$, for the wavemaker that minimises the distance of 1% distortion from the wavemaker, $X_{1\%}$. This study is presented in Chapter 6.

Hypothesis 1 and 2 do not strictly agree with each other. Hypothesis 1 suggests that the distortion caused by the evanescent waves can be minimised by designing a wavemaker's geometry so that its kinematics simulates the kinematics of the fluid in a progressive wave. On the other hand, Hypothesis 2 proposes to design the geometry of the wavemaker so as to optimise the phase shifts in the evanescent waves to cause the greatest level of destructive interference between evanescent waves, hence, minimising the distortion. Both hypotheses will be investigated in Chapters 5.

Though it is outside the scope of this thesis a simple experiment could validate the existence of the interference pattern between the evanescent waves, and thus

validate the phase shift experienced by some of the evanescent waves. By calculating the free surface elevation along the x axis at a given frequency generated by a flap wavemaker, similar to the free surface elevation shown in Figure 2.11, and generating an identical wave in a wave tank, the predicted free surface elevation can be compared to measurements of the free surface elevation taken in the tank, at specified locations using a wire gauge.

2.5 Validation of code

To validate that the in-house code used to generate the results in this thesis evaluated the wave field correctly, the Biesel coefficients, c_0 and c_n , are calculated by the in-house code and are compared with the expressions for the Biesel coefficients derived by [17] (also discussed in [13]). For a single piston wavemaker the Biesel coefficients predicted by both the in-house code and Maguire's expressions [17] are plotted as functions of kh in Figures 2.13. The Biesel coefficients for a single flap wavemaker, hinged on the wave tank floor, also predicted by both the in-house code and Maguire's expressions [17] are plotted as functions of kh in Figures 2.14. In both Figures 2.13 and 2.14, c_0 is presented in Part (a) while $\sum_{n=1}^{49} c_n$ is presented in Part (b). Figures 2.13 and 2.14 demonstrate that the wave field is being evaluated correctly by the in-house code as the results it generates are identical to those predicted by the expressions derived by [17]. Both sets of results are identical as they are both derived using linear potential wavemaker theory. In Part (b) of both Figures 2.13 and 2.14 the summation term was truncated at the 50th term of the infinite summation in Equation (2.56).

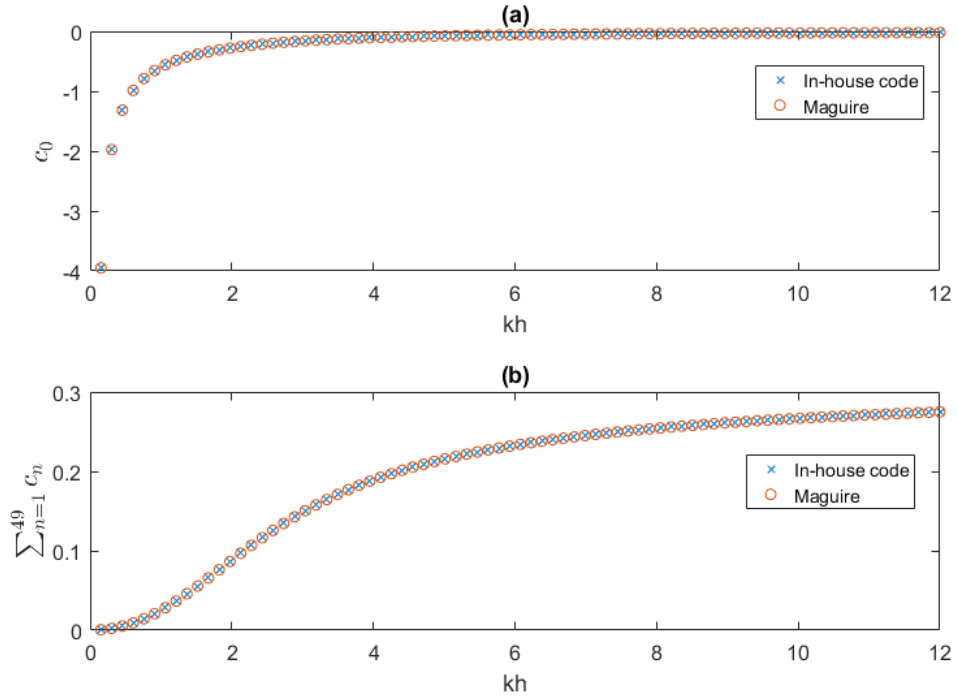


Figure 2.13: Comparison of the Biesel coefficients, (a) c_0 , (b) $\sum_{n=1}^{49} c_n$, for a single piston wavemaker calculated by the in-house code and those derived by [17], where $h = 0.6$ m.

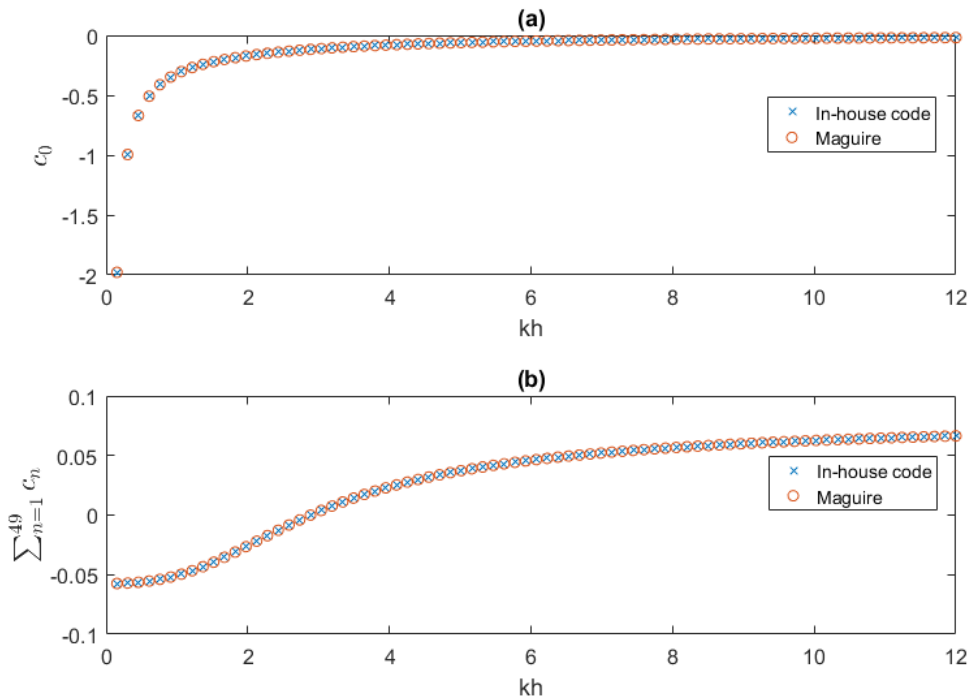


Figure 2.14: Comparison of the Biesel coefficients, (a) c_0 , (b) $\sum_{n=1}^{49} c_n$, for a single flap wavemaker, hinged on the wave tank's floor, calculated by the in-house code and those derived by [17], where $h = 0.6$ m.

Chapter 3

Designs of wavemakers: A literature survey

3.1 Introduction

Over the past hundred years wave tank testing facilities have been iteratively improved as new technologies emerged. Where once engineers were limited to wavemakers which offered little control over the sea-states generated, today we are spoiled by the use of rolling seals and effective active absorbers to create precise reproducible sea-states in wave tanks. The development of Numerical Wave Tanks (NWTs) has also helped to significantly improve the iterative prototyping process of devices. This chapter aims to present a survey of the wavemaker designs that have been developed to-date, what their purpose is and what their limitations are.

Section 3.2 provides a background of the development of different aspects in wavemaker theory. Sections 3.3 to 3.12 look at various designs of wavemakers, what their purpose is and how they perform. The chapter then goes on to discuss other topics that are relevant to wavemakers. Section 3.13 discusses different techniques that have been used for developing NWTs. Section 3.14 considers second-order wavemaker theory and Section 3.15 provides a brief discussion on the use of control systems in wavemakers.

3.2 History of wavemaker theory

Wavemaker theory was first presented by Havelock [8], who proposed a solution to the boundary value problem of the wavemaker for an incompressible and irrotational fluid. Havelock's solution required the superposition of an infinite number of waves in order to satisfy the boundary condition on the wavemaker, shown in Equation (2.35). This superposition is modelled by the infinite summation series in Equation (2.56), where each term in the series corresponds to an unique solution to the dispersion relation, discussed early on by [20], Equation (2.52).

The wave field generated during the transient starting and stopping stages of the wavemaker's motion was predicted by Madsen [21], who adopted the velocity potential presented by Kennard [20] which assumes the motion of the wavemaker starts from rest. Madsen [21] found that during the transient stages of the wavemaker's motion, waves are created with larger wave heights than intended. The effect of the larger wave at the end of a wave train is easily dismissed by simply ignoring the results from the end of the time series. However, a larger wave at the start of the wave train can be problematic, as the amplitudes of the waves following it taper towards the target amplitude. This effect has been shown to be more pronounced when the wavemaker starts from an extreme point [21]. Madsen [21] was able to minimise this problem by programming the wavemaker with a soft start, i.e., slowly increasing the amplitude of the paddle's motion towards the targeted stroke amplitude. Madsen [21] found very good agreement between their predictions and experimental results when they extended the linear transient wavemaker theory of [20] to the second-order.

Ursell *et. al.* [22] examined the limitations for which the assumptions of linear potential theory remain valid. Ursell *et. al.* [22] found that for a wave steepness range of $0.002 \leq H/\lambda \leq 0.03$ the experimental results for the wave height were, on average, 3.4% lower than the predictions of linear theory, with a scatter of 3% about the average. For greater wave steepness values of $0.045 \leq H/\lambda \leq 0.048$, the average error in the experimentally observed wave heights was 10% below the predicted values [22]. In a wave tank which had a constant depth of $h = 10$ feet in front of the wavemaker and then a constant depth of $h_f = 5$ feet after a gradual transition area, illustrated in Figure 3.1, [14] examined the validity of various wave theories for wave heights between 0.5 ft (0.05 m) and 1.6 ft (0.49 m). Chakrabarti [14] found that, after averaging the experimental results of the wave lengths that transitioned to shallower waters, airy wave theory (linear wave theory) holds for $0.56 \text{ ft/sec}^2 \leq h/T^2 \leq 3.2 \text{ ft/sec}^2$.

Although surface tension effects are negligible in linear wave theory, [23] pre-

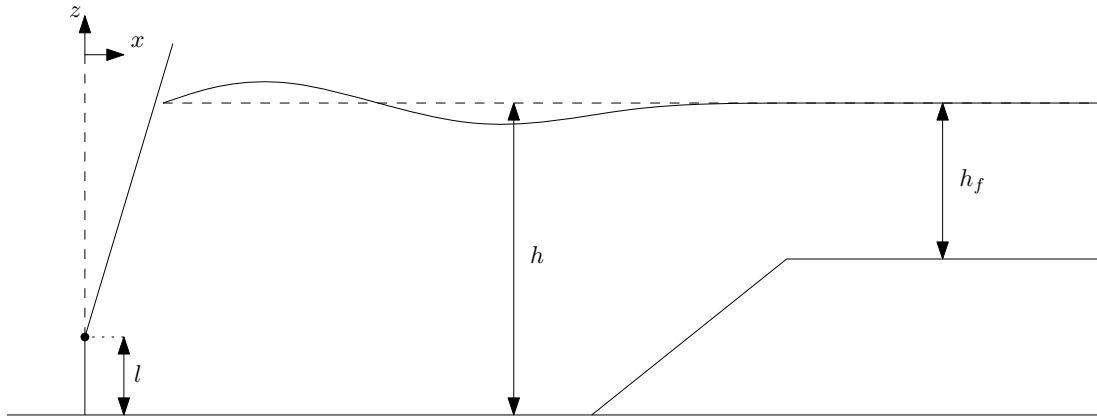


Figure 3.1: A wave tank with a gradual transition between two regions of constant still water depths.

sented a theory to account for surface tension. When predicting the wave field generated by a porous wavemaker paddle, [24] found that, using the model developed by [23], an evanescent wave field was predicted when the wavemaker’s angular frequency was zero. Chwang [24] provided the following explanation for this behaviour: *“In the absence of surface waves, ..., the fluid simply piles up in front of the wavemaker plate”*. Perhaps a more appropriate explanation for the effect [24] observed is simply capillary action, which is a well known effect of surface tension on a fluid’s free surface near a solid.

Many sources of literature use a parameter referred to as the wavemaker’s gain to assess the performance of the wavemaker. In line with most authors, in this thesis the gain is defined as the ratio of the progressive wave height to the amplitude of the wavemaker’s stroke, $\frac{H}{S_0}$. The stroke of a piston or flap is defined as the displacement of the paddle at the still water level from its mean position to its extreme position. Some other author’s definitions differ slightly, such as, $\frac{a}{S_0}$ or $\frac{S_0}{a}$, where a is the amplitude of the progressive wave, i.e., $H = 2a$.

3.3 Vertical paddle wavemakers

Flap and piston wavemakers are certainly the most common types of wavemakers. Their popularity can be attributed to their simple design, the repeatability of the sea states they create, that they can be analytically modelled and that they allow feedback absorption to be very effectively implemented. Many sources in the literature treat the flap and piston wavemakers as two separate designs, though they are closely related. For instance, consider the depth profile of the flap illustrated in Figure 2.1 Part (b) and described by Equation (2.13); if the

pivoting point of the flap was set so that $l = -\infty$, then the paddle's depth profile would be equivalent to that of a piston, Equation (2.12). The present section is dedicated to discussing the generalised design of vertical paddle wavemakers, where the traditional bottom hinged flap and the piston wavemakers are considered to be specific paddle designs with points of pivot at $l = 0$ and $l = -\infty$, respectively.

3.3.1 Design parameters

The two dimensional paddle wavemaker problem has two main design parameters which can be set: (a) the position of the point of pivot [25] and (b) the draft of the paddle [26], indicated in Figure 3.2. The selection of both parameters depends on the intended bandwidth of the waves the wavemaker will primarily be used to generate, as well as space restrictions that may exist in the wave tank. Two other design parameters can be considered: the submergence of the paddle (when the wavemaker does not pierce the free surface) and the angle between the paddle and the horizontal axis, indicated later in Figure 3.11. The submergence is mostly only relevant when considering the hydrodynamics of a submerged oscillating body. Paddles, for which the mean position is not normal to the horizontal axis, have been used for studying the generation of waves created by impulses in near-shore regions due to earthquakes [27] and are considered later in Section 3.8.

The wavemaker's point of pivot is generally chosen so that the motion of the wavemaker approximates that of the fluid in a progressive wave, thus reducing the contamination of the wave field by evanescent waves. It is generally accepted that piston wavemakers are ideal for generating low frequency, or shallow water waves, as the amplitude of the fluid's motion in such waves is almost uniform over depth. Similarly, for modelling high frequency, or deep water waves, flaps where $0 \leq l \leq h$ are advantageously used. When modelling waves within an intermediate bandwidth, a flap can be designed to have a virtual hinge below the floor of the tank, in this case l becomes negative. The concept of the virtual hinge (mentioned in Section 2.2) is achieved by having a second point of articulation at the bottom of the paddle.

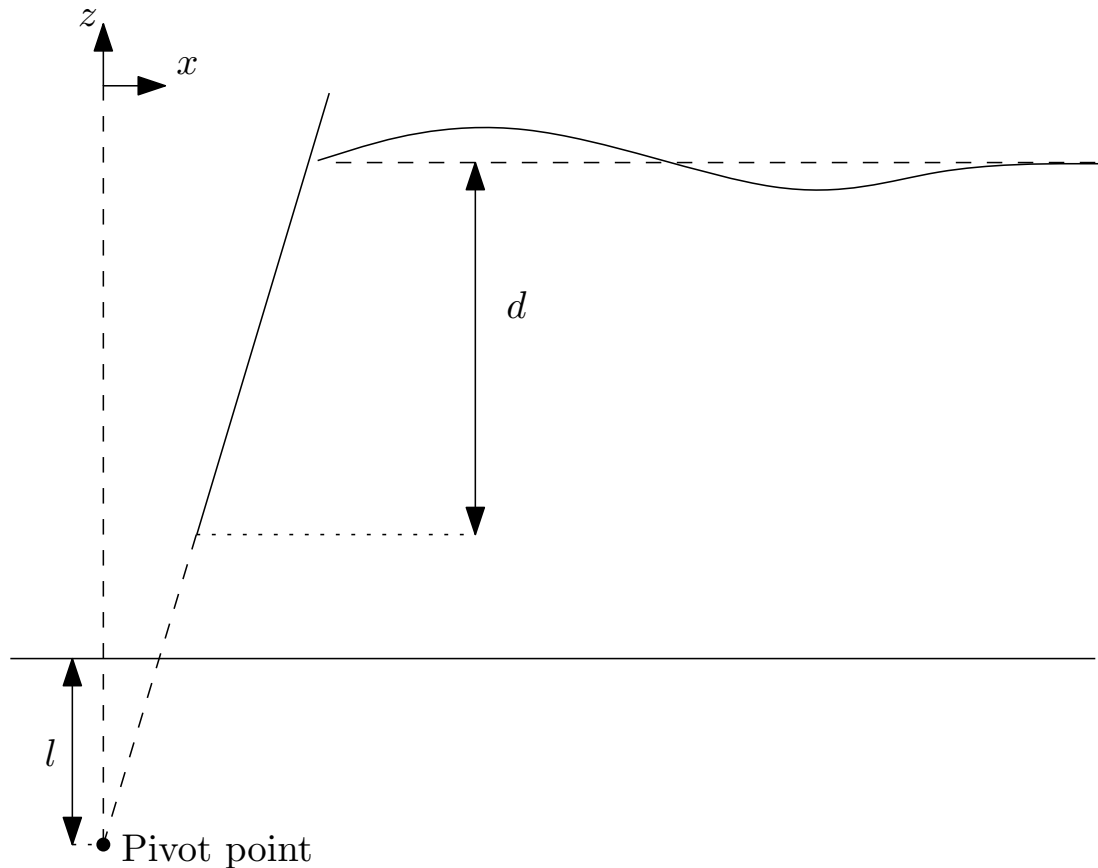


Figure 3.2: A wavemaker with a virtual hinge and a draft of d .

3.3.2 Consideration of evanescent waves

Biesel [9] extended the theory developed by Havelock [8] defining the depth profile of both a flap and a piston wavemaker of full draft, presented in Equations (2.12) and (2.13), respectively. This allowed for the velocity potential coefficients to be explicitly derived, Equation (2.55). Hyun [25] extended the wavemaker theory further by deriving an expression for the velocity potential created by a flap where the pivot point is positioned somewhere between $-h < z < 0$.

Hyun [25] considered the affect that the hinge height has on the amplitude of the evanescent waves by plotting the normalised horizontal displacement of the fluid particles on the surface of the wavemaker and the inertial pressure on the wavemaker, over the depth of the wave tank for a number of different hinge heights. The hydrodynamic inertial pressure and forces acting on the wavemakers are proportional to the amplitude of the evanescent waves, a relationship that will become more clear from Equation (4.4) and Section 4.4. Hyun's [25] analysis did not quantify the distortion to the intended wave field, caused by the evanescent waves, but it did show that flaps with shorter drafts reduce the inertial pressure, over depth, on the paddle at high frequencies. In general, [25] found that as the

frequency decreased, the lowest inertial pressure was achieved with increasing drafts. Hyun [25] remarked that flaps hinged closer to the free surface require much greater strokes in order to create waves of the same height; this can lead to the small angle assumptions and the condition of linearity being violated and suggests that a non-linear model should be employed. Both [25] and [28] found that in deep water waves, the hydrodynamic force on the wavemaker is largely due to the evanescent wave field. For intermediate and shallow water waves, the progressive wave is the main contributor to the hydrodynamic force, although the evanescent waves still have a notable influence [25, 28]. The predictions of [28] were supported by the experimental results from the companion paper [29], which had an average experimental error of 12.5% about Hudspeth's [28] prediction for the wavemaker gain.

3.3.3 Design curves

Probably the first practical guide to designing a flap or piston wavemaker was given by [26], who presented the design curves of the gain and hydrodynamic forces on a flap and piston wavemaker of full draft and a piston wavemaker with variable draft when generating regular (or monochromatic) waves. Gilbert [26] also provided similar design curves for generating irregular (or non-monochromatic) sea states, evaluating the maximum values for the wavemaker's stroke and driving force using the Cartwright method [30]. This work was extended by [28], who provided the same design curves for a flap wavemaker with a variable draft. The inertial force curves presented by [26] and [28] do not follow a monotonic behaviour over frequency. Neither study provides an explanation for this behaviour, however, from the discussion in Section 2.4.2, it would appear that this is due to the interference pattern between the evanescent waves. It has been well documented that full draft piston wavemakers have greater gains, producing larger wave heights for a given stroke, as they displace twice as much fluid as a full draft flap wavemaker [16, 25, 26, 31, 32].

3.3.4 Rolling seal design

To solve the problem of energy leaking around the sides of the paddle, [33] designed a rolling seal gusset to stop the flow of water down the sides of the paddle. The new gusset design had advantages for flap wavemakers as it meant that water could be removed from behind the paddle, effectively creating a dry-back flap wavemaker. The dry-back flap made it easier to implement force feedback control, as it removed the unpredictable hydrodynamic forces acting on the back of the flap caused by splashing water. Preventing the flow of fluid through the sides of the wavemaker also meant that accurate and repeatable directional waves could be generated by a bank of flaps positioned side-by-side. The use of seals on flaps has been quite successful at improving the wavemaker's accuracy and repeatability. Patel and Ionnaou [32] found that for waves with small steepness values, i.e., $0.0056 < \frac{2a}{\lambda} < 0.02$, where λ is the wavelength, the experimental results of the wavemaker's gain were within 2% of the predictions of potential theory. For steeper waves, i.e., $0.02 < \frac{2a}{\lambda} < 0.046$, [32] found the experimental results of the gain were within 3% of those predicted by potential theory. Patel and Ionnaou [32] suggested that these errors were due to the linear treatment of the reflected waves' influence on the free surface elevation.

Designing seals for piston wavemakers is however much more difficult. For a piston wavemaker, [32] reported that the energy leakage around the bottom of the piston was a significant issue with the potential theory over-predicting the experimental results by an average of 9.6%. Despite using seals, [22] found that linear potential theory over-predicted the experimental results by 10% for a piston wavemaker. The wedge-style piston, Figure 3.3, is often used as an alternative to seals [32], as it eliminates any splashing that would occur behind the paddle and thus eliminating the hydrodynamic forces from behind the wavemaker, however, it does increase the total inertia of the piston. A drawback to piston wavemakers is that they often require linear guides which introduce more friction into the mechanical system.

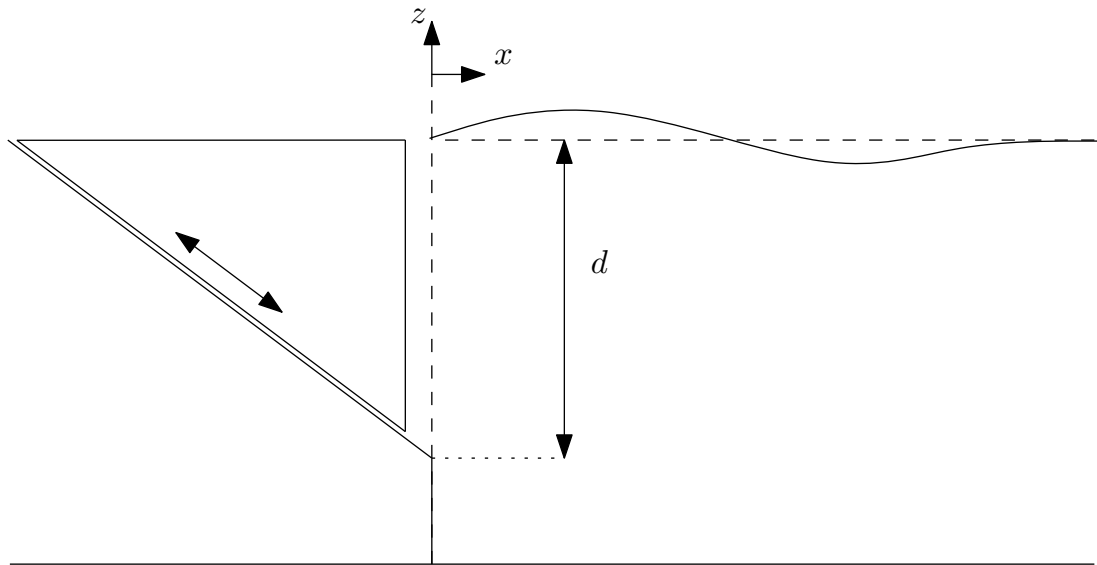


Figure 3.3: Design of a wedge-style piston wavemaker.

3.3.5 Double articulated paddles

As mentioned earlier in Section 3.3.1, for intermediate water waves a flap with a virtual hinge can be used, Figure 3.4. For monochromatic waves both articulation points will have the same frequency and phase. This can help the

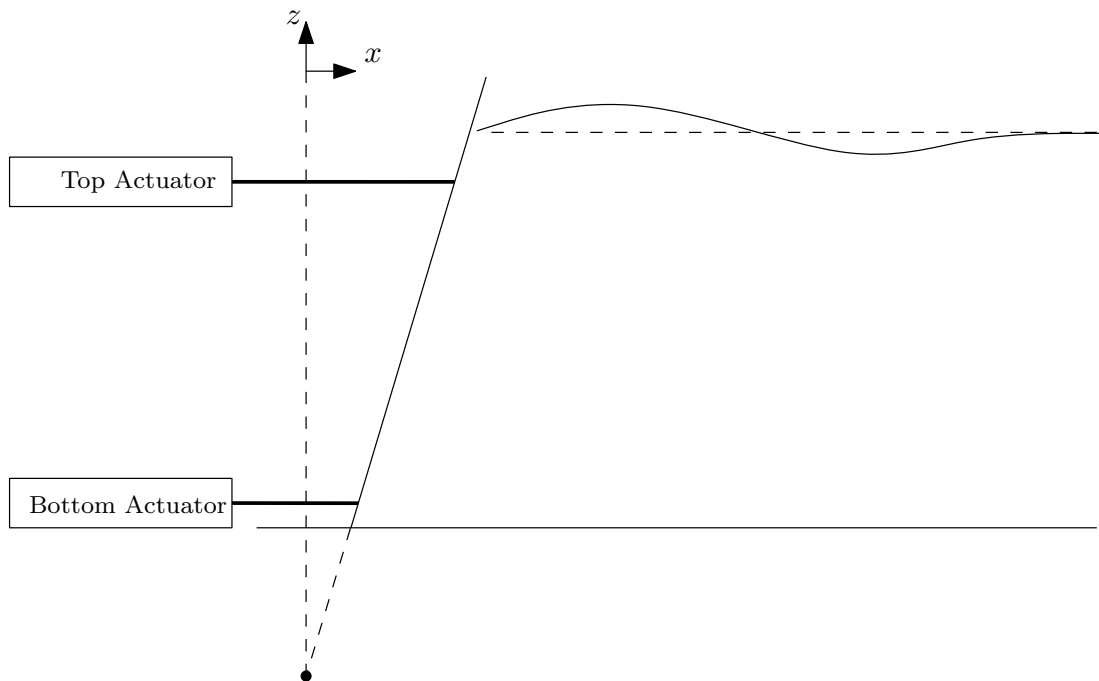


Figure 3.4: Design of a double actuated paddle.

paddle to better match the kinematics of the fluid in the progressive wave [34]. An extension of the theory derived by [9] for a flap wavemaker with a virtual hinge was presented by [34]. By providing a driving signal to the articulation

point at the bottom of the paddle, as well as the top, a wavemaker with a double actuated paddle can be well suited for generating both high and low frequency waves creating a buffer-tweeter type wavemaker. Such a wavemaker could be beneficial in generating two peaked Ochi-Hubble spectra [35]. When generating monochromatic intermediate waves, [35] found that their experimental results for the wavemaker's gain was in good agreement with the predictions of linear potential theory. However, when generating low frequency waves, the theory over-predicted the experimental results; [35] attributed this to the waves breaking in front of the paddle.

3.4 Double-flap wavemaker

The concept of a double-flap wavemaker, such as that use at the MARINTEK Ocean Laboratory and illustrated in Figure 3.5, was investigated by [4], who used linear wavemaker theory to predict the wave field generated by the two-body problem of the double-flap wavemaker. The angle between the top flap and

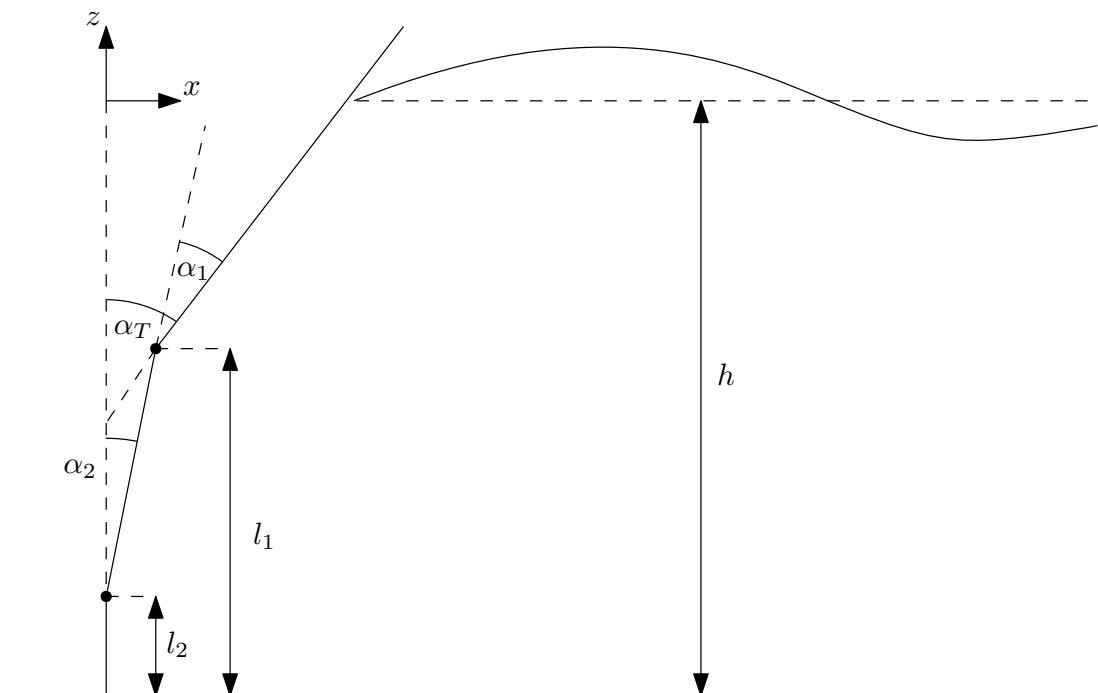


Figure 3.5: Design of a double-flap wavemaker.

the vertical axis is denoted as α_T while the angle between the bottom flap and vertical axis is denoted by α_2 . The acute angle between the flaps, indicated in Figure 3.5, is α_1 , giving: $\alpha_T = \alpha_1 + \alpha_2$. The height of the hinges, from the floor of the wave tank, are denoted as l_1 and l_2 for the top and bottom flaps, respectively.

Hyun [4] found that setting $l_2 = h/2$ and increasing the dimensionless parameter l_1/h from 0.5 (i.e., a single flap) to 0.9 resulted in the height of the generated wave decreasing as less fluid is being displaced by the wavemaker.

3.4.1 Effect on the evanescent wave field

Hyun [4] found that, for short and intermediate waves, increasing the angle ratio, $\frac{\alpha_1}{\alpha_2}$, reduces the inertial pressure, which is caused by a reduction the amplitude of the evanescent waves. Hyun [4] also reported that for $\frac{\lambda}{h} = 0.25, 0.5, 1$, the distortion of the wave field, due to the evanescent waves, at $x = 0$ decreases as $\frac{\alpha_1}{\alpha_2}$ increases. However, for longer waves, namely $\frac{\lambda}{h} = 2$, [4] found that the single flap configuration, i.e., $\frac{\alpha_1}{\alpha_2} = 0$, provided the lowest level of distortion. This result is hardly surprising given the discussion in Section 3.3.1. Clark and Menken [5] employed a linear regression method to find the most suitable angles for α_1 and α_2 , in order to minimise the error between the depth profiles of the progressive wave and the double-flap wavemaker. The double-flap wavemaker was designed with the parameters: $h = 16$ ft, $l_1 = 12.5$ ft and $l_2 = 7$ ft. Using the linear regression method, [5] found that for $\frac{\lambda}{h} < 2.2$ the top flap was in phase with the bottom flap. However, for $\frac{\lambda}{h} > 2.2$ the top flap was π radians out of phase with the bottom, i.e., they moved in opposite directions. At $\frac{\lambda}{h} = 2.2$, [5] found that the linear regression method determined the most suitable value for α_1 to be zero. When analysing the performance of the double-flap wavemaker on generating long waves, [5] observed reductions in the amplitude of the distortion to be in the range of 33% to 65% of that caused by a single flap wavemaker. Murdey [6] also reported that the linear regression method used by [5] for optimising the strokes of the flaps, provides better reduction of the distortion than setting $\alpha_2 = 0$, $\alpha_1 = 0$ and $\alpha_2 = \alpha_1$.

3.5 Plunger wavemaker

A plunger wavemaker refers to the heaving body type wavemakers illustrated in Figure 3.6. If the plunger is rectangular in shape, Figure 3.6 Part (a), then the principle of separation of variables, Equation (2.6), can be used [36] and the potential flow problem can be solved analytically [37], in the same manner as the flap and piston wavemakers. However, this cannot be done for the wedge or cylinder shaped plungers illustrated in Figure 3.6 Parts (b) and (c) [38, 39], respectively. Both of these designs must be modelled numerically [36]. It is

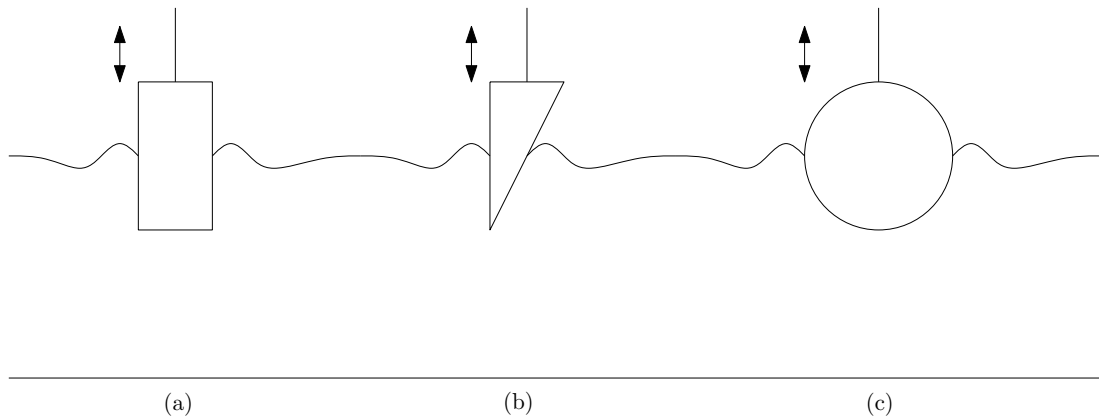


Figure 3.6: Plunger wavemaker designs.

important to differentiate between wedge-plunger wavemakers and the wedge-type pistons described in Section 3.3.4. The geometry of a plunger wavemaker is described by its draft, d , and its length, $b(z)$, which is a function of depth, Figure 3.7. Plunger wavemakers have the advantage of being very simple to

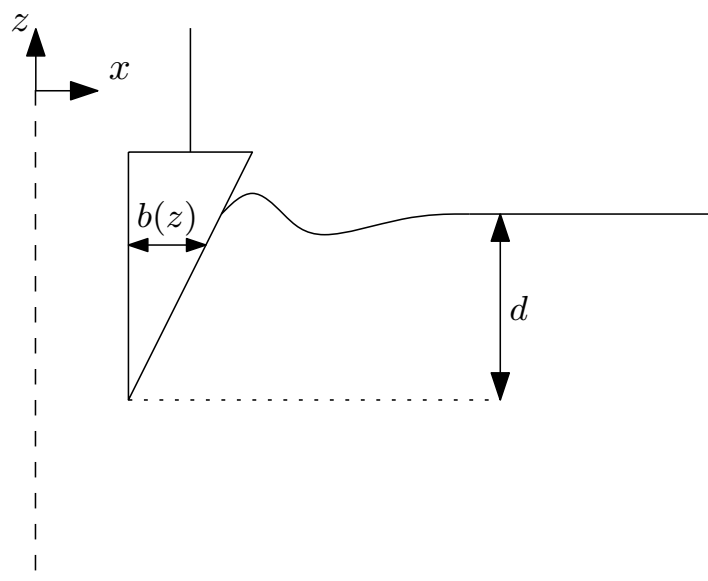


Figure 3.7: Design of a wedge plunger wavemaker.

construct. They remove the need for awkward rolling seals that have tendencies to leak, and since all of the wavemaker's mechanical components are contained above the water, they are easily adjusted and maintained.

Plunger wavemaker in wave basins

Many successful wave tanks have been built using plunging-wedge wavemakers, such as the AMOEBA (Advanced Multiple Organised Experimental BASin) [2]; a small circular tank with a diameter of 1.6 m and fifty plunging-wedge wavemakers around its circumference. Each of the wavemakers in the AMOEBA acts as an absorbing wavemaker and have proven to be very effective at cancelling out reflected waves [2]. Comparing the diffraction forces experienced by a model tested in the AMOEBA to similar tests in a larger wave basin, [2] found that both sets of measurements were in good agreement. This result indicates that small wave tanks may prove to be a useful tool for early stage testing of off-shore devices. Another advantage of the plunger wavemaker over both the flap and piston wavemakers is that, in a circular or curved tank with multiple wavemakers, the gaps between the plungers can be very small. This cannot be done when using flap or piston wavemakers in a curved tank, as slightly larger gaps are required between the wavemakers to ensure the paddles do not hit each other. As a result of larger gaps between the wavemakers, even with the use of rolling seals, the problem of energy leakage increases as does the occurrence of cross waves. The studies discussed in this section have documented the performance of plunger wavemakers using a variety of numerical modelling techniques. The merits and limitations of these numerical methods will be discussed later in Section 3.13.

3.5.1 Performance

Studying the radiated wave field created by a heaving rectangular wavemaker, [37] found that by increasing the length, b , of the plunger or decreasing the draft, d , leads to an increase in the wavemaker's gain. These results are echoed by [40] who also found that increasing the length-to-draft ratio, $\frac{b}{d}$, of a wedge-plunger wavemaker provides greater gain. Lee [37] also found that with increasing length-to-draft ratio the added mass and thus, the amplitude of the evanescent wave field, increased. Given that the wavemaking surface of a wedge-plunger wavemaker is not vertical, like the piston and flap wavemakers discussed in Section 3.3 in their mean position, the wave motion is created in the fluid at different positions on the x -axis over the depth. This leads to the fluid motion not having a constant phase over a vertical slice through the fluid. As a result, a destructive interference pattern arises, reducing the height of the progressive waves. This effect is not noticeable at low frequencies, but becomes very pronounced at high frequencies when the change in $b(z)$ becomes comparable to the wavelength of the radiated wave. Evidence of this has been reported by [41] and [42], who showed that

the gain initially increases with frequency until reaching a maximum, it then decreases with further increases in frequency.

Wang [41] estimated that the evanescent wave field created by wedge-plunger wavemakers can have an amplitude of 10% of the progressive wave amplitude at $x = 1.4h$, for high frequency waves. However, having only one measurement point means that the distortion cannot be interpolated for other distances away from the wavemaker; as Section 2.4.2 suggests, the distortion pattern along the x -axis cannot be easily predicted. Although not discussed, the distortion measurements presented by [41] are not monotonic over frequency, indicating the existence of an interference pattern between evanescent waves in anti-phases with one another, proposed in Section 2.4.2. Wu [38] found that the water depth has a significant affect on the wavemaker gain, with the gain decreasing as the still water depth increased. Similar observations were also made by [22] for the case of a piston wavemaker. Mikkola [42] found that increasing the length-to-draft ratio, and thus the wedge angle, increased the non-linearities in the wave form as the wave became asymmetrical about the horizontal and vertical axes.

The potential theory model developed by [37] proved to be very reliable for the special case of the heaving rectangular body, when [37] compared the predictions of the wavemaker's gain with those of a Boundary Element Method (BEM) and the experimental results of [43]. Comparing the predictions of the added mass and radiation damping from the analytical model and the BEM also showed good agreement. Comparing the conformal transformation method developed by [41] to Wu's [38] Boundary Collocation Method (BCM), both models are in good agreement with Wang's [41] experimental results of the wavemaker's gain for $b/d = 0.725$ (i.e., $\frac{d}{b} = 1.38$). However, for $b/d = 0.459$ (i.e., $\frac{d}{b} = 2.18$) the predictions of [38] diverge and become unreliable when $kb > 1.5$. The experimental results presented by [41] are scattered about the predictions of the conformal transformation method by approximately 6.5%, which is deemed to be an acceptable experimental error. Both Wang's [41] conformal transformation and Wu's [38] BCM over-estimate the experimental results for a wedge-plunger at $\frac{b}{d} = 0.625$ (i.e., $\frac{d}{b} = 1.6$) presented by [44]. Ellix and Arungam [44] attribute these discrepancies to energy leaking around the sides of and behind the plungers. To address this problem, [45] developed a Boundary Element Method (BEM) with a wedge-plunger wavemaker that accounted for the effects of energy leakage. The results showed that Wu's [45] BEM is a more superior model than those presented by [41] and [38] based on a comparison with the experimental results of [44].

3.5.2 Exponentially shaped plunger wavemaker

An exponentially shaped plunging wedge wavemaker was suggested by [46] to match the kinematics of a progressive deep water wave in an attempt to eliminate the evanescent wave field. The profile of such a wavemaker, illustrated in Figure 3.8, would be defined as:

$$b(z) = \beta \frac{\sinh[k_t(z+h)]}{\cosh(k_t h)}, \quad (3.1)$$

where β is a small constant of the same order as the free surface elevation [46]. It should be noted that the kinematics of a progressive wave only approximate an exponential function in deep water waves and that for shallow water waves Equation (3.1) resembles the uniform depth profile of a piston. The exponential-plunger can only be effective at eliminating the evanescent wave field at its geometrically tuned frequency, with $k = k_t$. Since the exponential-plunger's wave-making surface is not vertical, it suffers from the same inherent problem as the triangular wedge-plunger, that is, the fluid motion in a vertical slice will not be in phase over the depth, leading to significant loss in the wave height for high frequency waves.

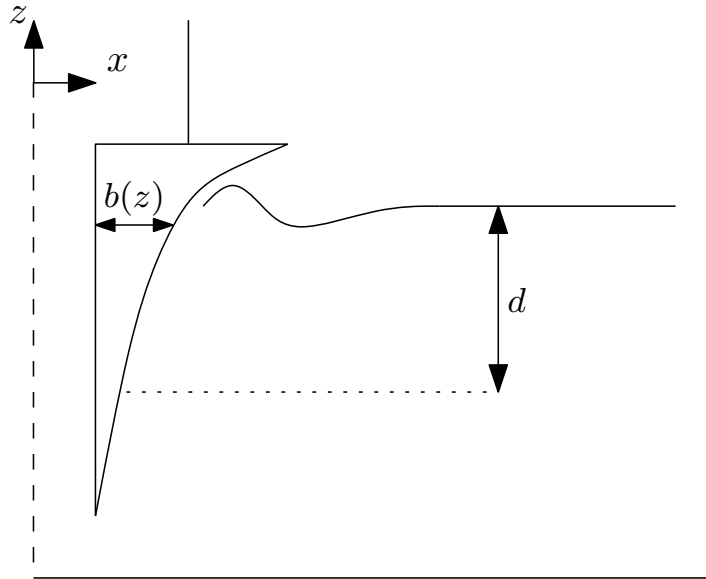


Figure 3.8: Design of an exponentially shaped plunger wavemaker.

3.6 Flexible wavemakers

A number of sources in the literature have discussed the concept of a flexible wavemaker that can bend to have the same depth profile as a progressive wave [3, 9, 13, 34, 47, 48], Equation (2.57). This allows the wavemaker to generate progressive waves without an evanescent wave field. The depth profile of such a flexible wavemaker, illustrated in Figure 3.9 Part (a), would be set as:

$$c(z) = \frac{\cosh[k_t(z + h)]}{\cosh(k_t h)}, \quad (3.2)$$

where k_t is the geometrically tuned wavenumber [13]. Inserting Equation (3.2)

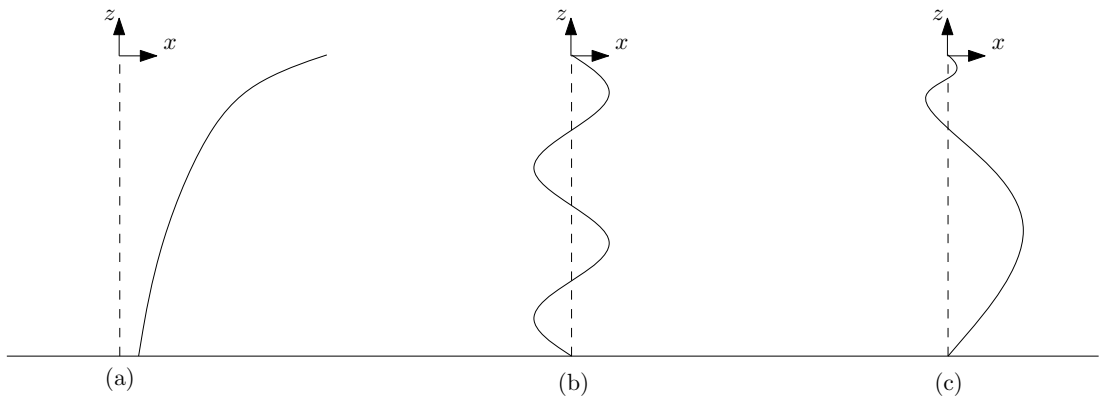


Figure 3.9: Profiles of flexible wavemakers, (a): Cosh, (b): Cos and (c): panchromatic spectrum.

into the expression for the Biesel coefficients, Equation (2.55), and then calculating Equation (2.56), the terms which represent evanescent waves vanish. However, the geometry of the flexible wavemaker can only be tuned to one frequency. In order to create progressive waves at other frequencies without any evanescent waves, the geometry of the wavemaker would need to be changed. Another design for a flexible wavemaker was proposed by [13] to generate only one evanescent wave, with an imaginary wavenumber m_n , and no progressive wave. This could be achieved with a wavemaker that has a depth profile, illustrated in Figure 3.9 Part (b) and defined as:

$$c(z) = \frac{\cos[m_n(z + h)]}{\cos(m_n h)}. \quad (3.3)$$

When generating a spectrum containing more than one frequency, the geometry of the ideal wavemaker becomes more complicated. As the different frequencies in the spectrum are mixed together with random phases, the depth profile of the wavemaker will be required to change in real time, and can form a more

complicated curve like that shown in Figure 3.9 Part (c). Obviously, it is not possible to build such a device, and to the authors knowledge there is no information available for such a numerical flexible wavemaker generating panchromatic spectra.

3.6.1 Evaluation of the evanescent wave field

Maguire and Ingram [48] investigated wavemakers with depth profiles described by both Equations (3.2) and (3.3), using analytical wavemaker theory; for the rest of this thesis these wavemakers will be referred to as the cosh and cos wavemakers, respectively. Maguire and Ingram [48] found that, at the wavemaker's geometrically tuned frequency, the added mass of the cosh wavemaker went to zero, indicating that no evanescent waves were generated; an explanation of this reasoning is provided in Section 4.4. Similarly, [48] also found that at the tuned frequency of the cos wavemaker the radiation damping of the wavemaker went to zero, indicating that no progressive wave was generated; again this reasoning is explained in Section 4.4. At either side of the tuned frequencies, [48] found that the added mass and radiation damping of the respective wavemakers increased quite rapidly. These results demonstrated that there is little value in constructing a cosh wavemaker that is geometrically tuned to only one frequency for the purpose of reducing the evanescent waves. However, the cosh wavemaker design has a lower added mass than a flap wavemaker which may prove useful for the purpose of absorbing waves, particularly at high frequencies. Another effect of the mismatch between the wavemaker's motion and the motion of the fluid in a progressive wave are spurious free waves which arise in second-order waves and panchromatic sea-states, spurious waves will be discussed further in Section 3.14. As far as the author is aware, no study has been done to date to see how the cosh wavemaker reduces the effect of spurious waves when generating panchromatic sea-states.

3.6.2 Construction of a flexible design

A cosh wavemaker, constructed as a cantilever beam and geometrically tuned to a single frequency, was installed in a wave tank in the Water Research Laboratory at the University of New South Wales [47]. However, no information is available on the performance of the cantilever wavemaker's ability to reduce the evanescent wave field. A design similar to the cantilever wavemaker was discussed in [9], which involved a flexible membrane actuated at several points over the depth by different sized gears. The depth profile of the wavemaker was controlled by choosing correctly sized gears. Biesel and Suquet [9] reported that this flexible membrane generated waves of a rather pure form. However, the inconvenience of changing the gear sizes for every frequency the user wanted to generate and problems with maintaining the seals proved to be too cumbersome [9, 34].

3.7 Pneumatic wavemakers

The design for a pneumatic wavemaker is shown in Figure 3.10. By injecting pressurised air into the chamber and releasing it through valves, the water surface in the chamber is forced to oscillate, thus, creating a radiating wave. Essentially the concept of a pneumatic wavemaker is an oscillating water column wave energy converter operating in reverse. An approximate theory for the wave field generated by the pneumatic wavemaker was presented in [49] for generating oscillating and surging waves.

Although pneumatic wavemakers are easy to construct, they have some inhibiting characteristics. Keulegan [49] found that it can be difficult to control the air pressure when the air is first injected into the chamber. This can cause some unwanted fluctuations in the free surface, though it only seems to last for a short period of time. O'Dea and Newman [50] found that non-uniform distribution of pressure in the chamber when the air is injected can lead to cross waves. Additionally, the transfer functions for the pneumatic wavemakers can be non-linear and difficult to calculate [50].

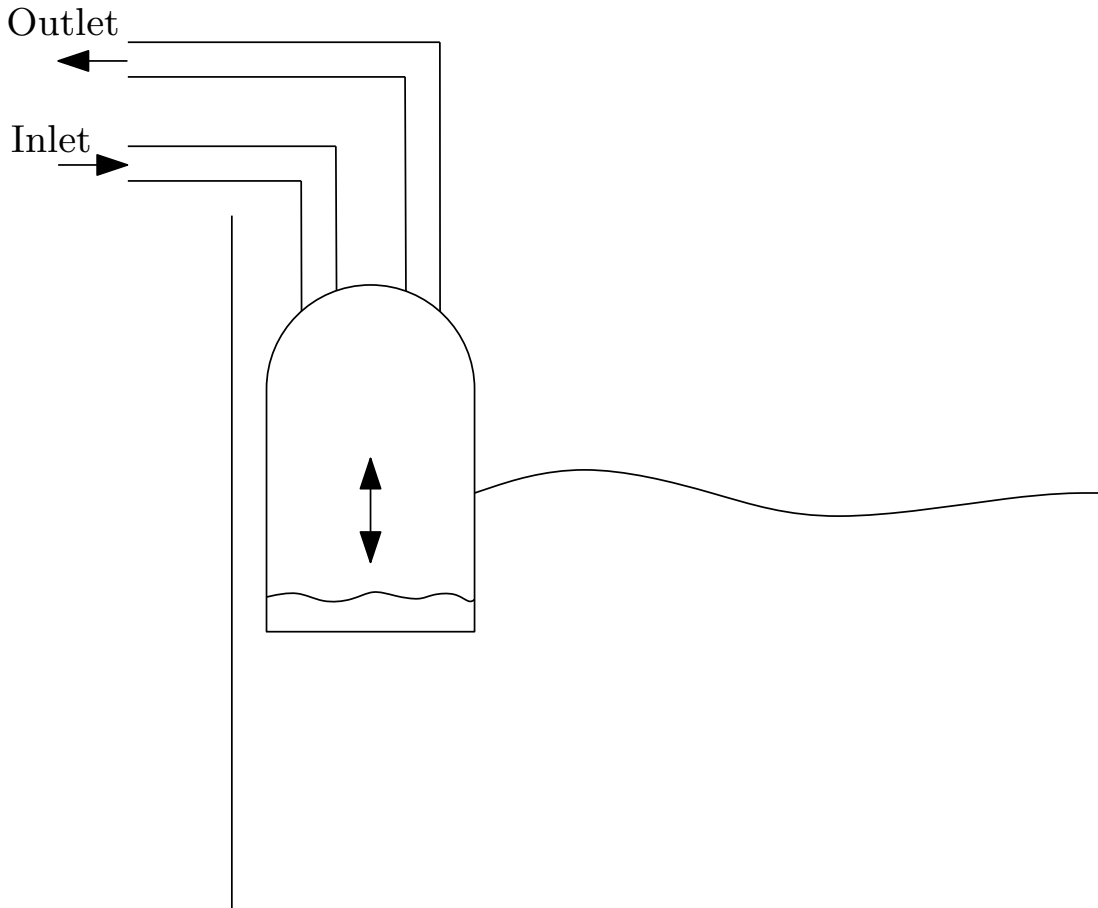


Figure 3.10: Design of a pneumatic wavemaker.

3.8 Inclined flap wavemaker

As mentioned in Section 3.3.1, inclined flap wavemakers, illustrated in Figure 3.11, have been used to model waves generated by the impulsive movement of sloping near shore regions, due to earthquakes [27, 51]. The problem of the inclined flap wavemaker has some similarities to the wedge-plunger problem. Firstly, the principles of separation of variables cannot be employed, so the problem must be solved numerically. Secondly, since the wavemaking surface is not vertical at its mean position, then in the same manner as discussed in Section 3.5.1, there will be a loss in wave height at high frequencies. In Region 1 of the fluid domain, indicated in Figure 3.11, this behaviour becomes more pronounced as Ω decreases, and hence, the angle between the flap and vertical axis increases. In Region 2 of the fluid domain, indicated in Figure 3.11, the loss in wave height at high frequencies is quite gentle. The greatest value for the wavemaker's gain is achieved in Region 2 with $\Omega = 70^\circ$ [51]. To solve the problem of the inclined flap wavemaker, [27] developed a BEM, while [51] used a BCM.

For a flap wavemaker, with $\Omega = 90^\circ$, the predictions of both Raichlen's [27]

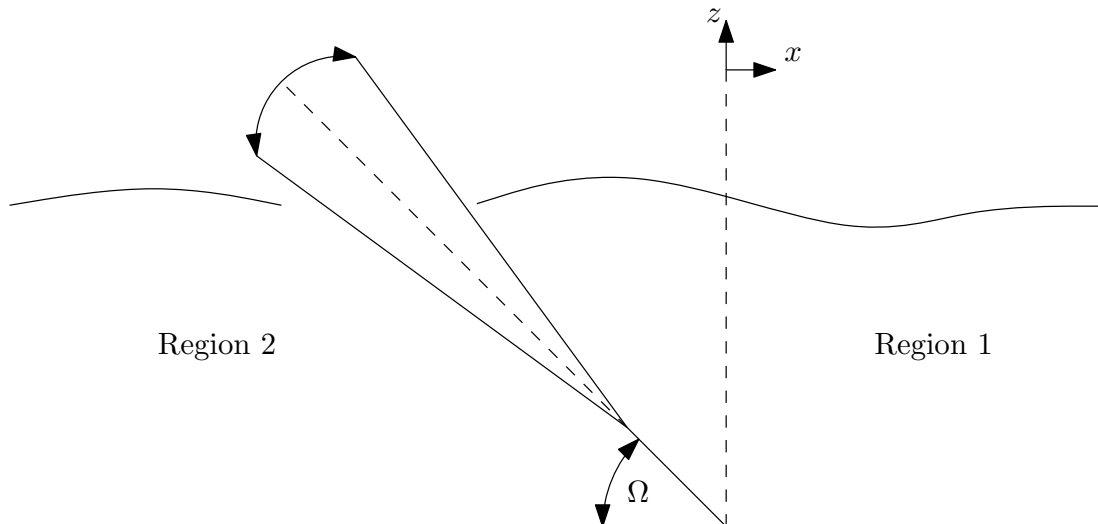


Figure 3.11: Design of a inclined flap wavemaker.

BEM and Wu's [51] BCM for the wavemaker's gain showed good agreement with the linear wavemaker theory, although the BCM performed slightly better than the BEM. Comparing the BEM and BCM to experimental results of a flap wavemaker's gain with $\Omega = 33.85^\circ$, [51] found that Raichlen's [27] BEM predicted the gain slightly more accurately for lower frequencies, while the BCM under-predicted the gain. For a flap angle of $\Omega = 45^\circ$, [51] found that both models drastically over-predicted the experimental results. Given the importance of accounting for energy leakage [45], the errors of the predictions may be considered to be within an acceptable bracket.

3.9 Duck wavemaker

Salter [52] proposed a wavemaker based on the Edinburgh duck wave energy converter operating in reverse, illustrated in Figure 3.12. The device combined the duck's geometry with a force feedback control system, allowing the wavemaker to act as an active absorber, cancelling out waves incident on the wavemaker. Since the duck's wavemaking surface is not vertical, the issue of loss in wave height at high frequencies may arise. However, bearing in mind the findings of [51] for the inclined flap wavemaker's gain in Region 2 of Figure 3.11, it is likely that the effect of the destructive interference will be negligible for a duck wavemaker.

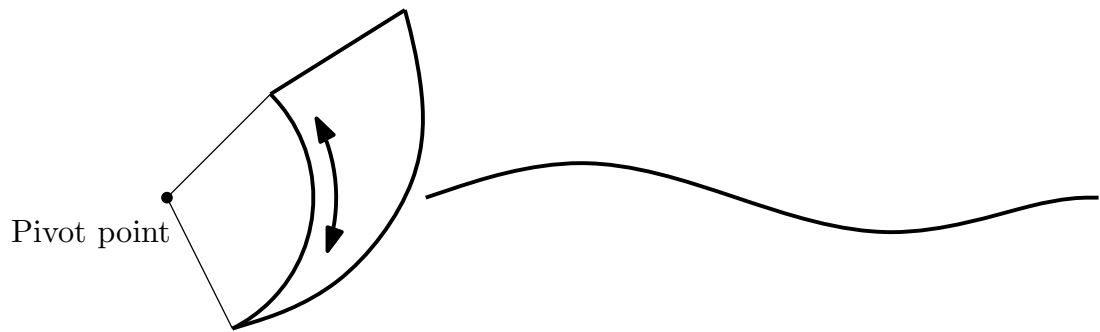


Figure 3.12: Design of a duck wavemaker.

3.10 Porous wavemakers

The porous wavemaker can be useful for understanding the effectiveness of damping zones. Sahoo [53] modelled the wave field generated by an oscillating cylindrical wavemaker surrounded by an outer porous cylinder. The aim was to understand the hydrodynamic forces experienced by a pile protected by a porous damping zone. Chwang [24] developed an analytical model for a porous piston wavemaker based on Taylor's [54] model of flow through a porous medium. The aim was to understand how the generated wave field was influenced by the dynamic viscosity, which is described as being similar to the Reynold's number for flow passing through the pores. Naturally the more porous the wavemaker is, the smaller its gain [24].

3.11 Sloped Piston

Two models of a piston wavemaker with a sloped face have been developed by [55] and [56] in order to estimate the hydrodynamic forces experienced by a sloped dam during an earthquake. The first approach was based on the Von Karman's momentum-balance method [55] and the second was a conformal transformation method used to solve the linear potential theory problem [56]. Comparing both models, there are significant discrepancies in the hydrodynamic pressures as functions of depth. However, after integrating the pressures over depth, the

hydrodynamic forces predicted by both approaches showed excellent agreement [56].

3.12 Spiral wavemaker

Dalrymple and Dean [57] developed the linear potential theory for a vertical cylinder moving in small circular patterns uniformly, Figure 3.13 Part (a), or with the bottom held stationary like a flap, Figure 3.13 Part (b). This spiral wavemaker was designed to model sediment transport by waves approaching a beach at an angle. Dalrymple and Dean [57] found that the wave crest radiated from the wavemaker could be described by an Archimedean spiral. The predictions for the wavemaker's gain were in good agreement with experimental results for $kh < 2$. Above this limit flow separation occurs and the assumption of the fluid being inviscid becomes invalid [57].

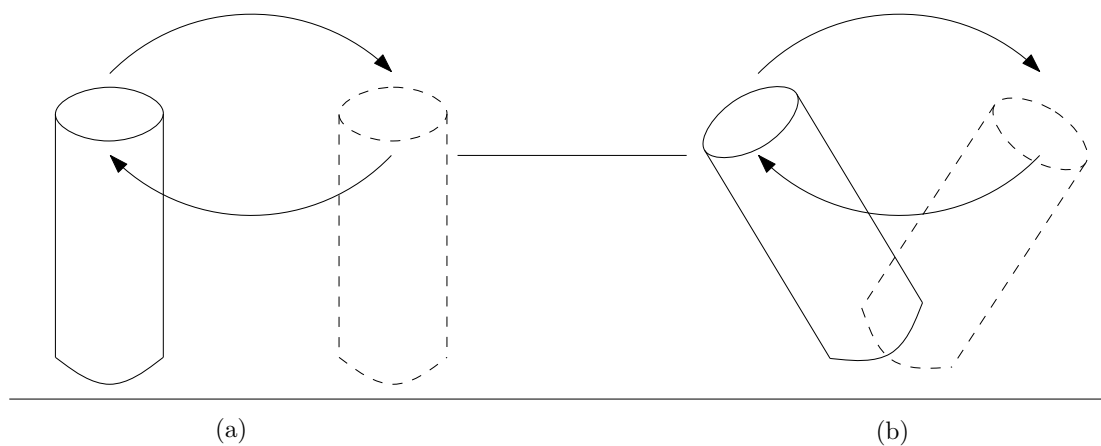


Figure 3.13: Spiral wavemakers.

3.13 Numerical wave tanks

The results presented in this thesis were generated using the analytical wavemaker theory developed in Chapter 2 and the hydrodynamic theory developed later in Chapter 4 which was implemented using an in-house code. The benefit of this approach over using a Numerical Wave Tank (NWT) is that it requires less computation time; this is significant when optimising the geometry of the wavemaker where the wave field is calculated several thousands of times. For this reason, NWTs are not directly relevant to the work presented in this thesis. However, given the extensive use of NWTs in off-shore engineering, the author felt it appropriate to include a section discussing the different approaches used to develop NWTs, with the aim to help inform any engineers who may be new to the area.

The use of NWTs can provide a lot of flexibility to researchers when prototyping and modelling off-shore and coastal structures; designs of devices can be easily and frequently adjusted to test different parameters without significant additional financial costs. A benchmark presented by [58] compared the predictions of four different fully nonlinear BEMs, a second order BEM, a fully nonlinear Finite Element Method (FEM) and a fully nonlinear Finite Volume Method (FVM), for a wave field generated by a heaving wedge-plunger wavemaker in a NWT to the experimental results presented by [59]. The results show that all the fully nonlinear NWTs agree with the experimental results quite well, however, the second order BEM shows notable discrepancies in predicting the experimental results. Since NWTs are not restricted to the same limitations as physical tanks, some authors have found innovative ways of generating waves to eliminate unwanted effects like evanescent waves, such as the spinning dipole wavemaker [60], discussed in Section 3.13.1. The following sections present different techniques for modelling NWTs and wavemakers, and discusses the experiences some researchers have had using them.

3.13.1 Spinning dipole wavemaker

Clement [60] developed a concept for a numerical wavemaker which resembles a spinning dipole in electromagnetism. The spinning dipole wavemaker can generate wave fields described by the kinematics of a progressive wave, hence preventing the generation of evanescent waves. Clement [60]'s spinning dipole wavemaker also does not interact with incident waves, allowing them to pass straight through without any reflections. A damping zone behind the wavemaker

can then be used to prevent the waves being reflected back towards the testing area [60].

3.13.2 Boundary element method

An advantage of potential theory is that the flow at any point in the fluid domain can be evaluated from the information supplied at the boundaries of the domain [61]. The BEM creates a mesh along the boundary of the domain and solves the boundary conditions using a boundary integral equation that can be formulated by Green's identity [45, 61]. An alternative BEM was developed by [62], for solving transient and non-linear waves using Cauchy's integral theorem. Dold and Peregrine [62] claimed that this was less computationally expensive.

BEMs can be very useful for modelling more complex features such as complex bathymetry as well as wave-structure interactions for geometries where the principle of separation of variables, Equation (2.6), cannot be used [61, 63]. Grilli and Watts [63] used the BEM developed by [61] to model a wave field generated by a landslide at a sloped coastal region. O'Dea and Newman [50] simulated a directional wavemaker in a three dimensional NWT using WAMIT, a commercial BEM code. A nonlinear BEM was developed by [64] to model the wave field generated from a wedge-plunger wavemaker.

Absorption of unwanted waves in a BEM

Absorbing unwanted reflected waves is as much of a problem in NWTs as it is in physical wave tanks. A common technique for absorbing short waves is a numerical beach. In a BEM, this is a damping zone at the end of the NWT, achieved by adding a dissipative term to the free surface boundary condition in the damping zone [65]. Long waves can be removed by using an absorbing piston wavemaker at the far end of the NWT, without much additional cost in computation time. Clement [65] developed a coupled absorber, consisting of both a numerical beach and an absorbing piston. The poorest absorption rate that the coupled absorber achieved for short and long waves was 96% of the wave energy. In comparison, the absorption rates for the numerical beach and the absorbing piston, individually, were as low as 10% of the wave energy when absorbing long or short waves, respectively [65].

3.13.3 Boundary collocation method

A BCM typically finds an exact solution to a problem's governing equation and then attempts to find an approximate solution which satisfies the boundary value problem. A BCM developed by [51] found exact solutions for the Laplace equation as well as the free surface, bottom and radiation boundary conditions. The boundary condition on the surface of the wavemaker was then solved using the least-squares method. Wu [45] compared the results from the BEM they developed to the BCM used by [38] and found good agreement between the results; although, for higher frequencies the predictions of the BCM were slightly less than those of the BEM.

Advantages of a BCM

The BCM developed by [51] has two main advantages over the BEM approach. The first is that the only region of the model that must be solved numerically is the wavemaker's surface. This significantly reduces the computation time in comparison to a BEM since there are less nodes. The second advantage of Wu's [51] BCM is that it can handle the corner point problem better, since the only boundary that the corner node needs to be solved numerically for is the wavemaker's boundary condition.

3.13.4 Conformal mapping

A conformal mapping approach was used by [41] for modelling the wave field generated by a heaving wedge-plunger wavemaker and by [56] for modelling the hydrodynamic forces on a sloping dam in the event of an earthquake. Comparing the predictions of Wang's [41] model and those of Wu's [38] BCM and Wu's [45] BEM to the experimental results of [44] for heaving wedge-plunger wavemakers, the conformal transformation approach seems to be the least reliable for low frequencies, but improves for high frequencies.

3.13.5 Computational fluid dynamics

Computational Fluid Dynamics (CFD) evaluates the fluid flow by solving the Navier-Stokes equation [66, 67]. In contrast to the boundary value solver's discussed so far, CFD computes the flow for the entire fluid domain. This of course makes it much more computationally expensive. However, with the ever increasing processing power of computers, CFD is becoming more practical, particularly when the flow characteristics of interest do not fall under the assumptions of nonlinear potential theory. All of the authors whose results are discussed in this section, [66, 67, 68, 69], used the same commercial code, ANSYS CFX, to model a NWT with a flap wavemaker.

Guidelines for NWTs

A set of guidelines for modelling a reliable NWT in CFD was presented by [66]. Silva *et. al.* [66] found that the schemes used for the temporal and spatial discretization have an impact on the results as well as the size of the time step and the mesh refinement. Silva *et. al.* [66] reported that for a reliable simulation, a resolution along the x -axis of 111 nodes per wavelength and along the z -axis of 10 nodes over the wave height were the minimum spatial resolution required. The temporal resolution should also be less than 100^{th} of the wavemaker's period [66]. It has been reported that downstream from the wavemaker in CFD NWTs, the wave height can become attenuated [66, 68]. Finnegan and Goggins [69] found that for shallow water waves, CFD predicted the wave theory quite well but this agreement did not hold for deep water waves. The deep water predictions did improve when the height of the hinge was increased from $z = -h$ to $z = -h/2$, though the comparison still remained poor [69].

3.14 Second order theories

Second order wavemaker theories have been developed by a number of authors. Perhaps the most significant contribution was provided by [11], who predicted the second-order Stokes wave and the spurious free waves in the generation of regular waves, along with the superharmonics and subharmonics that occur when generating irregular waves. The second-order Stokes waves are regarded to as "bound" waves, as they travel with the same speed as the first-order wave. In contrast, the spurious free waves, mentioned in Section 3.6.1, travel with a speed slower than the first-order wave [31]. Superimposing the first-order wave and the

Stokes wave produces a wave form where the crests are higher and the troughs are flatter, Figure 3.14. The spurious free waves arise from a mismatch between

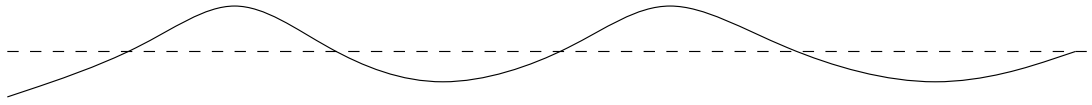


Figure 3.14: Stokes waves.

the boundary condition on the wavemaker and the kinematics of a progressive wave [31, 11]. The speed difference between the free wave and the first order wave causes the wave form to change in both time and space.

The unwanted free wave can be removed from the wave field by adding a term to the wavemaker's first order driving signal to generate a wave component with the same frequency and wave height as the free wave but in anti-phase, this will effectively cancel the free wave. Position transfer functions for suppressing free waves were derived by many researchers. One of the earlier models was presented by [70], which was limited to relative depths of $h/\lambda < O(0.1)$ and waves where:

$$\frac{H\lambda^2}{h^3} < \frac{8}{3\pi^2}. \quad (3.4)$$

Hughes [31] discusses an extension to [70] for a flap wavemaker with a pivot point either above or below the bottom of the tank.

Hudspeth and Sulisz [71] developed a theory to describe the Stokes drift and return flow of the fluid particles in a tank for monochromatic waves using a generalised paddle wavemaker design. Both [71] and [11] highlighted the importance of accounting for the evanescent wave field when considering second order wave theory. Hudspeth and Sulisz's [71] theory was extended in [72] to include bi-chromatic waves, and found that the strength of the evanescent wave field was strongly influenced by the combination of frequencies as well as the wavemaker geometry.

A second-order directional wavemaker theory was presented in [10] which discussed the importance of suppressing free waves. An extension to Schaffer's [11] complete second-order theory for irregular waves was presented in [73] for a multi-directional wavemaker. A comparison of the free wave amplitude predicted by the

second-order theories of [74], [70] and [75], to experimental results for monochromatic waves, was presented by [76]. Buhr Hansen and Svendsen [76] showed that Madsen's [70] model provided reasonably accurate results for $h/\lambda < 0.15$, while Fontanet's [74] results were reasonable for $h/\lambda > 0.2$. Daugaard (1972)'s model proved to be the most suitable over the entire range $0.1 < h/\lambda < 0.65$.

3.15 Control systems and wave basins

Unwanted waves in the tank can be problematic as they contaminate the test area and can be difficult to remove. When waves are radiated, reflected or scattered from a device back towards the wavemaker, it is essential that the wavemaker is able to absorb those incident waves. This can be done by generating additional wave components which will cancel out the waves that reflect off the surface of the wavemaker. Both position and force feedback control systems have received a considerable amount of attention for this purpose.

A position feedback controller presented in [77] and [78] used the signal from wave gauges, some distance in front of the wavemaker, in order to predict the waves incident on the wavemaker. The driving signal to the wavemaker was then adjusted accordingly. The phase of the feedback signal was corrected to account for the distance between the wavemaker and the gauges, however, there was still a significant level of error between the intended and the actual wave field travelling away from the wavemaker.

Force feedback allows for the wave field at the wavemaker's surface to be measured directly. Salter [79] took the approach of using a force feedback controller that measured the hydrodynamic forces acting on the wavemaker. This allowed the incident wave field to be determined and thus cancel out any reflected waves.

3.15.1 First and second-order control

Based on Schaffer's [11] second-order wavemaker theory, [12] derived the force transfer functions for a flap wavemaker and implemented force-feedback control. In terms of reducing the amplitude of the spurious free waves, [80] demonstrated, experimentally, that the second-order control theory developed in [12] performs remarkably well. When absorbing incident waves, [80] found that the first-order wavemaker theory proved to be quite effective, with some discrepancies that increase with frequency.

3.15.2 Comparison of force vs. position control

Newman [81] compared the quality of the wave field, in terms of the free surface elevation, created by position and force feedback controllers in directional wave basins using the commercial BEM code, WAMIT. In order for Newman's [81] position controller to produce a wave field of high quality, the waves incident on the active absorber must be a priori. However, when a structure is placed in the tank that reflects, scatters or radiates waves, forecasted knowledge of the incident wave field is very difficult. Furthermore, [12] also found that force feedback control was more effective than the position controller at reducing the amplitude of the spurious waves.

3.15.3 Active absorbers in NWTs

Spinneken *et. al.* [82] investigated the use of active absorbers in NWTs to help reduce the computational cost of a simulation, as active absorbers would remove the need for a large damping zone. This may be dependent on the type of numerical code used; for instance, with a BEM where only the boundaries are meshed, the time required to regenerate the mesh would be quite insignificant. However, this may not be the case for a NWT developed using CFD. Since CFD is a time series analysis and the wavemaker boundary condition is not linearised about the position $x = 0$, the fluid domain changes shape during the simulation. A considerable amount of additional computation is required to regenerate the mesh every few time steps in the region near the absorber, this could make [82]'s approach more computationally expensive than the use of a damping zone. Spinneken *et. al.* [82] reported that the active absorbers performed rather well in a NWT, although the performance did drop when simultaneously generating and absorbing large amplitude or non-linear waves. Finally, [82] found that when comparing the free surface elevation during consecutive repeat periods of the spectrum, there was very little deviation in the measured spectrum, indicating the effectiveness of the active absorbers and the repeatability of the model.

3.15.4 Directional wavemaking in wave basins

Directional wave generation is achieved by using a bank of wavemakers side-by-side in a wave basin. By controlling the phase difference between the paddles, the angle of propagation of the wave-front can be controlled [79]. Dalrymple [83] predicted the wave field at the test area in the wave basin based on the waves reflected off the side walls of the tank, as well as the waves travelling downstream from the wavemaker. Mansard *et. al.* [84] compared the directional theories developed in [83] and [85] to experimental results; [84] found that the experimental measurements were within 10% of the target wave height. More recent work on directional wavemakers in [86] considered the wavemaker's ability to absorb uni-directional, multi-directional and focused wave events. Spinneken and Swan [86] noted that the active absorbing wavemaker performed very well with the measured spectrum being quite close to the target spectrum. The measured spectrum did begin to differ from the target for short waves, particularly when the angle of propagation became large. Spinneken and Swan [86] attributed this to the finite width of the wavemaker paddles and found that a slight ad-hoc adjustment of the control signal's transfer functions improved the quality of the result. A second-order directional wavemaker theory for predicting the spurious free waves was developed in [87].

3.16 Conclusion

A survey of all previous wavemaker designs has been presented. The advantages and limitations of each wavemaker presented have also been discussed. Flap and piston wavemakers are generally preferred, as they are simple to construct, they can be modelled analytically and it is easy to implement force feedback control with flap and piston wavemakers.

A number of other topics have also been discussed, such as NWTs, control systems and higher order wave theories. The use of force feedback controllers has become very popular due to their success at creating repeatable sea states. However, the problem of evanescent waves and the tank space required in order to avoid contamination of the test results is still an issue. The proposed segmented wavemaker investigated in this thesis is designed to deal with this while still having the desirable characteristics of the flap and piston wavemakers.

Chapter 4

Segmented wavemaker design: A multi-body problem

4.1 Introduction

Considering the wavemaker theory developed in Chapter 2 and the discussion on previous designs of wavemakers' geometries in Chapter 3, it is clear that an optimal solution is a wavemaker for which the geometry can be easily adjusted to the optimal configuration for each frequency. Intuitively, a more accurate approximation of a curve than the stepwise and affine approximation provided by the piston and flap respectively, can be achieved by a number of line segments. Naito [3] proposed this concept in the form of a segmented wavemaker, illustrated in Figure 4.1 Part (a), which consisted of a number of pistons stacked on top of each other. The next logical step in the design of a wavemaker is to have the segments operate as flaps, shown in Figure 4.1 Part (b). Note that the segmented flaps in Figure 4.1 Part (b) are shown to be connected to each other by a hinge. The use of flaps provides two advantages over the segmented piston design; the

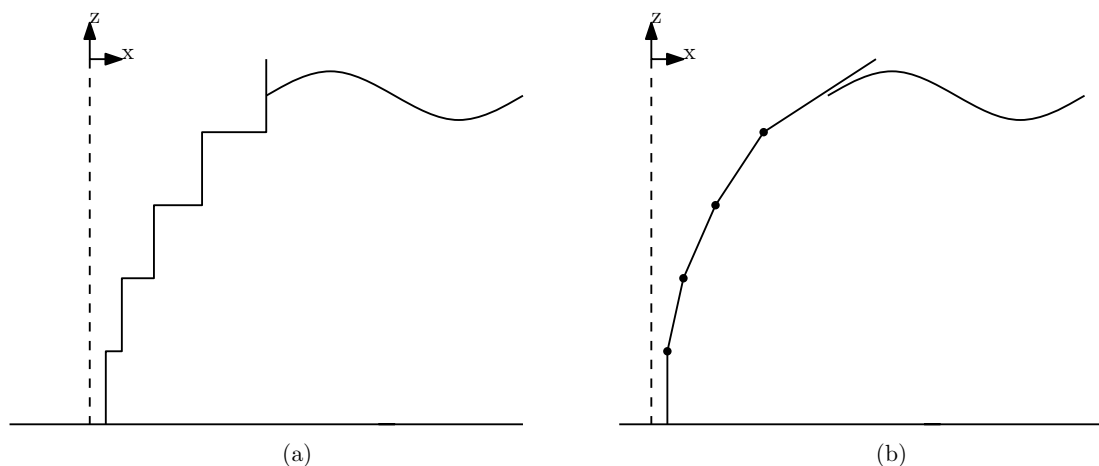


Figure 4.1: (a) Piston and (b) flap segmented wavemakers.

first is that it can approximate smooth curves more accurately and the second is that it would be easier to construct seals to prevent leaking between the segments. It is expected that the more segments in the wavemaker the better it will be at approximating any smooth curve.

Hypothesis 2 in Section 2.4.2, suggests that reducing the distortion of the wave field may be achieved by controlling the phases of the evanescent waves, via the wavemaker's geometry, rather than trying to match the motion of the fluid in a progressive wave with the motion of a wavemaker. This takes advantage of the flexibility in the segmented wavemaker's geometry, allowing us to study the potential of the interference pattern between the evanescent waves. Although [3] proposed the solution of the segmented wavemaker, it does not provide any analysis of how the system performs. An example of a two segment wavemaker is that of the dual-flap [4, 5] used in the MARINTEK laboratory. The dual-flap wavemaker has been quite useful in creating a wide bandwidth of waves; however, its affect on the distortion levels are not well understood. The case of the two segment flap wavemaker studied in this thesis differs from the MARINTEK dual-wavemaker, [4, 5], by allowing the bottom segment to have a virtual hinge below the tank floor, in a similar manner to the five segment flap wavemaker in Figure 4.1 Part (b).

For irregular sea states, the depth profile of the fluid's horizontal motion is a superposition of each wave component in the polychromatic spectrum, resulting in the fluid's depth profile changing continuously over time. For example, the form of the depth profile can change over one repeat period of the spectrum from a simple monotonic function of depth to a complicated form that is more difficult to approximate as previously discussed in Section 3.6 and illustrated in Figure 3.9, Part (c). The segmented wavemaker gives an obvious advantage for generating irregular sea states since its geometry can be changed in real time. However, this falls outside of the scope of this thesis, along with any non-linear effects that may be induced by the design.

The notation used to describe the segmented wavemaker is explained in Section 4.2. The forces that act on the multi-body segmented wavemaker are outlined and discussed in Section 4.3. The hydrodynamics, including the radiation damping and the added mass, of a multi-body system such as the segmented wavemaker are developed in Section 4.4. The hydrodynamic theory presented in Section 4.4 is validated in Section 4.5. In Section 4.6, the DOFs of the system are reduced to allow the hydrodynamics of the different wavemaker systems to be compared. Section 4.7 explains how each segment's stroke is programmed to approximate the horizontal velocity profile of a progressive wave. Finally, the chapters findings are concluded in Section 4.8.

4.2 Defining a segmented wavemaker

The multi-body system described by a segmented wavemaker is discussed in this chapter. The segments are labelled from top to bottom as 1 to N . A variable A describing the q^{th} segment is denoted by the convention, A_q . The variable A describing some coupling term between the q^{th} and p^{th} segments is denoted A_{qp} . In a wavemaker with N segments, where each segment has M degrees of freedom (DOF), the total number of DOFs in the system is $\aleph = \mathcal{N} \times \mathcal{M}$. This thesis will consider both of the segmented wavemaker configurations in Figure 4.1. In the flap configuration, Figure 4.1 Part (b), a constraint is imposed on the segments so that the ends of neighbouring segments must meet. The influence of the number of segments in the system will also be considered. In both configurations, the wavemaker spans the entire depth of the tank. The potential flow theory developed in Chapter 2, specifically Equation (2.56), can describe the wave field generated by a system of N oscillating bodies by simply superimposing the wave components generated by each DOF. In this chapter, the hydrodynamics of the segmented wavemaker systems are considered in order to provide an understanding of the force requirements of each system. The hydrodynamic coefficients are given as matrices of dimensions $\aleph \times \aleph$, so it can be difficult to compare the hydrodynamic coefficients of wavemakers with different numbers of DOF. To make the wavemakers' hydrodynamics comparable, their hydrodynamic terms are expressed as single scalar functions of kh . This is achieved by employing the Newton-Euler equations of motion with Eliminated Constraints (NE-EC) to reduce the DOFs of the wavemaker, in a similar manner as the DOF's of multi-body wave energy converters were reduced by [88].

The results presented in this chapter consider segmented wavemakers where all the segments are equal in length and that the strokes of the segments are prescribed by the kinematics of the progressive wave, Equation (2.57), i.e., the q^{th} segment has a stroke of

$$S_q = \frac{\cosh[k(h + \frac{(q-1)h}{N})]}{\cosh(kh)}. \quad (4.1)$$

4.3 Hydrodynamics of the segmented wavemaker

The hydrodynamics of a wavemaker are similar to those of any rigid body in marine hydrodynamics. The only difference is that the wavemaker is provided with a driving force from some actuator, whereas, in marine hydrodynamics, we predict how a free body will behave when a wave is incident upon it. Since the late 1970's, force control has become the preferred control strategy for wavemakers as it provides two advantages [79]:

1. Combining the force and velocity signals from the wavemaker's sensors allows us to control the rate at which energy is passed to the wave, which is useful for the effective absorption of incident waves.
2. It provides a reliable statistical average of the wave field across the face of the wavemaker, which is also key for the effective absorption of incident waves.

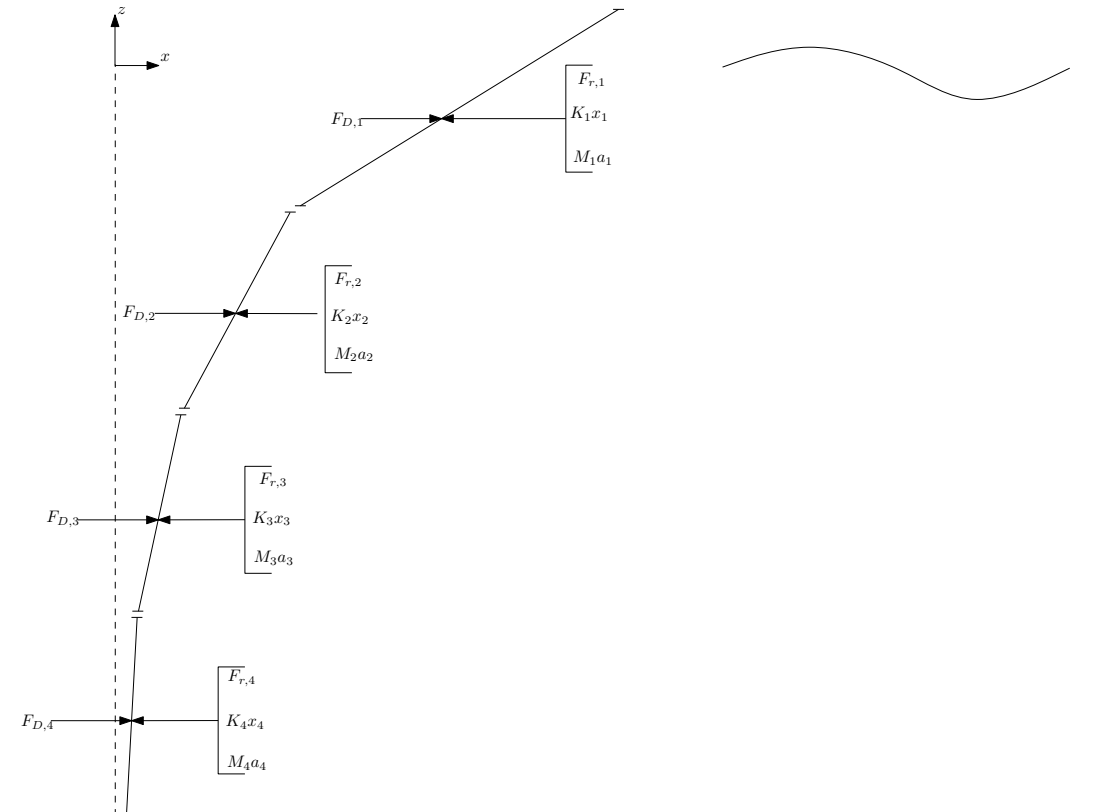


Figure 4.2: Forces acting on the wavemaker.

The forces acting on a segmented wavemaker are expressed in a force vector, denoted \mathbf{F} , where the q^{th} component of the vector represents the force experienced

by the q^{th} segment in the wavemaker. In the force vector,

$$\mathbf{F}_r = \begin{pmatrix} \vec{F}_{r,1} \\ \vdots \\ \vec{F}_{r,q} \\ \vdots \\ \vec{F}_{r,\mathcal{N}} \end{pmatrix}, \quad (4.2)$$

the subscript r indicates the radiation force, i.e., the force experienced by the wavemaker due to the wave field being generated, and the q^{th} component is the radiation force vector experienced by the q^{th} body in a system of \mathcal{N} bodies in the same direction as the wavemaker's velocity. The vectors and matrices for which the components are values representing a multi-body system are written in bold. Other force vectors describing a multi-body system will take the same form as Equation (4.2) and are indicated in Figure 4.2. In the case of the segmented wavemaker, the equation of motion describing the wavemaker is [17]:

$$\mathbf{F}_D = \mathbf{F}_r + \mathbf{m}\ddot{\mathbf{x}} + \mathbf{K}\mathbf{x}. \quad (4.3)$$

The driving force, \mathbf{F}_D , inertial force, $\mathbf{m}\ddot{\mathbf{x}}$, and spring force, $\mathbf{K}\mathbf{x}$, are vectors of the same form as Equation (4.2). The hydrodynamic pressure acting on the wavemaker system [13],

$$p = -i\omega\rho\phi, \quad (4.4)$$

can be integrated over the surface of the body to get the radiation force, $F_{r,i}$, which the wavemaker experiences as it generates a wave field [13],

$$\begin{aligned} F_{r,i} &= - \iint_S p n_i dS, \\ &= i\omega\rho \iint_S \phi_r n_i dS. \end{aligned} \quad (4.5)$$

In Equation (4.5), S is the wavemaker's wet surface area, of which dS is an infinitesimal area and $\phi_r = \varphi_j u_j$.

4.4 Radiation impedance

We now introduce the impedance of the wavemaker due to the radiating wave [13],

$$Z_{ij} = -\frac{F_{r,i}}{u_j}, \quad (4.6)$$

where u_j is the velocity of the wavemaker in the j^{th} mode. The term Z_{ij} is the radiation impedance of the body oscillating in the j^{th} mode, while being acted on by a wave being generated by a body oscillating in the i^{th} mode. Hence, the multi-body system's radiation impedance is a square matrix of size $\aleph \times \aleph$,

$$\mathbf{Z} = \begin{pmatrix} Z_{11} & \cdots & Z_{1q} & \cdots & Z_{1\aleph} \\ \vdots & \ddots & \vdots & & \vdots \\ Z_{p1} & \cdots & Z_{pq} & \cdots & Z_{p\aleph} \\ \vdots & & \vdots & \ddots & \vdots \\ Z_{\aleph 1} & \cdots & Z_{\aleph q} & \cdots & Z_{\aleph \aleph} \end{pmatrix}. \quad (4.7)$$

The radiation impedance can be expressed in terms of the velocity potential by substituting Equation (4.5) into Equation (4.6),

$$Z_{ij} = \frac{-i\omega\rho}{u_i} \iint_S \phi_r n_i dS. \quad (4.8)$$

Using the wavemaker boundary condition, Equation (2.36), gives [13],

$$Z_{ij} = \frac{-i\omega\rho}{u_i} \iint_S \phi_r c_i(z) dS. \quad (4.9)$$

Inserting Equation (2.56) into Equation (4.9) and working through the algebra, the integral in Equation (4.9) becomes a product of the Biesel coefficients c_{0i} and c_{0j} , thus showing that the radiation impedance matrix, \mathbf{Z} , is symmetrical [13]. When we insert the complete solution for the velocity potential, Equation (2.56), into Equation (4.8), it becomes clear that the radiation impedance is complex and can be expressed as,

$$Z_r = R(\omega) + iX(\omega), \quad (4.10)$$

where $R(\omega)$ is the radiation damping term due to the energy radiating from the wavemaker in a progressive wave. The radiation reactance, $X(\omega)$, is related to

the inertia the body experiences as it moves through the fluid,

$$X = \omega m(\omega). \quad (4.11)$$

This inertia, $m(\omega)$, referred to as added mass, is due to the inertia force the wavemaker experiences as it “pushes” the fluid. From our understanding of Equation (4.8), it is clear that the radiation damping is a result of the progressive wave, while the added mass is due to the evanescent waves,

$$\begin{aligned} R(\omega) &= \text{Re}\{Z\}, \\ m(\omega) &= \frac{1}{\omega} \text{Im}\{Z\}. \end{aligned} \quad (4.12)$$

After some extensive algebra the radiation damping and added mass for the general case of the piston and flap wavemakers illustrated in Figure 4.3 can be found. This long process is omitted here, the reader is directed to [13] and [17] for a more detailed discussion on the derivations, instead we will just state the expressions here. The radiation damping and added mass for a piston are given respectively as,

$$R(\omega) = \frac{\omega\rho}{kh} \left[\frac{4kh}{2kh + \sinh(2kh)} \right] \left[\frac{\sinh[k(h+a)] - \sinh[k(h+b)]}{k} \right]^2, \quad (4.13)$$

$$m(\omega) = \sum_{n=1}^{\infty} \frac{4\rho(\sin[m_n(h+a)] - \sin[m_n(h+b)])^2}{m_n^2(2m_nh + \sin(2m_nh))}, \quad (4.14)$$

and for a flap wavemaker as,

$$\begin{aligned} R(\omega) &= \frac{\omega\rho}{kh} \left[\frac{4kh}{2kh + \sinh(2kh)} \right] \left[\frac{\sinh[k(h+a)] - \sinh[k(h+b)]}{k} \right. \\ &\quad + \frac{a \sinh[k(h+a)] - b \sinh[k(h+b)]}{k} \\ &\quad \left. + \frac{\cosh[k(h+b)] - \cosh[k(h+a)]}{k^2} \right]^2, \end{aligned} \quad (4.15)$$

$$\begin{aligned}
 m(\omega) = \sum_{n=1}^{\infty} \left[\frac{4\rho}{(2m_n h + \sin(2m_n h))} \right] & \left[\frac{\sin[m_n(h+a)] - \sin[m_n(h+b)]}{m_n} \right. \\
 & + \frac{a \sin[m_n(h+a)] - b \sin[m_n(h+b)]}{m_n(h-l)} \\
 & \left. + \frac{\cos[m_n(h+a)] - \cos[m_n(h+b)]}{m_n^2(h-l)} \right]^2.
 \end{aligned} \tag{4.16}$$

For both the piston and flap wavemaker, a and b are the positions on the z axis of the wavemakers top and bottom, respectively, i.e., for a traditional piston or bottom hinged flap, $a = 0$ and $b = -h$. It should be noted that $0 \geq a > b$ and $b \geq h$. From Equation (4.12) we see that the radiation damping matrix, \mathbf{R} , and

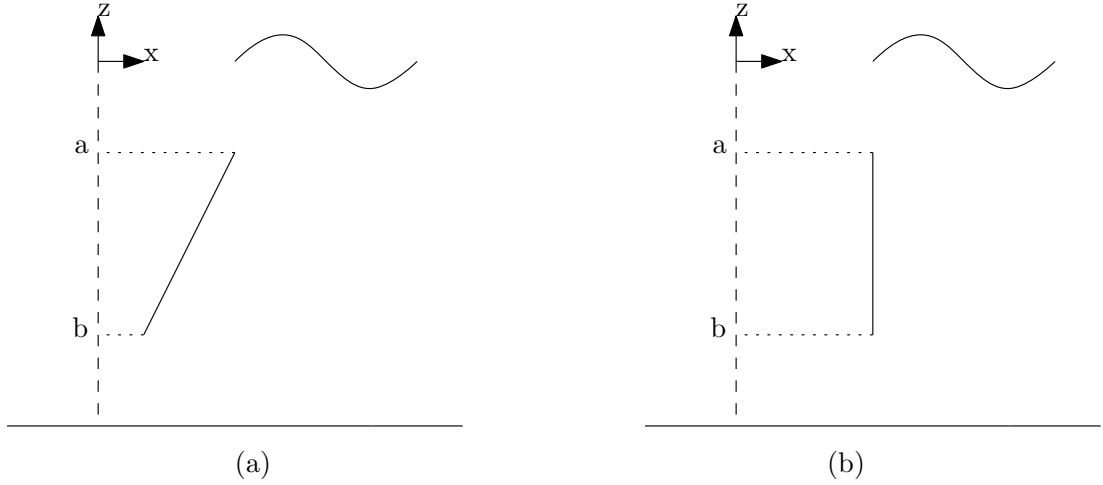


Figure 4.3: Illustration of (a) flap and (b) piston wavemakers which are neither surface piercing nor full-draft.

the added mass matrix \mathbf{M} are of the same form as the radiation impedance matrix, Equation (4.7). Substituting Equations (4.10) and (4.11) into Equation (4.6) gives the radiation force in terms of the hydrodynamic coefficients, $R(\omega)$ and $m(\omega)$, as

$$F_r(t) = i\omega m(\omega)\dot{x}(t) + R(\omega)\dot{x}(t). \tag{4.17}$$

For the purpose of this study, any parasitic mechanical impedance in the wavemaker system, i.e., friction, will be ignored.

To understand the behaviour of the segmented wavemaker's hydrodynamic coefficients and what this behaviour can tell us about the wave field created by a segmented wavemaker, each term of both the radiation damping and added mass matrices for segmented piston and flap wavemakers, Equations (4.13) to (4.16), are plotted as functions of kh in Figures 4.4 to 4.11, where the wavemakers contain

four and five segments.

4.4.1 Radiation damping

The diagonal terms of the radiation damping matrix of a segmented piston system and flap system, Equations (4.13) and (4.15), with four and five segments in the system are given as functions of kh in Figures 4.4 and 4.5, respectively. The off-diagonal terms of the radiation damping matrix, Equation (4.12), for a segmented piston system and flap system with four and five segments in the system are plotted as functions of kh in Figures 4.6 and 4.7, respectively. As would be expected from the nature of the hyperbolic depth function, Equation (2.42), being greater at $z = 0$ and decaying over depth, the diagonal components of the segmented piston wavemaker in Figure 4.4 shows that the closer a segment is to the free surface, the more effective it is at generating larger wave heights. The same behaviour can be seen in the diagonal terms of the segmented flap wavemaker in Figure 4.5, with the exception of the diagonal terms representing the bottom segments (R_{44} in part (a) and R_{55} in part (b)) for which, at low frequencies, the values of the radiation damping terms are greater than that of the diagonal term representing the segment above it. This could be expected since, at low frequencies, the displacement of the bottom segment is almost uniform over depth, thus, it behaves more like a piston than a flap.

We see again, with the off-diagonal terms of the radiation damping matrix for a segmented piston wavemaker with four and five segments in Figure 4.6, that the closer a segment is to the free surface, the greater its radiation damping. This can be interpreted by considering the distance from the mean position of the segments involved in the coupling term to the free surface. The exception to this behaviour is the term R_{23} in part (b) of Figure 4.6, which deviates from this behaviour for high frequencies. In Figure 4.7, the behaviour of the off-diagonal terms in the radiation damping matrix, for a segmented flap wavemaker consisting of four and five flaps, deviates further from the pattern that is shown in Figure 4.6. The behaviour of the matrix components in Figure 4.7 for the four and five segment flap wavemakers do not present a strong pattern, hence, a reliable description of this behaviour can not be proposed, as it was with Figure 4.6.

It can be seen that the radiation damping of the segment at the free surface peaks at a higher frequency than the rest of the segments and that either side of this peak frequency the radiation damping decreases. Intuitively, it would seem that the free surface piercing segment has a “tuned” frequency which is dependent on its geometry. This has also been reported by [26] for piston wavemakers that

are not full draft and by [17] for the Cosh wavemaker. It seems that the radiation damping peak is a result of the geometry of the wavemaker being better suited to generating progressive waves at a particular frequency, which is dependent on the draft of the wavemaker [26].

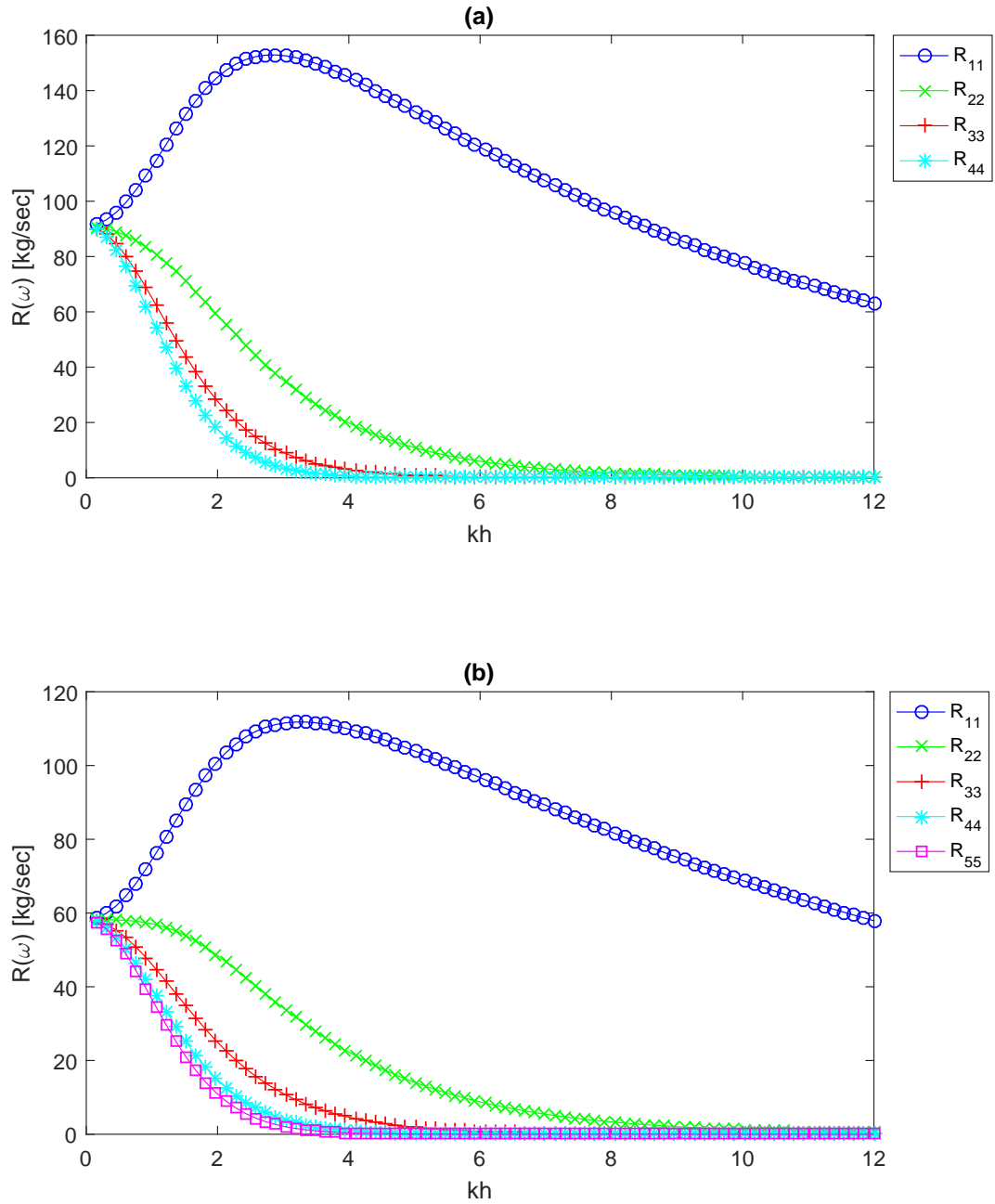


Figure 4.4: Diagonal components of the radiation damping matrix for a: (a) four piston wavemaker, (b) five piston wavemaker.

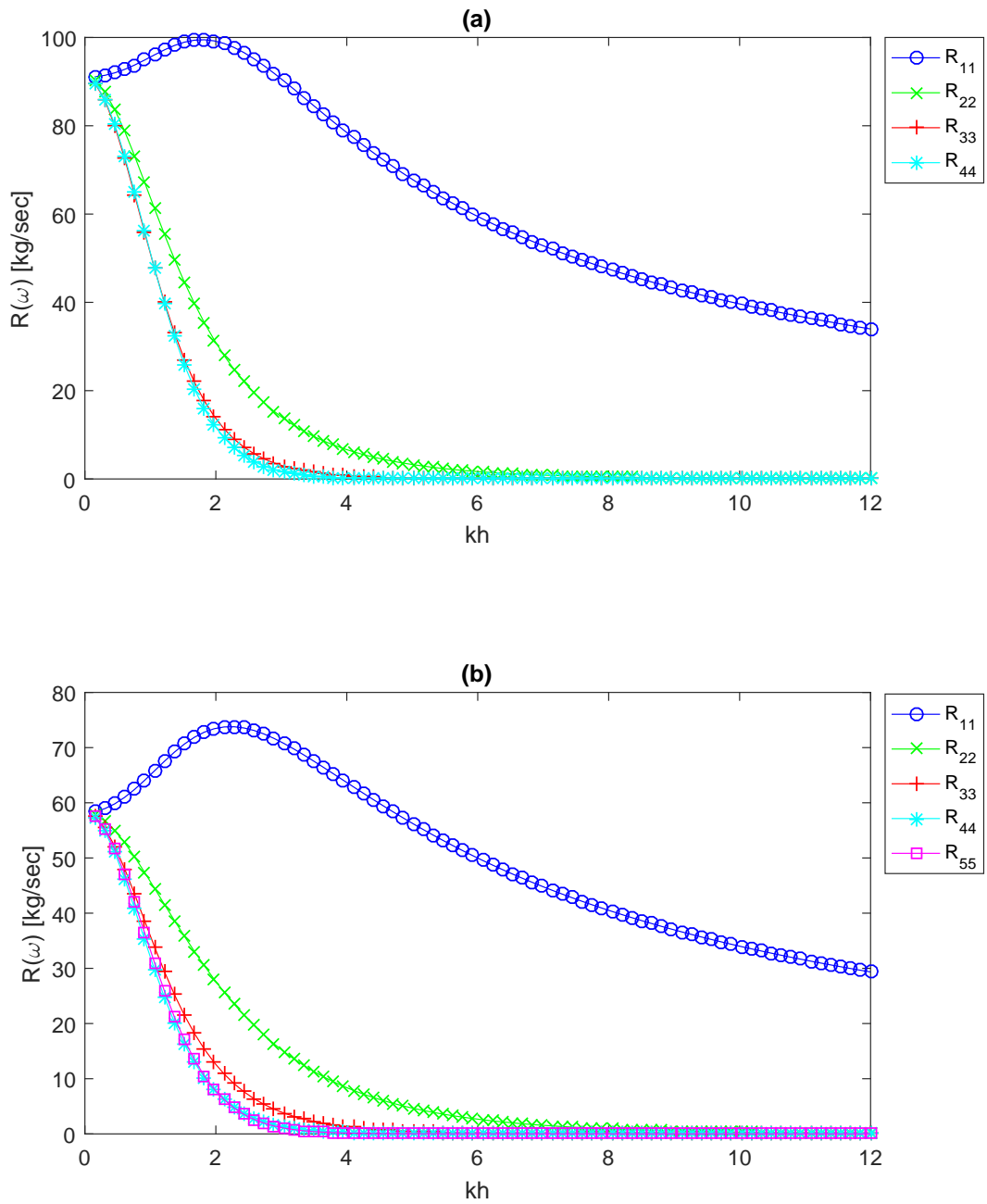


Figure 4.5: Diagonal components of the radiation damping matrix for a: (a) four flap wavemaker, (b) five flap wavemaker.

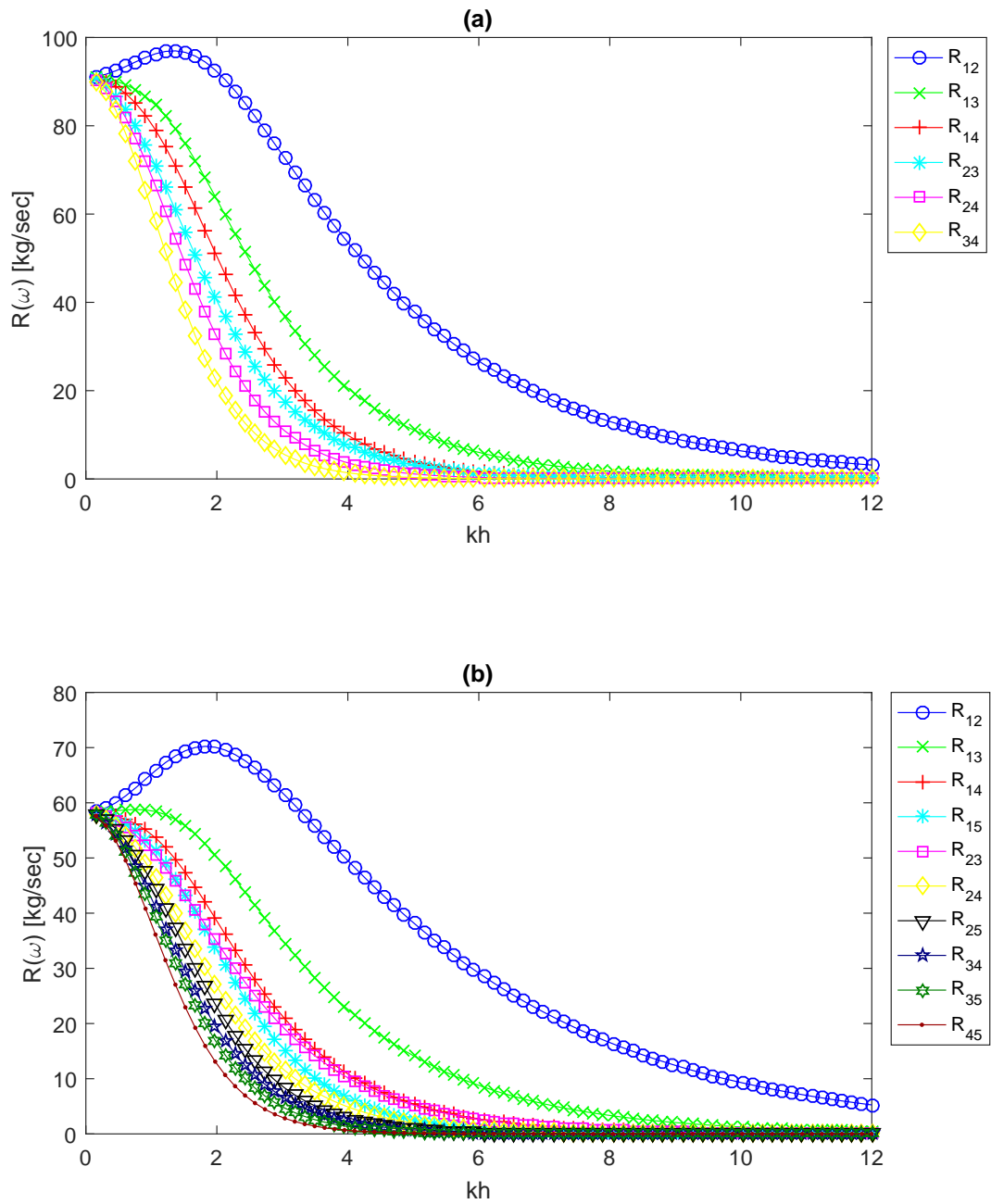


Figure 4.6: Off-diagonal components of the radiation damping matrix for a: (a) four piston wavemaker, (b) five piston wavemaker.

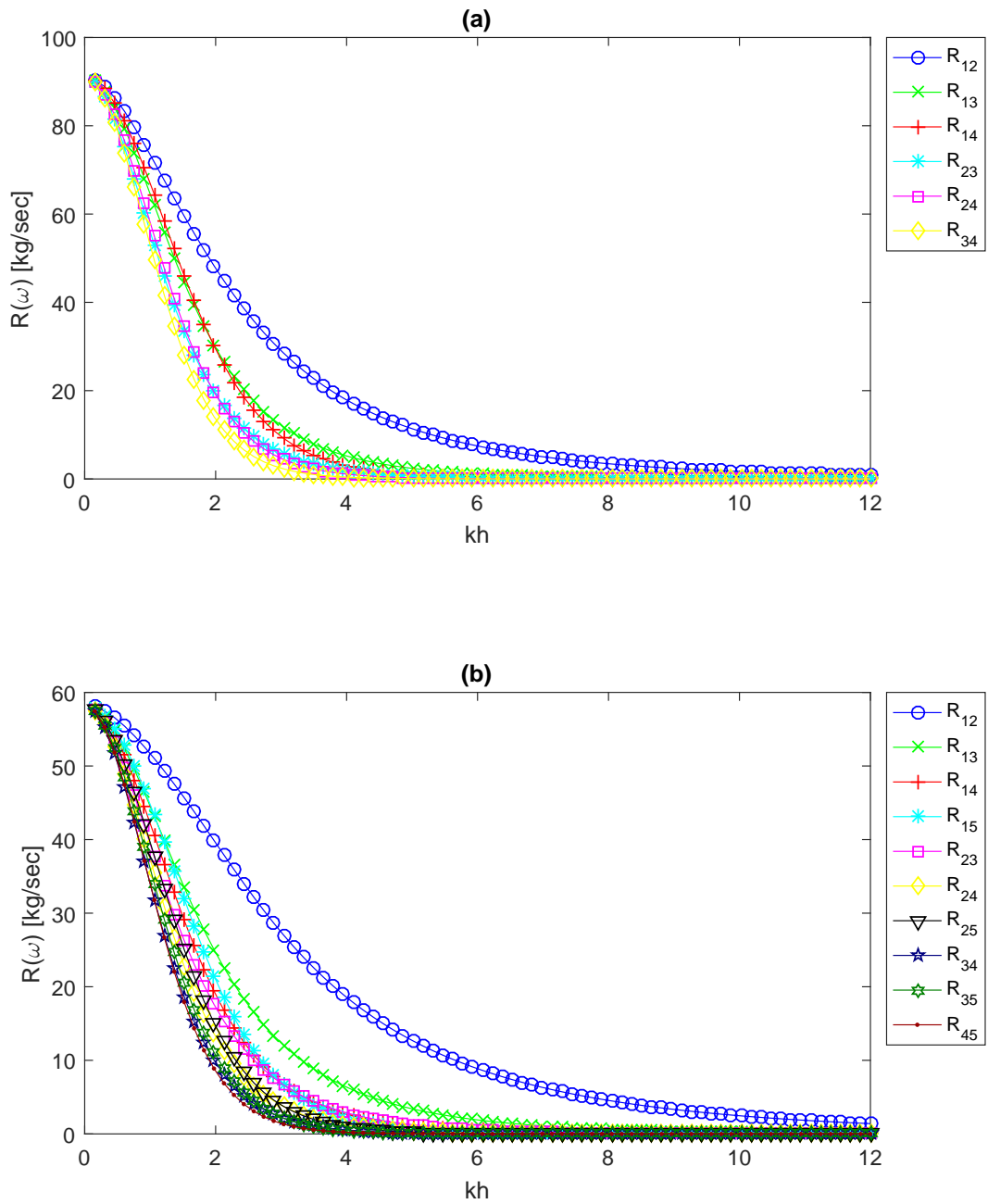


Figure 4.7: Off-diagonal components of the radiation damping matrix for a: (a) four flap wavemaker, (b) five flap wavemaker.

4.4.2 Added mass

The diagonal terms of the added mass matrix are plotted against kh for the segmented piston and flap wavemakers, Equation (4.14) and (4.16) in Figures 4.8 and 4.9, respectively, for wavemakers with four and five segments. The off-diagonal terms of the same added mass matrices, Equation (4.12), are plotted against kh in Figures 4.10 and 4.11.

Comparing the diagonal added mass matrix terms of the segmented piston wavemaker in Figure 4.8 to the same for the segmented flap wavemaker in Figure 4.9, we see that the segmented flap design achieves lower values for the added mass components. It is also evident that the segmented piston wavemaker is more appropriate for low frequency waves than for high frequency waves, as the value of the added mass terms increases with frequency for all segments except the top segment. In contrast to this, for segmented flap wavemakers, Figures 4.9 and 4.11, with increasing frequency, the added mass decreases asymptotically to some value close to zero for all the segments, indicating a decline in the strength of the evanescent wave field.

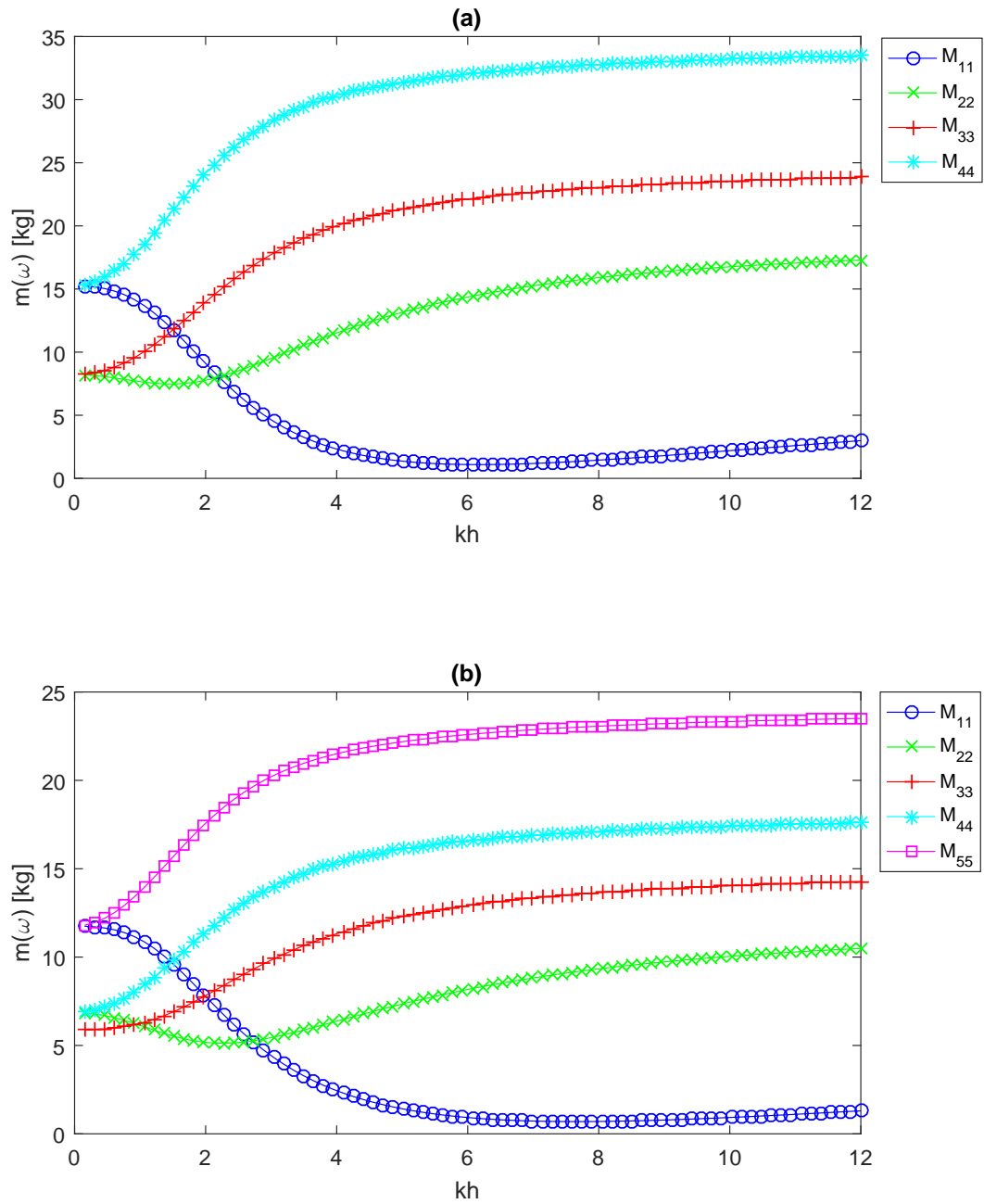


Figure 4.8: Diagonal components of the added mass matrix for a: (a) four piston wavemaker, (b) five piston wavemaker.

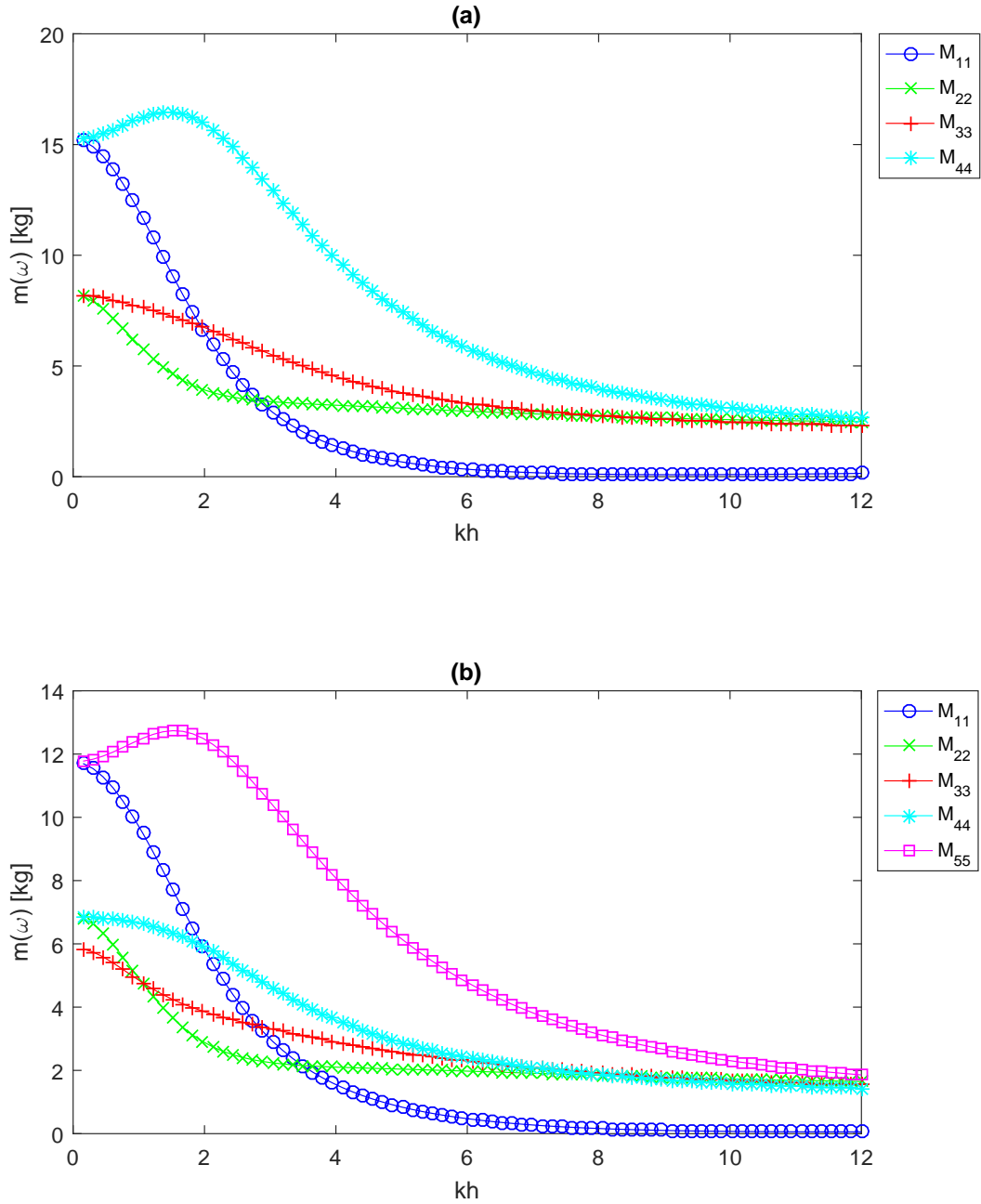


Figure 4.9: Diagonal components of the added mass matrix for a: (a) four flap wavemaker, (b) five flap wavemaker.

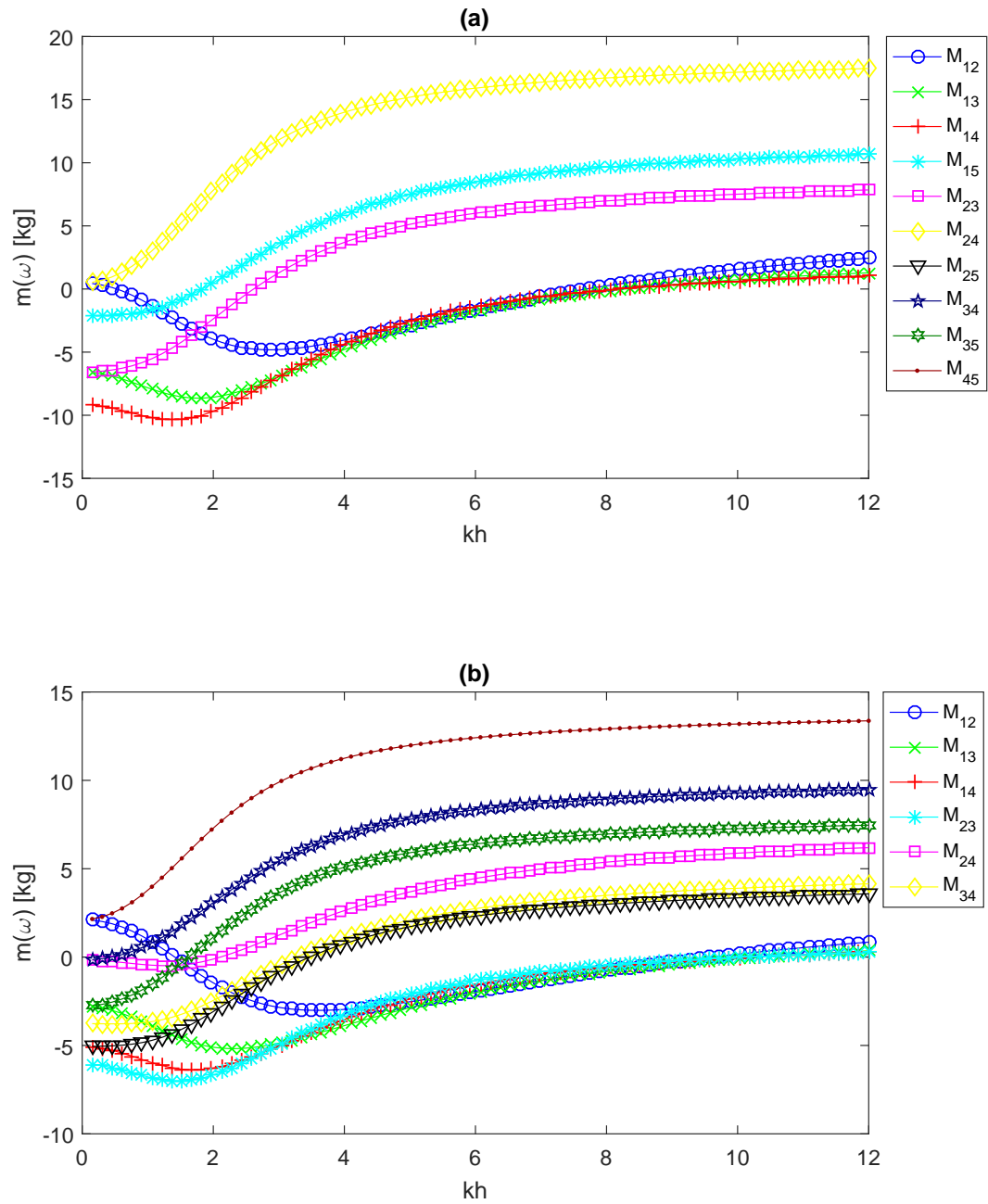


Figure 4.10: Off-diagonal components of the added mass matrix for a: (a) four piston wavemaker, (b) five piston wavemaker.

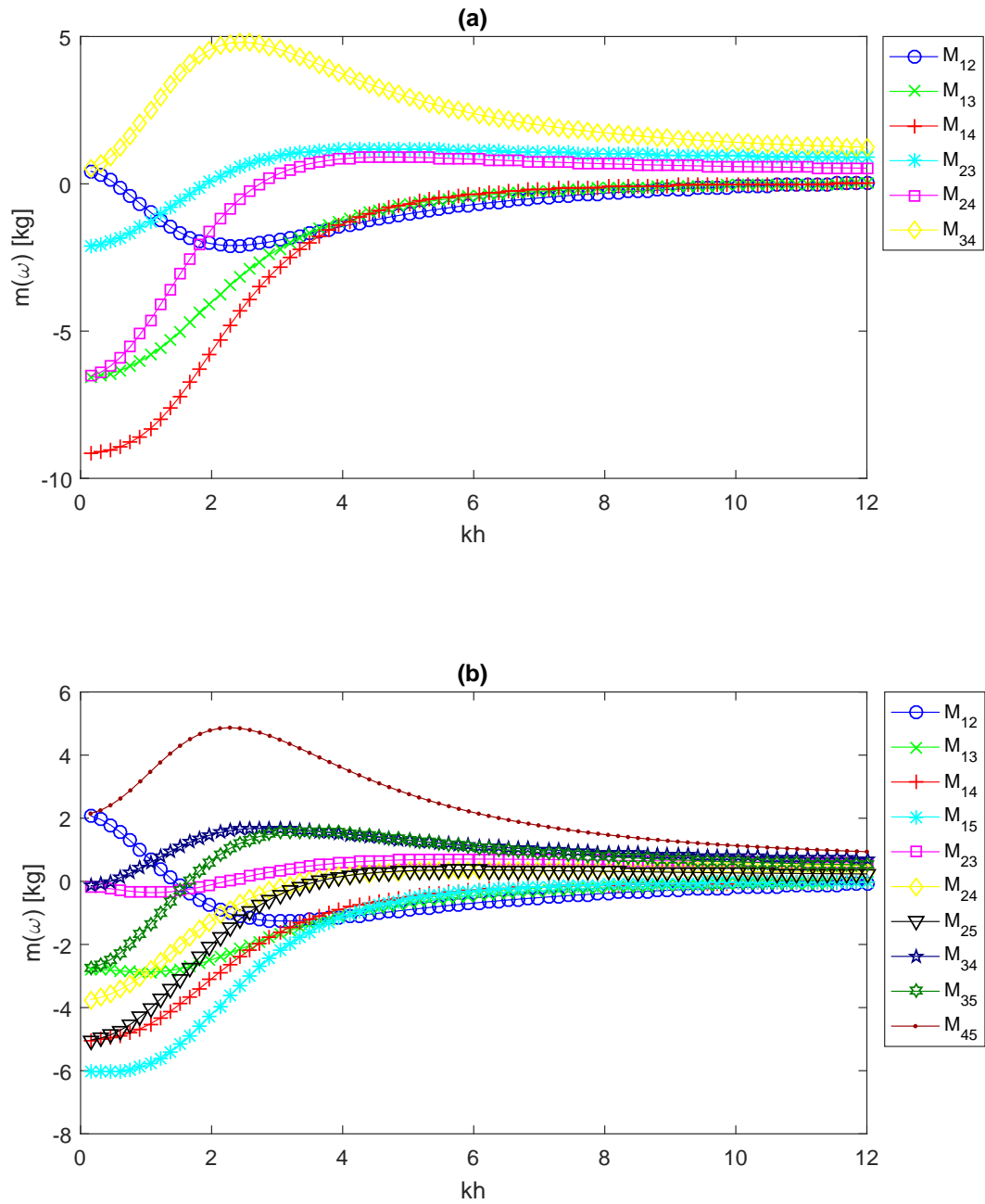


Figure 4.11: Off-diagonal components of the added mass matrix for a: (a) four flap wavemaker, (b) five flap wavemaker.

4.5 Validation of code

In order to verify the results presented in Figures 4.4 to 4.11, the in-house code used to generate these results was used to generate the radiation damping and added mass of single piston and flap wavemakers, where $a = 0$ and $b = -h$ in Equations (4.13) and (4.16), and compared to the corresponding radiation damping and added mass coefficients derived by [17]. For single piston and flap wavemakers Figures 4.12 and 4.13, respectively, plot the radiation damping calculated by the in-house code and that derived by [17] against kh in Parts (a) and the added mass calculated by the in-house code and that derived by [17] against kh in Parts (b) of Figures 4.12 and 4.13. These results can also be compared to those presented by [17]. Figures 4.12 and 4.13 show that the hydrodynamic coefficients calculated by the in-house code and those calculated by [17]’s expressions are identical, this indicates that the in-house code calculates the hydrodynamic coefficients of the wavemakers correctly. Both sets of results are identical as they are both derived using linear potential wavemaker theory.

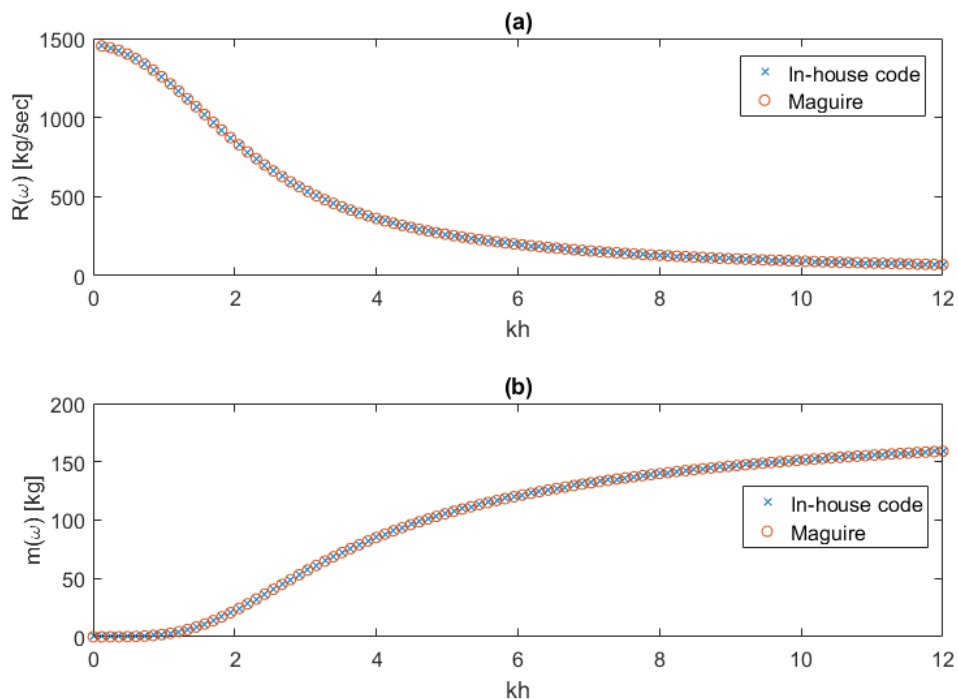


Figure 4.12: Comparison of the radiation damping, (a), and added mass, (b), for a single piston wavemaker calculated by the in-house code and those derived by [17], where $h = 0.6$.

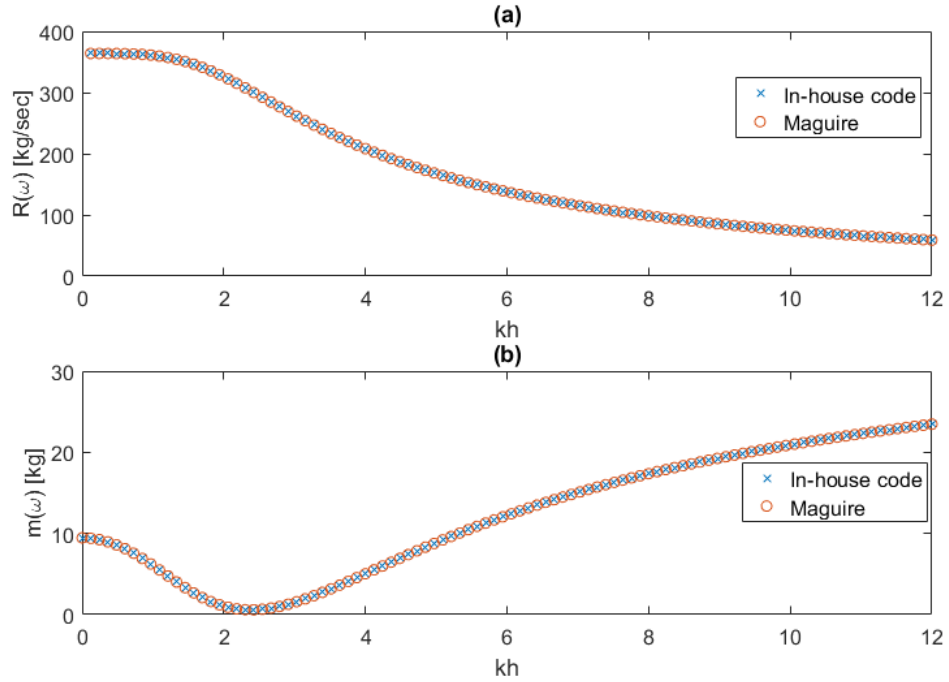


Figure 4.13: Comparison of the radiation damping, (a), and added mass, (b), for a single flap wavemaker calculated by the in-house code and those derived by [17], where $h = 0.6$.

4.6 Constrained dynamics of a segmented wavemaker

By imposing programmed constraints via a controller, the strokes of each segment can be set relative to the stroke of the top segment. The segmented wavemaker can then be programmed to approximate the ideal fluid motion, Equation (2.57), as accurately as possible. These programmed constraints allow for the hydrodynamics of the segmented wavemaker to be simplified so that the hydrodynamic functions can be expressed as single scalar quantities rather than matrices, allowing for the hydrodynamics of wavemakers with different DOFs to be compared. By doing this, the hydrodynamics of systems with different numbers of DOFs can be compared to each other. Of course it would be best to compare the wave fields generated by the different wavemakers, as done in Chapter 5 and 6, however, the comparison presented in this chapter helps us to understand how the hydrodynamics of the segmented wavemaker behave. This is achieved in Section 4.6.2 using the NE-EC to describe the multi-body system of a segmented wavemaker with less DOFs. First, we look at how the modes of motion of a wavemaker are defined in Section 4.6.1.

4.6.1 Modes of motion of a wavemaker

Single body wavemakers have one mode of motion, a piston operates in surge and a flap operates in pitch, as it pivots about a given point. The motion of a piston is described by the wavemaker's horizontal displacement while the motion of a flap wavemaker is described by the angle between the paddle and the vertical axis, indicated as θ in Figure 4.14. However, the horizontal displacement of a

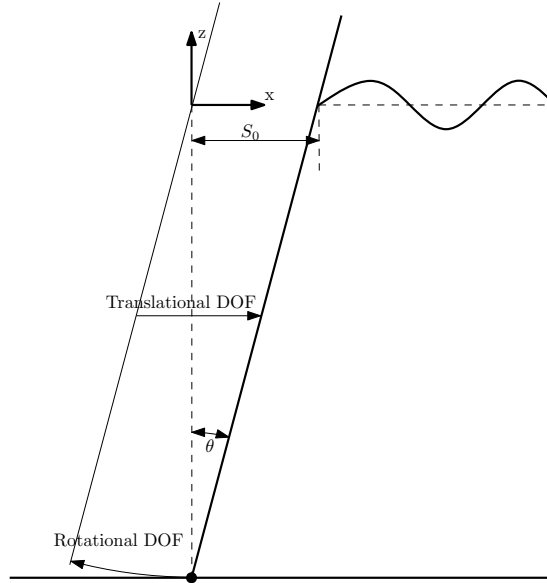


Figure 4.14: Motion of a flap wavemaker decomposed into a translational and a rotational DOF.

piston and the angle of a flap are not directly comparable. Instead, we use the depth profiles stated in Equations (2.12) and (2.13). For a piston the depth profile is simply a stroke of unit length. To derive the depth profile of a flap wavemaker we describe the flap's motion by two dependent DOFs, a translational and a rotational DOF, defined by the flap's motion relative to the origin of the coordinate system. By combining these two dependent DOFs, in the manner presented below, the flap wavemaker's motion is described. Starting with the position of the wavemaker,

$$\vec{S}(z, t) = S_0 c(z) \vec{i} e^{i\omega t}, \quad (4.18)$$

where S_0 is the wavemaker's stroke at $z = 0$, it then follows that the wavemaker's velocity is,

$$\vec{u}(z, t) = u_0 c(z) \vec{i} e^{i\omega t} = i\omega S_0 c(z) \vec{i} e^{i\omega t}. \quad (4.19)$$

The unit vectors along the x , y and z axis are denoted as \vec{i} , \vec{j} and \vec{k} , respectively. The wavemakers velocity can be decomposed into the combination of a translational velocity, \vec{U} , and a rotational (or angular) velocity, $\vec{\Omega}$, as follows [13],

$$\vec{u} = \vec{U} + (\vec{\Omega} \times \vec{s}), \quad (4.20)$$

where \vec{s} is the position vector of the point moving at velocity \vec{u} . For the flap wavemaker, the translational and rotational velocities are defined, respectively, as:

$$\begin{aligned} \vec{U} &= \dot{\vec{x}} = i\omega S_0 \vec{i} e^{i\omega t}, \\ \vec{\Omega} &= \dot{\vec{\theta}} = i\omega \theta \vec{j} e^{i\omega t}. \end{aligned} \quad (4.21)$$

Given that \vec{s} is the position of a point on the surface of the wavemaker and since the position of the wavemaker is approximated about $x = 0$, we can say,

$$\vec{s} \approx z \vec{k}. \quad (4.22)$$

Substituting Equations (4.21) and (4.22) into Equation (4.20) the resultant velocity becomes:

$$\vec{u} = i\omega [S_0 \vec{i} + \theta \vec{j} \times z \vec{k}] e^{i\omega t}. \quad (4.23)$$

Utilising the small angle approximation we have,

$$\theta \approx \sin(\theta) = \frac{S_0}{h}, \quad (4.24)$$

and substituting Equation (4.24) into Equation (4.23) gives,

$$\vec{u} = i\omega [S_0 \vec{i} + \frac{S_0 z}{h} \vec{j} \times \vec{k}] e^{i\omega t}. \quad (4.25)$$

Carrying out the cross product gives,

$$\vec{u} = i\omega S_0 [1 + \frac{z}{h}] \vec{i} e^{i\omega t}. \quad (4.26)$$

Comparing Equation (4.26) to Equation (4.19) gives the normalised horizontal displacement of the paddle as,

$$c(z) = 1 + \frac{z}{h-l}. \quad (4.27)$$

4.6.2 Newton-Euler equations of motion with eliminated constraints

When dealing with a multi-body system, such as the segmented wavemaker, the constrained hydrodynamic functions can be found from the NE-EC [88],

$$\mathbf{F}_{\mathbf{r},c} = \sum_{q=1}^{\mathcal{N}} \frac{\partial \vec{u}_q}{\partial \mathbf{s}} F_r = \mathbf{P} \mathbf{F}_{\mathbf{r}}, \quad (4.28)$$

where the subscript c indicates a constrained value, i.e., a value describing a multi-body system where the DOFs have been reduced, and \mathcal{N} is the number of bodies in the system. The vector \mathbf{P} is a transformation velocity vector. The independent velocity, \mathbf{s} , is a characteristic velocity of which the motion of each body in a multi-body system can be expressed in relation to. The independent velocity vector has a size of the number of reduced DOFs in the system. In the case of the segmented wavemaker, as we are reducing the number of DOFs to one, \mathbf{s} has a single component which we set as the velocity of the top segment,

$$\mathbf{s} = \vec{u}_1. \quad (4.29)$$

The constrained force $\mathbf{F}_{\mathbf{c}}$ is also a vector of the same size as \mathbf{s} . The general velocity vector, \mathbf{u} , is defined so that the q^{th} component is the velocity vector of the q^{th} segment,

$$\mathbf{u} = \begin{pmatrix} \vec{u}_1 \\ \vdots \\ \vec{u}_q \\ \vdots \\ \vec{u}_{\mathcal{N}} \end{pmatrix}, \quad (4.30)$$

and is related to the independent velocity [88], \mathbf{s} , by

$$\mathbf{u} = \mathbf{P}^T \mathbf{s}. \quad (4.31)$$

The transformation vector [88], \mathbf{P} , defined as

$$\mathbf{P} = \left(\frac{\partial u_1}{\partial \mathbf{s}} \quad \dots \quad \frac{\partial u_q}{\partial \mathbf{s}} \quad \dots \quad \frac{\partial u_{\mathcal{N}}}{\partial \mathbf{s}} \right), \quad (4.32)$$

is the vector that allows us to reduce the DOF, as demonstrated in the NE-EC, Equation (4.28). It should be noted that the notations in bold indicate vectors or matrices of which the components represent values associated with individual

segments in a segmented wavemaker, while $\vec{\tau}$ denotes a vector with a direction. Bear in mind that a vector \mathbf{A} may contain the direction vector \vec{a}_q .

We can use the constrained force, \mathbf{F}_c in Equation (4.28), to compare the radiation force experienced by both segmented piston and segmented flap wavemakers with different numbers of segments, shown in Figures 4.15 and 4.16, respectively. The force plotted as a function of kh in Figures 4.15 and 4.16 is the constrained force, \mathbf{F}_c , on the segmented wavemaker calculated from Equation (4.28), which is evaluated using the force vector, Equation (4.2), of which the individual components are given by Equation (4.5). The forces presented in Figures 4.15 and 4.16 are of the different segmented wavemakers generating progressive waves with the same amplitude as a single piston wavemaker with a unit stroke. It must be ensured that the piston and flap wavemakers are creating the same wave field when comparing the radiation force. To achieve this, the strokes of the wavemakers have been adjusted while generating the results in this thesis so that each wavemaker is creating a wave with the same wave height as that generated by a single piston wavemaker with a unit stroke. The need for this stroke correction will be discussed further in Section 4.6.3, Equation (4.38). In order to approximate the kinematics of a progressive wave, recall that the strokes of the segmented wavemaker, in this chapter, are defined in Equation (4.1) by the progressive wave's depth profile, Equation (2.57). By comparing Figures 4.15 and 4.16, it is clear that to create the same high frequency waves, a flap wavemaker requires much less force than a piston. In Figures 4.15 and 4.16, there is a drastic reduction in the radiation force of the two segment wavemakers at high frequencies, compared to the single segment wavemakers. However, as the number of segments in the system is increased further, the reduction in the radiation force is much less significant. In fact, there seems to be virtually no improvement after the three segmented flap wavemaker. The reduction in the radiation force in the segmented flap systems compared to the segmented piston systems, and also as the number of segments in the wavemaker is increased, is understood to be a result of a reduction in the amplitude of the evanescent waves. Hence, this supports Hypothesis 1, Section 2.4, as the more segments the wavemaker contains the better it approximates the kinematics of progressive waves and the better it is at reducing the evanescent wave field. For the sake of providing a clear idea of the effect of evanescent waves on the radiation force, Figure 4.17 shows the radiation force experienced by the wavemakers due to the progressive wave alone as a function of kh . Comparing the results presented in Figure 4.17 to Figures 4.15 and 4.16 highlights the evanescent waves' contribution to the radiation force experienced by a wavemaker. For shallow water waves, it is apparent from Figures 4.15, 4.16 and 4.17 that the contribution to the radiation force from the evanescent waves

is negligible, but can be significant for wavemakers with three or less segments at high frequencies.

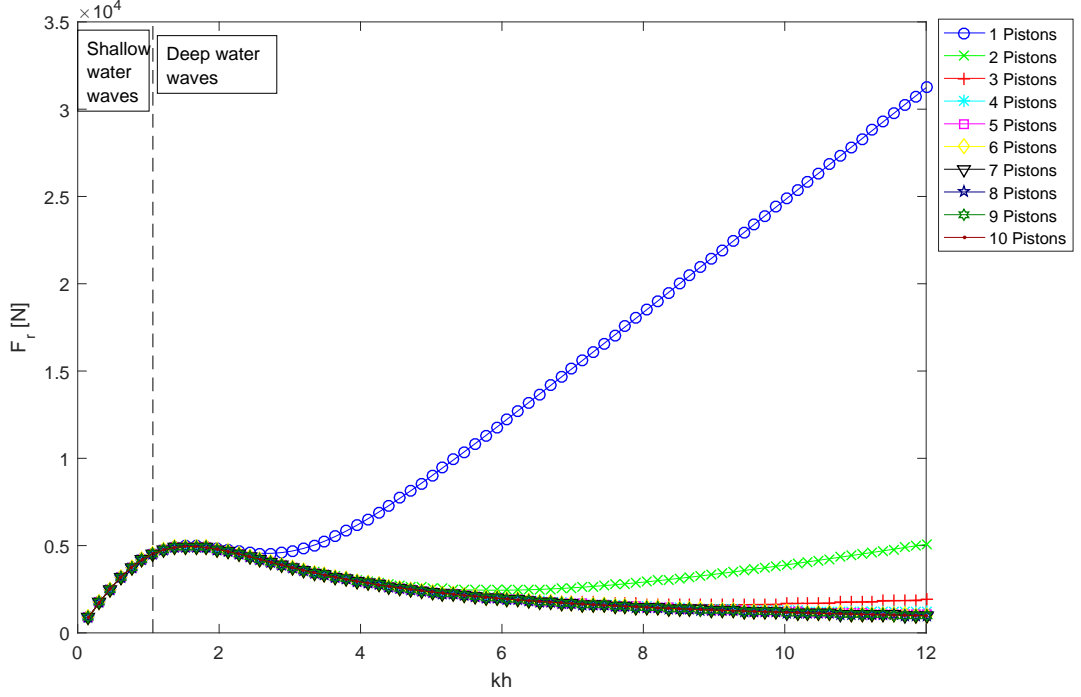


Figure 4.15: The total radiation force experienced by segmented piston wavemakers generating waves of the same amplitude as a single piston wavemaker with unit stroke, as a function of kh for ten different systems.

4.6.3 Constrained hydrodynamics

Expressing Equation (4.6) in matrix form,

$$\mathbf{F} = \mathbf{Z}\mathbf{u}, \quad (4.33)$$

where \mathbf{Z} is the radiation damping matrix, it stands to reason that we may express the constrained radiation force in terms of a constrained radiation impedance [88]:

$$\mathbf{F}_c = \mathbf{Z}_c \mathbf{s}. \quad (4.34)$$

Substituting Equation (4.33) and (4.31) into Equation (4.28) and equating with Equation (4.34), the constrained radiation impedance, Z_c , can be obtained as:

$$\mathbf{Z}_c = \mathbf{P}\mathbf{Z}\mathbf{P}^T. \quad (4.35)$$

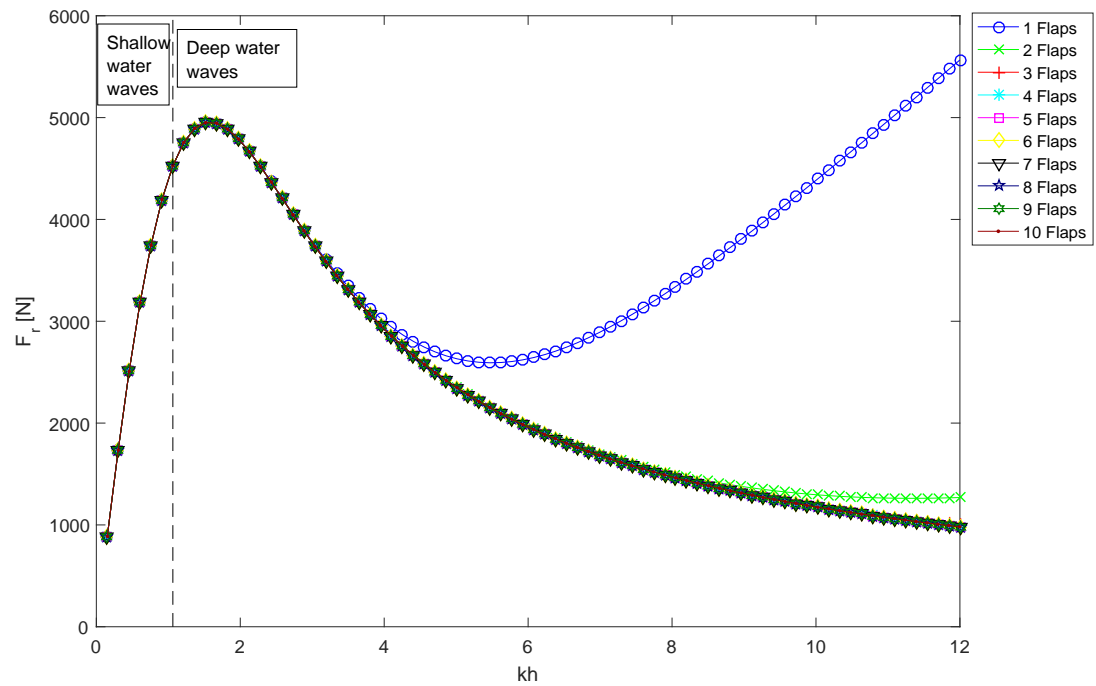


Figure 4.16: The total radiation force experienced by flap wavemakers generating waves of the same amplitude as a single piston wavemaker with unit stroke, as a function of kh for ten different systems.

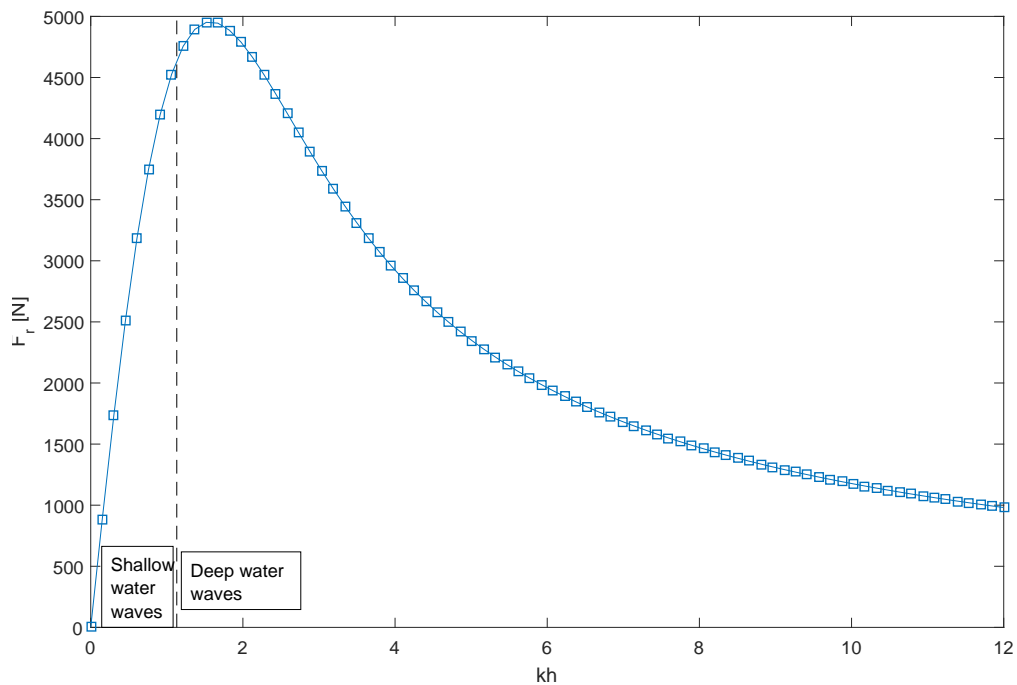


Figure 4.17: The radiation force experienced by a single piston wavemaker, with a unit stroke, due to the progressive wave, as a function of kh .

Subsequently, the constrained hydrodynamic coefficients are found to be [88]:

$$\mathbf{R}_c(\omega) = \mathbf{PRP}^T, \quad (4.36)$$

and

$$\mathbf{m}_c(\omega) = \mathbf{PMP}^T. \quad (4.37)$$

The constrained radiation damping of the segmented piston and flap wavemakers are plotted as a function of kh in Figures 4.18 and 4.19, respectively, for wavemakers containing one to ten segments. Comparing Figures 4.18 and 4.19 reveals that the constrained radiation damping is notably less for the segmented flap wavemakers than the segmented piston wavemakers. This is because the wavemaker is displacing a smaller volume of water per unit stroke and consequently, is generating waves with smaller wave heights. Recalling Figure 4.1, it is intuitive that, as the number of segments in the system is increased, the water displaced by the wavemaker decreases and, thus, so does the radiation damping and the progressive wave's height. In order for the wave fields created by the different wavemakers to be comparable, the strokes of the wavemaker's must be corrected. For this purpose, a correction factor is introduced,

$$\alpha = \frac{\varphi_{0P1}}{\varphi_{0W}}, \quad (4.38)$$

where the subscript 0 indicates the first term of the infinite summation in Equation (2.56), the subscript $P1$ indicates a single piston wavemaker and the subscript W represents the wavemaker system for which the hydrodynamics are being evaluated. The constrained velocity potential with the correction factor is:

$$\phi_c = \alpha\phi P^T. \quad (4.39)$$

The correction factor, Equation (4.38), does not apply to the radiation damping and added mass as they are both independent of the wavemaker's motion amplitude, but is considered in the calculation of Figures 4.15 and 4.16 and the rest of the results presented this thesis. Figures 4.18 and 4.19 show that at low frequencies the radiation damping for all the wavemakers tends towards the same value. This is because each wavemaker begins to operate more like a single piston wavemaker as the horizontal motion of the fluid in a progressive wave becomes more uniform over depth.

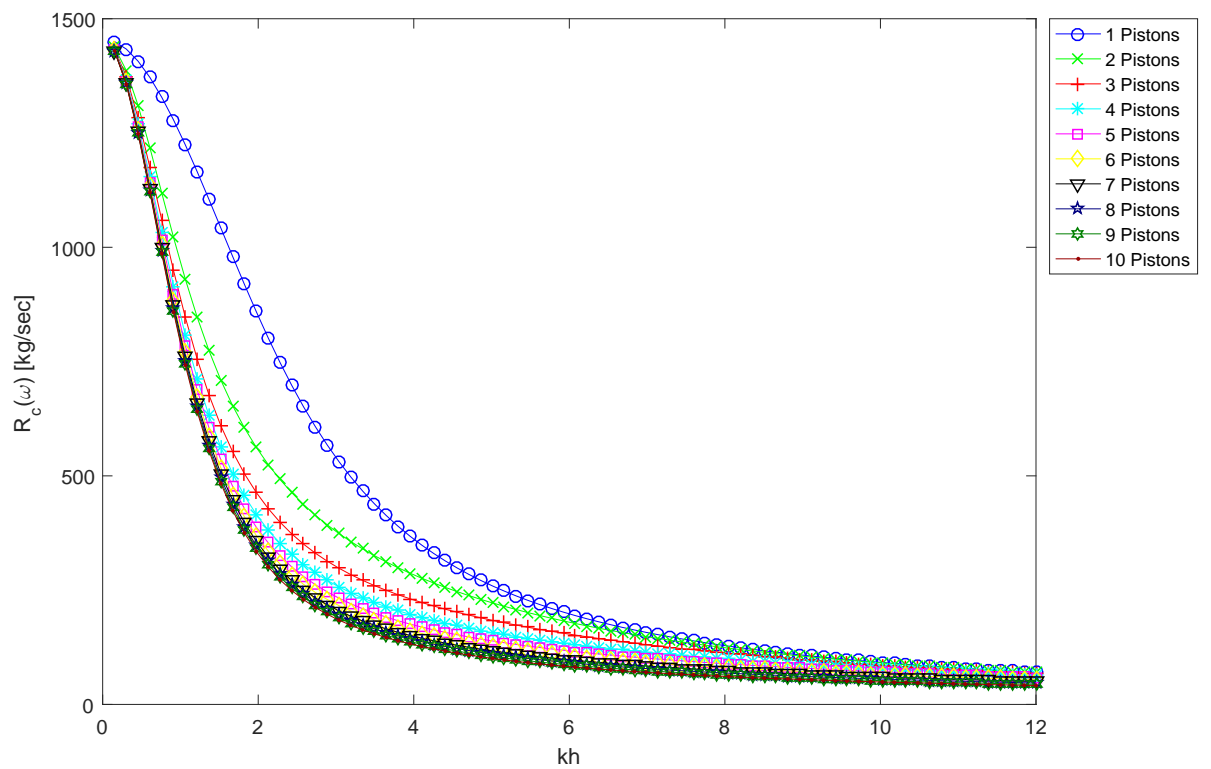


Figure 4.18: The constrained radiation damping of ten segmented piston wave-makers over kh .

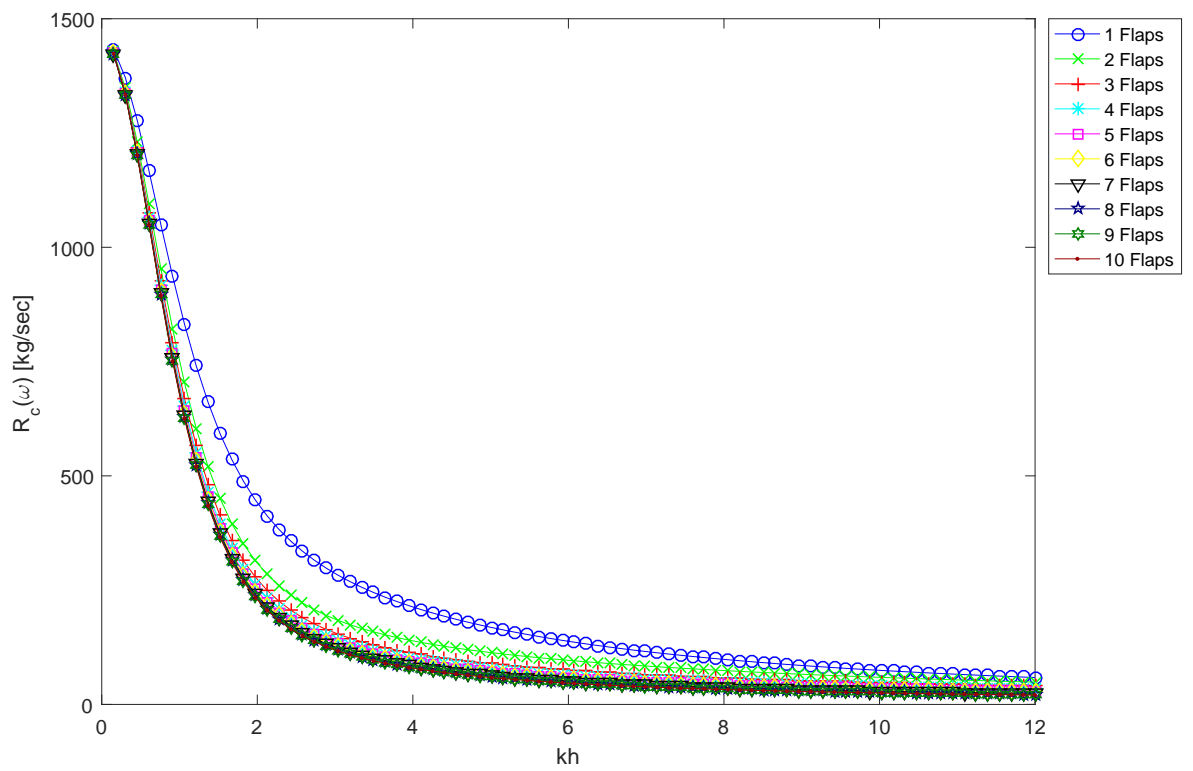


Figure 4.19: The constrained radiation damping of ten segmented flap wavemakers over kh .

The constrained added mass of the segmented piston and flap wavemakers, shown in Figures 4.20 and 4.21, respectively, as a function of kh , further supports Hypothesis 1, Section 2.4, as it is clear that the more segments in the wavemaker and hence, the better it approximates the kinematics of a progressive wave, the lower the value of the added mass. The insets in both Figures 4.20 and 4.21 show the behaviour of the constrained added mass for the wavemakers, with two to ten segments, with greater detail on lower values of the constrained added mass. The insets reveal that, with the exception of the single piston wavemaker, the constrained added mass of the segmented wavemakers is not a monotonic function of kh ; these results are similar to the findings presented in [26]. The non-monotonic behaviour of these curves is a result of the interference pattern between the evanescent waves with different phases and provides some validation for Hypothesis 2, discussed in Section 2.4.2.

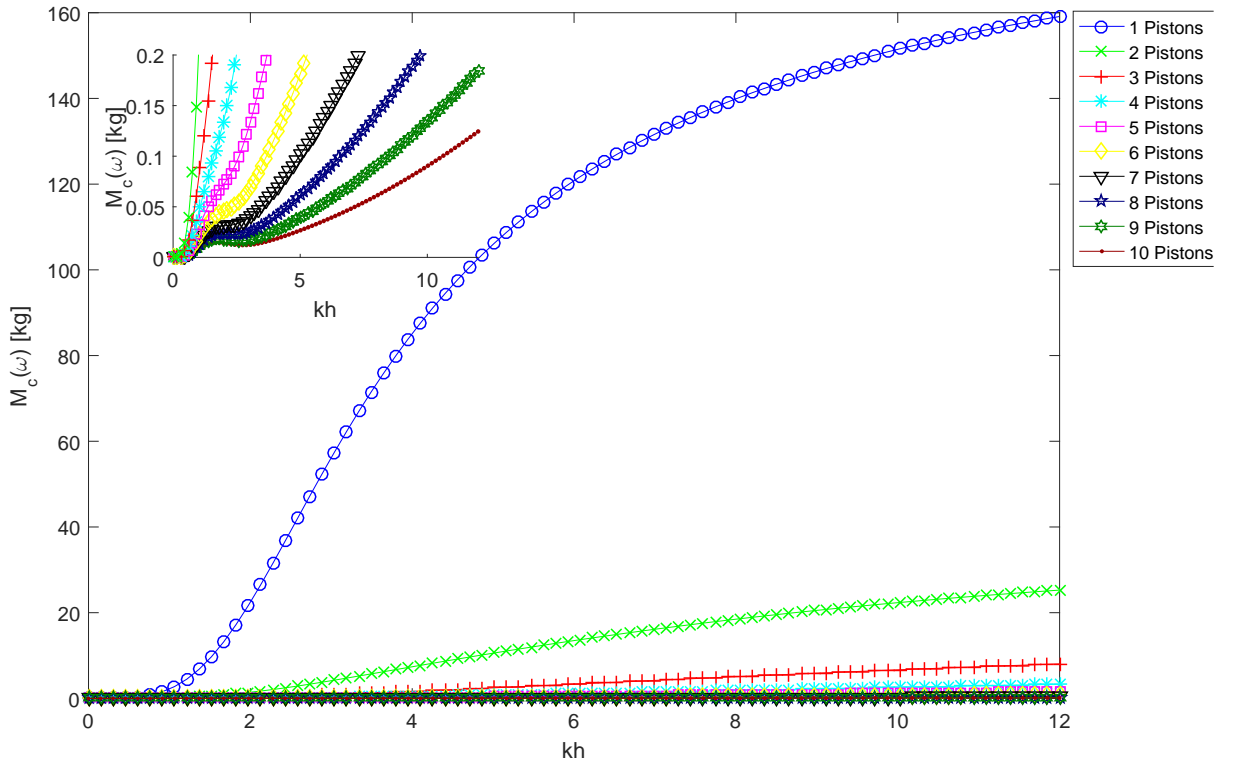


Figure 4.20: The constrained added mass of ten segmented piston wavemakers over frequency as functions of kh . The inset shows the behaviour of the constrained added mass with a greater magnification.

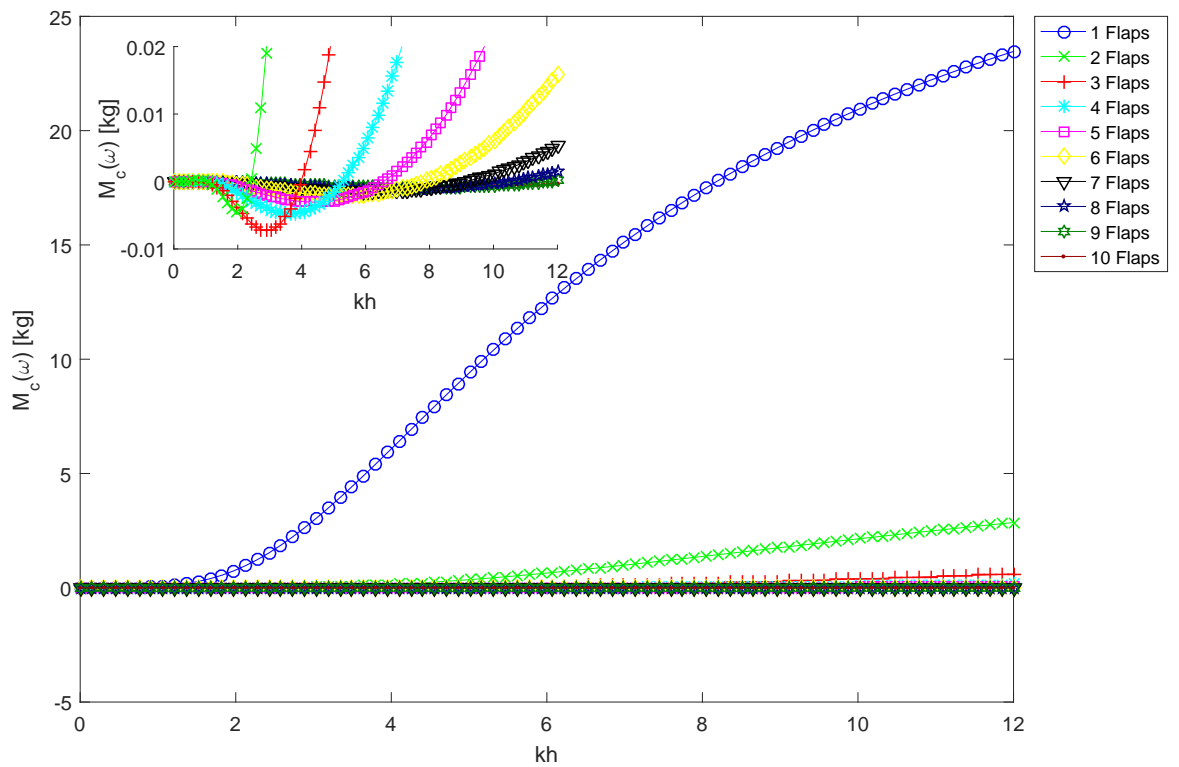


Figure 4.21: The constrained added mass of ten segmented flap wavemakers over frequency as functions of kh . The inset shows the behaviour of the constrained added mass with a greater magnification.

4.7 Control parameter

The transformation vector can be programmed to control the amplitude of motion for each segment in the wavemaker. For instance, the results presented in this chapter have been calculated with the segments programmed to approximate the horizontal fluid motion of the progressive waves over the depth of the tank by setting the independent velocity to:

$$\mathbf{s} = 1, \quad (4.40)$$

and setting the transformation vector as:

$$\mathbf{P} = \begin{pmatrix} 1 \\ \dots \\ \frac{\cosh[k(h + \frac{(q-1)h}{N})]}{\cosh(kh)} \\ \dots \\ \frac{\cosh[k(h + \frac{(N-1)h}{N})]}{\cosh(kh)} \end{pmatrix}. \quad (4.41)$$

Later, in Chapter 6, the transformation vector will be programmed to control the phase shifts of the evanescent waves with the aim of minimising the destructive interference between the evanescent waves.

4.8 Conclusion

This chapter has presented two designs for a segmented wavemaker, one where each segment acted as a piston operating in surge mode, and one where each segment acted as a flap operating in pitch mode. The hydrodynamics for the multi-body problem were developed and the DOFs of the segmented system were reduced so that systems with different quantities of segments could be compared. The results presented of the constrained added mass and radiation forces, Figures 4.15, 4.16, 4.20 and 4.21, support Hypothesis 1, Section 2.4, i.e., that the more accurately a wavemaker approximates the horizontal fluid motion in a progressive wave, the lesser the effect of the evanescent waves. Other than for the case of the single piston wavemaker, the constrained added mass was shown not to be a monotonic function of kh which can be explained by an interference pattern between evanescent waves that are in anti-phase with each other. This interference pattern leads to a reduction in the distortion of the wave field due to the evanescent waves, Section 2.4.2. It has been found that a drawback with the

segmented wavemakers is that they require larger strokes than a single segment piston or flap in order to generate waves with the same wave height.

Chapter 5

Optimisation of segment length

5.1 Introduction

A segmented wavemaker's depth profile, $c(z)$, discussed in Section 2.2 which describes the wavemaker's geometry, is dependent on two parameters; the length of each segment in the wavemaker and the segment strokes. The stroke parameters are controlled by the wavemaker's driving signal, and are further considered in Chapter 6. The segment lengths, however, are decided during the design phase and remain constant after that. This chapter focuses on optimising the segment lengths in order to reduce the distortion of the wave field caused by evanescent waves. The configurations of the segmented wavemakers which are considered here are those with two to six segments operating as both pistons and flaps. The designs are optimised by defining an objective function, a parameter which relates the segment lengths to the level of distortion caused by the evanescent waves. An optimisation algorithm then searches for the combination of segment lengths that gives the minimal value for the objective function. Since the optimised wavemaker design will change over frequency, as discussed in Section 2.4, the objective functions are averaged uniformly over the range: $0 \leq \omega \leq 14$ radians/sec ($0 \leq kh \leq 12$), similar to the operational range of the Omeq wave tank and the wave flume at the HMRC.

Section 2.4 discusses how a wavemaker which simulates the fluid motion in a progressive wave effectively eliminates the evanescent wave field, a concept that was examined theoretically by [18]. Bearing this in mind, it would be reasonable to make the assumption that the closer a wavemaker approximates the kinematics of a progressive wave, the smaller the evanescent waves will be. This was the logic behind the design of the flexible membrane wavemaker in [9] and the dual-flap wavemakers of [5] and [4]. The results for the constrained added mass of the segmented wavemakers, Figures 4.20 and 4.21 in Section 4.6.3, support this assumption as they clearly show that, as a segmented wavemaker approximates

the motion of a progressive wave more accurately, the added mass of the system decreases. The designs of the segmented wavemakers considered in Chapter 4 consist of segments of equal lengths. However, highlighted by Figure 5.1, is a concept where the kinematics of a progressive wave are better approximated by segments that decrease in size the closer they are to the free surface. The merit of this concept lies in the fact that the rate of change of the progressive wave's depth profile, specified in Equation (2.57), increases exponentially as $z \rightarrow 0$. Thus, in order to approximate Equation (2.57) with a better degree of accuracy, shorter segments are required close to the free surface, as illustrated in Figure 5.1. This reasoning agrees with the findings of [4], which reports that the total hydrodynamic load on the dual-flap wavemaker is minimised for a particular configuration where the top flap was shorter than the bottom flap. Hyun [4] did not extend the study to consider the effect on the distortion of the wave field directly.

Approximating a progressive wave reduces the distortion by minimising the Biesel coefficients [9] of evanescent terms in Equation (2.56). This requires optimisation of the wavemaker's depth profile so that the integral in Equation (2.55) tends to zero. However, achieving a depth profile that will eliminate the evanescent waves would require an infinite number of segments, something which is clearly not feasible for a physical device. Section 2.4.2 suggests the more practical approach of designing the depth profile to maximise the destructive interference between the evanescent waves. This is a novel concept that attempts to find combinations of values for the Biesel coefficients, both positive and negative, representing the evanescent terms in Equation (2.56), which causes a destructive interference pattern that minimises the evanescent wave field amplitude. Figure 5.2 provides an illustration of how a three segment flap wavemaker may be constructed. In Figure 5.2, springs push the flaps to the right, while stepper motors are pulling them to the left using wires which are coloured purple.

This chapter looks, for the first time, at the optimisation of segment lengths in wavemakers with the aim of reducing the area between the wavemaker and the test area in a tank that is contaminated by evanescent waves. Two approaches are used to optimise the segment lengths. Approach 1 is to design the geometry of the segments in a wavemaker so that it provides the best approximation to the kinematics of a progressive wave. This is similar to the approach taken by [5]. Approach 2 is to find the optimal segment lengths that minimises the distance between the wavemaker and the position of 1% distortion directly. A comparison of both approaches will provide the first piece of evidence that the destructive interference pattern between the evanescent waves can help reduce the effect of distortion in the wave tank, since Approach 2 can utilise this behaviour but Approach 1 can not.

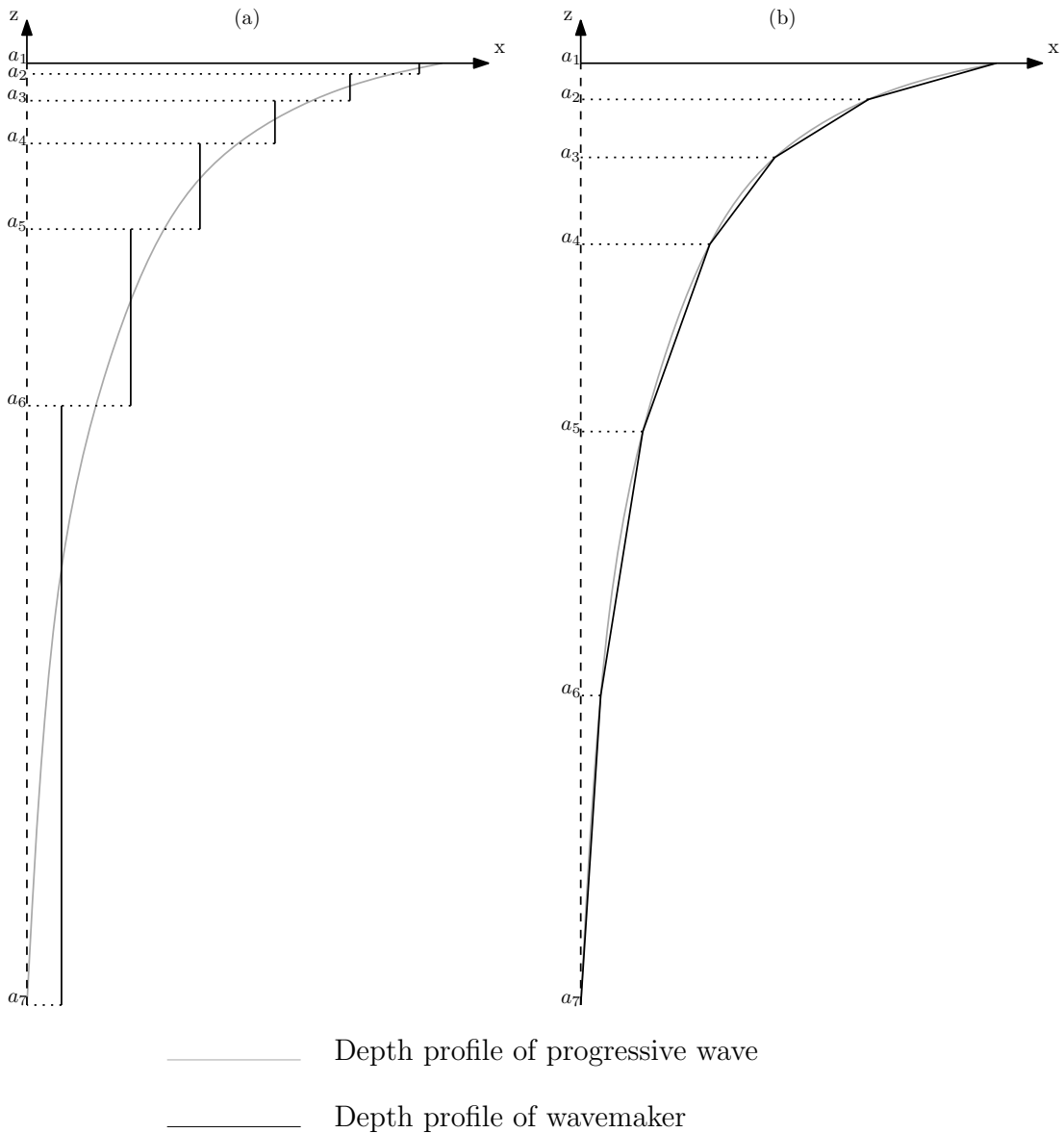


Figure 5.1: Illustration of (a) piston and (b) flap segmented wavemakers approximating the horizontal fluid displacement of a progressive wave.

Section 5.2 looks at the problem of optimising the lengths of the segments in a wavemaker, including the type of optimisation required, the constraints on the wavemaker design, the optimisation algorithm and the problem of identifying the objective function's global minima. Sections 5.3 and 5.4 describe two different strategies for optimising the segment lengths and tunes the parameters of the optimisation algorithm to allow for fast and reliable convergence. Sections 5.5 and 5.6 present the results of the optimisation of the segment lengths in a wavemaker using Approach 1 and 2, respectively, while a comparison of both approaches is provided in Section 5.7. Finally, Section 5.8 presents the concluding remarks on the optimisation of the wavemaker's segment lengths.

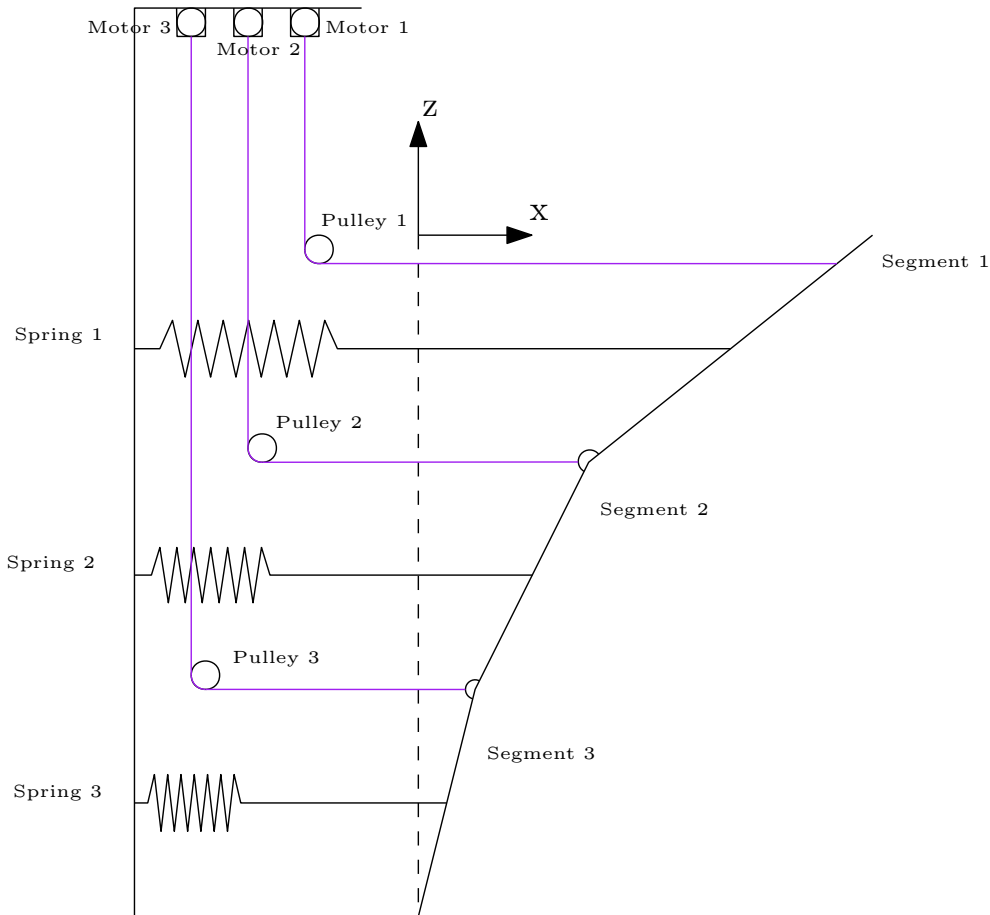


Figure 5.2: Illustration of how a segmented flap wavemaker could be constructed.

5.2 Setting up the optimisation problem

Optimisation algorithms have been used widely throughout engineering to find the minimum or maximum values of an objective function. The objective function is specified by the user to describe the effect that one wishes to minimise. This section describes the problem of finding the optimal segment lengths for a wavemaker which will minimise the distance between the wavemaker and the testable area. In this thesis, we consider the testable area in the wave tank to be where the distortion is no greater than 1%. A level of distortion of 1% is regarded as an acceptable error, as it is significantly less than the acceptable accumulated error from other sources, such as reflected waves and cross waves. The performance of the full-draft single segment piston and bottom hinged flap wavemakers, commonly used in wave tanks today, will also be presented for the purpose of comparison with the optimised segmented wavemakers.

Two strategies are proposed for optimising the design of the segmented wavemaker. The first one attempts to optimise the lengths of the segments in order to minimise the difference between the wavemaker's and the progressive wave's

depth profiles, following the idea of matching the progressive waves' kinematics with that of the wavemaker. This strategy is henceforth referred to in the rest of this thesis as the kinematic matching approach. The second strategy attempts to find a minimum distance away from the wavemaker where the distortion is 1% and does not increase above 1% thereafter. This allows the optimiser to find the best combination of segment lengths that cause an interference pattern that minimises the untestable area in front of the wavemaker. This strategy is referred to henceforth as the minimisation of distortion approach. It obviously makes more sense to use the second strategy; however, it is far more demanding on computation time as it requires the computation of the wave field, which is not necessary for the kinematic matching approach. Additionally, a comparison of both strategies allows us to test the hypothesis that optimising the interference pattern between the evanescent waves may perform better than simply approximating a natural progressive wave.

5.2.1 Optimisation algorithms

Appropriate choice of an optimisation algorithm is essential for ensuring that the objective function's global minimum is found in as short a time frame as possible. If the objective function can be specified as a linear or quadratic function of the variables of the optimisation problems, the minimum can be found using a simple optimisation algorithm, such as the Newton-Raphson method [89]. These types of algorithms search the objective function iteratively, comparing the value of the current candidate solution to the previous and can find a minimum in a relatively short period of time. However, nonlinear objective functions, such as the ones considered in this thesis, can have other local minima, in addition to the global minimum, i.e., the lowest possible value for the objective function. Since quadratic optimisation algorithms cannot differentiate between local and global minima, they are not appropriate for nonlinear optimisation problems. Evolutionary Algorithms (EAs) [90] and Genetic algorithms (GAs) [91] have been proven to be quite effective at finding global minima, though at the cost of significant computational time. EAs and GAs work by creating an initial random set of candidate solutions, referred to as a population. The algorithm then iteratively modifies the properties of the population's members until all the candidate solutions in the population appear to converge towards a single optimal solution. Following typical convention each iteration is called a generation [90]. The difference between EAs and GAs is how they create the new population. Both EAs and GAs can have many control parameters, such as population size, mutation

rate, *etc.*, all of which influence the algorithm's ability to find a global minimum and the rate of convergence. For each optimisation problem, the optimisation algorithm's control parameters need to be tuned to ensure effective, reliable and fast convergence towards an optimised solution. The optimisation algorithm used in this thesis, Differential Evolution (DE), is an elegant EA algorithm, which has been shown to have relatively fast convergence, with few parameters that require tuning [90]; this will be discussed in more detail in Section 5.2.3.

5.2.2 Wavemaker constraints

The variables of the optimisation problem are defined as the vertical position of the top and bottom edges of each segment, in both piston and flap segmented wavemakers, indicated in Figure 5.1 as a_i . The edges of the segments are labelled so that a_i represents the top edge of the i^{th} segment and the bottom edge of the $(i^{\text{th}}-1)$ segment. In a wavemaker with N segments, the a_1 and a_{N+1} edges are held constant at 0 and $-h$, respectively, enforcing the condition that the wavemaker covers the entire depth of the tank. Thus, the optimisation problem has $N - 1$ variables. The optimisation algorithm is programmed with the constraint:

$$a_{i+1} \leq a_i \leq a_{i-1}, \quad (5.1)$$

so that the candidate solutions are feasible and do not contain overlapping segments. The purpose of the equality condition in Equation (5.1) is to allow the optimisation algorithm to eliminate segments if it finds that a lower objective function can be achieved with fewer segments, although it is not expected that this will occur. For the purpose of optimising the lengths of the segments, the stroke of each segment is defined so that the horizontal displacement of each segment joint is given by:

$$x_i = \frac{\cosh[k(h + a_i)]}{\cosh[kh]}. \quad (5.2)$$

For the piston wavemakers, Equation (5.2) gives the horizontal displacement at the top of the segment, while for the flap wavemakers Equation (5.2) gives the horizontal displacement x_i at the joint a_i as denoted in Figure 5.1. The optimisation of the segment strokes will be considered in Chapter 6.

5.2.3 Differential evolution algorithm

The DE algorithm [90] has been selected for the optimisation of the segmented wavemakers as it provides fast convergence towards a solution and is relatively simple to implement [92]. The DE algorithm evaluates the objective function for each member of the current population and then creates a mutant population in which each member is a mutation of the corresponding member in the current population. A trial population is then created as a crossover between the current and mutant populations by randomly selecting members from both to become members of the trial population. If a member of the trial population has a objective function value which is less than or equal to that of the corresponding member in the current population, then that trial member is selected for the new generation, otherwise the member from the current population is kept on for another generation. This selection process makes the algorithm more focused on converging and reduces the run time, but it can also mean that the algorithm does not search as wide of a search space, thus limiting its application.

The simple implementation of the DE algorithm is due to it having only four parameters which need to be tuned: the population size; the maximum number of generations the algorithm will evaluate, or the threshold value for the objective function; a scale factor, which controls the scale of the mutation; and a crossover probability, which is the probability of a mutant being selected for the trial population. Increasing either the population size or the maximum number of generations will increase the algorithm's ability to converge to a minimum, however, they will also increase the computation time. In this thesis, a trial and error approach was used to find values for both of these parameters, for which little-to-no improvement to the objective function value can be found by increasing them further; this was carried out while the author was learning how to implement the DE algorithm. Generally the scale factor, which must be positive, should have a value between 0 and 1; however, [93] shows that the scale factor should be no less than 0.3. For problems where the variables cannot be optimised independently from each other a good crossover probability is often found between 0.9 and 1 [92].

The DE algorithm was implemented using the Matlab toolbox based on [90] (<http://www1.icsi.berkeley.edu/~storn/code.html>) and was modified by the author to impose the variable constraints in Equation (5.1). The author also modified the DE Matlab toolbox to enable the algorithm to compute in parallel, dividing the calculations up over eight cores in the computer, hence, making the optimisation process run significantly faster.

5.2.4 Finding a global minimum

Often, objective functions can have several local minima in addition to the global minimum, so when a minimum of the objective function is found it can be difficult to be sure that it is a global minimum, that is to say, no lower values of the objective function are possible. However, it can be sufficient to simply show that a solution found by the optimiser appears to be the minimum in a significantly large area of the search space. Some foresight is used to determine that the optimisation experiments carried out in this thesis should be repeated six times. If the standard deviations of the solutions found by the optimiser over the six optimisation experiments is sufficiently low, then it can be concluded with a reasonable amount of confidence that the optimiser has converged towards the minimum of the objective function. Each optimisation experiment will be referred to as an optimisation run.

5.3 Approach 1: Matching the progressive wave kinematics

The kinematic matching approach attempts to minimise the distortion in the wave tank by approximating the velocity depth profile of the progressive wave with the segmented wavemaker's velocity depth profile. The DE algorithm is used to find the optimal lengths of each segment that provides the most accurate approximation of the progressive wave's kinematics. This is similar to the approach taken by [5] who used a linear regression method based on least squares estimation to find the segment lengths in a dual-flap wavemaker that would provide the best approximation of the progressive wave's depth function. The objective function for the kinematic matching approach is defined as:

$$r = \sum_{i=1}^{N_z} \overline{|(c_t(z_i) - c_{wm}(z_i))|}, \quad (5.3)$$

where the difference term is the difference between the depth profile of the progressive wave, $c_t(z)$, and depth profile of the wavemaker, $c_{wm}(z)$. The bar above the difference term indicates that it has been averaged uniformly over the range of frequencies, $0 \leq \omega \leq 14$ radians/sec, and N_z is the number of elements, z_i , that the depth of the tank is divided uniformly into over depth.

5.3.1 Tuning the scale factor and crossover probability

The performance of the optimiser is considered by its ability to converge to the objective function's global minimum and the time required to do so; this is largely determined by the parameters of the optimiser discussed in Section 5.2.3. This section looks at tuning the parameters of the DE algorithm to achieve the best performance when optimising the segment lengths in the wavemaker using the kinematic matching approach.

It was found that a population size of 100 provides good convergence and since the kinematic matching approach does not require a lot of computation time, the algorithm was allowed to run for 1000 generations. With these settings, the algorithm took 5.5 mins to terminate. The DE algorithm was tuned by optimising the six-segmented piston wavemaker using a range of values for the scale factor and crossover probability. As discussed in Section 5.2.4, each optimisation run is repeated six times to test the reliability of the optimiser's setup. The results of tuning the DE algorithm for the kinematic matching approach are presented in Figure 5.3 for each combination of the scale factor, Fw , and the crossover probability, Cp .

Figure 5.3 shows how the DE algorithm performs at converging to a minimum value for the objective function over a range of values for the scale factor and cross probability. Figure 5.3 shows that for a scale factor greater than 0.5, the DE algorithm is quite reliable over all the values of the crossover probability, with very little variation between the objective function values in each run. Due to the approximate nature of numerical solvers, some variation can be expected. The most consistently low values for the objective functions, presented in Figure 5.3, appear to occur with a scale factor of 1 and a crossover probability between 0.3 and 0.7. Based on this analysis, the segment lengths of the wavemakers will be optimised using the kinematic matching approach in Section 5.5 with the scale factor and crossover probability of the DE algorithm set to 1 and 0.5, respectively.

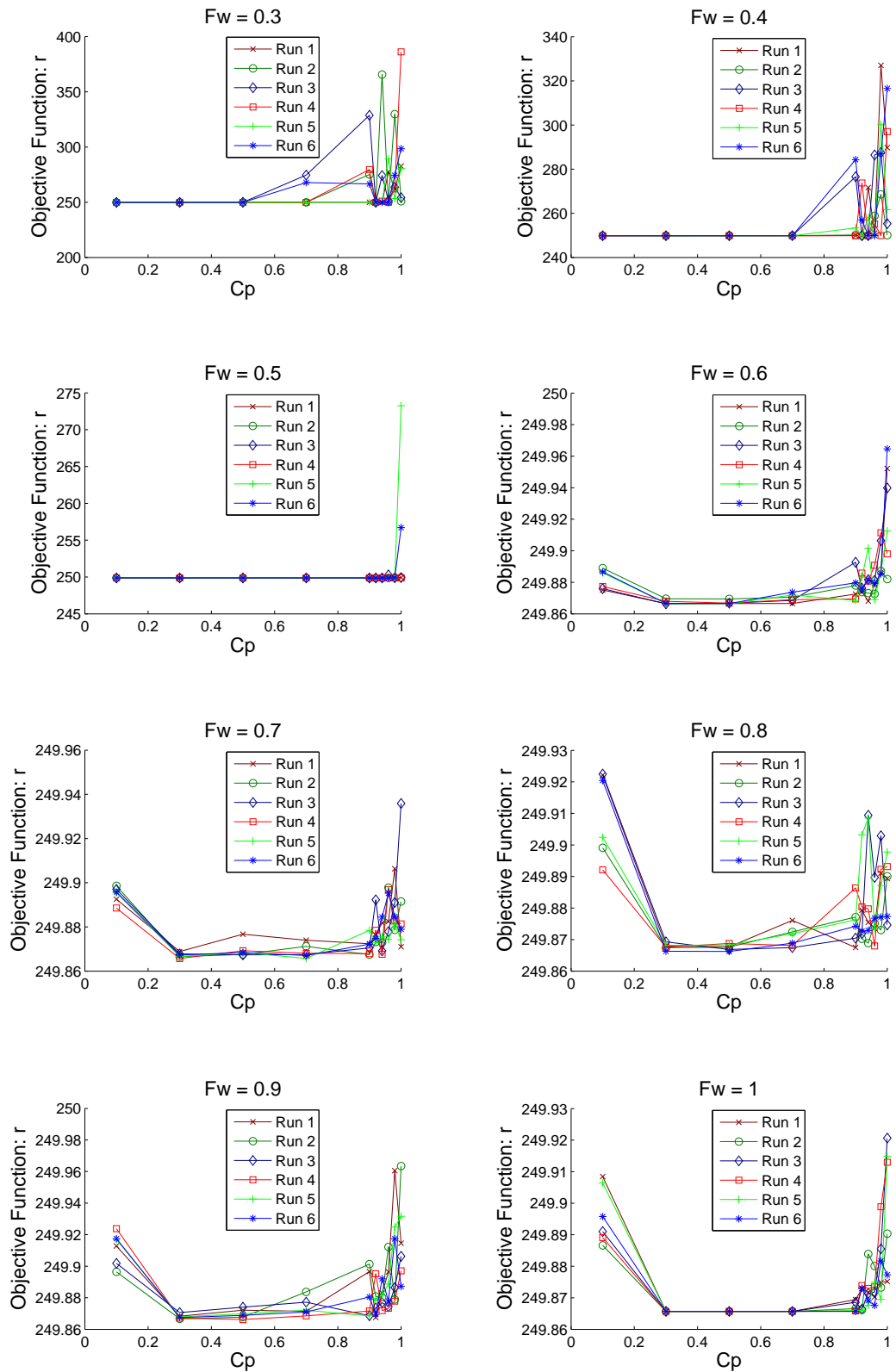


Figure 5.3: Results of tuning the scale factor, Fw , and crossover probability, Cp , for the kinematic matching approach using a six segment piston wavemaker, for six optimisation runs.

5.4 Approach 2: Minimising the wave field distortion

The advantages of using the minimisation of distortion approach is that it allows the optimiser to find the best wavemaker design for reducing the distance between the wavemaker and the testable area in the tank. Unlike the kinematic matching approach, it does not assume that the best way to reduce the distortion is to simulate a progressive wave. Instead, it can utilise the interference pattern between the evanescent waves, discussed in Section 2.4.2, to minimise the distortion. It is expected that this approach will produce better results than the kinematic matching approach, described in the previous section. So far it is unknown as to whether or not the interference pattern between the evanescent waves can help to reduce the distortion caused by the evanescent wave field. A comparison of the results from both approaches will provide validation of this.

5.4.1 Objective function: position of 1% distortion away from the wavemaker

The aim of the minimisation of distortion approach is to minimise the region in front of the wavemaker which is too contaminated with evanescent waves for meaningful tests to be performed on devices. The objective function, r , used is defined as the distance from the wavemaker to the position where the distortion is 1% and does not increase above 1% for greater values of x . This will be referred to as the position of 1% distortion and denoted as $X_{1\%}$. The interference between the evanescent waves makes it cumbersome to predict the distortion pattern along the x -axis. Hence, neither the total nor the maximum distortion values would make good objective functions, since they provide no information as to how far away from the wavemaker the testable area is. The position of 1% distortion is a pragmatic function as it provides the nearest location to the wavemaker where testing can be carried out while avoiding serious contamination from evanescent waves. As we are interested in the wavemaker's performance within the range $0 \leq \omega \leq 14$ radians/sec, the objective function is the position of 1% distortion averaged uniformly over this range.

The position of 1% distortion was found by use of a numerical solver. The numerical solver was initialised at the position $x = 5h$, and then iteratively worked towards the wavemaker, calculating the distortion of the candidate solution at each iteration, to find the 1st occurrence of the distortion having a value of 1%. This approach ensures that the distortion could not be greater than 1% for any

distance from the wavemaker greater than that reported as the position of 1% distortion. From the author's experience, it is not likely that the position of 1% distortion would be greater than $5h$.

5.4.2 Tuning the scale factor and the crossover probability

The DE algorithm behaves differently with different objective functions. Thus, the parameters of DE must be tuned again to allow it to converge efficiently towards the minima of the objective function, the position of 1% distortion. Unlike the kinematic matching approach, the minimisation of distortion approach requires Equation (2.56) to be calculated, up to the first 50 terms of the summation, for each candidate solution, at 10 uniformly distributed frequencies as it is being averaged. This can leave the optimisation very time consuming. The objective function is averaged over 10 frequencies as this provides reasonable distribution over the frequency range without requiring too much additional computation time. For the purpose of tuning the scale factor, the population size was set to 100 and the algorithm was limited to evaluate only 100 generations. When tuning the crossover probability, the population size was set to 10 and the algorithm was limited to evaluate only 10 generations. Although these settings did not provide convergence to a particular solution, they did allow us to determine suitable values for scale factor and the crossover probability. These values were determined by a trial and error basis, where it was found that increasing either parameter further did not result in different values of the scale factor and crossover probability being selected. To alleviate some of the time expense the tuning process was limited to save computation time. Rather than evaluating numerous combinations of both parameters like in Section 5.3.1, the scale factor was first tuned for a fixed crossover probability of 0.98. This crossover probability value was selected by an educated guess, backed up by the discussion in Section 5.2.3. When the preferred scale factor was found, the crossover probability was then tuned for the chosen scale factor.

The large variance in the results in Figure 5.5 is due to the optimisation algorithm being terminated before it was allowed to find a minimum. Since, at this stage, we are only interested in finding a value for the crossover probability that provides the fastest convergence towards a minimum, we can terminate the optimisation algorithm after just 10 generations, and observe which values are beginning to converge faster. This allowed us to reduce the computation time of tuning the parameters of the DE algorithm. By repeating this process six

times, we can identify which values for the scale factor and crossover probability consistently provide the fast convergences.

The results in Figure 5.4 show that the DE algorithm performs best for scale factors above 0.6. Considering these results along with the recommendations of [90], discussed in Section 5.2.3, a scale factor value of 1 was chosen for the minimisation of distortion approach.

The crossover probability was then tuned using a scale factor of 1 and the results are presented in Figure 5.5. The crossover probability was tuned more finely between the values 0.9 and 1, as [92] found this to be the best range of values for an optimisation problem where the variables cannot be optimised independently, discussed in Section 5.2.3. Based on the results in Figure 5.5, a crossover probability value of 0.98 is chosen for optimising the segment lengths using the minimisation of distortion approach. This value is selected as it gives the lowest value for the objective function and has quite a low variance between each run.

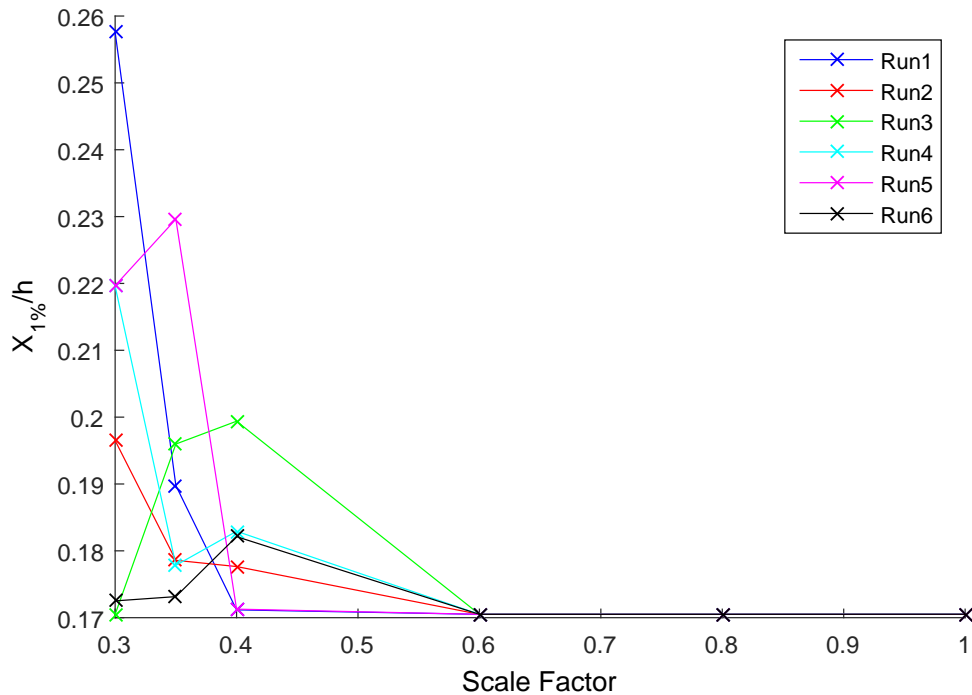


Figure 5.4: Results of tuning the scale factor, Fw , for the minimisation of distortion approach using a six segment piston wavemaker.

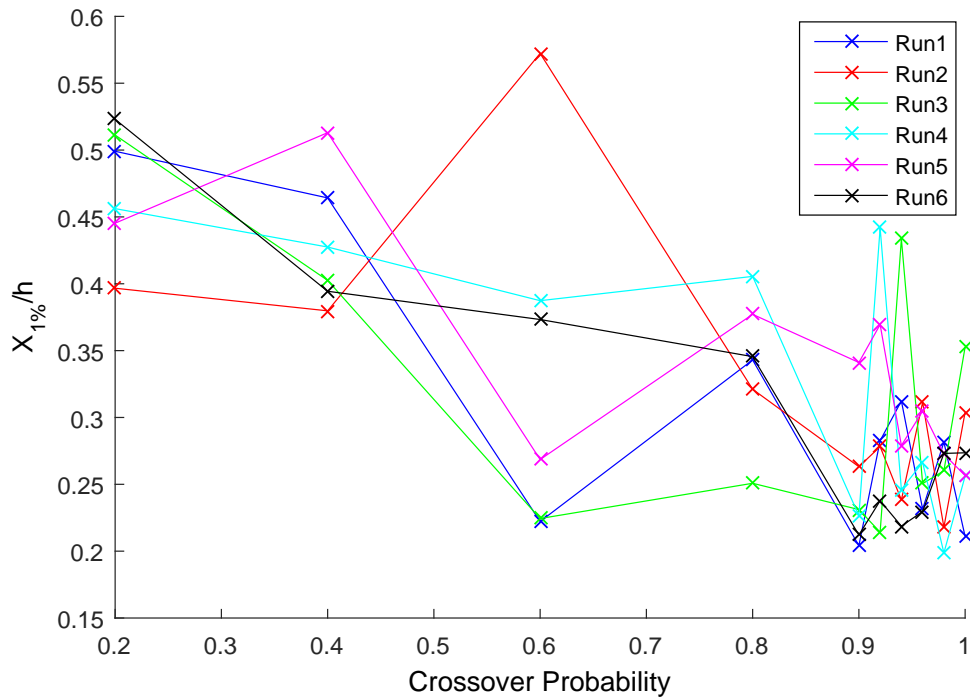


Figure 5.5: Results of tuning the crossover probability, Cp , for the minimisation of distortion approach using a six segment piston wavemaker, with increased resolution between 0.9 and 1.

5.5 Optimisation results: kinematics matching

This section presents the results of the segment lengths for wavemakers optimised using the kinematic matching approach discussed in Section 5.3. The scale factor and crossover probability were selected in Section 5.3.1 to be 1 and 0.5, respectively, while the population size was set to 100. The algorithm was allowed to evaluate 1000 generations which proved to be more than enough time for it to converge to a solution and only took 5.5 mins. The optimisation algorithm iteratively searches for the objective function defined in Equation (5.3), which measures how well the profile of the wavemaker matches the depth profile of the fluid in a progressive wave averaged over 10 frequencies uniformly distributed between $0 \leq \omega \leq 14$ radians/sec. The performance of the optimised wavemaker is assessed by the position of 1% distortion, normalised by h , away from the wavemaker which is plotted against the number of segments in the wavemaker as shown in Figure 5.6. The segment lengths of the optimised wavemakers are illustrated in Figure 5.7. The standard deviation of the objective function was taken over the six optimisation runs for each wavemaker system and are listed in Table 5.1. The standard deviations, which are 0 for wavemakers with two to four segments and of the order of 10^{-14} for wavemakers with five or six segments, pro-

Number of segments	Standard deviation over six optimisation runs	
	Piston	Flap
2	0	0
3	0	0
4	0	0
5	6.2269×10^{-14}	6.2269×10^{-14}
6	3.1134×10^{-14}	1.1257×10^{-14}

Table 5.1: Standard deviation of the six optimisation runs for the piston and flap wavemakers with two to six segments optimised using the kinematic matching approach, corresponding to the results presented in Figure 5.6.

vide confidence that the DE algorithm found the minimum within a large basin of attraction of the objective function.

The results presented in Figure 5.6 compare how the optimised segmented wavemakers perform against each other and the single segment wavemakers in terms of reducing the position of 1% distortion away from the wavemaker. The position of 1% distortion is normalised by the still water depth h and is denoted as $X_{1\%}/h$. The objective function was found by taking the difference between the wavemaker profile, $c(z)$, and the progressive wave's depth profile, denoted in Equation (5.3) as $c_{wm}(z)$ and defined in Equation (2.57), and averaging over frequency, as shown in Equation (5.3). Traditionally, for a single segment wavemaker, the rule of thumb has been to allow a distance of $2h$ to $3h$ between the wavemaker and the test area [16], which is justified in Figure 5.6. It is clear from Figure 5.6 that a wavemaker with multiple segments can provide a significant improvement on reducing the tank space in front of the wavemaker contaminated by evanescent waves. The results in Figure 5.6 supports the hypothesis that adding more segments to the wavemaker will always allow the wavemaker to further reduce the effect of the distortion caused by the evanescent waves. Given that the reduction becomes less significant as more segments are added to the wavemaker, this analysis does not include wavemakers with more than six segments. Unsurprisingly, since flap segments can approximate the kinematics of progressive waves better than piston segments, the flap type wavemakers performed better at reducing the distortion caused by the evanescent waves.

The designs of the segmented wavemakers optimised using the kinematic matching approach are illustrated in Figure 5.7. Parts (a) and (b) show the piston and flap wavemakers, respectively, for wavemakers with two to six segments as labelled. The lengths of the optimised segments, normalised by h , are indicated and although the drawings are not strictly to scale, it provides a good representation of the actual lengths of the segments. The normalised segment

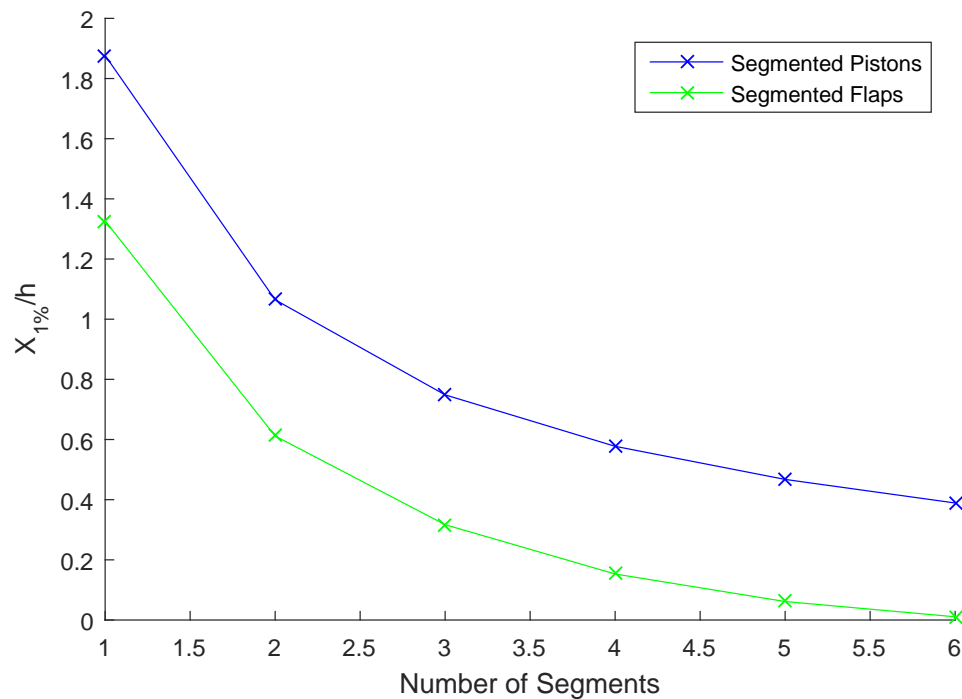


Figure 5.6: Normalised position of 1% distortion, $X_{1\%}/h$, averaged over frequency, against the number of segments in the wavemaker for both segmented piston and flap wavemakers, with segment lengths optimised using the kinematic matching approach.

lengths of the wavemakers, shown in Figure 5.7, agree with the hypothesis in Section 5.1 which proposes that the segments' lengths would decrease in size the closer they are to the free surface. This is because, as the value of z increases from $-h$ towards zero, the rate of change of the progressive wave's depth profile, Equation (2.57), increases and therefore should be approximated with shorter straight lines, as illustrated in Figure 5.1.

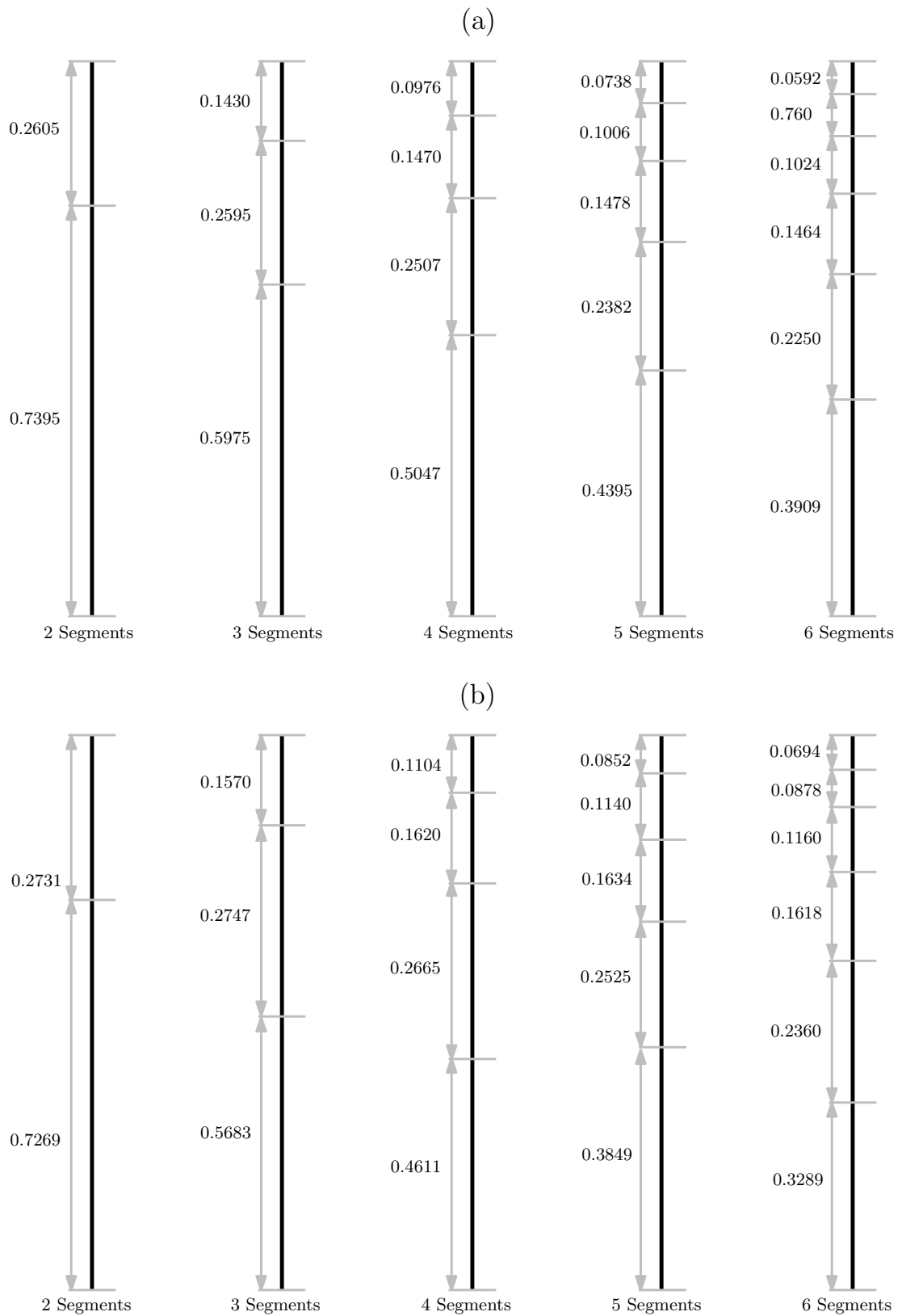


Figure 5.7: Optimised lengths of the segments, normalised by h , in (a) piston and (b) flap wavemakers optimised using the kinematic matching approach.

5.6 Optimisation results: minimisation of distortion

This section presents the results for the optimisation of the segment lengths in a wavemaker by the minimisation of distortion approach, discussed in Section 5.4, using the DE algorithm. As with the kinematic matching approach, the segment lengths are optimised for both piston and flap segmented wavemakers. The strokes of the segments were prescribed to match the displacement of a fluid in a progressive wave, given by Equation (5.2). The computational demand of the minimisation of distortion approach was discussed in Section 5.2. To reduce the time required to converge to a solution, the algorithm, which was set to have a population size of 100, was terminated after 150 generations. These parameters were determined with an trial and error approach and were found to be sufficiently large enough to allow the algorithm to converge. The scale factor and crossover probability are set to 1 and 0.98, respectively, as determined in Section 5.4.2. The position of 1% distortion for the wavemakers optimised using the minimisation of distortion approach is presented in Figure 5.8 along with that of the single segment piston and flap wavemakers for comparison. The reliability test, discussed in Section 5.2.4, was also performed and Table 5.2 gives the standard deviation of the objective function over the six optimisation runs to determine if the algorithm has converged towards the best available minima. The lengths of the optimised segments are presented in Figure 5.9.

The values of the standard deviations presented in Table 5.2 show a superior convergence towards a minimum value of the objective function than the results presented in Figure 5.5. This is because, unlike the process of tuning the crossover probability, for which the results are presented in Figure 5.5, while optimising the segment lengths, the DE algorithm was allowed to converge towards a minimum value of the objective function. In contrast to this, when tuning the crossover probability, the DE algorithm was terminated prematurely as discussed in Section 5.4.2.

As seen in Figure 5.6, the results presented in Figure 5.8 show that flap segmented wavemakers are better at reducing the position of 1% distortion than piston wavemakers and that further improvement is achieved by adding more segments to the wavemaker. The position of 1% distortion presented in Figure 5.8 is normalised by the still water depth h . What is most interesting about the results from Figure 5.8 is that, for the flap wavemakers with five and six segments, the level of distortion caused by the evanescent waves falls to 1% almost immediately in front of the wavemaker. As it is hoped that further improvement

may be achieved by optimising the strokes of the individual segments, this is a very promising result. It is worth noting that, for the relatively simple design of the flap wavemaker with three segments the position of 1% distortion is almost one fifth of the water depth in Figure 5.8. For some relatively shallow wave tanks it may not be possible, for practical reasons, to install a test device within a distance of $0.2h$ from the wavemaker. To provide context, when generating a wave, with $kh = 2.73$ and a wave height of 0.2 m in a tank with a depth of 0.6 m, a single bottom hinged flap wavemaker would require a normalised stroke of $S_0/h = 0.2590$ at the still water level. In such a case, further improvement on the performance of the flap wavemaker with three segments would not be of any significance.

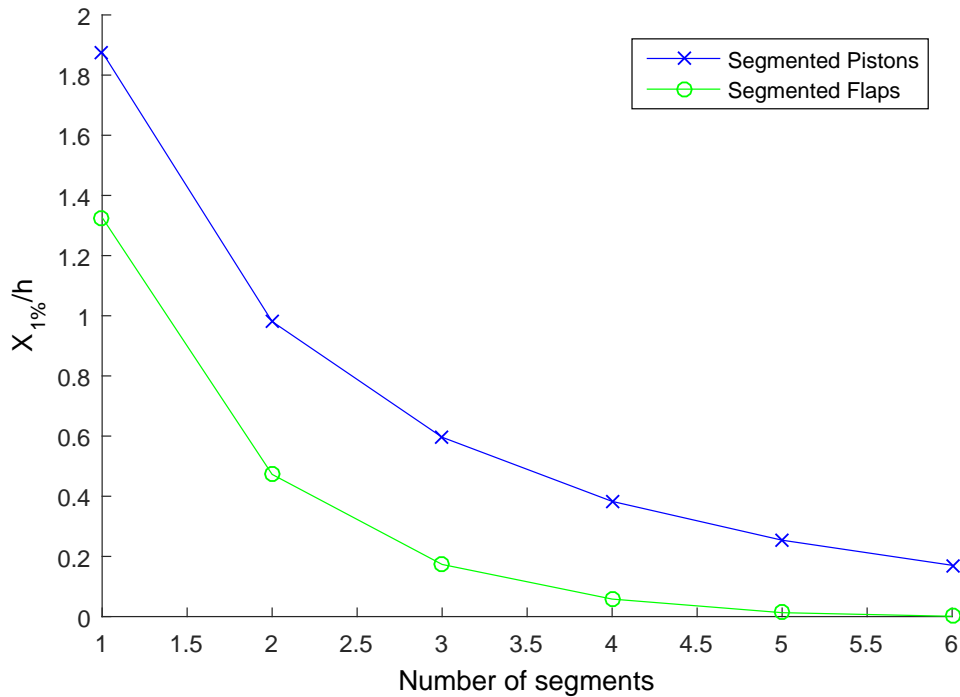


Figure 5.8: Normalised position of 1% distortion, $X_{1\%}/h$, averaged over frequency, against the number of segments in the wavemaker for both segmented piston and flap wavemakers, with the segment lengths optimised using the minimisation of distortion approach.

The standard deviation over the six optimisation runs was calculated for each wavemaker, and are presented in Table 5.2. The values reported in Table 5.2 being of the order 10^{-7} m or less, allow us to conclude confidently that the algorithm has found the minima of the objective function, at least within a large basin of attraction.

The designs of the segmented wavemakers optimised using the minimisation of distortion approach discussed above are illustrated in Parts (a) and (b) of Fig-

Number of segments	Piston	Flap
2	1.1729×10^{-14}	1.4619×10^{-14}
3	1.9283×10^{-14}	2.6398×10^{-15}
4	8.7676×10^{-15}	9.1011×10^{-16}
5	1.5971×10^{-12}	2.6300×10^{-10}
6	6.7372×10^{-9}	1.4622×10^{-7}

Table 5.2: Standard deviation of the six optimisation runs for the piston and flap segment wavemakers with two to six segments optimised using the minimisation of distortion approach, corresponding to the results presented in Figure 5.8.

ure 5.9 for the piston and flap, respectively, and normalised by h . Again, the drawings in Figure 5.9 are not to scale, but do provide a good representation of the correct segment lengths, which are indicated. It is clear from Figure 5.9 that the segment lengths do not strictly decrease the closer they are to the free surface. Unlike the case of the flap type wavemaker optimised using the kinematic approach, it is believed that the segment lengths, optimised using the minimisation of distortion approach, provides a destructive interference pattern which achieves the shortest attainable distance between the wavemaker and the position of 1% distortion.

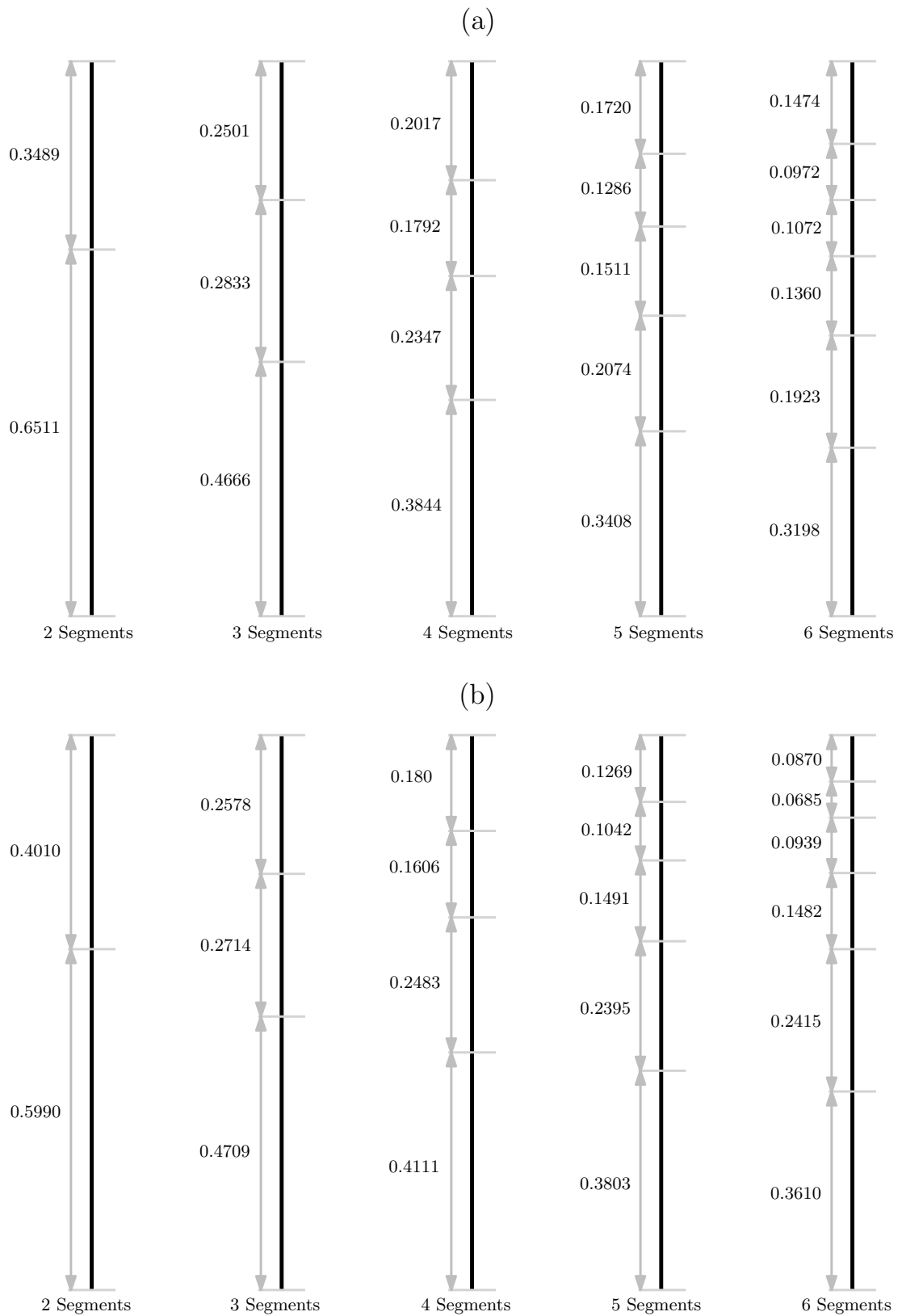


Figure 5.9: Optimised lengths of the segments, normalised by h , in (a) piston and (b) flap wavemakers optimised using the minimisation of distortion approach.

5.7 Comparison of results

The following section is a comparison of the results from both the kinematic matching and the minimisation of distortion approaches in Sections 5.5 and 5.6, respectively. A comparison is made to discuss the performance of both methods, the role of the interference pattern between the evanescent waves and the practical implementation of both approaches in terms of computational time. Both optimisation strategies were performed on the same PC with an i7, 2.9 GHz core with eight logical processors and 16 GBs of RAM.

It is clear from Figures 5.6 and 5.8 that the minimisation of distortion approach can yield better results. Intuitively, as discussed in Section 5.1, it could be expected that the segment lengths in a wavemaker would decrease the closer they are to the free surface. However, both types of segmented wavemakers optimised by the minimisation of distortion approach, shown in Figure 5.9, deviate from this behaviour. This is unsurprising since this approach utilises the phase shifts in the evanescent waves to cause as much destructive interference as possible in order to minimise the distortion, rather than simply approximating the fluid motion in a progressive wave. There still remains a clear trend in Figure 5.9 where the segments closer to the free surface tend to be shorter than those further away. This provides a compelling argument that the interference pattern between the evanescent waves, which was introduced in Section 2.4.2, can have a noticeable influence on the optimal design of a wavemaker when reducing the distance between the wavemaker and the testable area in the tank.

In terms of computation time, the kinematic matching approach is a great deal more efficient, terminating after an average of 5.5 mins per run compared to the minimisation of distortion approach which takes, on average, 2.5 hours per run to terminate. For the reader who wishes to optimise the design of their own segmented wavemaker with a given number of segments, by following the guidelines presented in this chapter the total time required to optimise the system should be approximately 33 mins using the kinematic matching approach and 15 hours using the minimisation of distortion approach. Even though it takes 27.3 times longer to compute, the time required to optimise a segmented wavemaker using the minimisation of distortion approach is reasonable in context with the time required to design the mechanics of the wavemaker and to develop the code to predict the hydrodynamic model.

5.8 Conclusion

The optimisation of the lengths of the segments in a wavemaker with the aim of reducing the effect of distortion in a wave tank caused by the presence of evanescent waves, has been discussed. Two separate strategies were employed to optimise the geometry of the wavemaker and the results from both approaches were presented. Approach 1 was simply to approximate the motion of the fluid in a progressive wave as accurately as possible with the motion of the wavemaker. Approach 2 was to minimise the distance between the wavemaker and the testable area in the tank directly. This approach aims to find the wavemaker design which creates a destructive interference pattern between the evanescent waves that minimises the amplitude of the evanescent wave field. This is possible by causing a phase shift of π radians to some of the evanescent waves. For both strategies, the DE algorithm was used to search for the segments' lengths which gave the lowest value of the objective functions. An extensive procedure was followed to ensure that the minima found by the DE algorithm were either the global or the best available minima of the objective function. The results show that minimising the distance between the wavemaker and the testable area yields notably better results, though this was expected. The comparison between both methods indicates that the phases of the individual evanescent waves can be optimised to create a destructive interference pattern which minimises the distortion in a wave tank.

Chapter 6

Optimisation of segment stroke

6.1 Introduction

The aim of this chapter is to find the optimal strokes of each segment in the wavemaker which minimises the distance between the wavemaker and the testable area in the tank. Hypothesis 2, Section 2.4.2, proposed that the optimal geometrical design for a rigid-body wavemaker for minimising the distortion would lead to some evanescent waves experiencing a phase shift of π radians in relation to other evanescent waves. The premise of Hypothesis 2 is that these phase shifts would then lead to a destructive interference pattern, hence, reducing the magnitude of the collective evanescent wave field.

The results presented in Chapter 5 confirmed Hypothesis 2 where it was demonstrated that, when optimising the segment lengths in a wavemaker, the interference pattern could be optimised to minimise the wave field distortion. Other evidence supporting Hypothesis 2 are the results of the constrained added mass for the segmented wavemakers in Figures 4.20 and 4.21, which were discussed in Section 4.6.3.

Although the results in Section 5.6 of the optimised segment lengths showed significant improvement over the traditional piston and flap wavemakers, the strokes of each segment were prescribed by the kinematics of the progressive wave, Equation (2.57), Section 2.4. According to Hypothesis 2, however, there is no reason that suggests the optimal strokes will be provided by Equation (2.57). Thus, it is conceivable that further improvement may be achieved by optimising the segment strokes to utilise the evanescent waves' interference pattern.

As discussed in Section 5.4.1, minimising the total distortion directly is difficult and cumbersome. Instead, the same objective function is employed that was proposed in Section 5.4.1 for the minimisation of distortion approach; that is the distance from the wavemaker to where the distortion level is $\leq 1\%$ and does not increase to be greater than 1% for further increases in x , this is referred to as

the position of 1% distortion and denoted by $X_{1\%}$. Certainly, we may presume that a wavemaker in which both the segments' lengths and strokes are optimised will provide the best performance in terms of reducing the position of 1% distortion. Yet, a question that emerges is, which has a greater influence on minimising the distortion: optimising the segment lengths or the segment strokes? The motivation behind this question is to understand which aspect is more important when designing a wavemaker for reducing the distortion, the physical geometry of each segment or the wavemaker's control system, which controls the strokes of each segment. To answer this question, the segment strokes are optimised for two cases: (1) where the segment lengths are equal and (2) where the segment lengths were optimised by the minimisation of distortion approach and are given in Figure 5.9, Section 5.6. The results from Case (1) can then be compared to those presented in Figure 5.8, where the segmented wavemakers have optimised segment lengths, but the strokes were determined by the kinematic matching approach, Equation (5.2). This comparison will allow us to determine whether the optimal segment lengths or strokes are more effective at reducing the wave field distortion. The results from Case (2) will provide the best achievable reduction of the distance between the wavemaker and the testable tank area using the segmented wavemakers. Unlike the segment lengths, it is feasible to tune the segment strokes for each individual frequency. It is to be expected that the poorest performance, in terms of minimising the distortion, will arise at the highest frequency considered; however, it is also useful to understand how the wavemaker performs over an operating frequency range.

The DE algorithm used in Chapter 5 is selected to optimise the segment strokes, as it proves to be effective at finding the minima of the objective function in a relatively short period of time and is rather simple to implement, having few parameters to tune [92]. The DE algorithm is demonstrated, by the results presented in this chapter, to be quite reliable at finding the lowest obtainable values of the objective function, the position of 1% distortion. From the results presented in Figure 5.8, it is clear that no further significant improvement in the reduction of the wave field distortion can be achieved by adding more than six segments into the flap wavemaker. Hence, our investigation in this chapter is restricted to both the piston and flap wavemakers with two to six segments. The performance of a single segment piston and flap, in terms of the position of 1% distortion, is also presented to allow for a comparison between the optimised segmented wavemakers and the traditional wavemakers.

In order to improve the performance of the DE algorithm during the optimisation process, the variable search space is limited by constraining the maximum amplitude of the segments' strokes to not exceed 2 unit strokes (a unit stroke is a

stroke of 1 m). This does not affect the results in any way, as the distortion of the wave field is not strictly dependent on the amplitude of the segments' strokes, but rather the ratio between the amplitudes of the progressive and evanescent wave fields. Reducing the search space of each variable allows the DE algorithm to converge to a solution much faster. It could certainly be argued that, in order to achieve the true optimal wavemaker configuration, the segment lengths and strokes should be optimised simultaneously. However, this optimisation problem becomes much more difficult, having roughly twice the number of variables. Bearing in mind the quality of results obtained from optimising the segment lengths alone, it seems reasonable to assume that no significant improvement would be achieved by doing so.

Presented in Section 6.2 is the analysis for tuning the parameters of the DE algorithm for the problem of optimising the strokes of the segmented wavemakers. In Section 6.3 the strokes are optimised for segmented wavemakers where all the segments are equal in length. A comparison is then made with the results of the segmented wavemakers with optimised segment lengths and strokes prescribed by Equation (5.2) in Figure 5.8, Section 5.6. The optimisation of the strokes for the segmented wavemakers designs with optimised segment lengths, shown in Figure 5.8, is presented in Section 6.4. The depth profiles of the segmented wavemakers where both the lengths and strokes are optimised is also presented in Section 6.4 to confirm the validity of Hypothesis 2, Section 2.4.2. Section 6.5 looks at the affect of the evanescent waves on the wave field when the strokes and lengths of the segments in the wavemaker are optimised. A sensitivity analysis as to how errors in the wavemaker's strokes affect the performance of the wavemaker in terms of the distortion to the wave field and the fidelity of the progressive wave height is presented in Sections 6.6.1 and 6.6.2, respectively. Finally, the findings of the optimisation of segment strokes in segmented wavemakers are concluded in Section 6.7.

6.2 Tuning the optimisation parameters

To ensure efficient and reliable convergence to a solution for the problem of optimising the segment strokes, the parameters of the DE algorithm must be tuned, as they were in Chapter 5. It was found that a population size of 100 solution candidates provided good convergence speeds with little benefit arising from larger population sizes which require more computation time. When optimising the flap segmented wavemakers at $kh = 12$ and the piston segmented wavemaker

over the entire range of $0 \leq kh \leq 12$, there was no further improvements to the solutions found by the optimiser after 300 generations. When optimising the flap segmented wavemakers for $kh \leq 10.8$ it was found that the DE algorithm did not find any better solutions after 120 generations. As explained in Section 5.2.4, it is important to ensure that the minimal value for the objective function found by the optimiser is in fact the lowest value that can be achieved. Here a little foresight is used by choosing to repeat the optimisation runs six times. This will be justified by the results presented in this chapter, which indicate that six optimisation runs is sufficient in determining that the DE algorithm is converging towards the same best available minimum.

While tuning the DE algorithm's scale factor, Fw , the population size was set to 100 and the crossover probability was set to a value of 1. For a range of values between 0.3 and 1, the scale factor was tuned for a piston type wavemaker with six segments. The DE algorithm was terminated after 100 generations. The six independent optimisation runs for the tuning process are presented in Figure 6.1. The results in Figure 6.1 clearly indicate that the fastest convergence

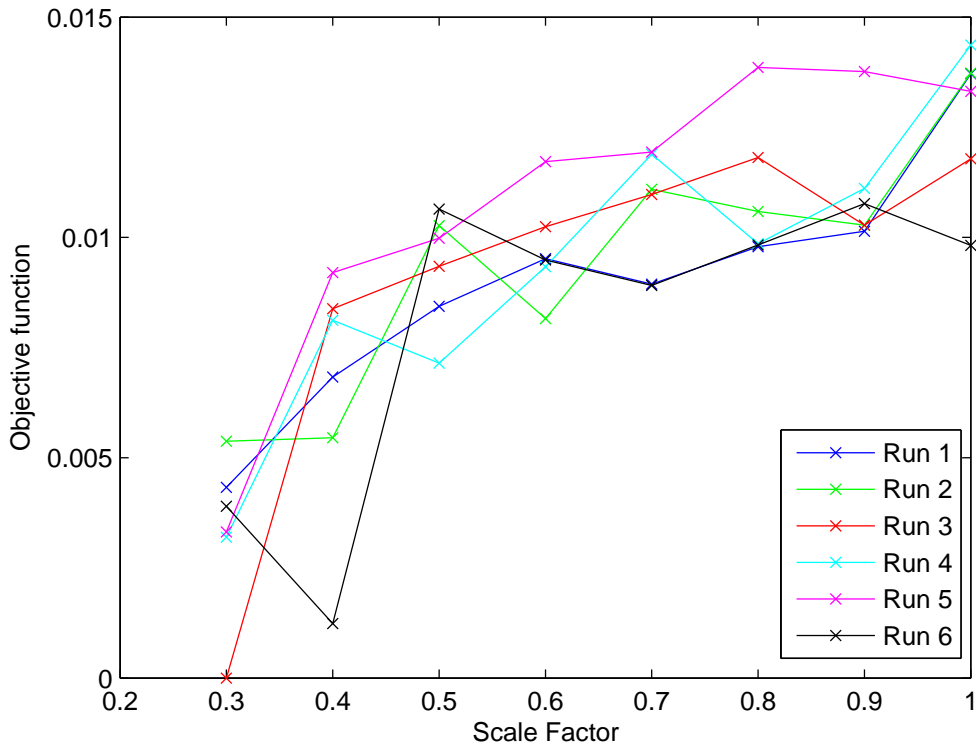


Figure 6.1: Results of tuning the scale factor, Fw , for optimising the strokes of each segment.

to a minimum is achieved with a scale factor value of 0.3. For reasons explained in Section 5.2.3 scale factor values less than 0.3 were not considered.

Following this, the crossover probability, Cp , was tuned between values of 0.3 and 1, using a scale factor of 0.3. Again the population size was set to 100 while the algorithm was terminated after 50 generations. Between values of 0.9 and 1, the resolution for tuning the crossover probability was increased, since the most appropriate value is often found within this range, as discussed in Section 5.2.3. The results of tuning the crossover probability, for the purpose of optimising the segments' strokes, are presented in Figure 6.2. Figure 6.2 indicates that the crossover probability value which finds the most reliably low value for the objective function is 1.

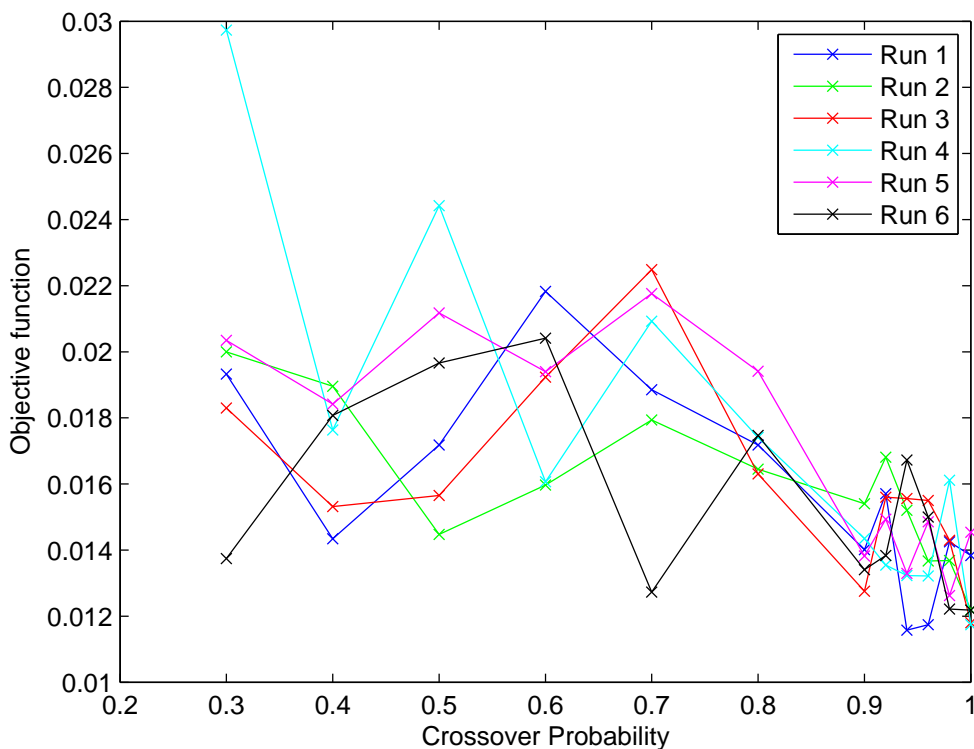


Figure 6.2: Results of tuning the crossover probability, Cp , for optimising the strokes of each segment.

Following from Figures 6.1 and 6.2 the optimisation of the segment strokes carried out in this chapter is done with the scale factor and crossover probability of the DE algorithm set to 0.3 and 1, respectively.

As with the results presented in Figure 5.5, there is a large variance in the results presented in Figures 6.1 and 6.2. The reason for this was described in Section 5.4.2, which is that for the purpose of tuning both the scale factor and the crossover probability, the optimisation algorithm was terminated before it fully converged to a minimum. By terminating the optimisation algorithm early, we were able to reduce the computational cost, while still being able to determine the

appropriate values for the scale factor and the crossover probability that provided the fastest convergence for the optimisation problem.

6.3 Case (1): Optimisation of strokes for segments of equal lengths

This section will address the problem of finding the optimal strokes for each segment in a wavemaker where all the segments are of equal lengths, as proposed in Section 6.1, Case (1). The segment strokes are optimised for a number of frequencies, for both piston and flap wavemakers with two to six segments. To provide confidence that the minima found are indeed the lowest available values of the objective function, the optimisation runs are repeated six times, as discussed in Section 6.2.

The lowest values for the objective function, the position of 1% distortion, obtained over the six optimisation runs are plotted against kh in Figures 6.3 and 6.4 for the piston and flap wavemakers, respectively. In both Figures 6.3 and 6.4, the y axis is the normalised position of 1% distortion, while kh is represented by the x axis. Immediately, we see in both Figures 6.3 and 6.4 that optimising the strokes of the segmented wavemakers provides a drastic reduction in the level of distortion in the tank compared to the traditional single segment wavemakers. Comparing Figures 6.3 and 6.4 we see that, just like the results presented in Figures 5.6 and 5.8, Chapter 5, the flap wavemakers are still more successful at reducing the effect of the wave field distortion caused by the evanescent waves. To answer the question as to which provides a greater reduction in the wave field distortion: optimising the segment lengths or strokes, Figures 6.3 and 6.4 are compared to the respective results for the piston and flap wavemakers in Figure 5.8, where the segment lengths have been optimised but the strokes are prescribed by Equation (5.2). It is evident from Figures 6.3, 6.4 and 5.8 that optimising the segment strokes yields better results for reducing the wave field distortion than optimising the segment lengths.

To provide context, we look at the two segment piston and flap wavemakers in Figure 5.8, where the segment lengths are optimised and the segment strokes are prescribed by the kinematics of a progressive wave. The normalised positions of 1% distortion, $X_{1\%}/h$, at $kh = 12$ are 1.1412 and 0.6951, for the piston and flap wavemakers, respectively. The corresponding values presented in Figures 6.3 and 6.4 for the normalised positions of 1% distortion are 0.4464 and 0.08594 at $kh = 12$ for the piston and flap segmented wavemakers, respectively, where the

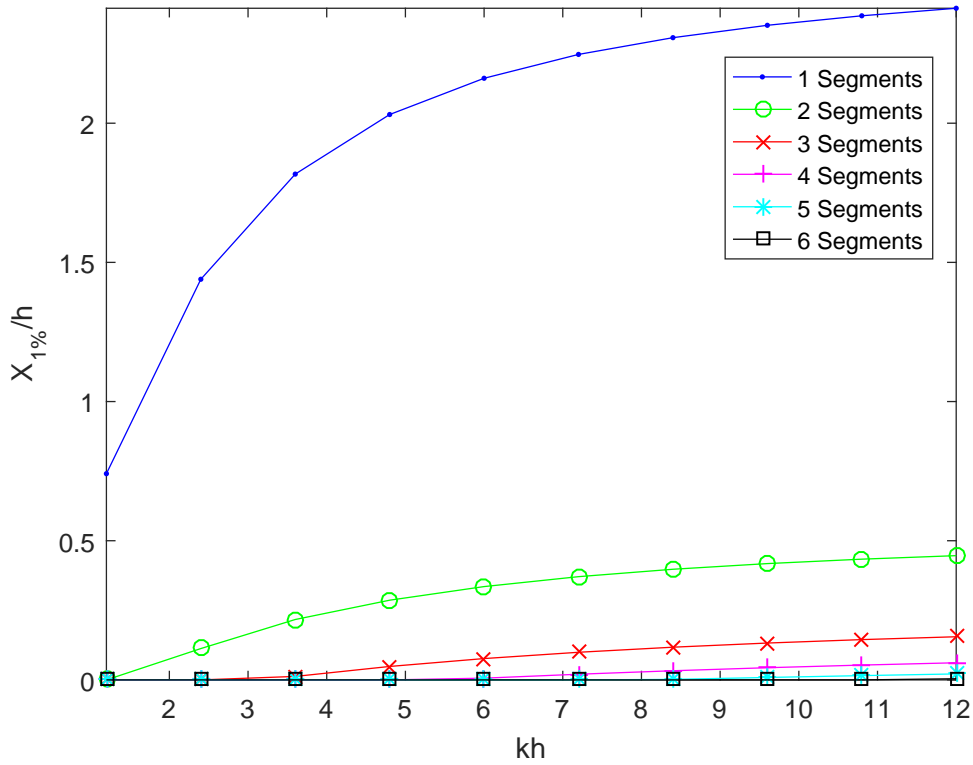


Figure 6.3: Lowest value of $X_{1\%}/h$ obtained by optimising the segments' strokes for piston wavemakers where the segments are of equal length, where $h = 0.6$.

segments are of equal length. An argument can be made that this is partly due to the segment lengths not being optimised for each frequency like the strokes were; however, having the segment lengths change for each frequency is clearly impractical, even when monochromatic waves are being considered. Perhaps what is most encouraging about the results in Figure 6.4 is that the normalised position of 1% distortion for a two segment flap wavemaker goes to zero for $kh \leq 4.9$. For flap wavemakers with more than three segments in Figure 6.4, the normalised position of 1% distortion is zero for the entire range of kh . This suggests that the wave field distortion can effectively be eliminated using a rather simple wavemaker design.

Regarding the generation of random waves, by simply applying the principle of superposition we could work out the resulting distortion pattern. However, by optimising the segment strokes of the wavemaker specifically for the spectrum being generated, it may be possible that the evanescent waves generated at one frequency would help cancel out the evanescent waves generated at another frequency, reducing the effect of the distortion further.

The minimum values for the objective function found by the optimiser during each optimisation run are presented in Tables A.1 to A.5 for the segmented piston

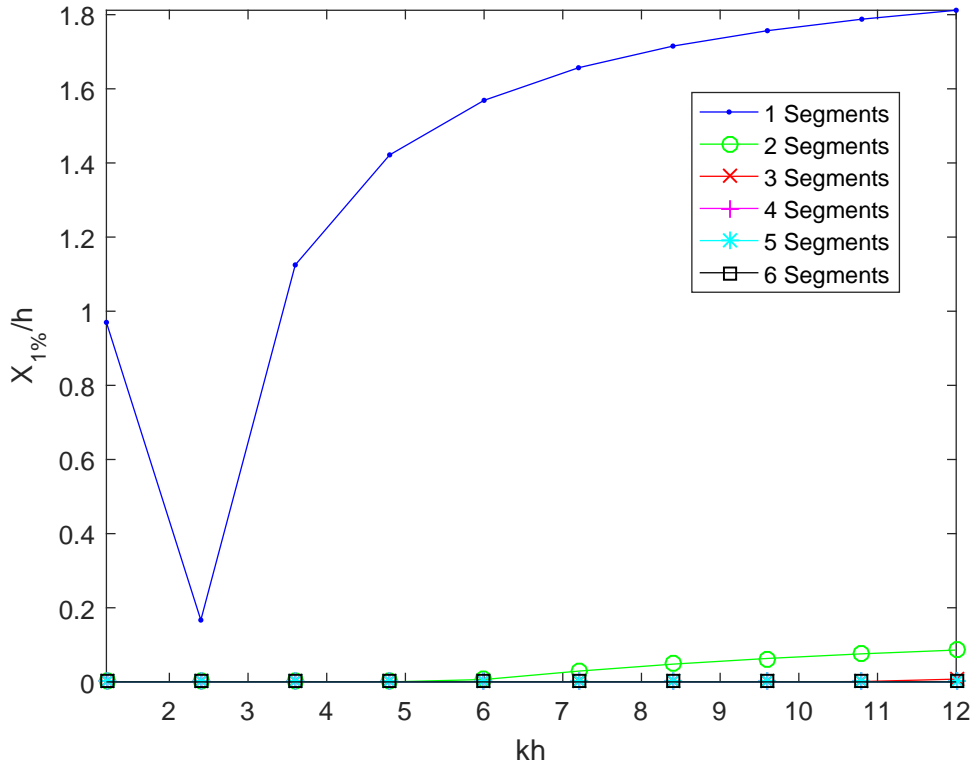


Figure 6.4: Lowest value of $X_{1\%}/h$ obtained by optimising the segments' strokes for flap wavemakers where the segments are of equal length, where $h = 0.6$.

configurations, and Tables A.6 to A.10 for the segmented flap configurations in Appendix A. The standard deviations of the six independent runs for each wavemaker are presented in Tables A.11 and A.12 in Appendix A for the piston and flap wavemakers, respectively. Tables A.1 to A.12, in Appendix A, are provided for completeness and demonstrate the consistency of the minimum objective function value found by the optimisation algorithm. The optimised segment strokes that resulted in the lowest positions of 1% distortion achieved by the piston configuration wavemakers, at each frequency in Tables A.1 to A.5, are presented in Tables A.13 to A.17 in Appendix A. Similarly, the optimised segment strokes for the flap wavemakers are given in Tables A.18 to A.22 in Appendix A. Bear in mind that the segmented flap wavemaker is actuated at the joints between the flaps as well as at the positions $z = 0$ and $z = -h$. Hence, a flap wavemaker with N segments has $(N + 1)$ strokes. The values for segment strokes presented in Tables A.13 to A.22, in Appendix A, can be used as inputs for a controller designed to operate the segmented wavemaker. In situations where the optimiser reports an objective function value of zero, we can be certain that the true minimum has been found, since a negative value would indicate a location behind the wavemaker. For the cases when the lowest value for the objective function

is not zero, the standard deviation of the results from the independent optimisation runs presented in Tables A.11 and A.12 are sufficiently low to conclude with confidence that the optimiser has found the best available minimum.

6.4 Case (2): Optimisation of strokes for optimised segment lengths

The second problem considered in this chapter is the optimisation of the strokes for the segmented wavemakers illustrated in Figure 5.9, where the segment lengths have been optimised by the minimisation of distortion approach in Section 5.6. The ambition of this section is to find the configuration of each segmented wavemaker which provides the lowest value of the position of 1% distortion that can be achieved by the wavemakers. For the rest of this thesis the wavemakers optimised in this section will be referred to as “completely optimised” segmented wavemakers since both the segment lengths and strokes have been optimised.

As before, the strokes are optimised for piston and flap wavemakers with two to six segments. The best obtained values of the position of 1% distortion over the six optimisation runs are plotted for each optimised segment piston and flap wavemaker in Figures 6.5 and 6.6, respectively. It is apparent, from comparing Figures 6.5 and 6.6 to the results presented in Figures 6.3 and 6.4, that the completely optimised segmented wavemakers provide only a small improvement from wavemakers where the strokes alone were optimised. It is reasonable to determine that the most important factor, in terms of reducing the effect of distortion in the wave tank, to be considered when designing a segmented wavemaker, is the strokes of the segments. Although, as constructing the wavemakers illustrated in Figure 5.9 presents no additional challenges in comparison with wavemakers where the all segments are equal in length, there is no obvious reason as to why the optimal segment lengths should not be used. It is worth noting from Figure 6.6 that the three segment flap wavemaker achieves a distortion level less than 1% at the surface of the wavemaker for the entire range of kh .

The results of the six independent optimisation runs for each segmented wavemaker are presented in Tables A.23 to A.27 for the piston wavemakers and Tables A.28 to A.32 for the flap wavemakers, in Appendix A. The standard deviations over the six optimisation runs are presented in Tables A.33 and A.34 for the piston and flap wavemakers, respectively, in Appendix A. The optimised

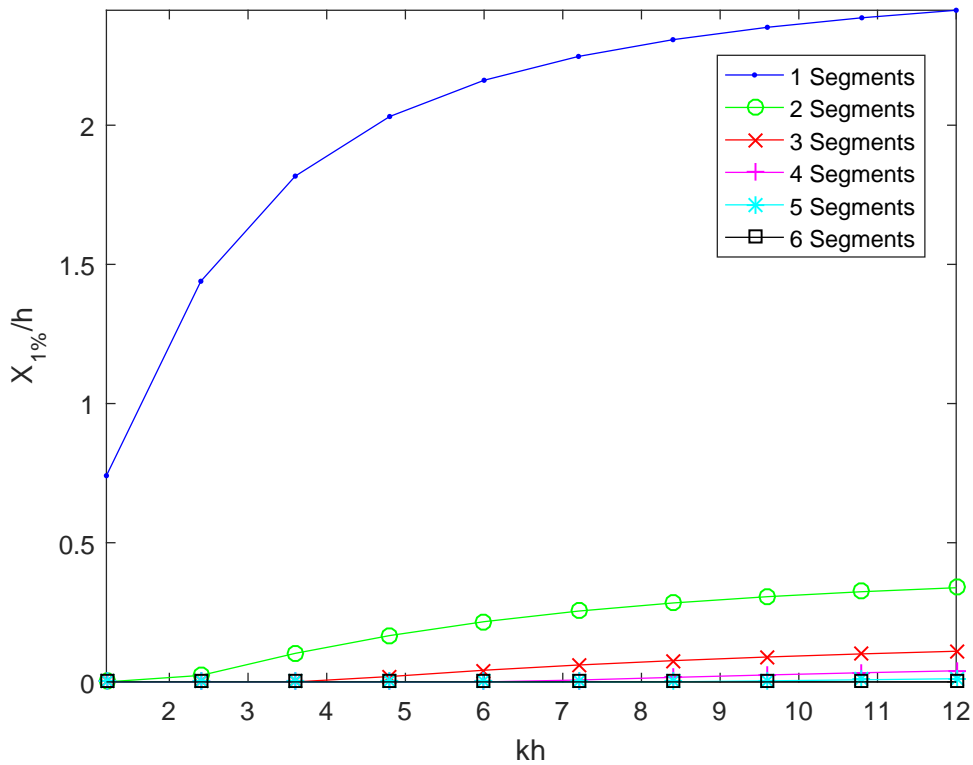


Figure 6.5: Lowest value of $X_{1\%}/h$ obtained by optimising the segments' strokes for piston wavemakers with optimised segment lengths, where $h = 0.6$.

strokes which provided the lowest position of 1% distortion of the six optimisation runs for each wavemaker are presented in Tables A.35 to A.39 for the piston wavemakers and Tables A.40 to A.44 for the flap wavemakers. Again, recalling from Section 6.3 that a flap wavemaker with N segments has $(N + 1)$ strokes. For the instances where an objective function value of zero was not obtained, the maximum standard deviation presented in Tables A.33 and A.34 are so low that it seems safe to conclude that the minimum values of the objective function was found in each case.

To provide graphical context of the completely optimised segmented wavemakers, the depth profiles, normalised by the stroke of the top segment, for each wavemaker at $k = 2, 10$ and 20 m^{-1} are illustrated in Figures 6.7 and 6.8 for the piston and flap wavemakers, respectively. The depth profiles in Figures 6.7 and 6.8 highlight how different the optimised wavemakers' depth profiles are to that of the progressive waves, Equation (2.57). The significance of the results presented in this chapter is not solely the success in reducing the level of distortion in the wave field, but also in the validation of Hypothesis 2, Section 2.4.2. The depth profiles of the segmented wavemakers in Figures 6.7 and 6.8 suggest that the success in reducing the distortion was achieved by utilising the inter-

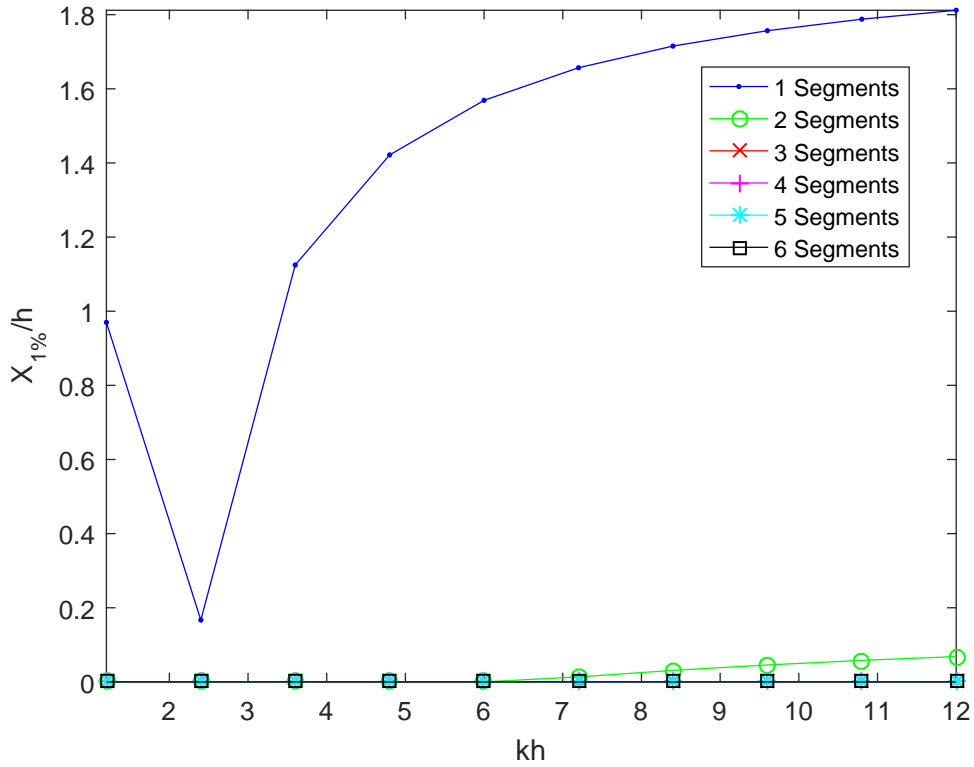


Figure 6.6: Lowest value of $X_{1\%}/h$ obtained by optimising the segments' strokes for flap wavemakers with optimised segment lengths, where $h = 0.6$.

ference pattern between the evanescent waves. This contradicts the traditional assumptions that, to reduce the distortion, a wavemaker should approximate the kinematics of a progressive wave, as stated in Hypothesis 1, Section 2.4. It should be noted that the segments in the wavemakers in Figures 6.7 and 6.8 are either in phase or in anti-phase with each other. It is worth mentioning that the wavemakers illustrated in Figures 6.7 and 6.8 don't displace as much fluid for a given stroke, S_0 (i.e., the stroke at the free surface elevation), resulting in smaller wave heights being generated. To account for this, the amplitude of the all the segments strokes can be increased using a correction factor, Equation (4.38) Section 4.6.3.

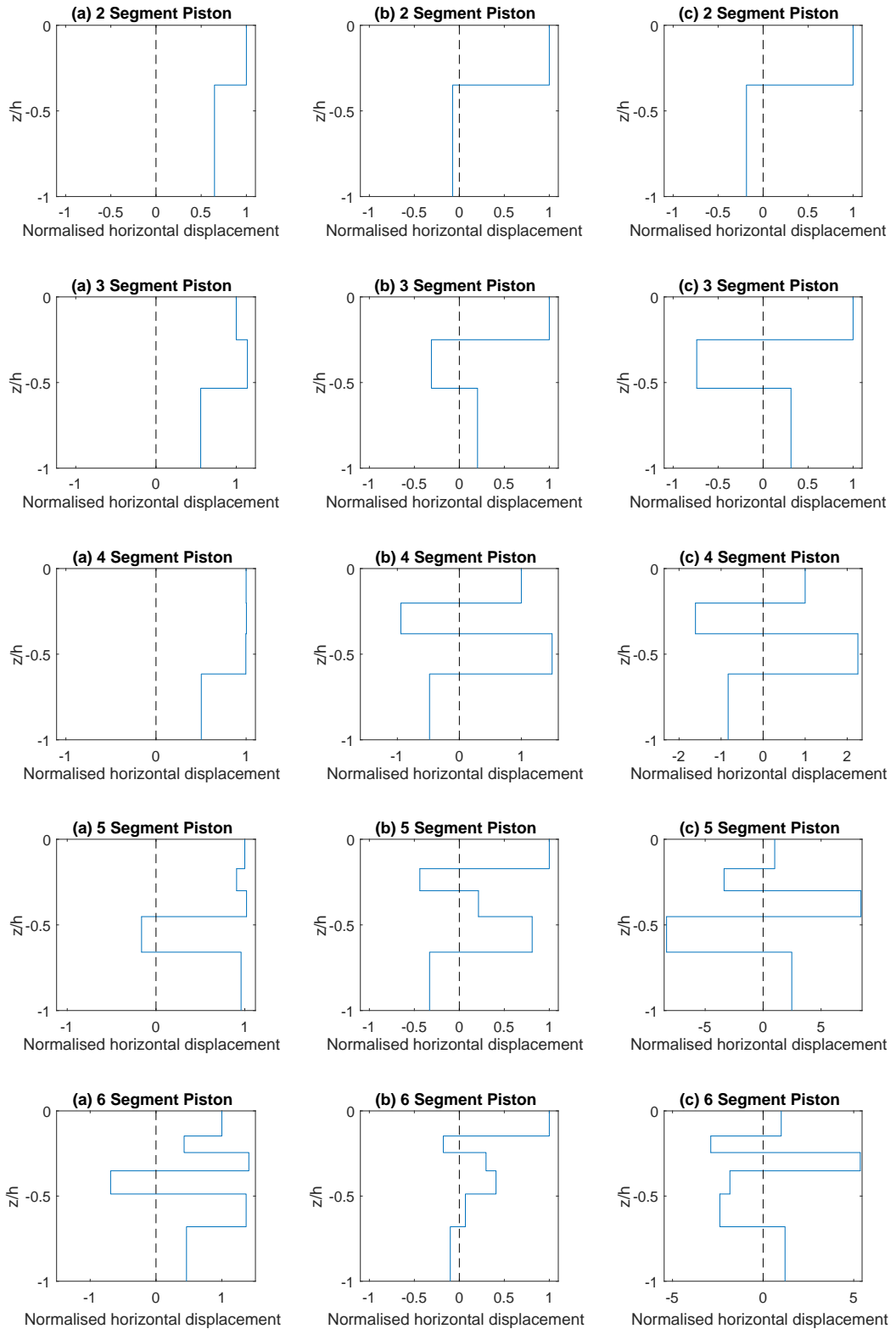


Figure 6.7: Depth profiles of completely optimised segmented piston wavemakers, normalised by the stroke of the top segment, for (a) $\omega = 4$ rad/sec, (b) $\omega = 9.9$ rad/sec and (c) $\omega = 14$ rad/sec.

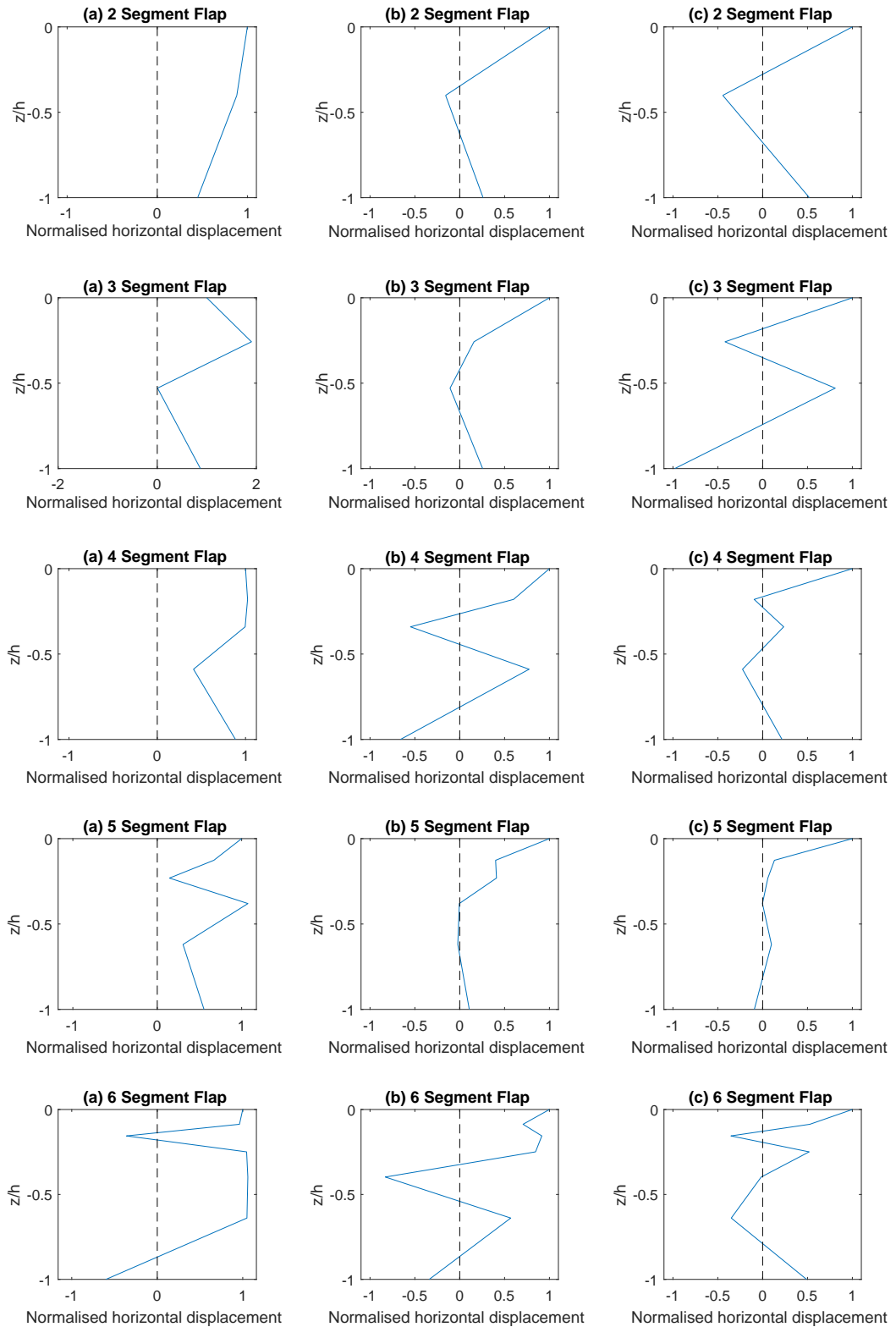


Figure 6.8: Depth profiles of completely optimised segmented flap wavemakers, normalised by the stroke of the top segment, for (a) $\omega = 4$ rad/sec, (b) $\omega = 9.9$ rad/sec and (c) $\omega = 14$ rad/sec.

6.5 Analysis of the evanescent wave field (sample results)

The affect of the interference pattern on the wave field distortion is illustrated in Figures 6.9 and 6.10, where the distortion is plotted against the normalised distance away from the wavemaker, x/h . The distortion patterns shown in Figures 6.9 and 6.10 are those caused by the wavemakers' depth profiles presented in Figures 6.7 and 6.8, respectively. The horizontal line in Figures 6.9 and 6.10 highlights the level of 1% distortion, the threshold distortion level considered in this thesis.

If none of the evanescent waves underwent a phase shift, the distortion functions presented in Figures 6.9 and 6.10 would decrease in a exponential manner with increasing x , as shown in Section 2.4.1, Figure 2.7 and by [19]; however, this is obviously not the case. Instead, the distortion functions shown in Figures 6.9 and 6.10 are the results of the superposition of 49 different exponential functions, Equation (2.56), containing various exponents and with positive and negative coefficients. The peaks in the distortion function are indicative of areas of constructive interference between the evanescent waves, while the occurrences of the distortion level going to zero arise from destructive interference. In each plot in Figures 6.9 and 6.10 after the last distortion peak (i.e., the peak furthest away from the wavemaker's surface at $x = 0$), the distortion does appear to exhibit asymptotic behaviour by approaching zero as $x \rightarrow \infty$.

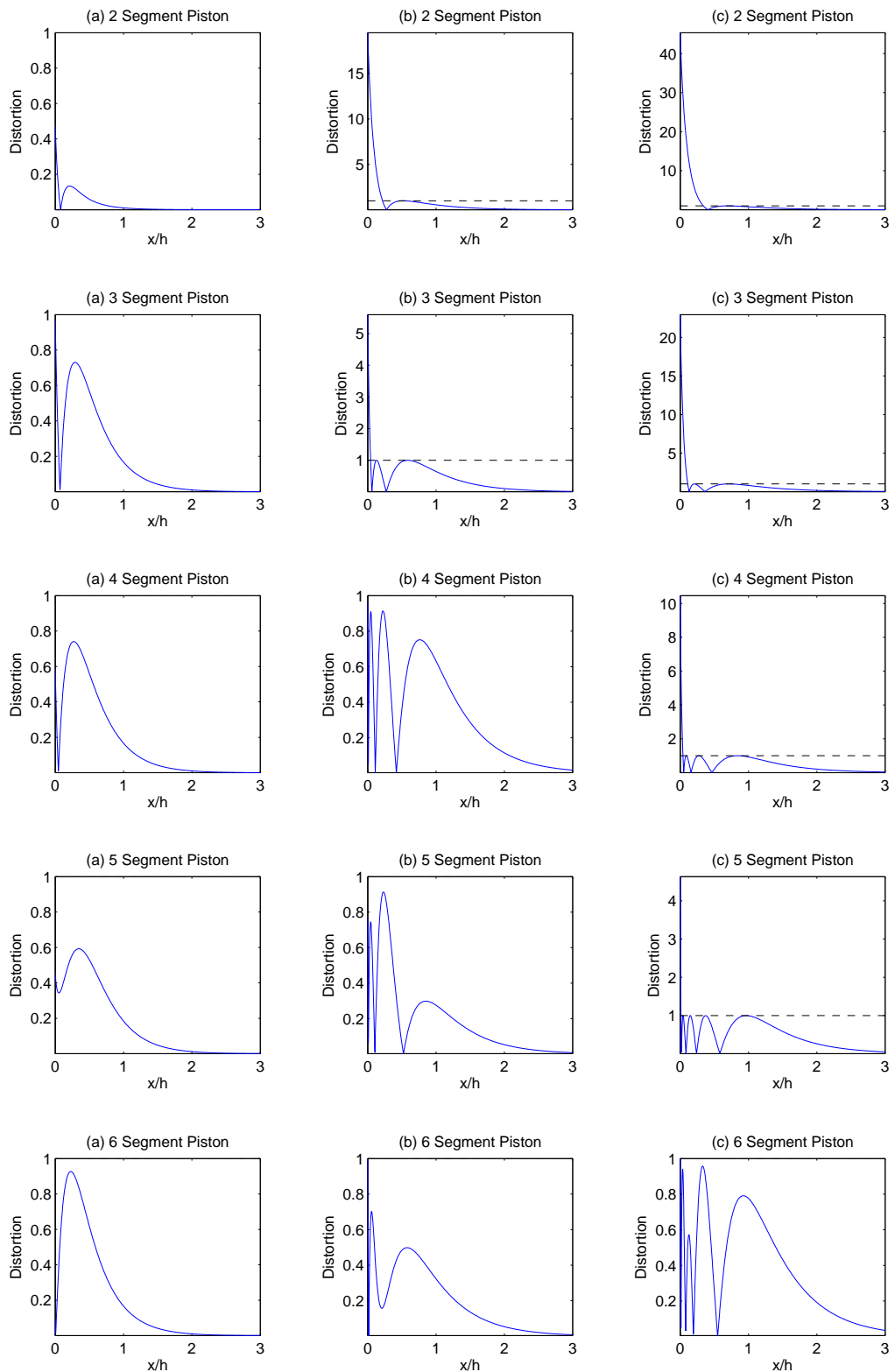


Figure 6.9: Wave field distortion [%] against the distance away from the wave-maker normalised by the tank depth, x/h , created by the depth profiles of completely optimised segmented piston wavemakers for (a) $\omega = 4$ rad/sec, (b) $\omega = 9.9$ rad/sec and (c) $\omega = 14$ rad/sec. The dashed line marks the 1% distortion level.

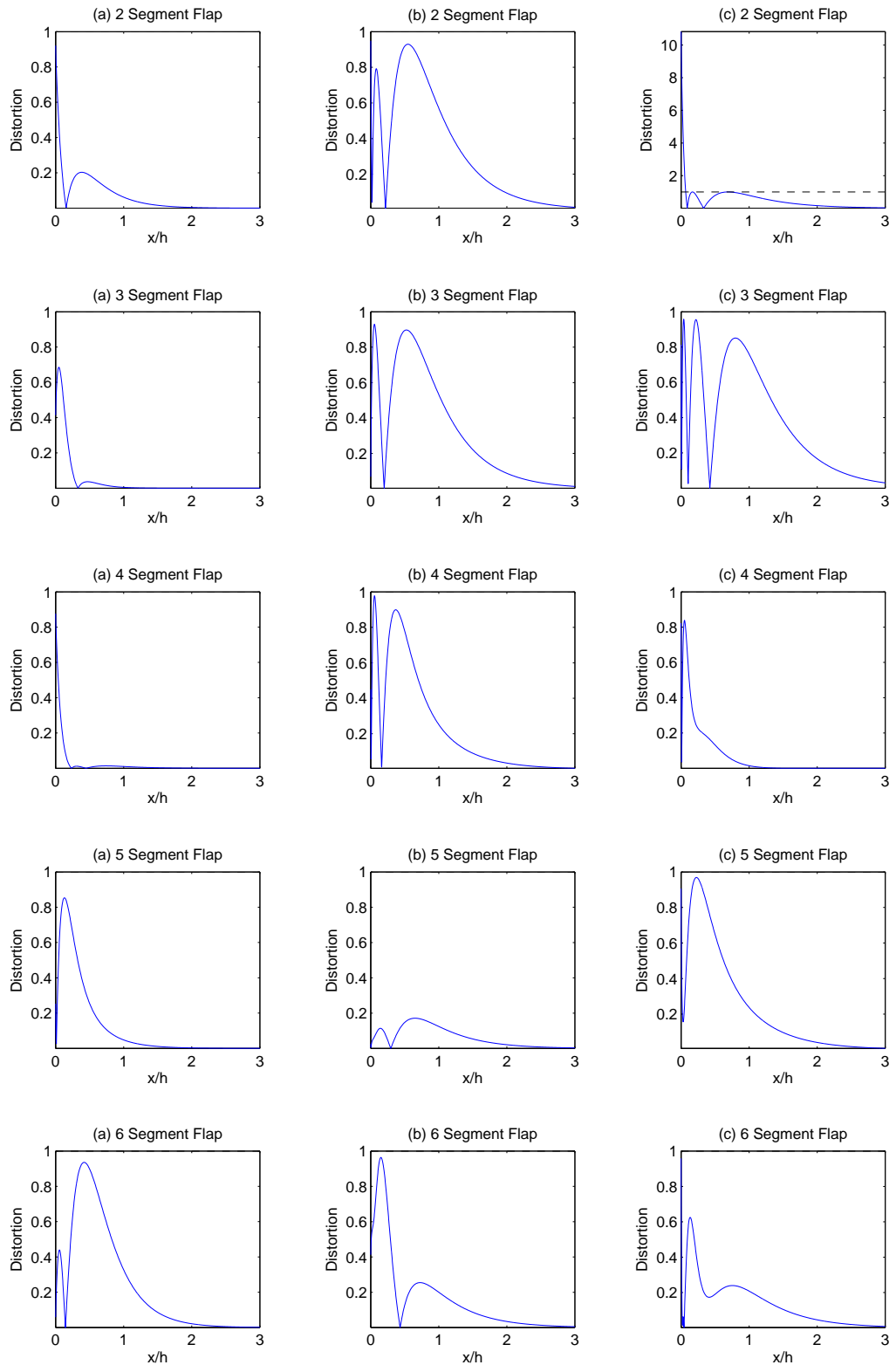


Figure 6.10: Wave field distortion [%] against the distance away from the wave-maker normalised by the tank depth, x/h , created by the depth profiles of completely optimised segmented flap wavemakers for (a) $\omega = 4$ rad/sec, (b) $\omega = 9.9$ rad/sec and (c) $\omega = 14$ rad/sec. The dashed line marks the 1% distortion level.

To illustrate the evanescent wave phase shift, the contributions to the fluid's horizontal velocity component due to each evanescent wave is presented in Figure 6.11 for the six segment piston generating a wave with $kh = 1.2$. Parts (a) through to (j) in Figure 6.11 illustrate the first ten terms of the infinite summation series in Equation (2.56), respectively, where Part (a) represents the progressive wave. In a similar manner to Figures 2.9 and 2.10, in Figure 6.11 the depth is represented by the y -axis of the graphs while the horizontal velocity component is represented by the x -axis. As anticipated, the 1st, 4th, 5th and 9th evanescent waves, Parts (b), (e), (f) and (j) of Figure 6.11, respectively, are π radians out of phase at $z = 0$ with the 2nd, 3rd, 6th, 7th and 8th evanescent waves, Parts (c), (d), (g), (h) and (i) of Figure 6.11, respectively, thus, creating an interference pattern. Another observation is that the amplitude of the evanescent waves vary in a manner which appears random. For instance, the amplitude of the eighth summation term in Part (h) Figure 6.11, is greater than the amplitudes of the second, third, fourth, fifth, sixth and seventh terms. This is a unique result as most sources of literature only consider the case of the single piston wave-maker when analysing the evanescent waves, in which case the amplitude of the evanescent waves decrease with larger imaginary wavenumbers (i.e., the higher its index in the infinite summation series in Equation (2.56)). The importance of this result is that, when evaluating a truncated version of Equation (2.56), care must be taken to not ignore some of the larger amplitude evanescent waves. For this thesis it has been determined, via trial and error, that considering the first fifty terms of the infinite series seems to suffice in providing accurate evaluations of Equation (2.56).

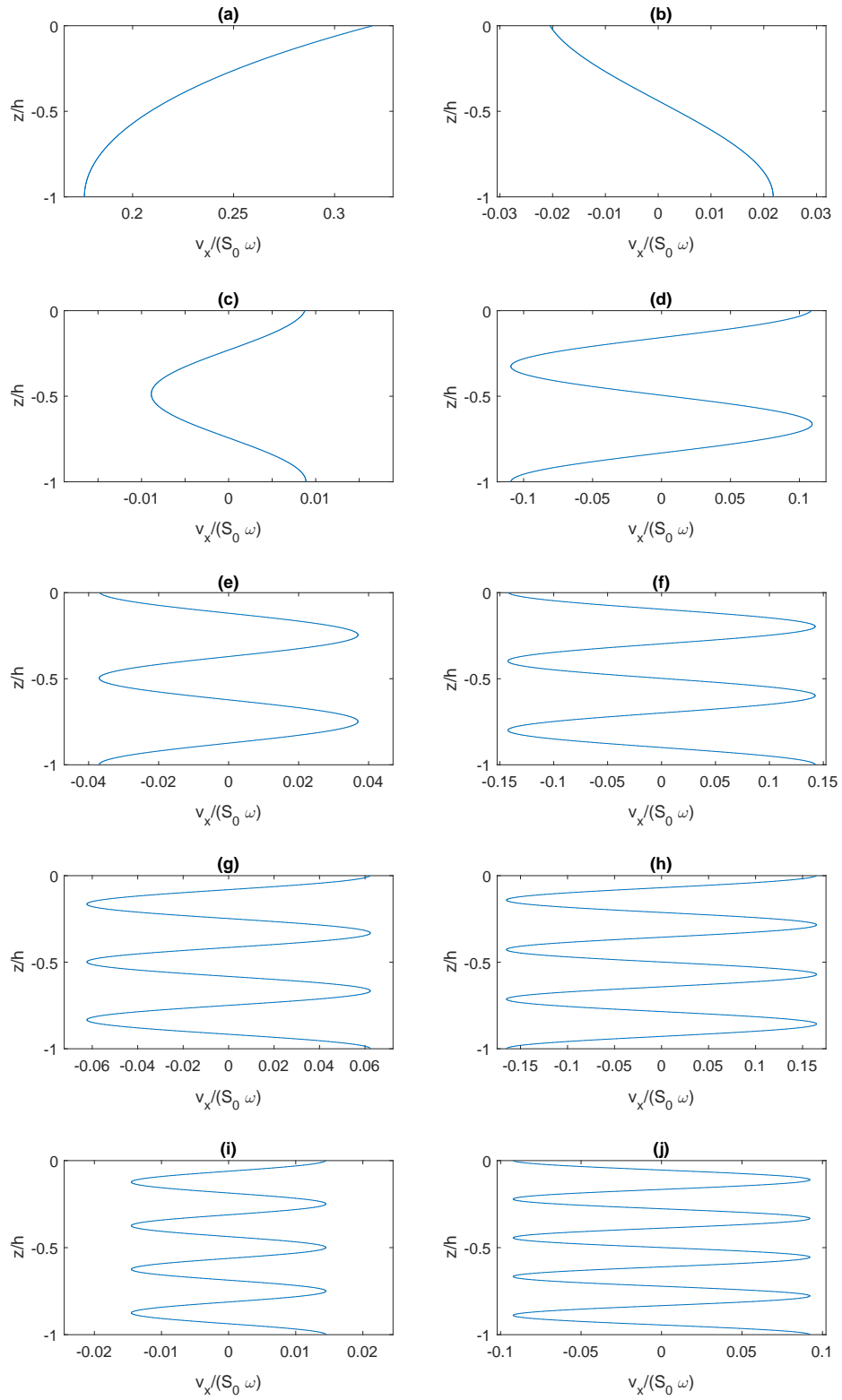


Figure 6.11: The contribution of the first ten terms in the velocity potential's summation series, (a) to (j), to the horizontal velocity component of the fluid on the wavemaker's surface, for a piston wavemaker with six segments at $\omega = 4$ rad/sec.

6.6 Sensitivity Analysis

So far in this thesis it has been assumed that the wavemakers are constructed and operate with perfect accuracy. Yet, it can be certain that when building a physical segmented wavemaker, the actual device will be flawed and errors will creep in. As a result, the performance of the wavemaker will differ and the distortion levels will increase from the minimum. For example, the lengths of the segments may not be manufactured accurately or the actuators driving the segments may not be precise. It has already been determined in Section 6.3 that small variations in the segment lengths will have little consequence on the distortion level compared to the segment stroke. Instead, the attention of this sensitivity analysis is directed to errors in the segment strokes of the completely optimised segmented wavemakers. Aside from the distortion level, another concern is the fidelity of the progressive wave's wave height, H . From the relationship between the velocity potential and the wavemaker's motion amplitude, Equation (2.4), it is easy to see how changes in the segment strokes may impact the height of the progressive wave. It may be reasonable to think that if more actuators are used, the wavemaker will have a greater sensitivity to errors in the segments' strokes. However, as shown by the analysis of the segmented wavemaker's constrained radiation damping, Figures 4.18 and 4.19, the deeper the segment is, the less influence it has on the progressive wave. Presented in this section is a sensitivity analysis which assesses the degree to which the wave field will be affected by relative errors in the strokes of each segment in the wavemaker.

Relative errors between the segment strokes of 1×10^{-3} m, 5×10^{-4} m and 5×10^{-5} m were used in carrying out this sensitivity analysis, meaning that the position of the actuator may have a error of $\pm 0.5 \times 10^{-3}$ m, $\pm 2.5 \times 10^{-4}$ m and $\pm 2.5 \times 10^{-5}$ m. During the sensitivity analysis, constraints of the McCowan breaking wave height limit, $0.78h$ [16], and the wave steepness limit, $H/\lambda = 0.142$ (or $Hk = 0.8922$) [31], were imposed on the wave heights. The sensitivity analysis was performed over a range of kh and normalised wave height, H/h , values in a wave tank of depth, $h = 0.6$ m. The sensitivity analysis was carried out by evaluating all possible combinations of relative errors between the segment strokes for each value of H/h and kh . The combination of relative error in the segments' strokes that result in the greatest errors in the wave field are then presented below.

6.6.1 Sensitivity of the distortion level

The maximum positions of 1% distortion occurring due to relative errors of 1×10^{-3} m, 5×10^{-4} m and 5×10^{-5} m between the segment strokes, has been evaluated for both piston and flap wavemakers with two to six segments. The results are presented as contour plots where the contour levels indicates the normalised position of 1% distortion, $X_{1\%}/h$, with kh represented on the x -axis and the normalised wave height, H/h , represented on the y -axis. Figures 6.12 and 6.16 show the position of 1% distortion for segmented piston wavemakers with two to six segments, respectively, allowing for a relative error between the segments' strokes, while Figures 6.17 and 6.21 show the same for the segmented flap wavemakers. The position of 1% distortion allowing for a relative error of 1×10^{-3} m is presented in Part (a) of Figures 6.12 to 6.21, while Parts (b) and (c) show the position of 1% distortion allowing for relative errors of 5×10^{-4} m and 5×10^{-5} m, respectively. For the segmented piston wavemakers, Figures 6.12 to 6.16, it seems that, in general, the position of 1% distortion, accounting for relative errors, increases with kh and decreases with increasing numbers of segments in the wavemaker. For the segmented flap wavemakers, Figures 6.17 to 6.21, the position of 1% distortion, accounting for relative errors, does decrease as more segments are added to the wavemaker, however, it does not follow the pattern of increasing with kh . All the segmented flap wavemakers perform better than the corresponding segmented piston wavemakers at reducing the position of 1% distortion, even when a relative error between the segment strokes is considered. Part (c) of Figure 6.18 has been omitted, when allowing for a relative error of 5×10^{-5} m, as the distortion caused by a three segment flap is less than 1% for the entire ranges of kh and H/h considered.

The results for the three segment flap wavemaker are very encouraging, as even with the presence of relative errors of 1×10^{-3} m and 5×10^{-4} m, the position of 1% distortion remains close to zero for almost all of the kh and H/h ranges and reaches a maximum value of approximately $0.4h$. For the segmented piston wavemaker, the results presented in Figures 6.12 to 6.16 indicate that wavemakers with more segments still perform better overall at reducing the position of 1% distortion. It should be noted that the two segment piston wavemaker still performs quite well with a maximum position of 1% distortion of approximately $0.5h$ with a relative error of 1×10^{-3} m. It seems from this analysis that the best choice in wavemaker configuration is the three segment flap wavemaker, as it reduces the level of distortion to below 1% for much of the H/h and kh range and at most, the position of 1% distortion increases to $0.4h$ from the wavemaker, while allowing for errors of up to 1×10^{-3} m in the segments' strokes. The three

segment flap wavemaker also remains relatively simple to implement.

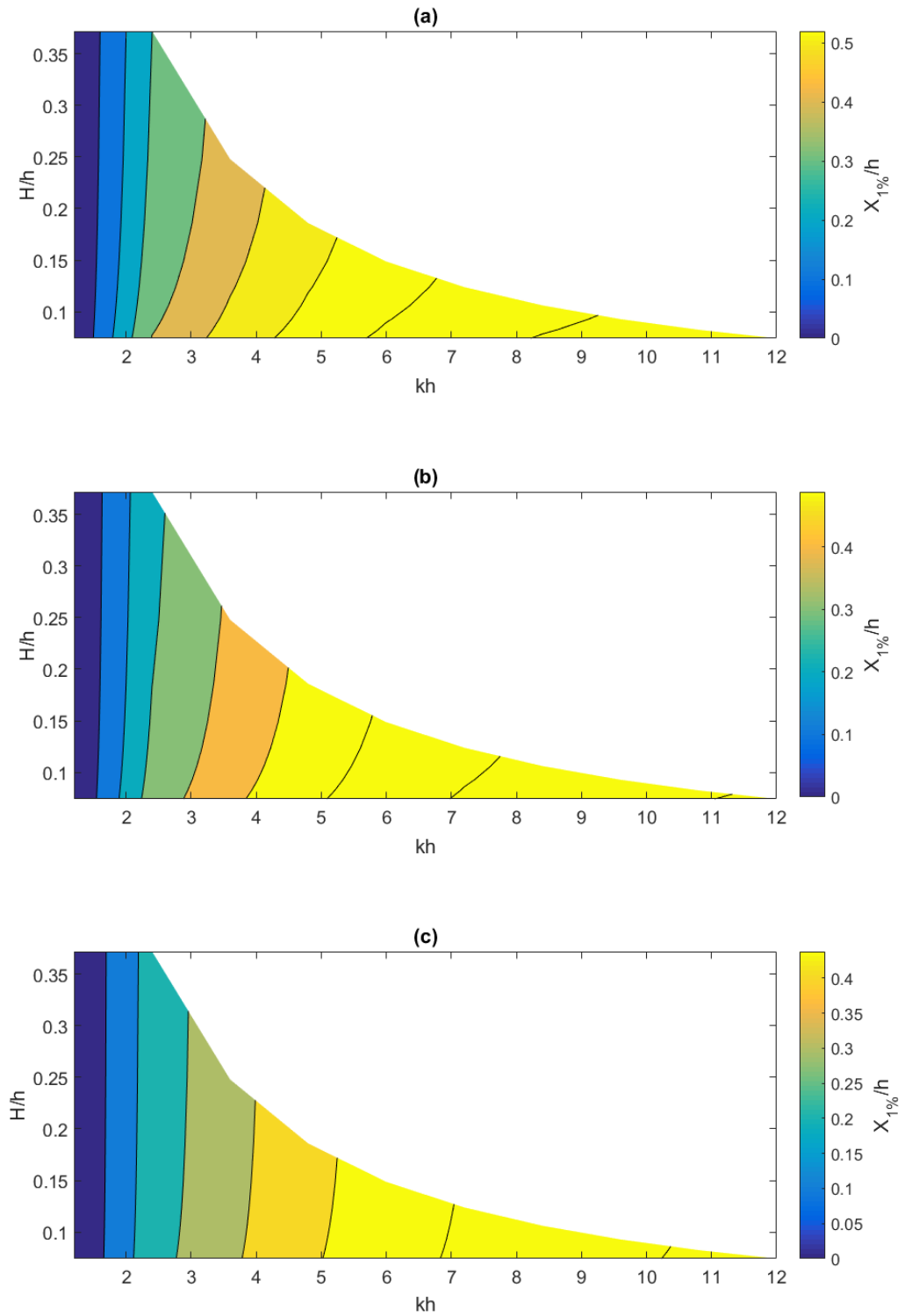


Figure 6.12: Contour plot of the position of 1% distortion against kh and H/h for a two segment piston wavemaker with relative errors between the segment strokes of (a) 1×10^{-3} m, (b) 5×10^{-4} m and (c) 5×10^{-5} m.

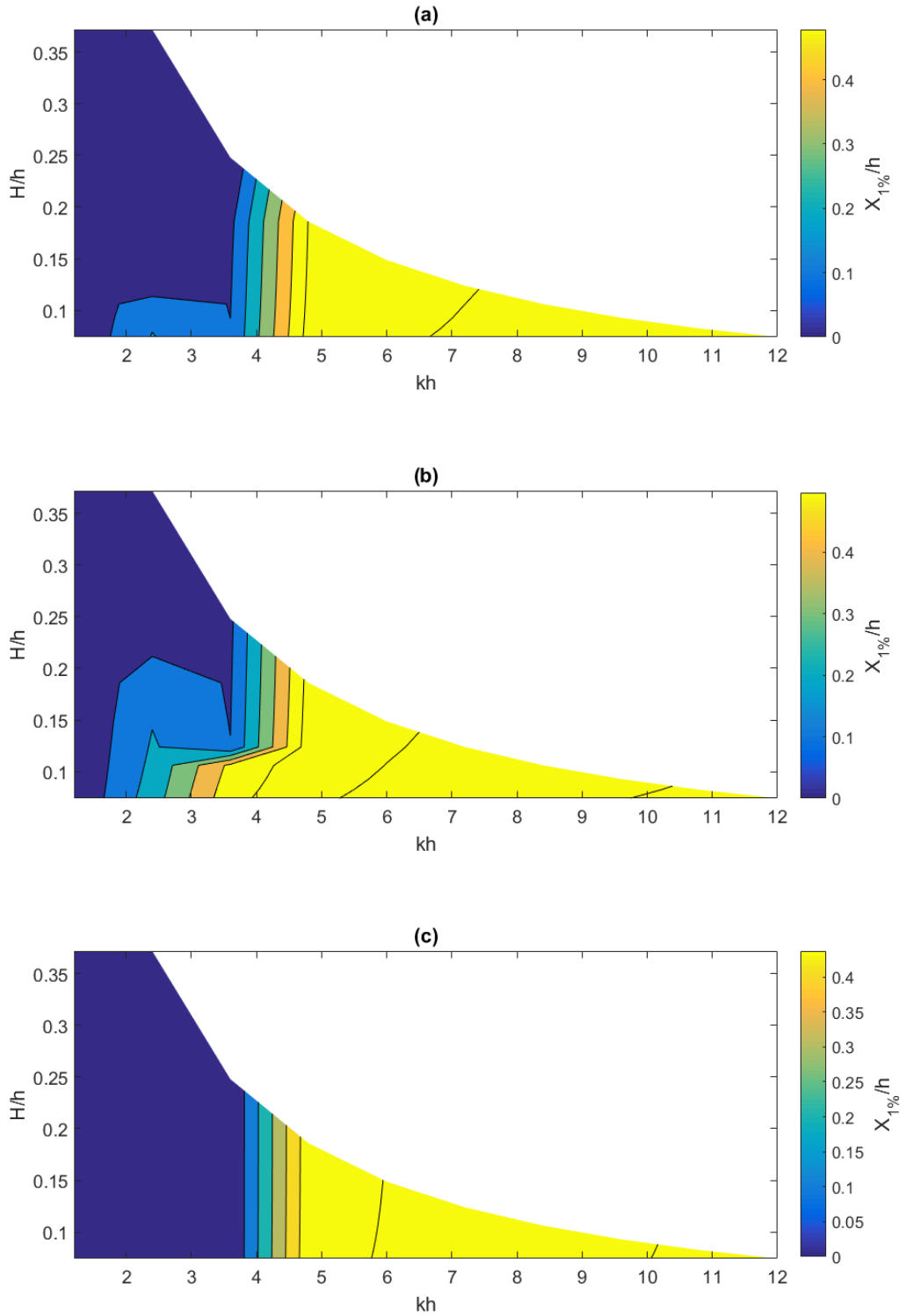


Figure 6.13: Contour plot of the position of 1% distortion against kh and H/h for a three segment piston wavemaker with relative errors between the segment strokes of (a) 1×10^{-3} m, (b) 5×10^{-4} m and (c) 5×10^{-5} m.

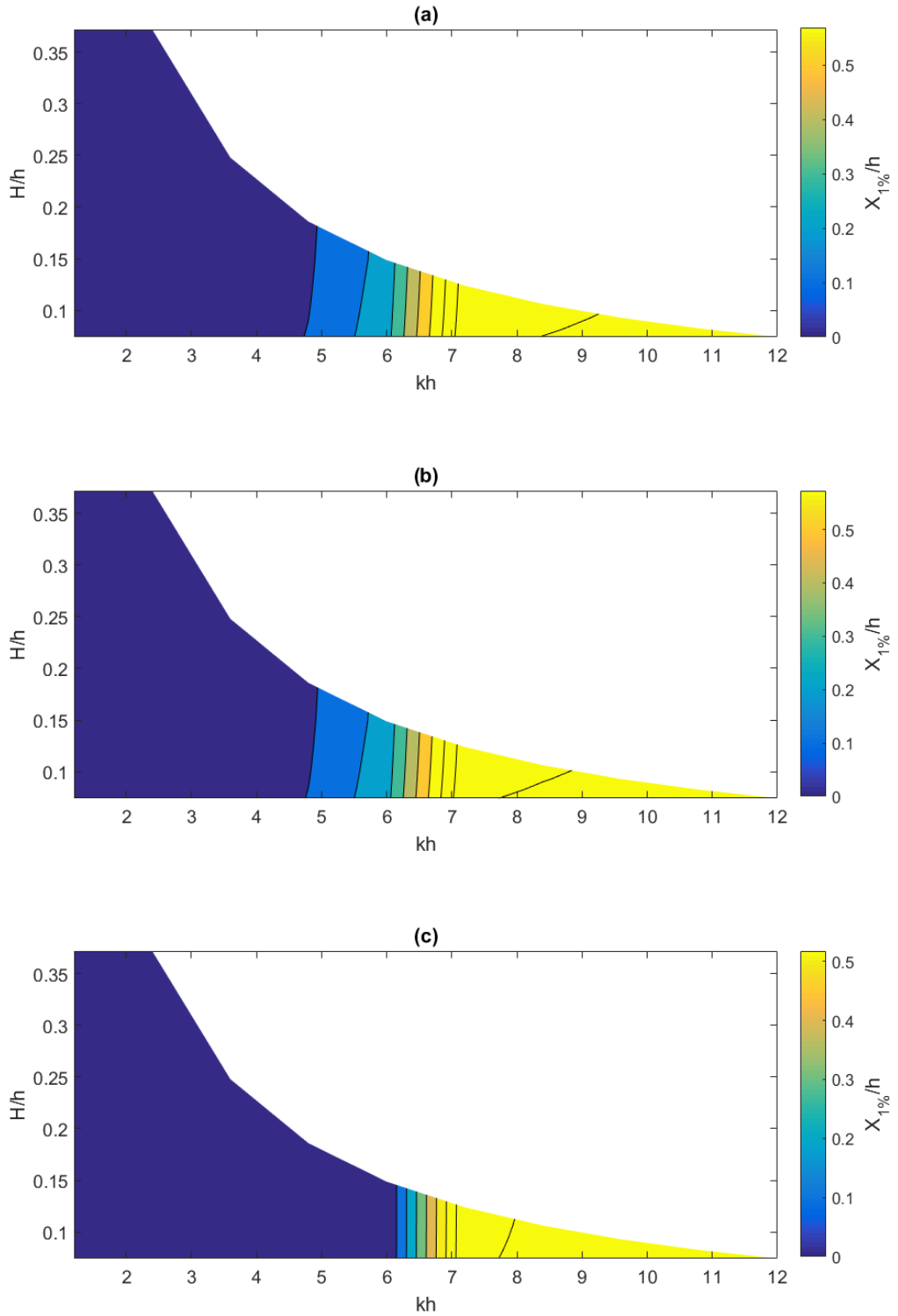


Figure 6.14: Contour plot of the position of 1% distortion against kh and H/h for a four segment piston wavemaker with relative errors between the segment strokes of (a) 1×10^{-3} m, (b) 5×10^{-4} m and (c) 5×10^{-5} m.

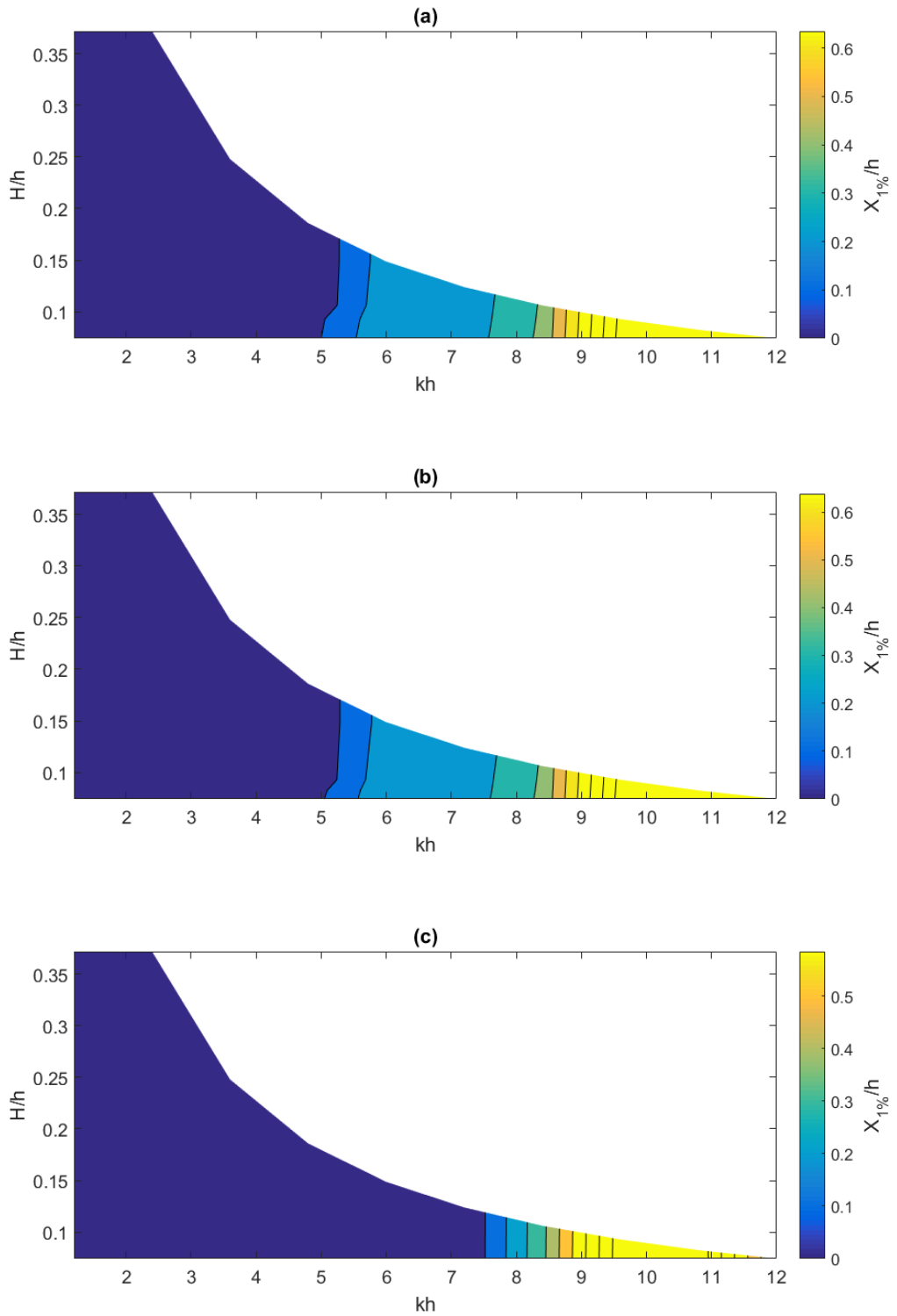


Figure 6.15: Contour plot of the position of 1% distortion against kh and H/h for a five segment piston wavemaker with relative errors between the segment strokes of (a) 1×10^{-3} m, (b) 5×10^{-4} m and (c) 5×10^{-5} m.

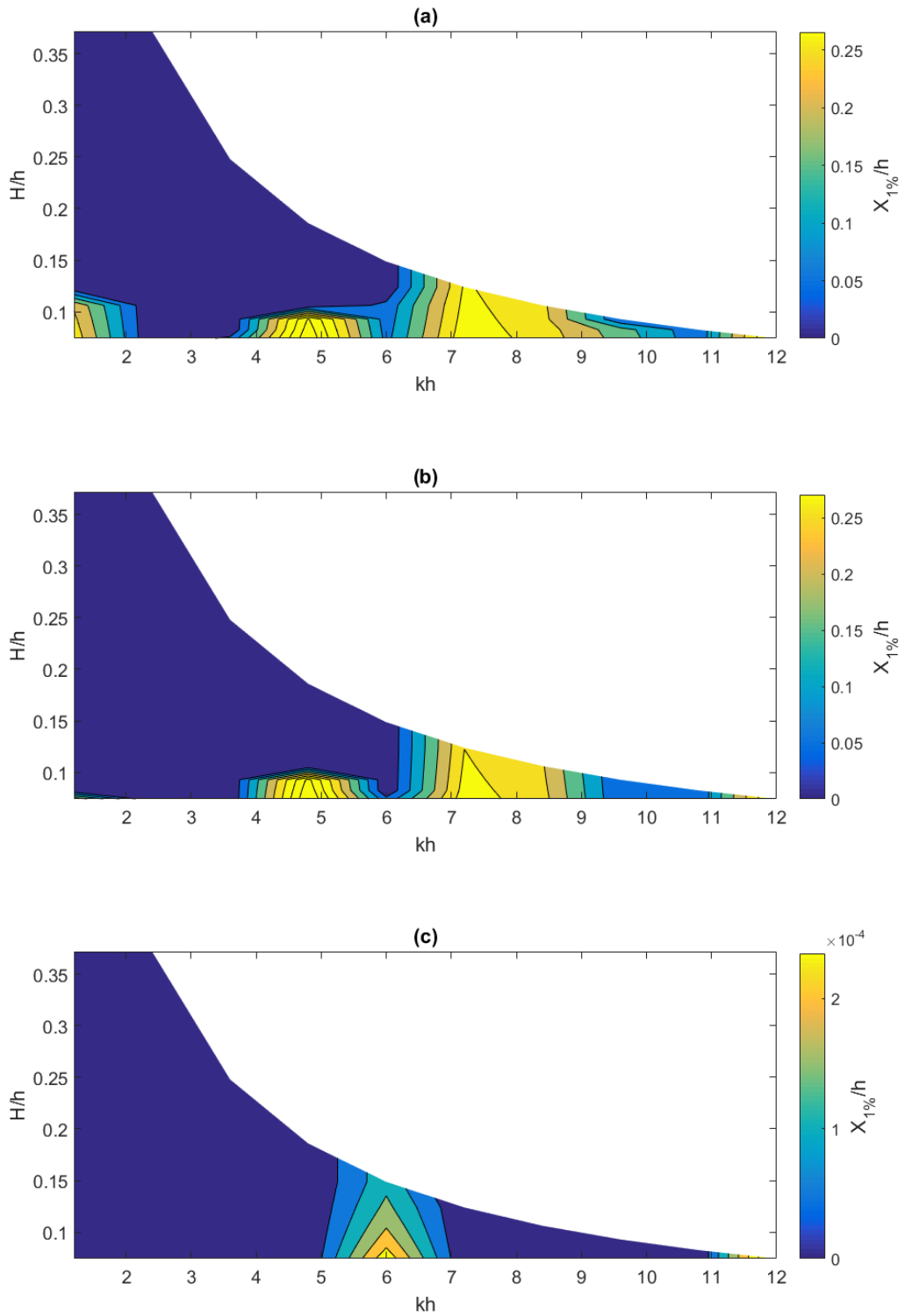


Figure 6.16: Contour plot of the position of 1% distortion against kh and H/h for a six segment piston wavemaker with relative errors between the segment strokes of (a) 1×10^{-3} m, (b) 5×10^{-4} m and (c) 5×10^{-5} m.

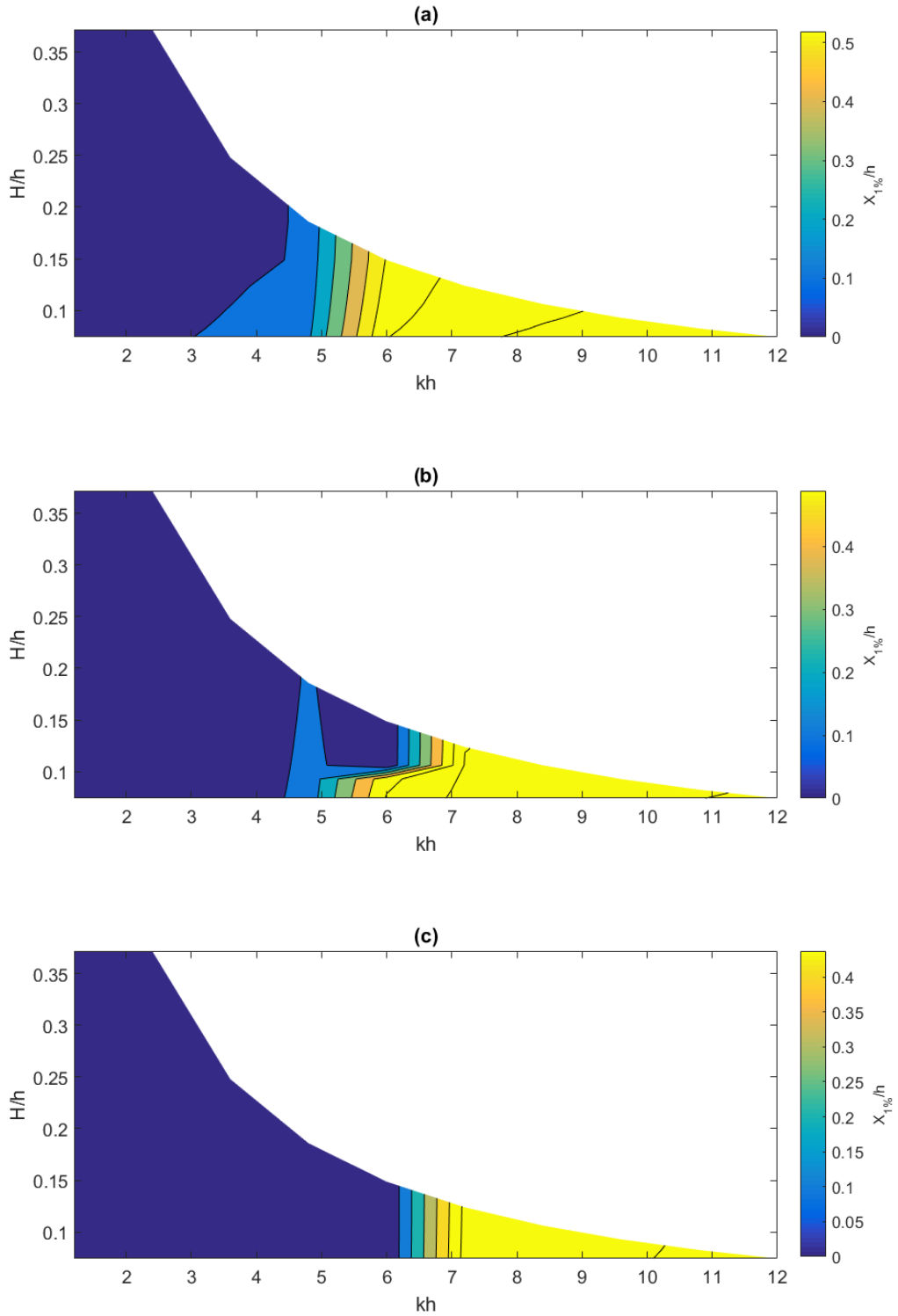


Figure 6.17: Contour plot of the position of 1% distortion against kh and H/h for a two segment flap wavemaker with relative errors between the segment strokes of (a) 1×10^{-3} m, (b) 5×10^{-4} m and (c) 5×10^{-5} m.

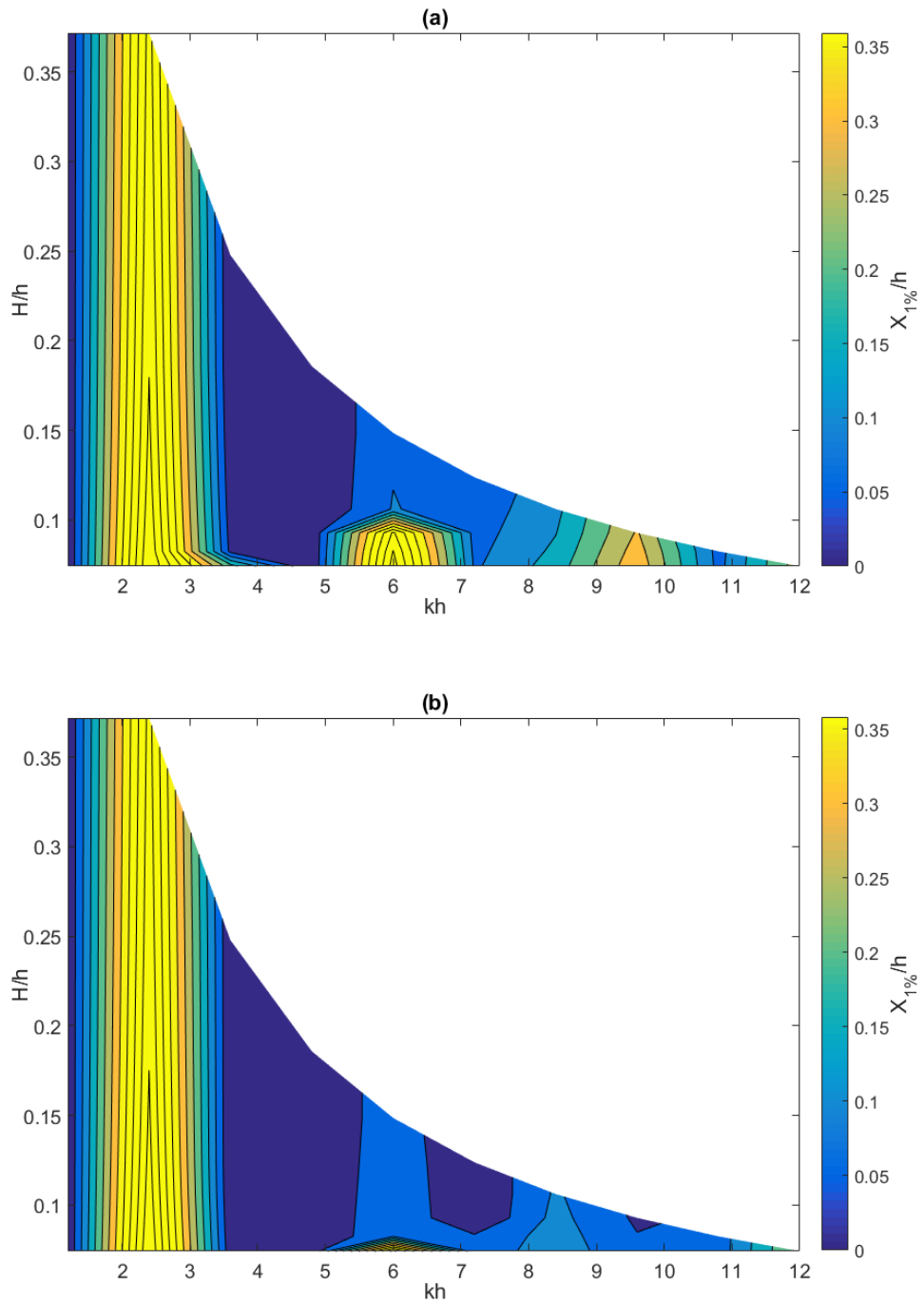


Figure 6.18: Contour plot of the position of 1% distortion against kh and H/h for a three segment flap wavemaker with relative errors between the segment strokes of (a) 1×10^{-3} m, (b) 5×10^{-4} m and (c) 5×10^{-5} m.

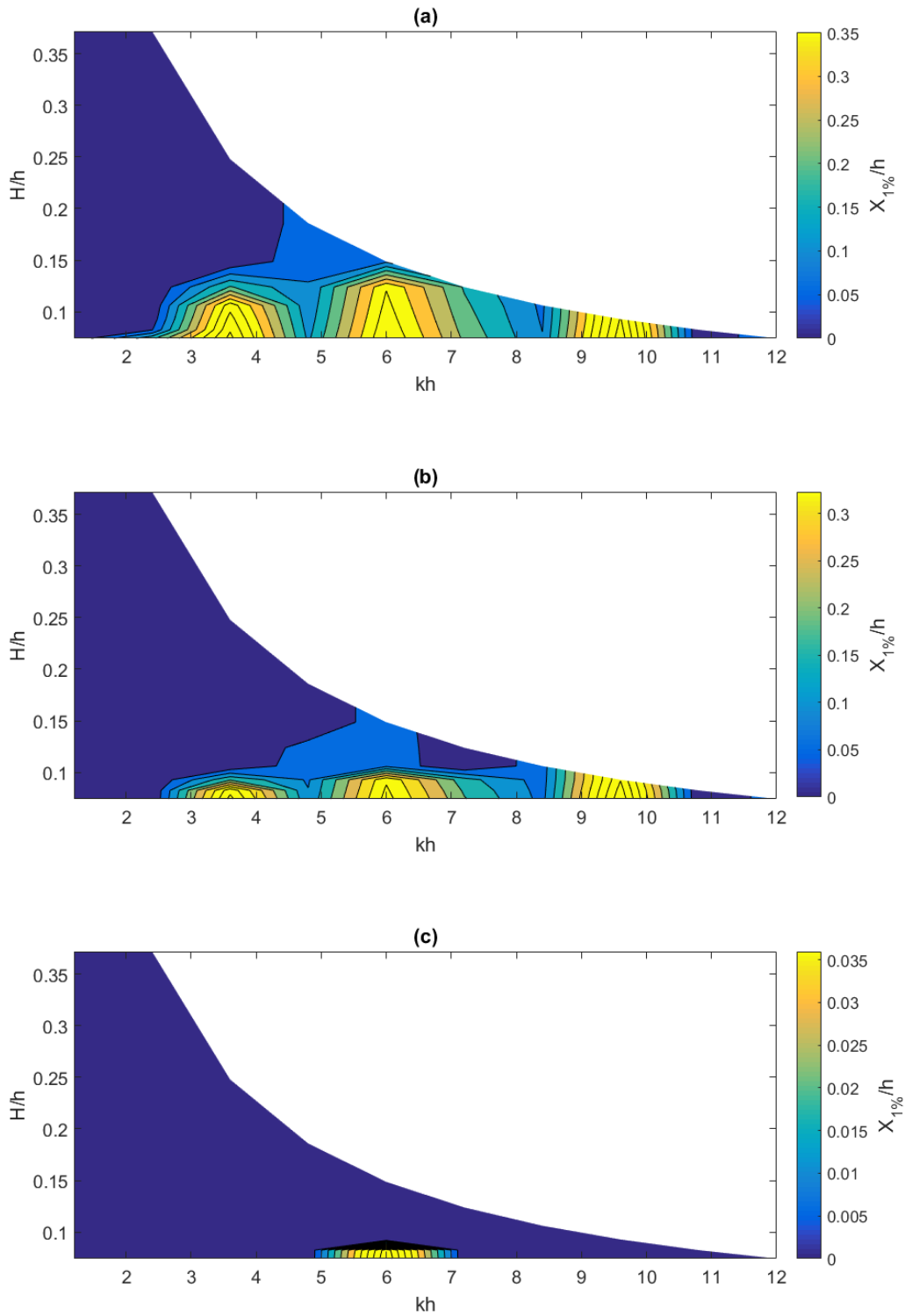


Figure 6.19: Contour plot of the position of 1% distortion against kh and H/h for a four segment flap wavemaker with relative errors between the segment strokes of (a) 1×10^{-3} m, (b) 5×10^{-4} m and (c) 5×10^{-5} m.

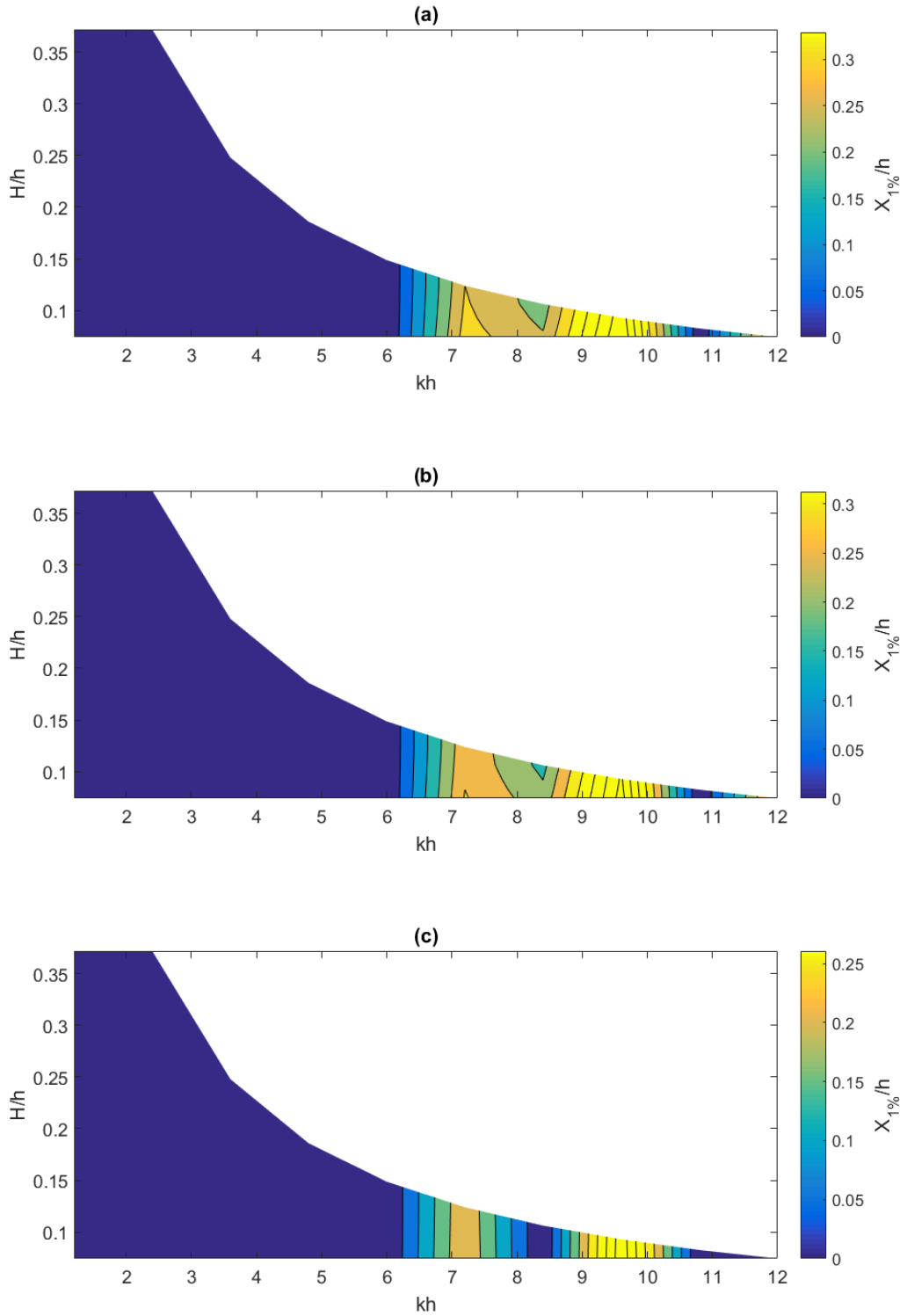


Figure 6.20: Contour plot of the position of 1% distortion against kh and H/h for a five segment flap wavemaker with relative errors between the segment strokes of (a) 1×10^{-3} m, (b) 5×10^{-4} m and (c) 5×10^{-5} m.

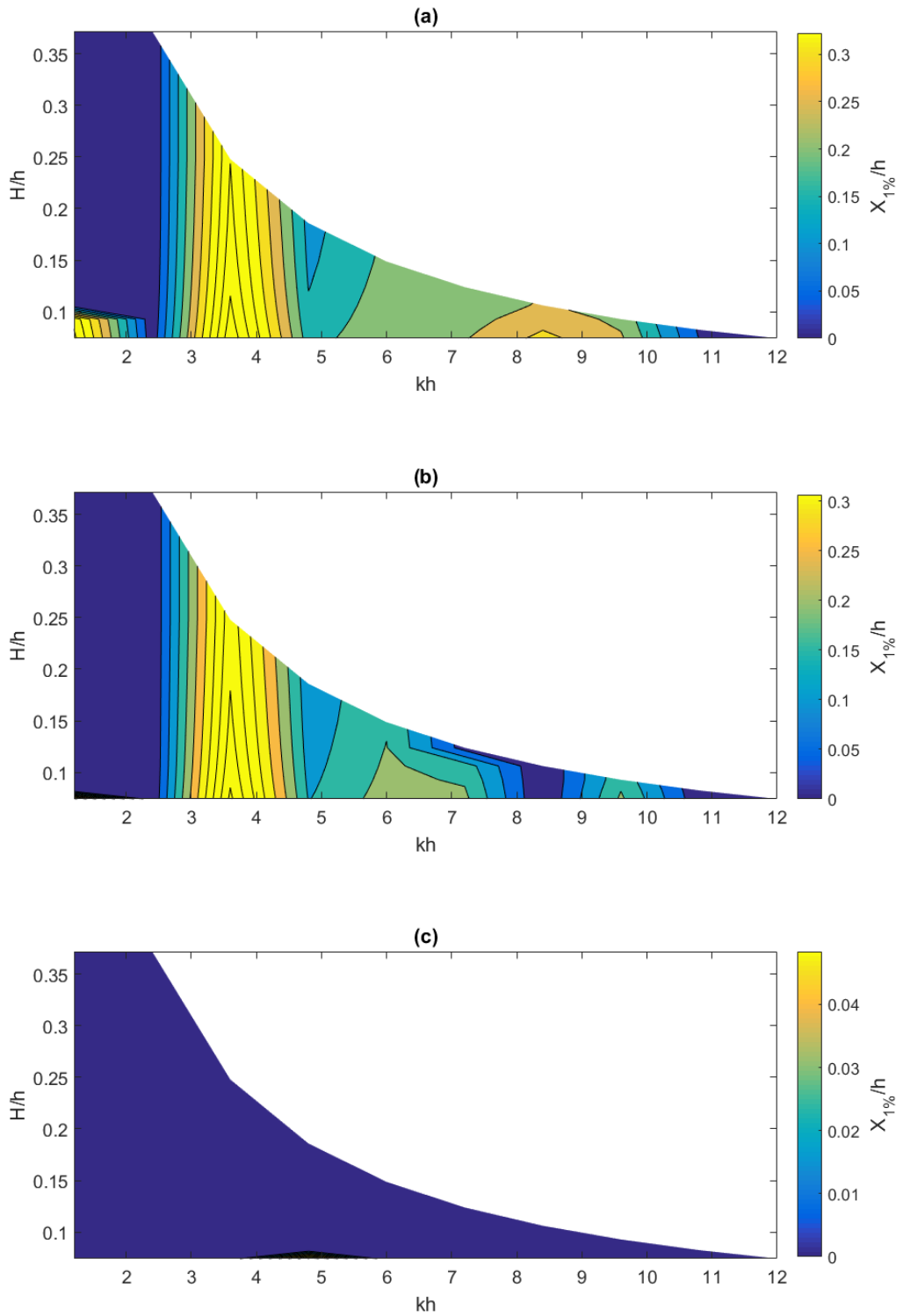


Figure 6.21: Contour plot of the position of 1% distortion against kh and H/h for a six segment flap wavemaker with relative errors between the segment strokes of (a) 1×10^{-3} m, (b) 5×10^{-4} m and (c) 5×10^{-5} m.

6.6.2 Sensitivity analysis: progressive wave height

During wave tank testing, the repeatability and fidelity of waves produced by the wavemaker is critical for developing an understanding as to how a device responds to various wave conditions. Hence, the sensitivity of the progressive wave height to errors in the segments' strokes is of great interest. The results of the progressive wave heights' sensitivity to relative errors of 1×10^{-3} m, 5×10^{-4} m and 5×10^{-5} m in the segments' strokes are presented for segmented piston wavemakers with two to six segments in Figures 6.22 to 6.26 and similarly in Figure 6.27 and 6.31 for segmented flap wavemakers with two to six segments, respectively.

For the contour plots in Figures 6.22 and 6.31, the x -axis represents kh and the y -axis represents the intended normalised wave height, H/h . The contour levels in Figures 6.22 to 6.31 represent the percentage error between the generated wave heights, accounting for a relative error between the segmented wavemakers and the intended wave height. Parts (a), (b) and (c) present the percentage error in the wave height given a relative error between the segment strokes of 1×10^{-3} m, 5×10^{-4} m and 5×10^{-5} m, respectively.

Figures 6.32 and 6.33 show the average percentage error occurring with two to six segments in piston and flap wavemakers, respectively. The error bars in both Figures 6.32 and 6.33 indicate the maximum and minimum percentage error that arises, over the range of kh and normalised wave heights in Figures 6.22 to 6.31, when errors exist in the segment strokes. Parts (a), (b) and (c) present the percentage error of the wave height with relative errors of 1×10^{-3} m, 5×10^{-4} m and 5×10^{-5} m, respectively, in the segment strokes. Figures 6.32 and 6.33 indicate that the fidelity of the progressive wave height is acceptable when relative errors of 1×10^{-3} m, 5×10^{-4} m and 5×10^{-5} m are present in the segment strokes for all the wavemakers. The maximum percentage error of 2.2% occurs for the flap wavemaker with four segments, Figure 6.33 Part (a). It is interesting to note that the fidelity of the progressive wave heights is slightly poorer for the segmented flap wavemakers than the segmented piston wavemakers. Figures 6.32 and 6.33 alleviate the concern that more segments in the wavemaker would result in too much unreliability in the progressive wave heights, Section 6.1.

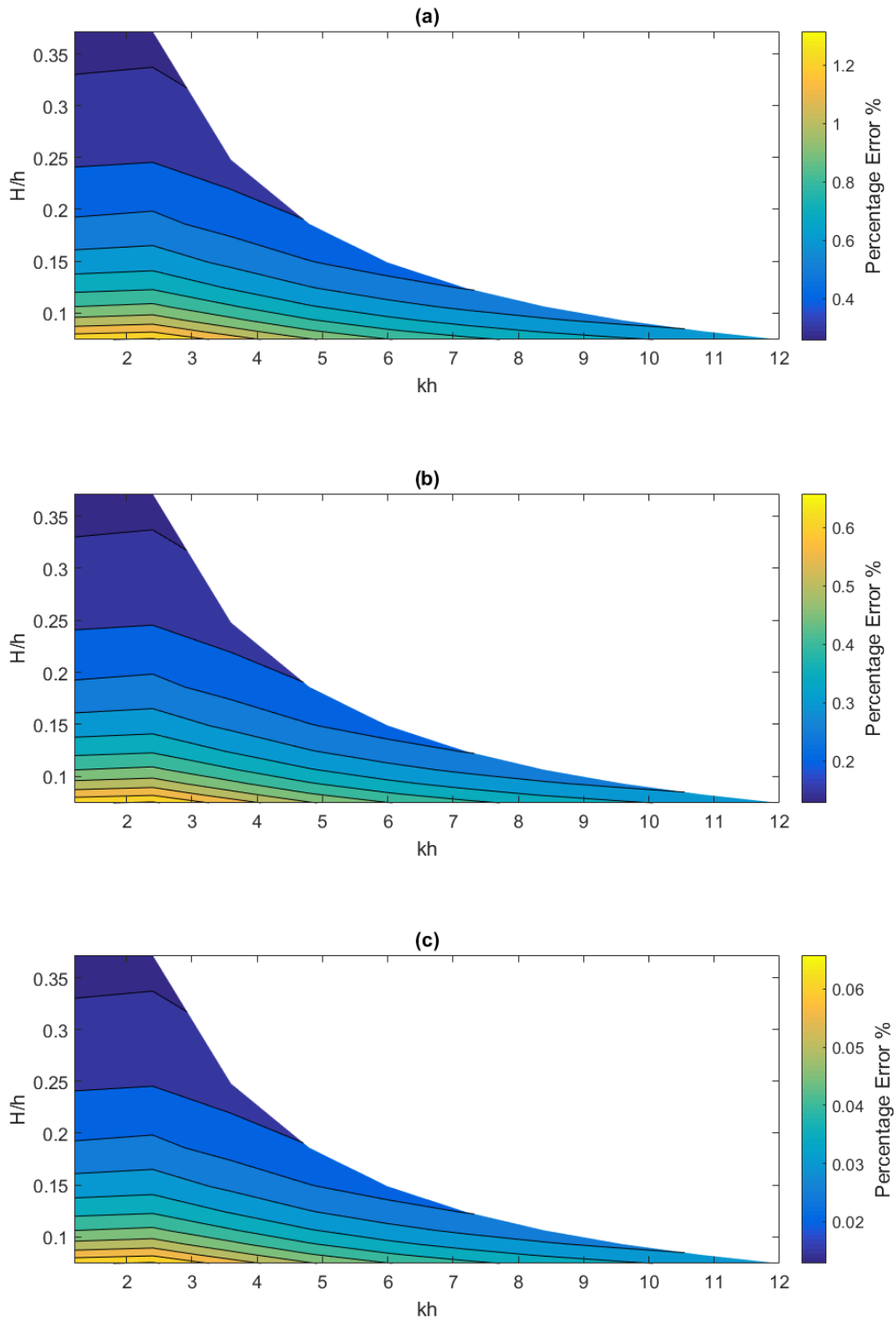


Figure 6.22: Contour plot of the percentage error between the generated wave height to the intended wave height, H , against kh and H/h for a two segment piston wavemaker with relative errors between the segment strokes of (a) 1×10^{-3} m, (b) 5×10^{-4} m and (c) 5×10^{-5} m.

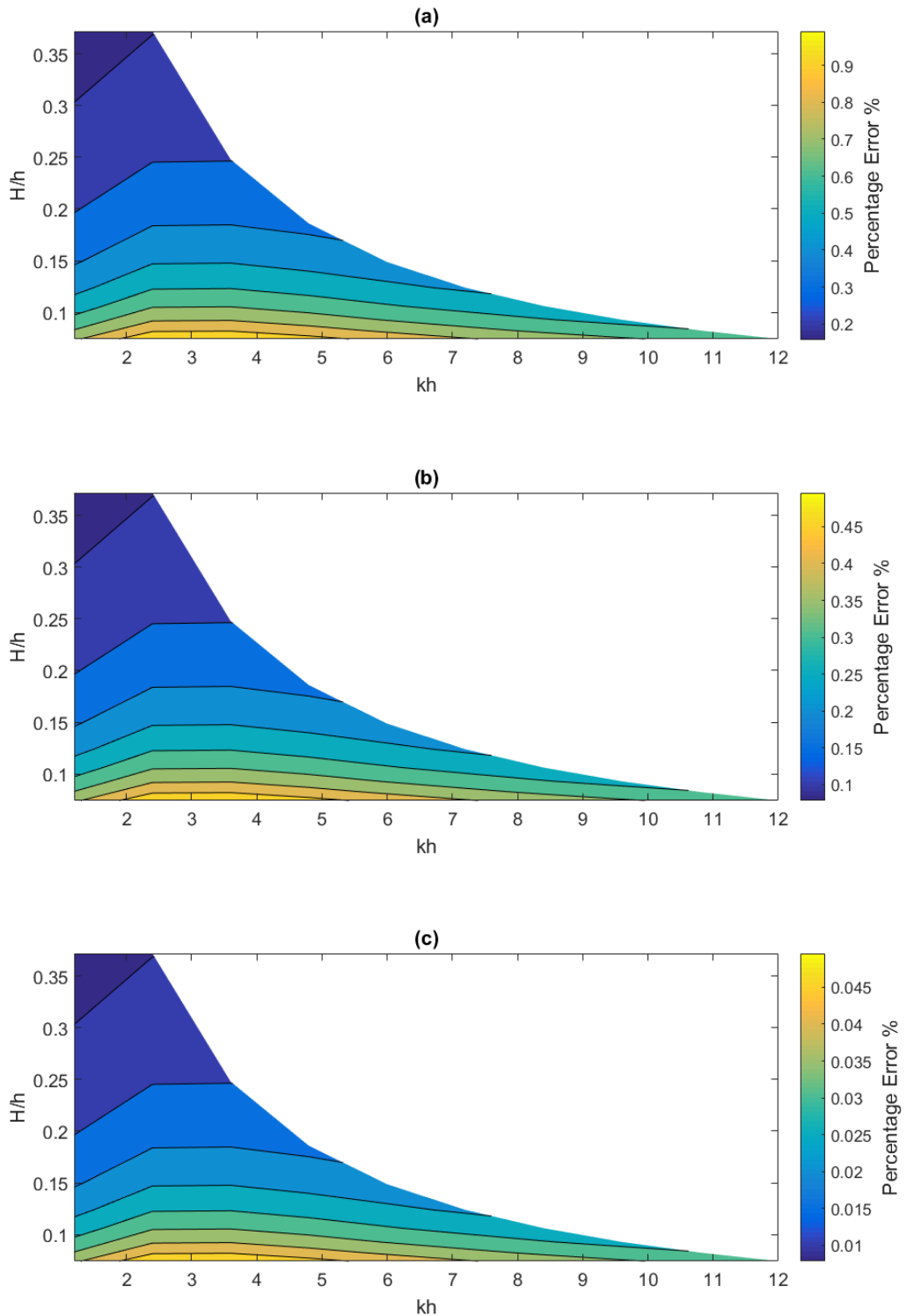


Figure 6.23: Contour plot of the percentage error between the generated wave height to the intended wave height, H , against kh and H/h for a three segment piston wavemaker with relative errors between the segment strokes of (a) 1×10^{-3} m, (b) 5×10^{-4} m and (c) 5×10^{-5} m.

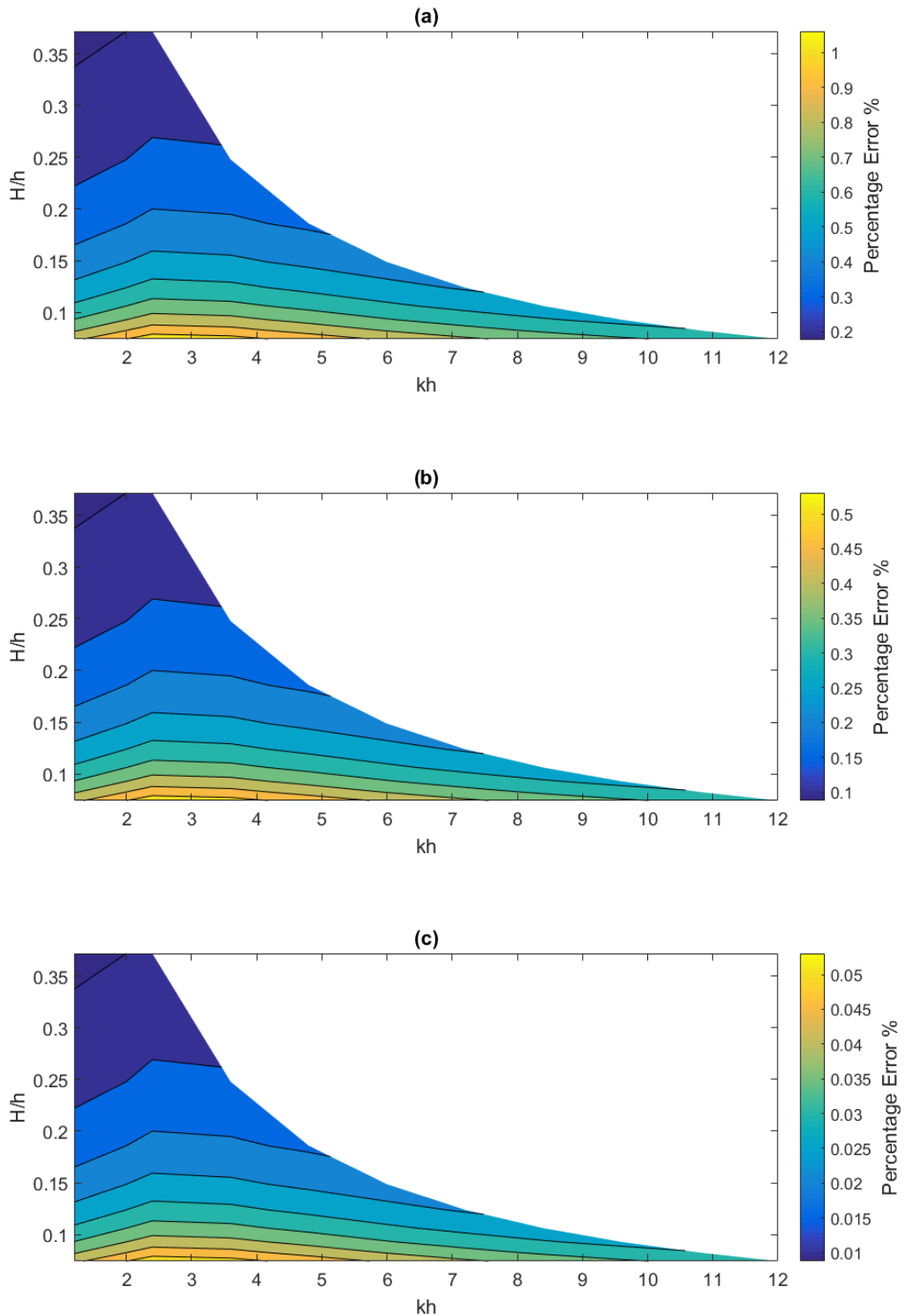


Figure 6.24: Contour plot of the percentage error between the generated wave height to the intended wave height, H , against kh and H/h for a four segment piston wavemaker with relative errors between the segment strokes of (a) 1×10^{-3} m, (b) 5×10^{-4} m and (c) 5×10^{-5} m.

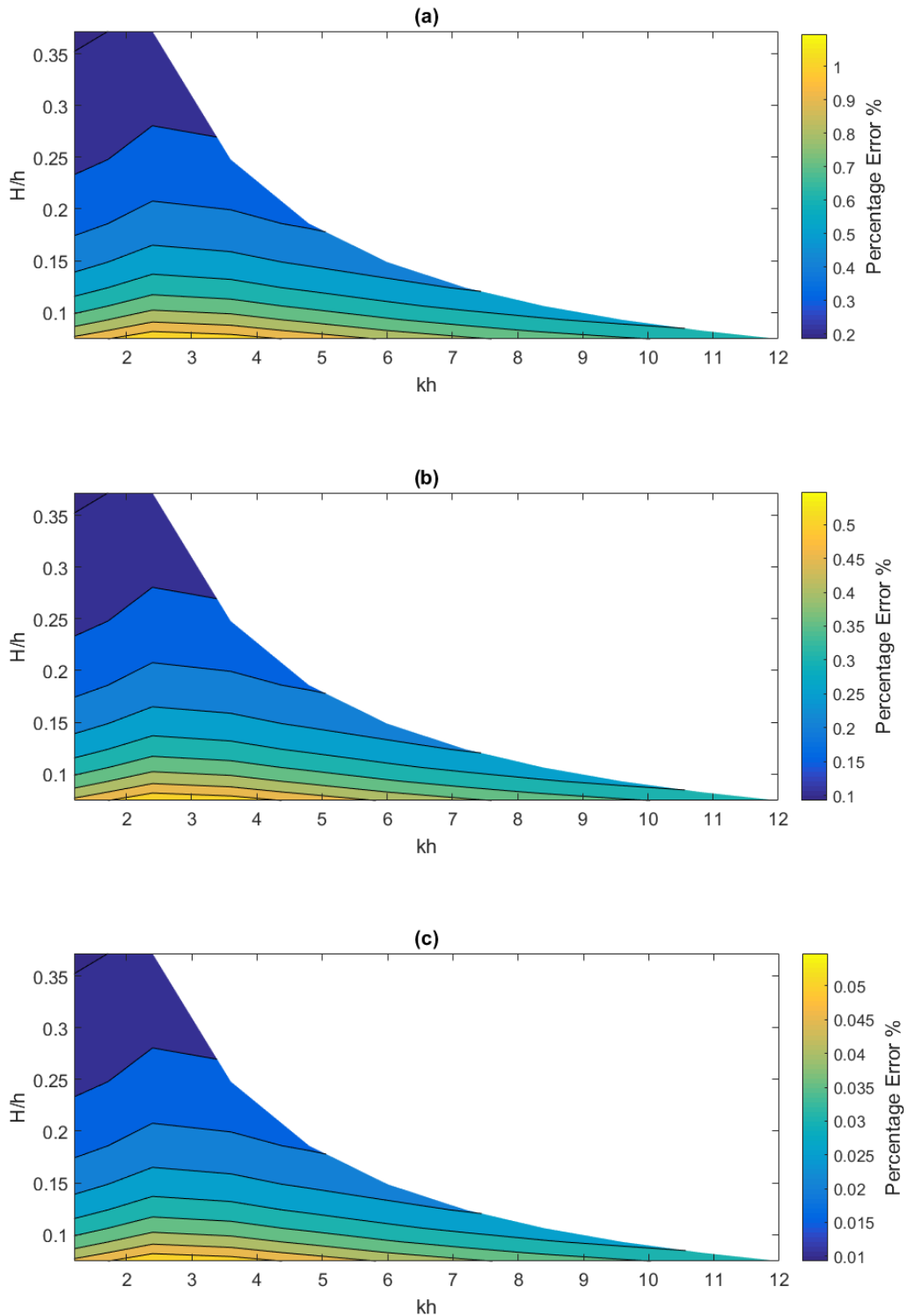


Figure 6.25: Contour plot of the percentage error between the generated wave height to the intended wave height, H , against kh and H/h for a five segment piston wavemaker with relative errors between the segment strokes of (a) 1×10^{-3} m, (b) 5×10^{-4} m and (c) 5×10^{-5} m.

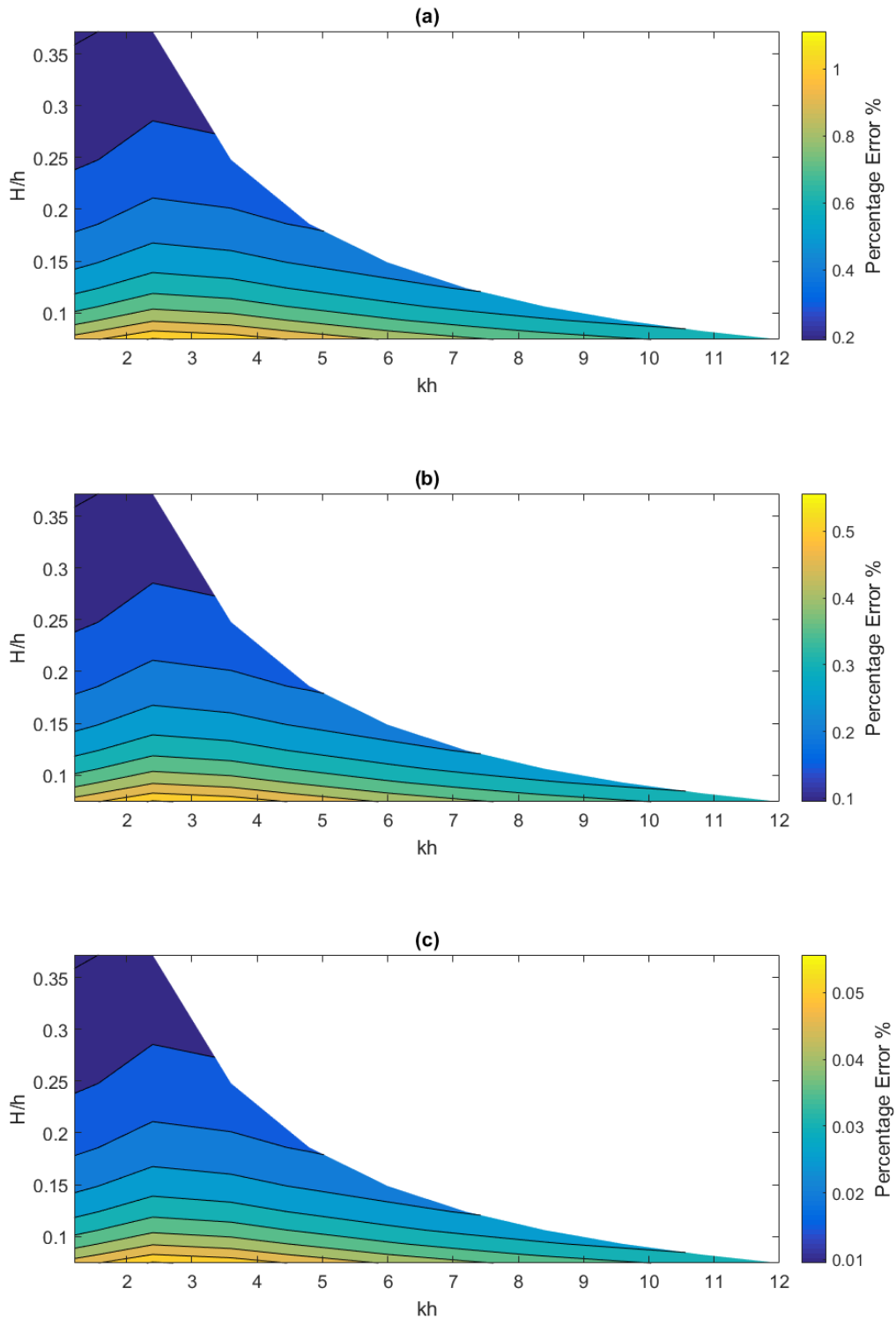


Figure 6.26: Contour plot of the percentage error between the generated wave height to the intended wave height, H , against kh and H/h for a six segment piston wavemaker with relative errors between the segment strokes of (a) 1×10^{-3} m, (b) 5×10^{-4} m and (c) 5×10^{-5} m.

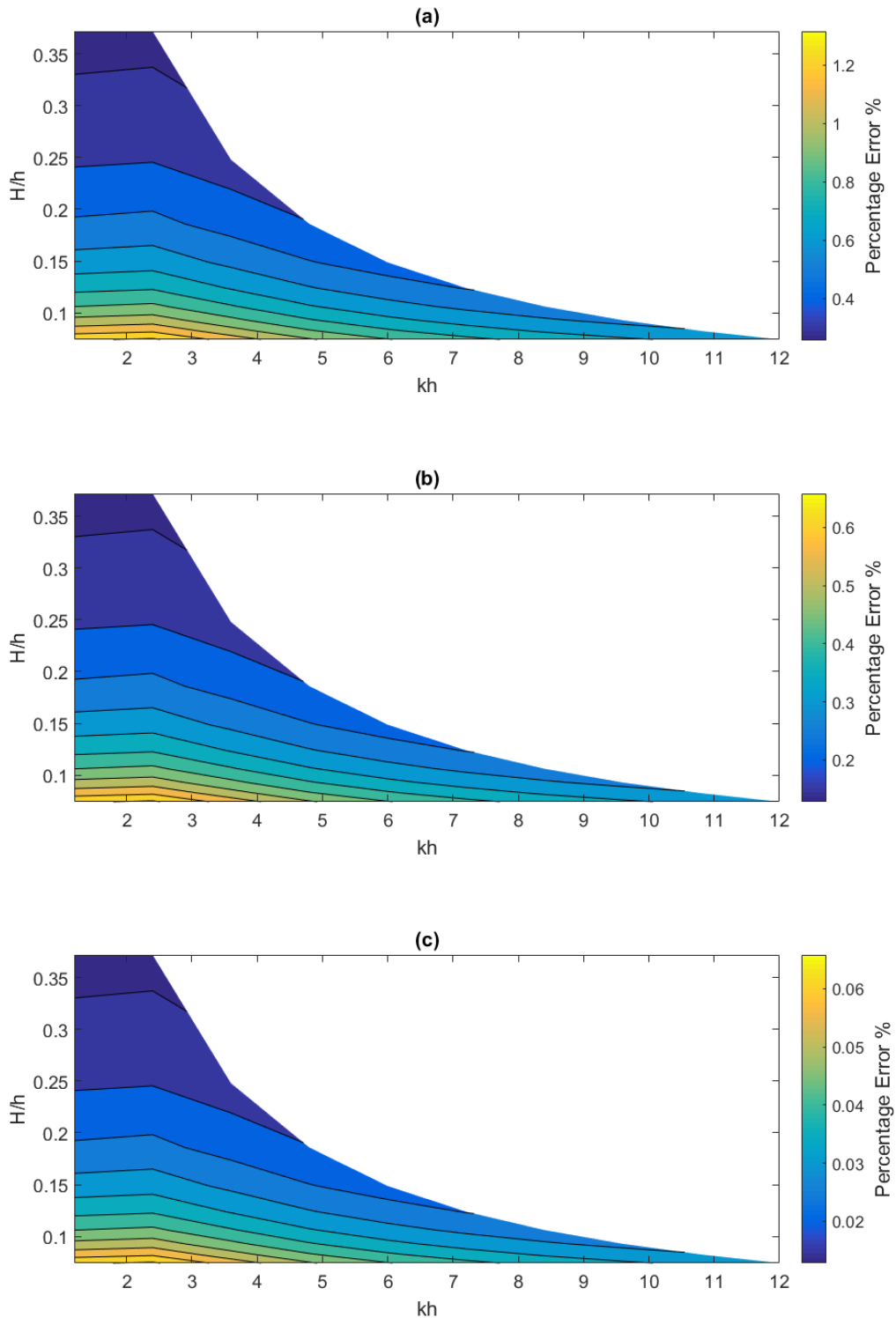


Figure 6.27: Contour plot of the percentage error between the generated wave height to the intended wave height, H , against kh and H/h for a two segment flap wavemaker with relative errors between the segment strokes of (a) 1×10^{-3} m, (b) 5×10^{-4} m and (c) 5×10^{-5} m.

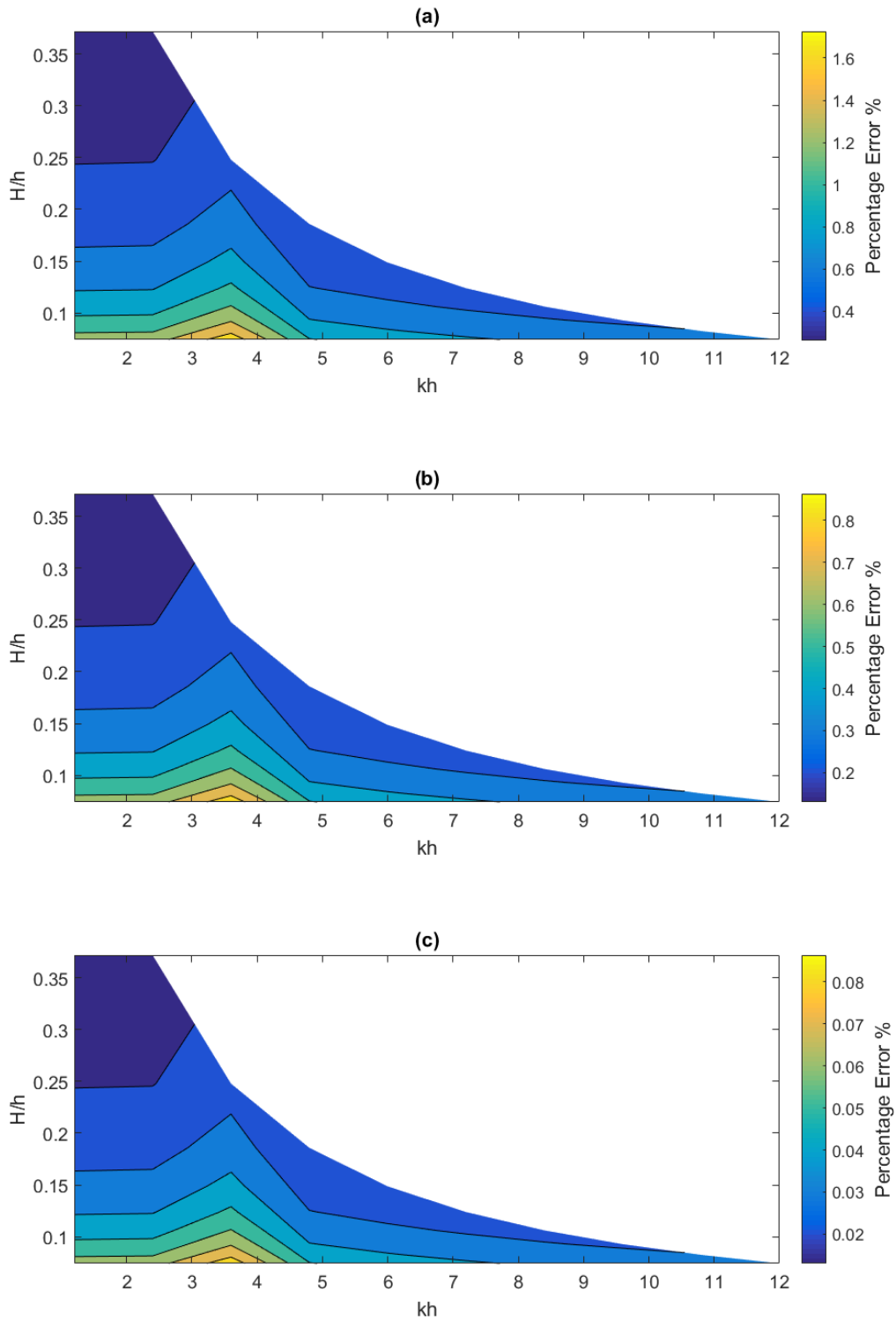


Figure 6.28: Contour plot of the percentage error between the generated wave height to the intended wave height, H , against kh and H/h for a three segment flap wavemaker with relative errors between the segment strokes of (a) 1×10^{-3} m, (b) 5×10^{-4} m and (c) 5×10^{-5} m.

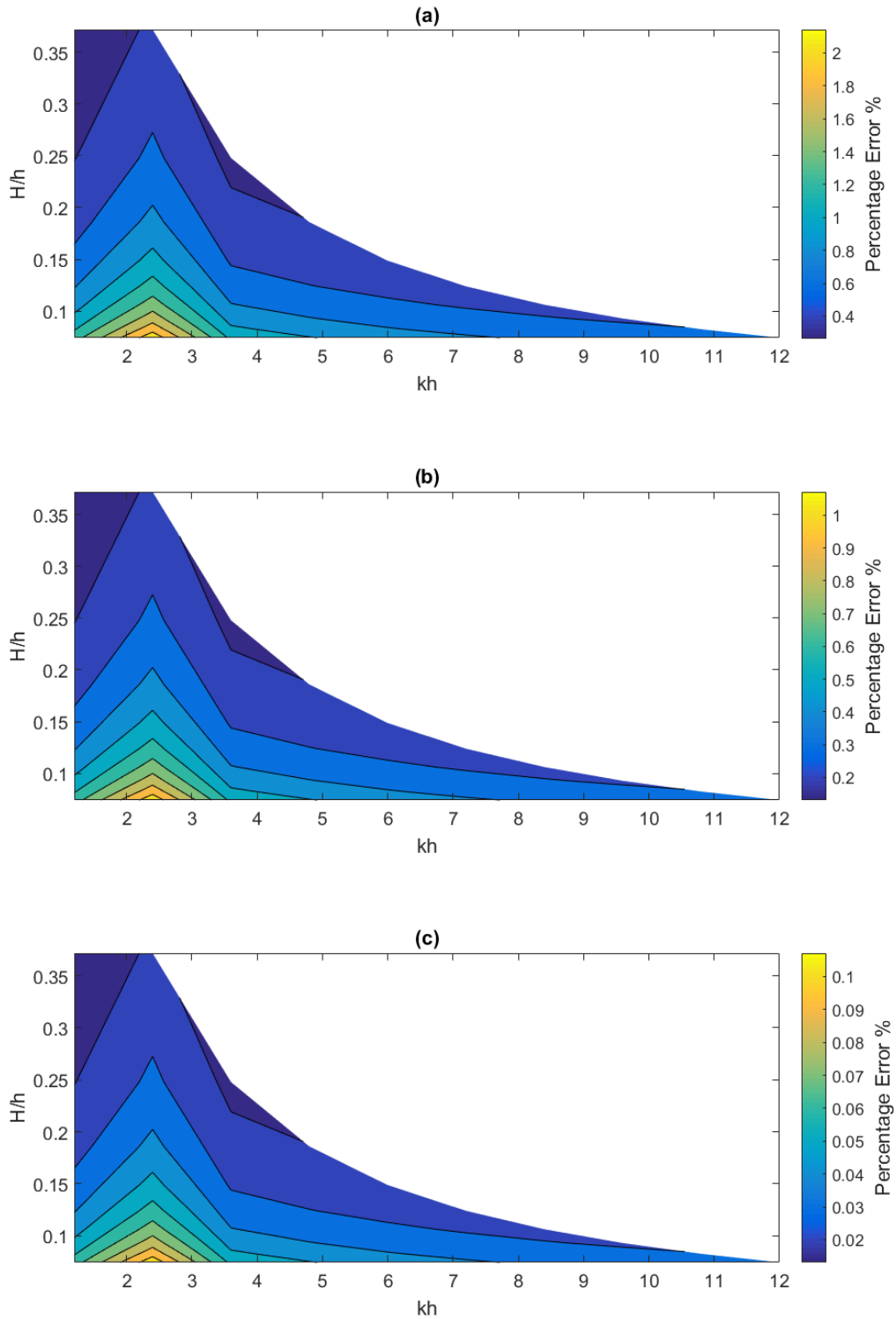


Figure 6.29: Contour plot of the percentage error between the generated wave height to the intended wave height, H , against kh and H/h for a four segment flap wavemaker with relative errors between the segment strokes of (a) 1×10^{-3} m, (b) 5×10^{-4} m and (c) 5×10^{-5} m.

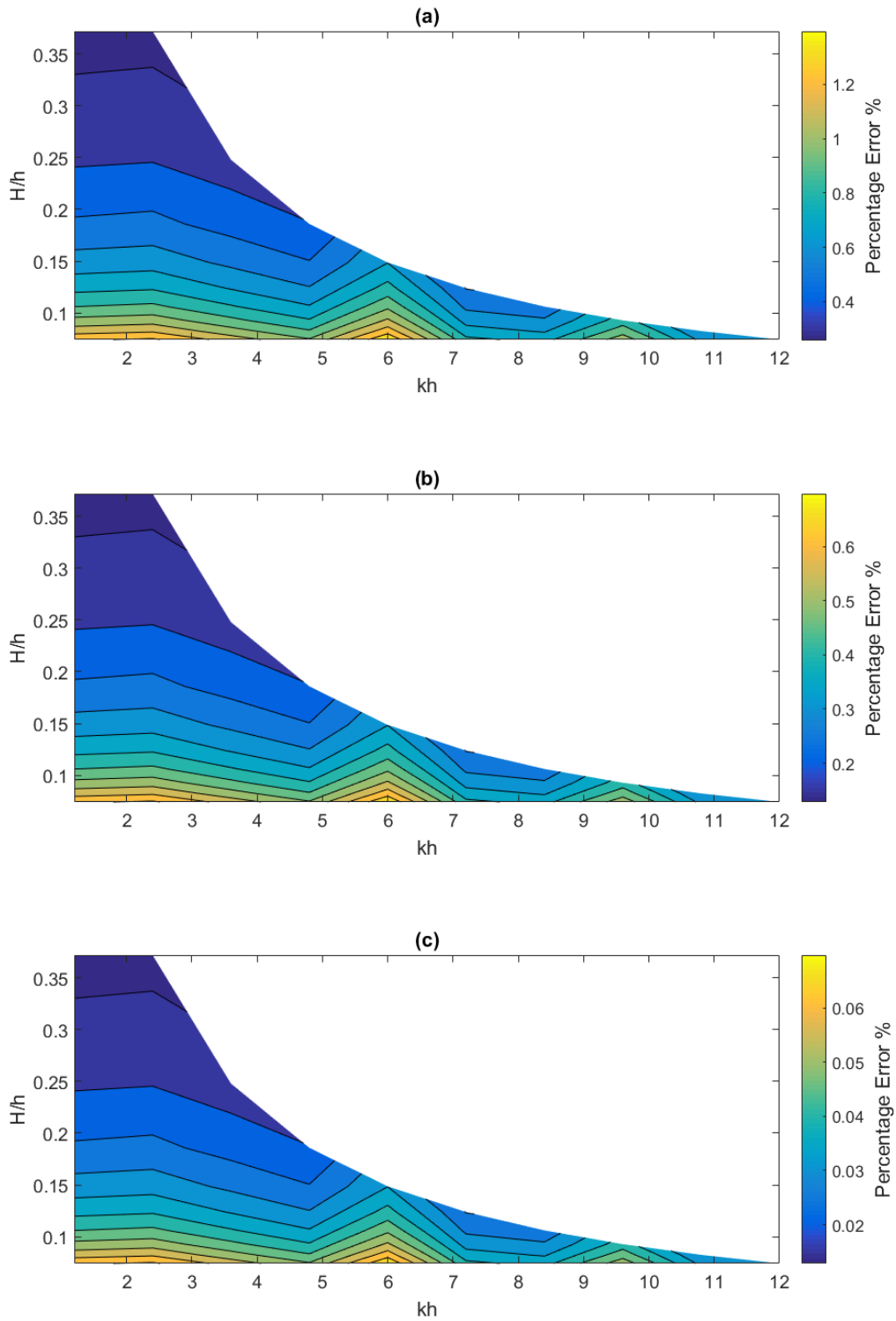


Figure 6.30: Contour plot of the percentage error between the generated wave height to the intended wave height, H , against kh and H/h for a five segment flap wavemaker with relative errors between the segment strokes of (a) 1×10^{-3} m, (b) 5×10^{-4} m and (c) 5×10^{-5} m.

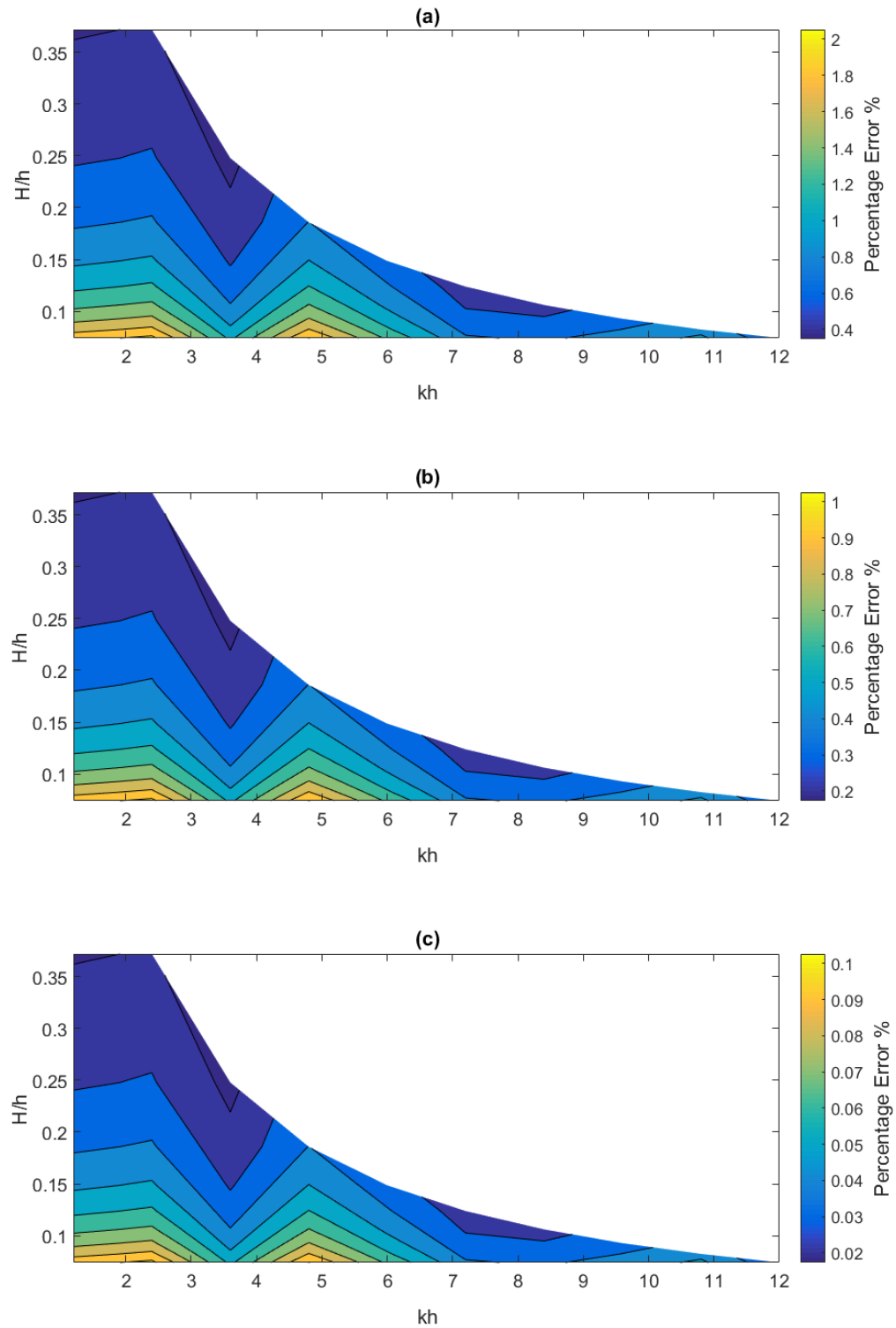


Figure 6.31: Contour plot of the percentage error between the generated wave height to the intended wave height, H , against kh and H/h for a six segment flap wavemaker with relative errors between the segment strokes of (a) 1×10^{-3} m, (b) 5×10^{-4} m and (c) 5×10^{-5} m.

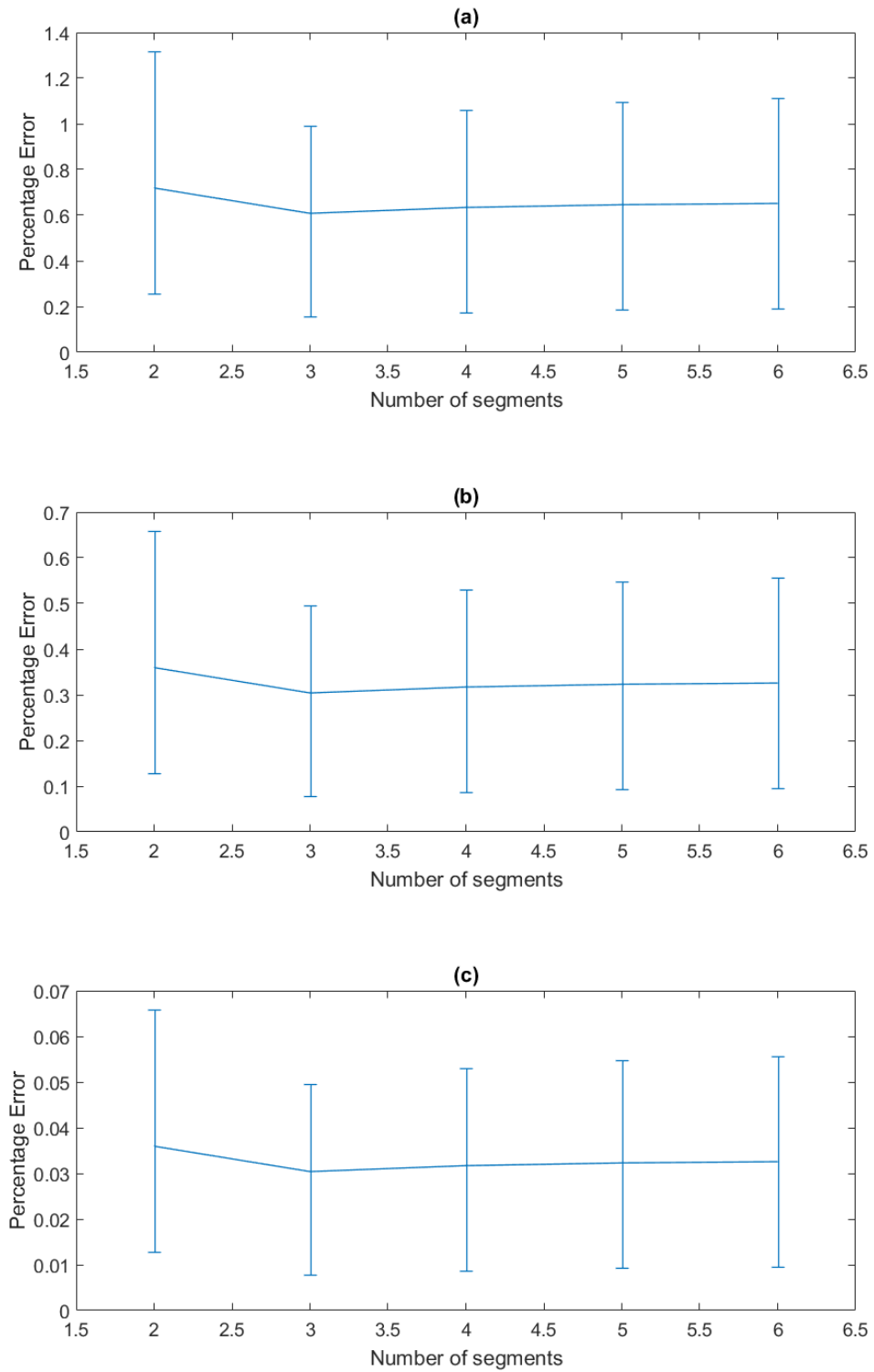


Figure 6.32: The maximum, minimum and average percentage error of the generated wave heights to the intended wave heights, H , over kh and H/h in segmented piston wavemakers with two to six segments and with relative errors between the segment strokes of (a) 1×10^{-3} m, (b) 5×10^{-4} m and (c) 5×10^{-5} m.

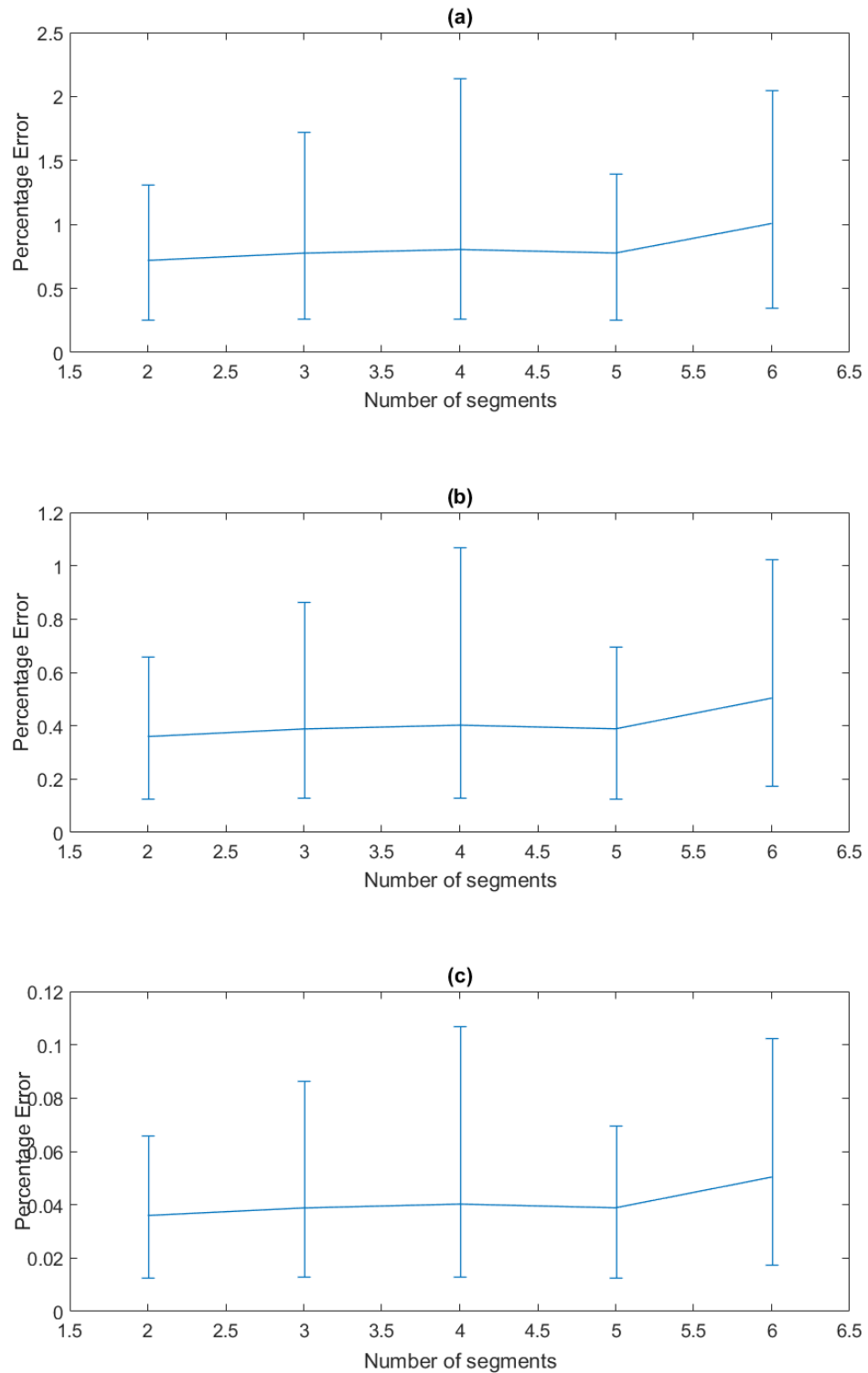


Figure 6.33: The maximum, minimum and average percentage error of the generated wave heights to the intended wave heights, H , over kh and H/h in segmented flap wavemakers with two to six segments and with relative errors between the segment strokes of (a) 1×10^{-3} m, (b) 5×10^{-4} m and (c) 5×10^{-5} m.

6.7 Conclusion

With the aim of minimising the distortion to the wave field caused by evanescent waves when generating monochromatic waves, the segment strokes of both piston and flap segmented wavemakers with two to six segments have been optimised for two different cases.

In Case (1) the segments in the wavemaker are all equal in length. This allowed for a comparison between the performance of a wavemaker where just the segment strokes were optimised, Figures 6.3 and 6.4, and a wavemaker where just the segment lengths were optimised, Figure 5.8. It was clear from this comparison that optimising the strokes of the segments yields a notably better reduction in the wave field distortion than optimising the segment lengths. However, it was suggested that this could be due to the fact that the strokes are optimised for each individual frequency.

In Case (2) the optimisation of the strokes for wavemakers with optimised segment lengths was carried out. In this case the completely optimised two segment flap wavemaker seemed to be promising as the maximum position of 1% distortion was only $0.06827h$ at $kh = 12$, and for $kh \leq 5.9$, the distortion never increases above 1%, Figure 6.6. The sensitivity analysis performed in Section 6.6.1 indicates that, with the presence of errors in the segment strokes of up to 1×10^{-3} m, the performance of the two segment flap wavemaker decreased significantly. For instance, with a relative error of 5×10^{-5} m between the segments, the maximum position of 1% distortion increased to over $0.4h$; although, this is still better than a single segment flap for which the maximum position of 1% distortion is $1.8h$.

The preferred wavemaker design is the completely optimised three segment flap, as it has relatively few segments and it reduces the distortion level to be less than 1% over the range $0 \leq kh \leq 12$. Even with the presence of a relative error of 1×10^{-3} m between the segments' strokes, the position of 1% distortion remains quite low.

Chapter 7

Conclusion

The objective of this thesis was to minimise the distortion in a wave tank caused by the presence of evanescent waves using a segmented wavemaker. Chapters 2 and 4 look at the relevant wavemaker theory and the hydrodynamics of the segmented wavemaker, respectively. Chapter 3 gives an overview of the work carried out by other researchers who have contributed towards the development of wavemakers, along with the technologies surrounding wavemakers, including feedback control systems, second order wavemaker theory and rolling seals. The focus of this thesis was to investigate Hypotheses 1 and 2, stated in Chapter 2 respectively as:

1. The closer the depth profile of the wavemaker matches that of the progressive wave, the smaller the amplitude of the evanescent waves, and hence the lesser the distortion caused by evanescent waves.
2. The distortion of the wave field, and more specifically the distance of 1% distortion from the wavemaker, can be minimised by developing a multi-body wavemaker which is designed to maximise the destructive interference between the evanescent waves.

Chapter 4 presents the hydrodynamics of piston and flap segmented wavemakers consisting of one to ten segments, where all the segments in the wavemaker are equal in length. The geometries of the wavemakers were optimised in accordance with both Hypothesis 1 and 2 separately. Chapter 5 deals with the optimisation of the segment lengths while Chapter 6 discusses the optimisation of the segment strokes. The results presented in Chapters 4, 5 and 6 show that all configurations of the segment wavemaker provide substantial reduction in the wave field distortion in comparison to the single segment wavemakers. While Hypothesis 1 and 2 both hold true, the results that prove Hypothesis 2, in Chapters 5 and 6, demonstrate that a greater reduction in the distortion can be achieved by utilising the

interference pattern between the evanescent waves, rather than approximating the kinematics of the progressive wave.

Previous to this work, it was always assumed that the infinite number of evanescent waves created during the wavemaking process were in phase with each other at $z = 0$. A consequence of this assumption is that the evanescent wave field's amplitude would decay exponentially with distance away from the wavemaker. Another assumption made by previous researchers was that the amplitude of the evanescent waves decrease as their imaginary wavenumber increases in value. In Section 2.4.2, aspects of wavemaker theory were presented, for the first time, which show that neither of these assumptions hold for wavemakers whose depth profiles vary over z . The theory predicted that some of the evanescent waves experienced a phase shift of π radians, which leads to destructive interference between the evanescent waves. As a result of this phase shift, the distortion pattern can be very different from the exponential function of x that was expected by other researchers. It was demonstrated in Figure 2.9, Section 2.4.2, and in Figure 6.11, Section 6.5, that for a wavemaker profile which is not constant over depth, the amplitude of the evanescent waves does not decrease with increasing imaginary wavenumbers as expected. This is an entirely novel concept.

It was observed that optimising the segment lengths and strokes using the minimisation of distortion approach achieved superior results than the kinematic matching approach. This was demonstrated by comparing the results presented in Figures 6.5 and 6.6 to those presented in Figure 5.6, which illustrated the performance of the segmented wavemakers in reducing the distortion when optimised using the minimisation of distortion approach and the kinematic matching approach, respectively.

To understand whether optimising the segment lengths or strokes of the piston and flap wavemakers is more beneficial, a comparison was made between Figure 5.8, where the segment lengths were optimised using the minimisation of distortion approach and where the strokes were prescribed using kinematic matching, to the results presented in Figures 6.3 and 6.4, where the segments are of equal lengths and where the minimisation of distortion approach was used to optimise the segment strokes. The comparison shows that optimising the strokes is more beneficial than optimising the segment lengths. This result can be largely attributed to the fact that the segment strokes can be optimised for each frequency, while the segment length cannot. This is an important result as it is much easier for testing facilities to control the strokes of their segments rather than the segment lengths.

The results presented in Figures 4.20 and 4.21, Section 4.6.3, for the con-

strained added mass of the segmented wavemaker, confirmed the fundamental hypothesis of this thesis, that the amplitude of the evanescent waves is reduced when more segments are added to the wavemaker. The significance of the reduction in the added mass lessens as more segments are added. For most of the segmented wavemakers considered in Chapter 4, the constrained added mass of the wavemakers is not monotonic over kh ; this is due to the interference between the evanescent waves. Without the occurrence of the phase shift, the constrained added mass would be monotonic over kh for each of these wavemakers, similar to the single piston wavemaker.

It was proposed in Hypothesis 2, that the interference between the evanescent waves could be optimised in order to increase the destructive interference and hence, minimise the distortion. Hypothesis 2 was investigated in Chapters 5 and 6, where the lengths and strokes of the segmented wavemaker were optimised in order to minimise the distance between the wavemaker and the testable area in a wave tank. This approach allows the optimiser to find the segmented wavemaker configuration which achieves the minimal level of distortion by optimising the destructive interference between the evanescent waves. In order to draw a comparison between Hypothesis 2 and the traditional ideas, the segments' lengths and strokes were also optimised to approximate the kinematics of a progressive wave, Hypothesis 1. Comparing the two approaches for optimising the segmented wavemaker, in both Chapters 5 and 6, clearly demonstrates that utilising the interference between the evanescent waves is more successful than simply approximating the kinematics of a progressive wave. The significance of this result is that a short wave tank can be equipped with a wavemaker that drastically reduces the distortion caused by the evanescent wave field.

A sensitivity analysis was presented in Section 6.6.1 to see how errors in the actuator's position can affect the ability of the segmented wavemaker to reduce the distortion in the wave tank. This analysis was carried out by allowing for errors between the relative segment strokes of 1×10^{-3} m, 5×10^{-4} m and 5×10^{-5} m. The results presented in Figures 6.12 to 6.21 demonstrated that the segmented wavemaker designs perform quite well even with relative errors of 1×10^{-3} m, 5×10^{-4} m and 5×10^{-5} m between the segment positions. Another sensitivity analysis is presented in Section 6.6.2 which considers how errors in the segment position affected the wave height of the progressive wave. The results in Figures 6.22 to 6.31 show that relative errors of 1×10^{-3} m, 5×10^{-4} m and 5×10^{-5} m between the segment positions have very little effect on the wave height of the progressive wave. Furthermore, the variance in the errors in the progressive wave height between the different piston and flap segmented wavemakers, presented in Figures 6.32 and 6.33, respectively, was very small.

The final conclusion of this thesis is that a flap wavemaker with three segments is the most appropriate design of segmented wavemaker for reducing the evanescent wave field in a wave flume, as it effectively reduces the position of 1% distortion significantly over the ranges of kh and wave height values considered. Additionally, the three segment flap wavemaker is not very susceptible to actuator errors and remains relatively simple to construct.

7.1 Suggestions for future work

Although we have demonstrated the success of the segmented wavemakers in reducing the distortion caused by evanescent waves in regular waves, there remains some areas for which the suitability of the segmented wavemaker is still unknown. First is the affect the segmented wavemaker has on the spurious free waves created by the mismatch between the motion of the wavemaker and that of the fluid in a progressive wave. Second is the practicality of generating irregular waves and to what extent the segmented wavemaker can reduce the distortion in an irregular wave field. It would also be interesting to see how the segmented wavemaker will perform, when its ability to reduce the distortion is averaged over frequency with a non-uniform weighting. The third suggestion of future work is to perform the experimental validation of the existence of the interference pattern between the evanescent waves, discussed in Section 2.4.2.

It would also be interesting to see how useful an understanding of the interference pattern between the evanescent waves and thus, the minimisation of a devices' added mass, will be to other topics, such as the absorption of unwanted waves and wave energy conversion.

7.2 Closing remarks

For the past hundred years, wavemakers have been iteratively improved as new technologies have emerged. The topic of generating waves has helped to deepen our understanding of how structures interact with waves, namely wave energy converters. Over the last thirty years, as the use of feedback controllers has become more widespread, some truly impressive wave tanks have been built. The author is eager to see how wavemakers progress in the future and would recommend any young engineers to become involved in this enlightening topic.

Appendix A

Results of complete optimised wavemakers

Run number	Wavenumber									
	$2 m^{-1}$	$4 m^{-1}$	$6 m^{-1}$	$8 m^{-1}$	$10 m^{-1}$	$12 m^{-1}$	$14 m^{-1}$	$16 m^{-1}$	$18 m^{-1}$	$20 m^{-1}$
1	0	0.0676	0.1302	0.1718	0.2012	0.2225	0.2385	0.2507	0.2603	0.2678
2	0	0.0676	0.1301	0.1718	0.2012	0.2225	0.2385	0.2507	0.2603	0.2678
3	0	0.0676	0.1302	0.1718	0.2012	0.2225	0.2385	0.2507	0.2603	0.2678
4	0	0.0676	0.1302	0.1718	0.2012	0.2225	0.2385	0.2507	0.2603	0.2678
5	0	0.0676	0.1302	0.1718	0.2012	0.2225	0.2385	0.2507	0.2603	0.2678
6	0	0.0676	0.1302	0.1718	0.2012	0.2225	0.2385	0.2507	0.2603	0.2678

Table A.1: Lowest obtained values of the position of 1% distortion, in meters, for a two segment piston wavemaker with segments of equal lengths and optimised segment strokes, where $h = 0.6$ m.

Run number	Wavenumber									
	$2 m^{-1}$	$4 m^{-1}$	$6 m^{-1}$	$8 m^{-1}$	$10 m^{-1}$	$12 m^{-1}$	$14 m^{-1}$	$16 m^{-1}$	$18 m^{-1}$	$20 m^{-1}$
1	0	0	0.007501	0.02899	0.04600	0.05955	0.07050	0.07945	0.08685	0.09301
2	0	0	0.007501	0.02899	0.04600	0.05955	0.07050	0.07945	0.08685	0.09301
3	0	0	0.007501	0.02899	0.04600	0.05955	0.07050	0.07945	0.08685	0.09301
4	0	0	0.007501	0.02899	0.04600	0.05955	0.07050	0.07945	0.08685	0.09301
5	0	0	0.007501	0.02899	0.04600	0.05955	0.07050	0.07945	0.08685	0.09301
6	0	0	0.007501	0.02899	0.04600	0.05955	0.07050	0.07945	0.08685	0.09301

Table A.2: Lowest obtained values of the position of 1% distortion, in meters, for a three segment piston wavemaker with segments of equal lengths and optimised segment strokes, where $h = 0.6$ m.

Run number	Wavenumber									
	$2 m^{-1}$	$4 m^{-1}$	$6 m^{-1}$	$8 m^{-1}$	$10 m^{-1}$	$12 m^{-1}$	$14 m^{-1}$	$16 m^{-1}$	$18 m^{-1}$	$20 m^{-1}$
1	0	0	0	0	0.003769	0.01224	0.01974	0.02628	0.03196	0.03693
2	0	0	0	0	0.003769	0.01224	0.01974	0.02628	0.03196	0.03693
3	0	0	0	0	0.003769	0.01224	0.01974	0.02628	0.03196	0.03693
4	0	0	0	0	0.003769	0.01224	0.01974	0.02628	0.03196	0.03693
5	0	0	0	0	0.003769	0.01224	0.01974	0.02628	0.03196	0.03693
6	0	0	0	0	0.003769	0.01224	0.01974	0.02628	0.03196	0.03693

Table A.3: Lowest obtained values of the position of 1% distortion, in meters, for a four segment piston wavemaker with segments of equal lengths and optimised segment strokes, where $h = 0.6$ m.

Run number	Wavenumber									
	$2 m^{-1}$	$4 m^{-1}$	$6 m^{-1}$	$8 m^{-1}$	$10 m^{-1}$	$12 m^{-1}$	$14 m^{-1}$	$16 m^{-1}$	$18 m^{-1}$	$20 m^{-1}$
1	0	0	0	0	0	0	0.001124	0.005298	0.009307	0.01292
2	0	0	0	0	0	0	0.001119	0.005279	0.009257	0.01291
3	0	0	0	0	0	0	0.001174	0.005425	0.009221	0.01291
4	0	0	0	0	0	0	0.001121	0.005271	0.009255	0.01293
5	0	0	0	0	0	0	0.001120	0.005312	0.009328	0.01291
6	0	0	0	0	0	0	0.001147	0.005334	0.009245	0.01292

Table A.4: Lowest obtained values of the position of 1% distortion, in meters, for a five segment piston wavemaker with segments of equal lengths and optimised segment strokes, where $h = 0.6$ m.

Run number	Wavenumber									
	$2 m^{-1}$	$4 m^{-1}$	$6 m^{-1}$	$8 m^{-1}$	$10 m^{-1}$	$12 m^{-1}$	$14 m^{-1}$	$16 m^{-1}$	$18 m^{-1}$	$20 m^{-1}$
1	0	0	0	0	0	0	0	0	0	0.002984
2	0	0	0	0	0	0	0	0	0	0.003525
3	0	0	0	0	0	0	0	0	0	0.002858
4	0	0	0	0	0	0	0	0	0	0.003616
5	0	0	0	0	0	0	0	0	0.0004538	0.003870
6	0	0	0	0	0	0	0	0	0.0001429	0.002500

Table A.5: Lowest obtained values of the position of 1% distortion, in meters, for a six segment piston wavemaker with segments of equal lengths and optimised segment strokes, where $h = 0.6$ m.

Run number	Wavenumber									
	$2 m^{-1}$	$4 m^{-1}$	$6 m^{-1}$	$8 m^{-1}$	$10 m^{-1}$	$12 m^{-1}$	$14 m^{-1}$	$16 m^{-1}$	$18 m^{-1}$	$20 m^{-1}$
1	0	0	0	0	0.003904	0.01746	0.02877	0.03796	0.04544	0.05156
2	0	0	0	0	0.003905	0.01746	0.02877	0.03796	0.04544	0.05156
3	0	0	0	0	0.003908	0.01746	0.02877	0.03796	0.04544	0.05156
4	0	0	0	0	0.003909	0.01746	0.02877	0.03796	0.04544	0.05156
5	0	0	0	0	0.003912	0.01746	0.02877	0.03796	0.04544	0.05156
6	0	0	0	0	0.003905	0.01746	0.02877	0.03797	0.04544	0.05156

Table A.6: Lowest obtained values of the position of 1% distortion, in meters, for a two segment flap wavemaker with segments of equal lengths and optimised segment strokes, where $h = 0.6$ m.

Run number	Wavenumber									
	$2 m^{-1}$	$4 m^{-1}$	$6 m^{-1}$	$8 m^{-1}$	$10 m^{-1}$	$12 m^{-1}$	$14 m^{-1}$	$16 m^{-1}$	$18 m^{-1}$	$20 m^{-1}$
1	0	0	0	0	0	0	0	0	0.0006257	0.004500
2	0	0	0	0	0	0	0	0	0.0008378	0.004500
3	0	0	0	0	0	0	0	0	0.0006869	0.004500
4	0	0	0	0	0	0	0	0	0.0006786	0.004501
5	0	0	0	0	0	0	0	0	0.0006372	0.004500
6	0	0	0	0	0	0	0	0	0.0005590	0.004500

Table A.7: Lowest obtained values of the position of 1% distortion, in meters, for a three segment flap wavemaker with segments of equal lengths and optimised segment strokes, where $h = 0.6$ m.

Run number	Wavenumber									
	$2 m^{-1}$	$4 m^{-1}$	$6 m^{-1}$	$8 m^{-1}$	$10 m^{-1}$	$12 m^{-1}$	$14 m^{-1}$	$16 m^{-1}$	$18 m^{-1}$	$20 m^{-1}$
1	0	0	0	0	0	0	0	0	0	0
2	0	0	0	0	0	0	0	0	0	0
3	0	0	0	0	0	0	0	0	0	0
4	0	0	0	0	0	0	0	0	0	0
5	0	0	0	0	0	0	0	0	0	0
6	0	0	0	0	0	0	0	0	0	0

Table A.8: Lowest obtained values of the position of 1% distortion, in meters, for a four segment flap wavemaker with segments of equal lengths and optimised segment strokes, where $h = 0.6$ m.

Run number	Wavenumber									
	$2 m^{-1}$	$4 m^{-1}$	$6 m^{-1}$	$8 m^{-1}$	$10 m^{-1}$	$12 m^{-1}$	$14 m^{-1}$	$16 m^{-1}$	$18 m^{-1}$	$20 m^{-1}$
1	0	0	0	0	0	0	0	0	0	0
2	0	0	0	0	0	0	0	0	0	0
3	0	0	0	0	0	0	0	0	0	0
4	0	0	0	0	0	0	0	0	0	0
5	0	0	0	0	0	0	0	0	0	0
6	0	0	0	0	0	0	0	0	0	0

Table A.9: Lowest obtained values of the position of 1% distortion, in meters, for a five segment flap wavemaker with segments of equal lengths and optimised segment strokes, where $h = 0.6$ m.

Run number	Wavenumber									
	$2 m^{-1}$	$4 m^{-1}$	$6 m^{-1}$	$8 m^{-1}$	$10 m^{-1}$	$12 m^{-1}$	$14 m^{-1}$	$16 m^{-1}$	$18 m^{-1}$	$20 m^{-1}$
1	0	0	0	0	0	0	0	0	0	0
2	0	0	0	0	0	0	0	0	0	0
3	0	0	0	0	0	0	0	0	0	0
4	0	0	0	0	0	0	0	0	0	0
5	0	0	0	0	0	0	0	0	0	0
6	0	0	0	0	0	0	0	0	0	0

Table A.10: Lowest obtained values of the position of 1% distortion, in meters, for a six segment flap wavemaker with segments of equal lengths and optimised segment strokes, where $h = 0.6$ m.

Number of segments in Wavemaker	Wavenumber									
	$2 m^{-1}$	$4 m^{-1}$	$6 m^{-1}$	$8 m^{-1}$	$10 m^{-1}$	$12 m^{-1}$	$14 m^{-1}$	$16 m^{-1}$	$18 m^{-1}$	$20 m^{-1}$
2	0	2.189×10^{-15}	5.782×10^{-16}	6.645×10^{-16}	5.409×10^{-15}	2.018×10^{-15}	8.619×10^{-16}	1.467×10^{-16}	1.246×10^{-15}	3.109×10^{-15}
3	0	0	2.074×10^{-12}	7.156×10^{-13}	1.417×10^{-12}	2.264×10^{-12}	1.816×10^{-12}	1.268×10^{-12}	1.193×10^{-12}	9.962×10^{-13}
4	0	0	0	0	3.976×10^{-08}	3.019×10^{-07}	1.131×10^{-07}	1.486×10^{-07}	1.862×10^{-07}	2.998×10^{-07}
5	0	0	0	0	0	0	2.208×10^{-05}	5.620×10^{-05}	4.018×10^{-05}	1.039×10^{-05}
6	0	0	0	0	0	0	0	0	1.828×10^{-04}	5.247×10^{-05}

Table A.11: Standard deviation of the lowest obtained values of the position of 1% distortion for a segmented piston wavemaker with segments of equal lengths and optimised segment strokes, corresponding to the results presented in Tables A.1 to A.5.

Number of segments in Wavemaker	Wavenumber									
	$2 m^{-1}$	$4 m^{-1}$	$6 m^{-1}$	$8 m^{-1}$	$10 m^{-1}$	$12 m^{-1}$	$14 m^{-1}$	$16 m^{-1}$	$18 m^{-1}$	$20 m^{-1}$
2	0	0	0	0	3.027×10^{-06}	1.932×10^{-06}	2.370×10^{-06}	2.339×10^{-06}	1.423×10^{-06}	2.600×10^{-12}
3	0	0	0	0	0	0	0	0	9.365×10^{-05}	1.299×10^{-07}
4	0	0	0	0	0	0	0	0	0	0
5	0	0	0	0	0	0	0	0	0	0
6	0	0	0	0	0	0	0	0	0	0

Table A.12: Standard deviation of the lowest obtained values of the position of 1% distortion for a segmented flap wavemaker with segments of equal lengths and optimised segment strokes, corresponding to the results presented in Tables A.6 to A.10.

Stroke number	Wavenumber									
	$2 m^{-1}$	$4 m^{-1}$	$6 m^{-1}$	$8 m^{-1}$	$10 m^{-1}$	$12 m^{-1}$	$14 m^{-1}$	$16 m^{-1}$	$18 m^{-1}$	$20 m^{-1}$
1	1.4197	-1.6848	-1.5558	1.7969	1.3603	-1.4166	-0.3493	1.1809	-0.4511	-0.5022
2	0.8047	-0.2572	0.1268	-0.3801	-0.3951	0.4848	0.1322	-0.4780	0.1916	0.2211

Table A.13: Optimised strokes, in meters, for a two segment piston wavemaker with segments of equal lengths, where $h = 0.6$ m.

Stroke number	Wavenumber									
	$2 m^{-1}$	$4 m^{-1}$	$6 m^{-1}$	$8 m^{-1}$	$10 m^{-1}$	$12 m^{-1}$	$14 m^{-1}$	$16 m^{-1}$	$18 m^{-1}$	$20 m^{-1}$
1	-1.8474	1.4063	1.8260	1.1410	1.7140	1.6300	-1.2037	1.1716	-0.8223	-1.1600
2	-1.1747	-0.0714	-0.7002	-0.6415	-1.2346	-1.4030	1.1844	-1.278	0.9735	1.4659
3	-1.2538	0.7241	0.9111	0.5822	0.9691	1.03525	-0.8504	0.9065	-0.686	-1.0305

Table A.14: Optimised strokes, in meters, for a three segment piston wavemaker with segments of equal lengths, where $h = 0.6$ m.

Stroke number	Wavenumber									
	$2 m^{-1}$	$4 m^{-1}$	$6 m^{-1}$	$8 m^{-1}$	$10 m^{-1}$	$12 m^{-1}$	$14 m^{-1}$	$16 m^{-1}$	$18 m^{-1}$	$20 m^{-1}$
1	-0.7976	1.2957	-0.9704	-0.9373	-0.4119	0.4848	0.4689	-0.4133	-0.3917	-0.3256
2	-0.8144	1.1883	0.4671	0.7547	0.5593	-0.7213	-0.7631	0.7325	0.7515	0.6715
3	0.5420	-1.8177	-1.5998	-1.7982	-1.4308	1.7951	1.8766	-1.7948	-1.8423	-1.6500
4	-1.2939	1.9577	0.8455	0.9948	0.9431	-1.2025	-1.2695	1.2214	1.2581	1.1289

Table A.15: Optimised strokes, in meters, for a four segment piston wavemaker with segments of equal lengths, where $h = 0.6$ m.

Stroke number	Wavenumber									
	$2 m^{-1}$	$4 m^{-1}$	$6 m^{-1}$	$8 m^{-1}$	$10 m^{-1}$	$12 m^{-1}$	$14 m^{-1}$	$16 m^{-1}$	$18 m^{-1}$	$20 m^{-1}$
1	-1.8166	1.9570	0.9090	-1.5368	-1.0521	0.0757	0.07127	-0.0412	-0.0315	-0.0419
2	-1.5877	0.3465	-0.0931	0.4308	0.7336	-0.1748	-0.1915	0.1139	0.0901	0.1251
3	-1.7315	1.9767	0.1426	-1.1191	-0.9851	0.7685	0.8813	-0.5253	-0.4184	-0.5869
4	0.02041	-0.5283	1.8953	-0.0256	-1.5185	-1.4624	-1.7823	1.0791	0.8706	1.2342
5	-1.8952	0.6166	-1.4353	0.2737	1.7820	0.8591	1.0797	-0.6581	-0.5338	-0.7597

Table A.16: Optimised strokes, in meters, for a five segment piston wavemaker with segments of equal lengths, where $h = 0.6$ m.

Stroke number	Wavenumber									
	$2 m^{-1}$	$4 m^{-1}$	$6 m^{-1}$	$8 m^{-1}$	$10 m^{-1}$	$12 m^{-1}$	$14 m^{-1}$	$16 m^{-1}$	$18 m^{-1}$	$20 m^{-1}$
1	1.8503	-1.9292	-1.8770	-1.4271	-1.8423	0.2717	0.3057	-0.0173	0.0063	0.0098
2	1.0699	0.4681	-0.1733	-0.0312	0.6754	-0.3244	-0.5063	0.0582	-0.0279	-0.0415
3	1.5728	-1.9920	-0.3543	-0.8170	-1.5255	1.0350	1.6477	-0.3670	0.2002	0.2916
4	1.3753	-1.3896	-1.7348	0.9114	-0.7530	-0.9876	-1.8695	1.1886	-0.7248	-1.0443
5	0.4279	-1.6943	-0.0606	-1.3577	1.9143	-0.6013	-0.1424	-1.8873	1.2423	1.7714
6	1.5721	1.9802	0.7383	0.5025	-0.6281	0.9048	0.8378	1.0108	-0.6922	-0.9809

Table A.17: Optimised strokes, in meters, for a six segment piston wavemaker with segments of equal lengths, where $h = 0.6$ m.

Stroke number	Wavenumber									
	$2 m^{-1}$	$4 m^{-1}$	$6 m^{-1}$	$8 m^{-1}$	$10 m^{-1}$	$12 m^{-1}$	$14 m^{-1}$	$16 m^{-1}$	$18 m^{-1}$	$20 m^{-1}$
1	0.9277	-1.3844	1.9679	-1.8770	1.9257	1.4144	-0.7414	1.8946	1.1227	-0.6345
2	1.3200	-0.3984	-0.1682	0.3742	-0.6477	-0.5939	0.3631	-1.040	-0.6733	0.4081
3	-0.0898	-0.2126	0.6954	-0.6927	0.9589	0.8180	-0.4864	1.3791	0.8901	-0.5397

Table A.18: Optimised strokes, in meters, for a two segment flap wavemaker with segments of equal lengths, where $h = 0.6$ m.

Stroke number	Wavenumber									
	$2 m^{-1}$	$4 m^{-1}$	$6 m^{-1}$	$8 m^{-1}$	$10 m^{-1}$	$12 m^{-1}$	$14 m^{-1}$	$16 m^{-1}$	$18 m^{-1}$	$20 m^{-1}$
1	1.3464	-1.7733	1.7041	1.9715	1.4396	-1.9539	-0.8170	-0.5661	-0.4572	0.5280
2	0.4218	-1.4056	0.5710	0.0840	-0.0379	0.4231	0.2851	0.2743	0.2713	-0.3451
3	1.4964	-1.8923	-0.3544	0.4722	0.1039	-0.8076	-0.7796	-0.7285	-0.7678	0.9697
4	-0.3819	0.4995	0.9873	-0.4715	0.0819	0.8264	1.2081	1.0935	1.1815	1.4929

Table A.19: Optimised strokes, in meters, for a three segment flap wavemaker with segments of equal lengths, where $h = 0.6$ m.

Stroke number	Wavenumber									
	$2 m^{-1}$	$4 m^{-1}$	$6 m^{-1}$	$8 m^{-1}$	$10 m^{-1}$	$12 m^{-1}$	$14 m^{-1}$	$16 m^{-1}$	$18 m^{-1}$	$20 m^{-1}$
1	1.0950	1.3048	1.6239	1.7817	1.6849	-0.7473	-1.8450	1.1053	-1.9971	-1.2989
2	0.9581	1.0700	0.8921	0.1945	0.2945	0.0187	0.1474	-0.2544	0.5891	0.4828
3	0.3390	-0.3493	-0.4607	0.8426	0.0006	-0.2624	-0.3804	0.6652	-1.0258	-0.7685
4	1.9282	1.4763	1.4418	-0.9765	0.0407	0.2269	0.5636	-0.8093	0.6923	0.0343
5	-1.3844	-0.9878	-1.3926	1.0933	0.1095	-0.0624	-0.8532	0.6712	-0.2351	0.8224

Table A.20: Optimised strokes, in meters, for a four segment flap wavemaker with segments of equal lengths, where $h = 0.6$ m.

Stroke number	Wavenumber									
	$2 m^{-1}$	$4 m^{-1}$	$6 m^{-1}$	$8 m^{-1}$	$10 m^{-1}$	$12 m^{-1}$	$14 m^{-1}$	$16 m^{-1}$	$18 m^{-1}$	$20 m^{-1}$
1	1.5119	-1.9729	-1.4298	1.9402	1.8227	-1.8419	-1.9851	-1.6498	-1.3395	-1.9756
2	1.8816	-1.8665	-0.4692	1.0237	0.4686	-0.3854	-0.1081	0.1944	0.1355	0.3165
3	0.5339	0.2943	-0.4439	-0.7866	0.3611	0.3663	-0.4277	-1.1085	0.0619	-0.0598
4	1.9180	-1.4718	-0.4323	1.9927	-0.3928	-1.5981	0.7781	1.8258	-1.4545	-1.4165
5	0.9034	0.5347	-0.4296	-1.9281	0.4770	1.8166	-1.3298	-0.9004	1.6872	1.5760
6	-0.5793	-1.9331	1.1929	1.9351	-0.4849	-1.2955	1.6396	-0.1155	-0.7835	-0.7322

Table A.21: Optimised strokes, in meters, for a five segment flap wavemaker with segments of equal lengths, where $h = 0.6$ m.

Stroke number	Wavenumber									
	$2 m^{-1}$	$4 m^{-1}$	$6 m^{-1}$	$8 m^{-1}$	$10 m^{-1}$	$12 m^{-1}$	$14 m^{-1}$	$16 m^{-1}$	$18 m^{-1}$	$20 m^{-1}$
1	-1.2225	1.9832	1.5025	1.8256	1.9531	-1.7402	1.8915	-1.5686	0.9076	0.9607
2	-1.0959	1.5858	0.7960	1.2342	0.9323	-0.6236	0.0619	-0.1705	-0.1073	-0.1375
3	-1.4697	.7846	0.9871	1.6510	1.3343	0.8472	1.1281	-0.02576	0.7293	-0.2481
4	-1.5002	1.7512	1.4853	0.0628	0.3565	-1.8152	-1.8078	0.2709	-1.2508	0.6536
5	-0.5485	-1.3091	-1.6470	-0.0446	-0.4561	-0.0500	1.7115	-1.5802	0.9146	-1.7001
6	-1.5809	1.8889	0.0390	-0.3338	0.7069	1.9440	-0.5535	1.1746	-0.3565	1.2225
7	1.9204	-0.7771	1.2851	0.5194	-1.2032	-1.9481	-0.3134	0.2031	0.2692	-0.1464

Table A.22: Optimised strokes, in meters, for a six segment flap wavemaker with segments of equal lengths, where $h = 0.6$ m.

Run number	Wavenumber									
	$2 m^{-1}$	$4 m^{-1}$	$6 m^{-1}$	$8 m^{-1}$	$10 m^{-1}$	$12 m^{-1}$	$14 m^{-1}$	$16 m^{-1}$	$18 m^{-1}$	$20 m^{-1}$
1	0	0.01399	0.06153	0.09986	0.1298	0.1527	0.1701	0.1837	0.1943	0.2030
2	0	0.01399	0.06153	0.09986	0.1298	0.1527	0.1701	0.1837	0.1943	0.2030
3	0	0.01399	0.06153	0.09986	0.1298	0.1527	0.1701	0.1837	0.1943	0.2030
4	0	0.01399	0.06153	0.09986	0.1298	0.1527	0.1701	0.1837	0.1943	0.2030
5	0	0.01399	0.06153	0.09986	0.1298	0.1527	0.1701	0.1837	0.1943	0.2030
6	0	0.01399	0.06153	0.09986	0.1298	0.1527	0.1701	0.1837	0.1943	0.2030

Table A.23: Lowest obtained values of the position of 1% distortion, in meters, for a two segment piston wavemaker, with both the segments' strokes and lengths optimised, where $h = 0.6$ m.

Run number	Wavenumber									
	$2 m^{-1}$	$4 m^{-1}$	$6 m^{-1}$	$8 m^{-1}$	$10 m^{-1}$	$12 m^{-1}$	$14 m^{-1}$	$16 m^{-1}$	$18 m^{-1}$	$20 m^{-1}$
1	0	0	0	0.01158	0.02517	0.03642	0.04581	0.05370	0.06038	0.06609
2	0	0	0	0.01158	0.02517	0.03642	0.04581	0.05370	0.06038	0.06609
3	0	0	0	0.01158	0.02517	0.03642	0.04581	0.05370	0.06038	0.06609
4	0	0	0	0.01158	0.02517	0.03642	0.04581	0.05370	0.06038	0.06609
5	0	0	0	0.01158	0.02517	0.03642	0.04581	0.05370	0.06038	0.06609
6	0	0	0	0.01158	0.02517	0.03642	0.04581	0.05370	0.06038	0.06609

Table A.24: Lowest obtained values of the position of 1% distortion, in meters, for a three segment piston wavemaker, with both the segments' strokes and lengths optimised, where $h = 0.6$ m.

Run number	Wavenumber									
	$2 m^{-1}$	$4 m^{-1}$	$6 m^{-1}$	$8 m^{-1}$	$10 m^{-1}$	$12 m^{-1}$	$14 m^{-1}$	$16 m^{-1}$	$18 m^{-1}$	$20 m^{-1}$
1	0	0	0	0	0	0.004068	0.009728	0.01498	0.01971	0.02393
2	0	0	0	0	0	0.004068	0.009728	0.01498	0.01971	0.02393
3	0	0	0	0	0	0.004068	0.009728	0.01498	0.01971	0.02393
4	0	0	0	0	0	0.004068	0.009728	0.01498	0.01971	0.02393
5	0	0	0	0	0	0.004068	0.009728	0.01498	0.01971	0.02393
6	0	0	0	0	0	0.004068	0.009728	0.01498	0.01971	0.02393

Table A.25: Lowest obtained values of the position of 1% distortion, in meters, for a four segment piston wavemaker, with both the segments' strokes and lengths optimised, where $h = 0.6$ m.

Run number	Wavenumber									
	$2 m^{-1}$	$4 m^{-1}$	$6 m^{-1}$	$8 m^{-1}$	$10 m^{-1}$	$12 m^{-1}$	$14 m^{-1}$	$16 m^{-1}$	$18 m^{-1}$	$20 m^{-1}$
1	0	0	0	0	0	0	0.0002104	0.002252	0.004533	0.006933
2	0	0	0	0	0	0	0.0002096	0.002250	0.004526	0.006903
3	0	0	0	0	0	0	0.0002119	0.002261	0.004519	0.006903
4	0	0	0	0	0	0	0.0002084	0.002256	0.004510	0.006925
5	0	0	0	0	0	0	0.0002088	0.002259	0.004534	0.006924
6	0	0	0	0	0	0	0.0002078	0.002252	0.004510	0.006907

Table A.26: Lowest obtained values of the position of 1% distortion, in meters, for a five segment piston wavemaker, with both the segments' strokes and lengths optimised, where $h = 0.6$ m.

Run number	Wavenumber									
	$2 m^{-1}$	$4 m^{-1}$	$6 m^{-1}$	$8 m^{-1}$	$10 m^{-1}$	$12 m^{-1}$	$14 m^{-1}$	$16 m^{-1}$	$18 m^{-1}$	$20 m^{-1}$
1	0	0	0	0	0	0	0	0	0	0
2	0	0	0	0	0	0	0	0	0	0
3	0	0	0	0	0	0	0	0	0	0
4	0	0	0	0	0	0	0	0	0	0
5	0	0	0	0	0	0	0	0	0	0
6	0	0	0	0	0	0	0	0	0	0

Table A.27: Lowest obtained values of the position of 1% distortion, in meters, for a six segment piston wavemaker, with both the segments' strokes and lengths optimised, where $h = 0.6$ m.

Run number	Wavenumber									
	$2 m^{-1}$	$4 m^{-1}$	$6 m^{-1}$	$8 m^{-1}$	$10 m^{-1}$	$12 m^{-1}$	$14 m^{-1}$	$16 m^{-1}$	$18 m^{-1}$	$20 m^{-1}$
1	0	0	0	0	0	0.008092	0.01860	0.02747	0.03483	0.04096
2	0	0	0	0	0	0.008092	0.01860	0.02746	0.03483	0.04096
3	0	0	0	0	0	0.008093	0.01860	0.02746	0.03483	0.04096
4	0	0	0	0	0	0.008094	0.01860	0.02746	0.03483	0.04096
5	0	0	0	0	0	0.008092	0.01860	0.02746	0.03483	0.04096
6	0	0	0	0	0	0.008091	0.01860	0.02746	0.03483	0.04096

Table A.28: Lowest obtained values of the position of 1% distortion, in meters, for a two segment flap wavemaker, with both the segments' strokes and lengths optimised, where $h = 0.6$ m.

Run number	Wavenumber									
	$2 m^{-1}$	$4 m^{-1}$	$6 m^{-1}$	$8 m^{-1}$	$10 m^{-1}$	$12 m^{-1}$	$14 m^{-1}$	$16 m^{-1}$	$18 m^{-1}$	$20 m^{-1}$
1	0	0	0	0	0	0	0	0	0	0
2	0	0	0	0	0	0	0	0	0	0
3	0	0	0	0	0	0	0	0	0	0
4	0	0	0	0	0	0	0	0	0	0
5	0	0	0	0	0	0	0	0	0	0
6	0	0	0	0	0	0	0	0	0	0

Table A.29: Lowest obtained values of the position of 1% distortion, in meters, for a three segment flap wavemaker, with both the segments' strokes and lengths optimised, where $h = 0.6$ m.

Run number	Wavenumber									
	$2 m^{-1}$	$4 m^{-1}$	$6 m^{-1}$	$8 m^{-1}$	$10 m^{-1}$	$12 m^{-1}$	$14 m^{-1}$	$16 m^{-1}$	$18 m^{-1}$	$20 m^{-1}$
1	0	0	0	0	0	0	0	0	0	0
2	0	0	0	0	0	0	0	0	0	0
3	0	0	0	0	0	0	0	0	0	0
4	0	0	0	0	0	0	0	0	0	0
5	0	0	0	0	0	0	0	0	0	0
6	0	0	0	0	0	0	0	0	0	0

Table A.30: Lowest obtained values of the position of 1% distortion, in meters, for a four segment flap wavemaker, with both the segments' strokes and lengths optimised, where $h = 0.6$ m.

Run number	Wavenumber									
	$2 m^{-1}$	$4 m^{-1}$	$6 m^{-1}$	$8 m^{-1}$	$10 m^{-1}$	$12 m^{-1}$	$14 m^{-1}$	$16 m^{-1}$	$18 m^{-1}$	$20 m^{-1}$
1	0	0	0	0	0	0	0	0	0	0
2	0	0	0	0	0	0	0	0	0	0
3	0	0	0	0	0	0	0	0	0	0
4	0	0	0	0	0	0	0	0	0	0
5	0	0	0	0	0	0	0	0	0	0
6	0	0	0	0	0	0	0	0	0	0

Table A.31: Lowest obtained values of the position of 1% distortion, in meters, for a five segment flap wavemaker, with both the segments' strokes and lengths optimised, where $h = 0.6$ m.

Run number	Wavenumber									
	$2 m^{-1}$	$4 m^{-1}$	$6 m^{-1}$	$8 m^{-1}$	$10 m^{-1}$	$12 m^{-1}$	$14 m^{-1}$	$16 m^{-1}$	$18 m^{-1}$	$20 m^{-1}$
1	0	0	0	0	0	0	0	0	0	0
2	0	0	0	0	0	0	0	0	0	0
3	0	0	0	0	0	0	0	0	0	0
4	0	0	0	0	0	0	0	0	0	0
5	0	0	0	0	0	0	0	0	0	0
6	0	0	0	0	0	0	0	0	0	0

Table A.32: Lowest obtained values of the position of 1% distortion, in meters, for a six segment flap wavemaker, with both the segments' strokes and lengths optimised, where $h = 0.6$ m.

Number of segments in Wavemaker	Wavenumber									
	$2 m^{-1}$	$4 m^{-1}$	$6 m^{-1}$	$8 m^{-1}$	$10 m^{-1}$	$12 m^{-1}$	$14 m^{-1}$	$16 m^{-1}$	$18 m^{-1}$	$20 m^{-1}$
2	0	8.8113×10^{-18}	8.6833×10^{-17}	1.3677×10^{-15}	4.1168×10^{-17}	0	1.4544×10^{-15}	2.4825×10^{-17}	0	4.0869×10^{-15}
3	0	0	0	1.8579×10^{-12}	1.7748×10^{-12}	1.0081×10^{-12}	1.8464×10^{-12}	1.5641×10^{-12}	2.3736×10^{-12}	4.6612×10^{-13}
4	0	0	0	0	0	8.9412×10^{-08}	7.7266×10^{-08}	3.9169×10^{-08}	8.7964×10^{-08}	3.1354×10^{-08}
5	0	0	0	0	0	0	1.4933×10^{-06}	4.3186×10^{-06}	1.0550×10^{-05}	1.3222×10^{-05}
6	0	0	0	0	0	0	0	0	0	0

Table A.33: Standard deviation of the lowest obtained position of 1% distortion for completely optimised segmented piston wavemaker, corresponding to the results presented in Tables A.23-27.

Number of segments in Wavemaker	Wavenumber									
	$2 m^{-1}$	$4 m^{-1}$	$6 m^{-1}$	$8 m^{-1}$	$10 m^{-1}$	$12 m^{-1}$	$14 m^{-1}$	$16 m^{-1}$	$18 m^{-1}$	$20 m^{-1}$
2	0	0	0	0	0	8.2384×10^{-07}	1.7504×10^{-06}	3.5374×10^{-06}	9.9809×10^{-07}	4.9556×10^{-13}
3	0	0	0	0	0	0	0	0	0	0
4	0	0	0	0	0	0	0	0	0	0
5	0	0	0	0	0	0	0	0	0	0
6	0	0	0	0	0	0	0	0	0	0

Table A.34: Standard deviation of the lowest obtained position of 1% distortion for completely optimised segmented flap wavemaker, corresponding to the results presented in Tables A.28-32.

Stroke Number	Wavenumber									
	$2 m^{-1}$	$4 m^{-1}$	$6 m^{-1}$	$8 m^{-1}$	$10 m^{-1}$	$12 m^{-1}$	$14 m^{-1}$	$16 m^{-1}$	$18 m^{-1}$	$20 m^{-1}$
1	1.7221	-1.1230	-0.8468	-1.6663	0.6234	-1.5191	1.6455	-1.1513	-0.7753	0.3158
2	1.1146	-0.2918	-0.0676	0.0275	-0.0464	0.1709	-0.2290	0.1827	0.1345	-0.0584

Table A.35: Optimised strokes, in meters, for a two segment piston wavemaker with optimised segment lengths, where $h = 0.6$ m.

Stroke Number	Wavenumber									
	$2 m^{-1}$	$4 m^{-1}$	$6 m^{-1}$	$8 m^{-1}$	$10 m^{-1}$	$12 m^{-1}$	$14 m^{-1}$	$16 m^{-1}$	$18 m^{-1}$	$20 m^{-1}$
1	-1.6050	-1.6112	1.8132	-1.5026	-1.2598	-0.8125	1.7194	1.7398	-1.6568	1.6329
2	-1.8281	-0.7413	-0.0557	0.2798	0.3912	0.3411	-0.8869	-1.0437	1.1158	-1.2049
3	-0.8940	-0.3785	0.4161	-0.3013	-0.2550	-0.1781	0.4153	0.4615	-0.4777	0.5060

Table A.36: Optimised strokes, in meters, for a three segment piston wavemaker with optimised segment lengths, where $h = 0.6$ m.

Stroke Number	Wavenumber									
	$2 m^{-1}$	$4 m^{-1}$	$6 m^{-1}$	$8 m^{-1}$	$10 m^{-1}$	$12 m^{-1}$	$14 m^{-1}$	$16 m^{-1}$	$18 m^{-1}$	$20 m^{-1}$
1	1.8368	1.8963	1.8982	1.6004	-0.8404	0.9428	-1.0589	-0.9504	0.7489	-0.7230
2	1.8427	1.1600	-0.4395	-0.7648	0.7928	-1.0792	1.3314	1.3060	-1.1175	1.1635
3	1.8313	0.3070	1.6739	1.5780	-1.2575	1.6344	-1.9418	-1.8634	1.5753	-1.6297
4	0.9232	0.6363	-0.2492	-0.4279	0.4039	-0.5705	0.6961	0.6784	-0.5787	0.6017

Table A.37: Optimised strokes, in meters, for a four segment piston wavemaker with optimised segment lengths, where $h = 0.6$ m.

Stroke Number	Wavenumber									
	$2 m^{-1}$	$4 m^{-1}$	$6 m^{-1}$	$8 m^{-1}$	$10 m^{-1}$	$12 m^{-1}$	$14 m^{-1}$	$16 m^{-1}$	$18 m^{-1}$	$20 m^{-1}$
1	-1.6657	1.8146	-1.9331	1.9929	1.9837	1.8110	-0.1448	0.1932	0.2258	0.2133
2	-1.5121	1.3656	-0.2511	-0.4398	-0.8708	-1.8039	0.4340	-0.6155	-0.7378	-0.7188
3	-1.6987	0.6930	-1.9999	0.8786	0.4220	1.9748	-1.0652	1.5377	1.8420	1.7998
4	0.2709	-0.3793	1.1348	0.6067	1.6059	0.5882	0.9694	-1.4692	-1.7919	-1.7766
5	-1.5960	0.9424	-0.6169	-0.1491	-0.6560	-0.5942	-0.2723	0.4282	0.5277	0.5274

Table A.38: Optimised strokes, in meters, for a five segment piston wavemaker with optimised segment lengths, where $h = 0.6$ m.

Stroke Number	Wavenumber									
	$2 m^{-1}$	$4 m^{-1}$	$6 m^{-1}$	$8 m^{-1}$	$10 m^{-1}$	$12 m^{-1}$	$14 m^{-1}$	$16 m^{-1}$	$18 m^{-1}$	$20 m^{-1}$
1	1.3717	-1.5523	-1.8911	1.1578	-1.9871	1.3114	-1.7035	0.7296	-0.2992	-0.3233
2	0.5857	-1.6487	-1.9730	-0.1011	0.3544	-0.609	1.5553	-1.2154	0.7305	0.9340
3	1.9345	1.6777	1.4703	1.6608	-0.5897	0.5123	-1.2298	1.5410	-1.4953	-1.7337
4	-0.9455	-1.9451	-0.5007	-1.8613	-0.8104	0.3374	-1.2532	0.4644	1.0290	0.5927
5	1.8782	-1.7645	-1.7910	1.3905	-0.1336	0.1470	1.0546	-1.4495	-0.1498	0.7722
6	0.6354	0.3955	0.3210	-0.1841	0.1998	-0.0932	-0.1961	0.5102	-0.0412	-0.3913

Table A.39: Optimised strokes, in meters, for a six segment piston wavemaker with optimised segment lengths, where $h = 0.6$ m.

Stroke Number	Wavenumber									
	$2 m^{-1}$	$4 m^{-1}$	$6 m^{-1}$	$8 m^{-1}$	$10 m^{-1}$	$12 m^{-1}$	$14 m^{-1}$	$16 m^{-1}$	$18 m^{-1}$	$20 m^{-1}$
1	-1.9018	-1.3591	1.5193	1.7862	1.9936	1.8555	-1.2433	-1.8614	-0.8485	-1.8142
2	-1.6789	-0.4849	0.1808	-0.0445	-0.3136	-0.4522	0.3812	0.6697	0.3438	0.8063
3	-0.8528	-0.2388	0.1685	0.2570	0.5194	0.6115	-0.4763	-0.8068	-0.4068	-0.9453

Table A.40: Optimised strokes, in meters, for a two segment flap wavemaker with optimised segment lengths, where $h = 0.6$ m.

Stroke Number	Wavenumber									
	$2 m^{-1}$	$4 m^{-1}$	$6 m^{-1}$	$8 m^{-1}$	$10 m^{-1}$	$12 m^{-1}$	$14 m^{-1}$	$16 m^{-1}$	$18 m^{-1}$	$20 m^{-1}$
1	-0.8258	-1.2149	1.8610	1.0666	-0.5555	-1.8800	-1.7326	1.5886	-1.0573	1.3779
2	-1.5710	-0.2006	0.5122	0.2815	-0.0881	0.0446	0.1770	-0.3450	0.3270	-0.5778
3	-0.0045	-1.0570	0.5584	-0.0183	0.0598	-0.3438	-0.5116	0.5390	-0.5880	1.1145
4	-0.7198	0.7106	-0.1383	0.1583	-0.1419	0.3245	0.6523	-0.5092	0.6867	-1.3500

Table A.41: Optimised strokes, in meters, for a three segment flap wavemaker with optimised segment lengths, where $h = 0.6$ m.

Stroke Number	Wavenumber									
	$2 m^{-1}$	$4 m^{-1}$	$6 m^{-1}$	$8 m^{-1}$	$10 m^{-1}$	$12 m^{-1}$	$14 m^{-1}$	$16 m^{-1}$	$18 m^{-1}$	$20 m^{-1}$
1	1.9427	1.1209	1.6378	-1.9481	1.4718	-1.9623	-1.7286	-1.9353	-1.9973	1.4669
2	1.9878	1.4372	1.3670	-1.0002	0.8830	-0.2307	-0.3246	0.1352	0.1811	-0.1390
3	1.9343	-0.7576	-0.4001	0.09335	-0.8080	-1.0217	0.3919	-0.7555	-0.4106	0.3441
4	0.7979	-1.2829	1.5345	-0.6892	1.1384	1.5235	-1.1450	0.4801	-0.1894	-0.3294
5	1.7215	1.3634	-1.4268	0.6069	-0.9723	-1.7931	1.4661	-0.2240	0.5185	0.3172

Table A.42: Optimised strokes, in meters, for a four segment flap wavemaker with optimised segment lengths, where $h = 0.6$ m.

Stroke Number	Wavenumber									
	$2 m^{-1}$	$4 m^{-1}$	$6 m^{-1}$	$8 m^{-1}$	$10 m^{-1}$	$12 m^{-1}$	$14 m^{-1}$	$16 m^{-1}$	$18 m^{-1}$	$20 m^{-1}$
1	-1.4680	-1.6837	-1.1000	-1.8467	1.9877	1.9844	-1.9380	1.8278	1.9200	1.9642
2	-0.9843	-1.6294	-0.8217	-1.5938	0.7952	1.8107	-0.7568	0.9396	0.3977	0.2580
3	-0.2118	-1.3499	-1.9921	0.6109	0.8144	-1.5015	0.5801	1.5038	0.0276	0.1142
4	-1.5778	0.2000	0.6093	-1.2118	-0.0088	1.1486	-1.5476	1.0723	0.3651	-0.0040
5	-0.4480	-1.2078	-0.4671	-0.3120	-0.0427	0.7126	1.5823	-1.8366	-0.4540	0.1925
6	-0.8135	0.1676	-0.1870	0.6960	0.2120	-1.3240	-1.6390	1.8253	0.4948	-0.1824

Table A.43: Optimised strokes, in meters, for a five segment flap wavemaker with optimised segment lengths, where $h = 0.6$ m.

Stroke Number	Wavenumber									
	$2 m^{-1}$	$4 m^{-1}$	$6 m^{-1}$	$8 m^{-1}$	$10 m^{-1}$	$12 m^{-1}$	$14 m^{-1}$	$16 m^{-1}$	$18 m^{-1}$	$20 m^{-1}$
1	1.8829	1.9500	-1.8757	1.4163	-1.9535	-1.9051	1.9107	-1.9819	-1.8990	1.9015
2	1.8104	1.9078	-1.2629	1.0821	-1.3791	-1.5241	1.2052	-1.8605	-0.7002	1.0009
3	-0.6771	1.8418	-0.0666	1.4695	-1.7880	0.3578	0.0081	1.3061	-0.8698	-0.6729
4	1.9679	1.3743	-1.5065	1.0408	-1.6507	-0.6506	0.6525	-1.5755	-0.8467	0.9856
5	1.9951	1.6562	-0.4906	1.3702	1.6199	-0.4353	-0.3726	-1.8811	1.2296	-0.0304
6	1.9753	1.0225	0.0791	-0.2811	-1.1114	0.2703	0.6033	1.8928	-0.8620	-0.6653
7	-1.1290	-0.5385	-0.1465	0.0203	0.6641	-0.1960	-0.6025	-1.9238	0.5635	0.9311

Table A.44: Optimised strokes, in meters, for a six segment flap wavemaker with optimised segment lengths, where $h = 0.6$ m.

Bibliography

- [1] P. McIver and D. V. Evans, “The occurrence of negative added mass in free-surface problems involving submerged oscillating bodies,” *Journal of Engineering Mathematics*, vol. 18, no. 1, pp. 7–22, 1984.
- [2] S. Naito, M. Minoura, and E. Okuyama, “Diffraction force in compact basin with absorbing wave maker,” in *The 12th International Offshore and Polar Engineering Conference*, vol. 3, pp. 399–405, 2002.
- [3] S. Naito, “Wave Generation and Absorption -Theory and Application,” in *International Offshore and Polar Engineering Conference*, vol. 4, (San Francisco), 2006.
- [4] J. M. Hyun, “Theory for articulated double-flap in water of constant wave-makers depth,” *Journal of the society of naval architects of Japan*, vol. 141, no. 1, pp. 78–85, 1977.
- [5] A. Clark and M. Menken, “Dual flap wavemaker phasing and motion apportionment by linear regression,” in *Proceedings of the 18th general meeting of the american towing tank conference* (B. Johnson and B. Nehrling, eds.), (Annapolis), pp. 705–718, 1977.
- [6] D. Murdey, “Wavemaker design consideration for the new laboratory of the NRC Institute for Marine Dynamics - double flap wavemaker design,” in *Proceeding of the 17th International Towing Tank Conference*, pp. 360–362, 1984.
- [7] I. Keaney, R. Costello, and J. V. Ringwood, “Evanescent Wave Reduction Using a Segmented Wavemaker in a Two Dimensional Wave Tank,” in *ASME 2014 33rd International Conference on Ocean, Offshore and Arctic Engineering*, (San Francisco), ASME, jun 2014.
- [8] T. H. Havelock, “Forced surface waves on water,” *Philosophical Magazine Series 7*, vol. 8, no. 51, pp. 569–576, 1929.

- [9] F. Biesel and F. Suquet, “Laboratory wave-generating apparatus”, St. Anthony Falls Hydraulic Laboratory, University of Minnesota, Minneapolis,” 1951.
- [10] K. Suh and R. A. Dalrymple, “Directional wavemaker theory: a spectral approach,” in *Proc. IAHR-Seminar Wave Analysis and Generation in Laboratory Basins*, (Lausanne), pp. 389–395, 1987.
- [11] H. A. Schäffer, “Second-order wavemaker theory for irregular waves,” *Ocean Engineering*, vol. 23, no. 1, pp. 47–88, 1996.
- [12] J. Spinneken and C. Swan, “Second-order wave maker theory using force-feedback control. Part I: A new theory for regular wave generation,” *Ocean Engineering*, vol. 36, pp. 539–548, jun 2009.
- [13] J. Falnes, *Ocean Waves and Oscillating Systems*. Cambridge: Cambridge University Press, 2002.
- [14] S. K. Chakrabarti, “Laboratory generated waves and wave theories,” *Journal of the Waterway, Port, Coastal and Ocean Divison*, vol. 106, no. WW3, pp. 349 – 367, 1980.
- [15] J. D. Fenton, “A fifth-order Stokes theory for steady waves,” *Journal of Waterway, Port, Coastal and Ocean Engineering*, vol. 111, no. 2, pp. 216–234, 1985.
- [16] R. G. Dean and R. A. Dalrymple, *Water Wave Mechanics For Engineers and Scientists*. Singapore: World Scientific, 1st ed., 1984.
- [17] A. E. Maguire, *Geometric design considerations and control methodologies for absorbing wavemakers*. PhD thesis, University of Edinburgh, 2011.
- [18] A. E. Maguire and D. Ingram, “On geometric design considerations and control methodologies for absorbing wavemakers,” *Coastal Engineering*, vol. 58, pp. 135–142, feb 2011.
- [19] J. Spinneken, *Wave Generation and Absorption using Force-feedback Control*. PhD thesis, Imperial College London, 2010.
- [20] E. H. Kennard, “Generation of surface waves by a moving partition,” *Quarterly of Applied Mathematics*, vol. 7, no. 3, pp. 303–312, 1949.
- [21] O. S. Madsen, “Waves generated by a piston-type wavemaker,” in *Proceeding of the 12th Conference on Coastal Engineering*, (Washington D.C.), pp. 589–608, ICCE, 1970.

- [22] F. Ursell, R. G. Dean, and Y. S. Yu, “Forced small-amplitude water waves: a comparison of theory and experiment,” *Journal of Fluid Mechanics*, vol. 7, p. 33, mar 1960.
- [23] P. F. Rhodes-Robinson, “On the forced surface waves due to a vertical wave-maker in the presence of surface tension,” *Mathematical Proceedings of the Cambridge Philosophical Society*, vol. 70, pp. 323–337, oct 1971.
- [24] A. T. Chwang, “A porous-wavemaker theory,” *Journal of Fluid Mechanics*, vol. 132, pp. 395–406, 1983.
- [25] J. M. Hyun, “Theory for hinged wavemakers of finite draft in water of constant depth,” *Journal of Hydronautics*, vol. 10, no. 1, pp. 2–7, 1976.
- [26] G. Gilbert, D. M. Thompson, and A. J. Brewer, “Design curves for regular and random wave generators,” *Journal of Hydraulic Research*, vol. 9, no. 2, pp. 163–196, 1971.
- [27] F. Raichlen and J.-J. Lee, “An inclined-plate wave generator,” in *Proceeding of the 16th coastal engineering conference*, no. 1970, (Hamburg), pp. 388–399, 1978.
- [28] R. T. Hudspeth and M.-C. Chen, “Design curves for hinged wavemakers: Theory,” *Journal of the Hydraulics Division*, vol. 107, no. 5, pp. 533–552, 1981.
- [29] R. T. Hudspeth, M. Chen, and J. Leonard, “Design curves for hinged wave-makers: Experiments,” *Journal of the Hydraulics Division*, vol. 107, no. 5, pp. 553–574, 1981.
- [30] D. E. Cartwright, “On Estimating the Mean Energy of Sea Waves from the Highest Waves in a Record,” *Proceedings of the Royal Society A: Mathematical, Physical and Engineering Sciences*, vol. 247, pp. 22–48, sep 1958.
- [31] S. A. Hughes, *Physical Models and Laboratory Techniques in Coastal Engineering*. Singapore: World Scientific, 1 ed., 1993.
- [32] M. H. Patel and P. A. Ionnaou, “Comparative Performance Study of Paddle-and Wedge-Type Wave Generators,” *Journal of Hydronautics*, vol. 14, pp. 5–9, jan 1980.
- [33] K. Taniguchi and H. Kasai, “A New Flap-type Wave Maker without Water on Back Side,” *Journal of the Society of Naval Architects of Japan*, vol. 132, pp. 129–136, 1972.

- [34] E. R. Chappell, *Theory and design of a wave generator for a short flume*. Masters thesis, The University of British Columbia, 1969.
- [35] R. T. Hudspeth, J. M. Grassa, J. Medina, and J. Lozano, "TYPE E double-actuated wavemakers," *Journal of Hydraulic Research*, vol. 32, pp. 387–400, may 1994.
- [36] D. M. Henderson, M. S. Patterson, and H. Segur, "On the laboratory generation of two-dimensional, progressive, surface waves of nearly permanent form on deep water," *Journal of Fluid Mechanics*, vol. 559, pp. 413–427, jul 2006.
- [37] J. F. Lee, "On the heave radiation of a rectangular structure," *Ocean Engineering*, vol. 22, no. 1, pp. 19–34, 1995.
- [38] Y. C. Wu, "Plunger-type wavemaker theory," *Journal of hydraulic research*, vol. 26, no. 4, pp. 483–491, 1988.
- [39] F. Ursell, "On the heaving motion of a circular cylinder on the surface of a fluid," *Quarterly Journal of Mechanics and Applied Mathematics*, vol. 2, no. 2, pp. 218–231, 1949.
- [40] J. Rytönen and G. Granholm, "Experimental investigation of the plunger type wave maker," *Rakenteiden Mekaniikka*, vol. 22, no. 3, pp. 25–46, 1989.
- [41] S. Wang, "Plunger-type wavemakers - theory and experiment," *Journal of Hydraulic Research*, vol. 12, no. 3, pp. 357–388, 1974.
- [42] T. Mikkola, "Simulation of plunger-type wave makers," *Journal of Structural Mechanics*, vol. 40, no. 4, pp. 19–39, 2007.
- [43] J. L. Black, C. C. Mei, and M. C. G. Bray, "Radiation and scattering of water waves by rigid bodies.," *Journal of Fluid Mechanics*, vol. 46, pp. 151–164, 1971.
- [44] D. Ellix and K. Arungam, "An experimental study of waves generated by an oscillating wedge," *Journal of Hydraulic Research*, vol. 22, no. 5, pp. 299–313, 1984.
- [45] Y. C. Wu, "Waves generated by a plunger-type wavemaker," *Journal of hydraulic research*, vol. 29, no. 6, pp. 851–860, 1991.
- [46] J. Falnes, "Topic on Extraction of Ocean-Wave Energy," 2002.

- [47] M. L. Banner and W. L. Peirson, “Wave breaking onset and strength for two-dimensional deep-water wave groups,” *Journal of Fluid Mechanics*, vol. 585, pp. 93–115, 2007.
- [48] A. E. Maguire and D. Ingram, “Hydrodynamics and absorption efficiencies of wavemakers,” in *8th European Wave and Tidal Energy Conference*, (Uppsala), pp. 859–868, 2009.
- [49] G. H. Keulegan, “The approximate theories of pneumatic wave generators,” Tech. Rep. 2, U.S. Army Engineer Waterways Experiment Station, Vicksburg, 1966.
- [50] J. F. O’Dea and J. N. Newman, “Numerical studies of directional wavemaker performance,” in *28th American Towing Tank Conference*, no. August, pp. 9–10, 2007.
- [51] Y. C. Wu, “Waves generated by an inclined-plate wave generator,” *International Journal for Numerical Methods in Fluids*, vol. 8, no. 1, pp. 803–811, 1988.
- [52] S. H. Salter, “Apparatus for creating surface waves in a body of liquid, US715403,” 1979.
- [53] T. Sahoo, “On the generation of water waves by cylindrical porous wave maker,” *Acta Mechanica*, vol. 126, pp. 231–239, mar 1998.
- [54] G. Taylor, “Fluid flow in regions bounded by porous surfaces,” *Proceeding of the royal society London A*, vol. 234, no. 1199, pp. 456–475, 1956.
- [55] A. T. Chwang and G. W. Housner, “Hydrodynamic pressures on sloping dams during earthquakes. Part 1. Momentum method,” *Journal of Fluid Mechanics*, vol. 87, pp. 335–341, apr 1978.
- [56] A. T. Chwang, “Hydrodynamic pressures on sloping dams during earthquakes. Part 2. Exact theory,” *Journal of Fluid Mechanics*, vol. 87, no. 2, pp. 343–348, 1978.
- [57] R. A. Dalrymple and R. G. Dean, “The spiral wavemaker for littoral drift studies,” *Proceeding of 13th Coastal Engineering Conference*, pp. 689–705, 1972.
- [58] K. Tanizawa and A. Clément, “Report of the 2nd workshop of ISOPE numerical wave tank group: benchmark test cases of radiation problem,” in *The 10th ISOPE Conference*, no. May, (Seattle), pp. 175–184, 2000.

- [59] S. Yamashita, “Calculations of the hydrodynamic forces acting upon thin cylinders oscillating vertically with large amplitude,” *Journal of the Society of Naval Architects of Japan*, vol. 1977, pp. 61–69, jan 1977.
- [60] A. Clement, “The spinning dipole: an efficient unsymmetrical numerical wavemaker,” in *Proceeding of the 14th International Workshop Water Waves and Floating Bodies*, (Port Huron), pp. 29–32, 1999.
- [61] S. T. Grilli, J. Skourup, and I. A. Svendsen, “An efficient boundary element method for nonlinear water waves,” *Engineering Analysis with Boundary Elements*, vol. 6, pp. 97–107, jun 1989.
- [62] J. W. Dold and D. H. Peregrine, “An efficient boundary-integral method for steep unsteady water waves,” *Numerical methods for fluid dynamics II*, pp. 671–679, 1986.
- [63] S. Grilli and P. Watts, “Modeling of waves generated by a moving submerged body. Applications to underwater landslides,” *Engineering Analysis with Boundary Elements*, vol. 23, pp. 645–656, sep 1999.
- [64] W. C. Koo and M. H. Kim, “Numerical simulation of nonlinear wave and force generated by a wedge-shape wave maker,” *Ocean Engineering*, vol. 33, pp. 983–1006, jun 2006.
- [65] A. Clement, “Coupling of two absorbing boundary conditions for 2D time-domain simulations of free surface gravity waves,” *Journal of Computational Physics*, no. 126, pp. 139–151, 1996.
- [66] M. C. Silva, M. de Araujo Vitola, W. T. Pinto, and C. A. Levi, “Numerical simulation of monochromatic wave generated in laboratory: Validation of a CFD code,” in *23 Congresso Nacional de Transporte Aquaviário , Construção Naval e Offshore*, 2010.
- [67] A. Lal, M. Elangovan, and A. P. Setup, “CFD Simulation and Validation of Flap Type,” *World Academy of Science, Engineering and Technology*, vol. 48, pp. 76–82, 2008.
- [68] A. E. Maguire and D. M. Ingram, “Wavemaking in a commercial CFD code,” in *Proceeding of the 3rd International Conference on the Application of Physical Modelling to Port and Coastal Protection*, 2010.
- [69] W. Finnegan and J. Goggins, “Numerical simulation of linear water waves and wavestructure interaction,” *Ocean Engineering*, vol. 43, pp. 23–31, apr 2012.

- [70] O. S. Madsen, “On the generation of long waves,” *Journal of Geophysical Research*, vol. 76, no. 36, pp. 8672–8683, 1971.
- [71] R. T. Hudspeth and W. Sulisz, “Stokes drift in two-dimensional wave flumes,” *Journal of Fluid Mechanics*, vol. 230, pp. 209–229, 1991.
- [72] W. I. Moubayed and A. N. Williams, “Second-order bichromatic waves produced by a generic planar wavemaker in a two-dimensional wave flume,” *Journal of Fluids and Structures*, vol. 8, pp. 73–92, jan 1994.
- [73] H. A. Schäffer and C. M. Steenberg, “Second-order wavemaker theory for multidirectional waves,” *Ocean Engineering*, vol. 30, pp. 1203–1231, jul 2003.
- [74] P. Fontanet, “Theorie de la generation de la houle cylindrique par un batteur plan,” *La Houille Blanche*, vol. 16, jan 1961.
- [75] E. Daugaard, *Generation of regular waves in the laboratory*. PhD thesis, Technical University of Denmark, 1972.
- [76] J. Buhr Hansen and I. A. Svendsen, “Laboratory generation of waves of constant form,” in *Proceedings of the 14th Coastal Engineering Conference*, pp. 321–339, American Society of Civil Engineers, 1974.
- [77] J. H. Milgram, *Compliant water wave absorbers*. PhD thesis, Massachusetts Institute of Technology, 1965.
- [78] J. H. Milgram, “Active water-wave absorbers,” *Journal of Fluid Mechanics*, vol. 42, p. 845, mar 1970.
- [79] S. H. Salter, “Absorbing wave-makers and wide tanks,” in *Proceeding of the conference on directional wave spectra application* (R. L. Wiegell, ed.), pp. 182–202, American Society of Civil Engineers, 1981.
- [80] J. Spinneken and C. Swan, “Second-order wave maker theory using force-feedback control. Part II: An experimental verification of regular wave generation,” *Ocean Engineering*, vol. 36, pp. 549–555, jun 2009.
- [81] J. N. Newman, “Analysis of wave generators and absorbers in basins,” *Applied Ocean Research*, vol. 32, pp. 71–82, feb 2010.
- [82] J. Spinneken, M. Christou, and C. Swan, “Force-controlled absorption in a fully-nonlinear numerical wave tank,” *Journal of Computational Physics*, vol. 272, pp. 127–148, sep 2014.

- [83] R. A. Dalrymple, “Directional wavemaker theory with sidewall reflection,” *Journal of Hydraulic Research*, vol. 27, pp. 23–34, jan 1989.
- [84] E. P. D. Mansard, M. D. Miles, and R. A. Dalrymple, “Numerical validation of directional wavemaker theory with sidewall reflections.,” in *Proceeding of the International Conference on Coastal Engineering, No.23*, (Venice), pp. 3469–3481, 1992.
- [85] M. Isaacson, “Prediction of directional waves due to a segmented wave generator,” *Proc. of 23rd IAHR Congress*, 1989.
- [86] J. Spinneken and C. Swan, “The operation of a 3D wave basin in force control,” *Ocean Engineering*, vol. 55, pp. 88–100, 2012.
- [87] F. Bonnefoy, D. Le Touzé, and P. Ferrant, “Second order directional wave-maker theory: prediction and control of free waves,” in *Proceeding of the 18th International Workshop on Water Waves and Floating Bodies*, 2003.
- [88] M. O’Cathain, *Modelling of Multibody Marine Systems*. PhD thesis, National University of Ireland Maynooth, 2007.
- [89] J. Nocedal and S. J. Wright, *Numerical Optimization*. New York: Springer, 1999.
- [90] K. Price, R. Storn, and J. Lampinen, *Differential Evolution, A Practical Approach to Global Optimization*. Springer, 2005.
- [91] D. E. Goldberg, “Genetic Algorithms in Search, Optimization and Machine Learning,” oct 1989.
- [92] R. Storn and K. Price, “Differential Evolution A Simple and Efficient Heuristic for Global Optimization over Continuous Spaces,” *Journal of Global Optimization*, vol. 11, pp. 341–359, 1997.
- [93] D. Zaharie, “Critical values for the control parameters of differential evolution algorithms,” in *Proceedings of the 8th International Conference on Soft Computing (MENDEL)* (R. Matousek and P. Osmera, eds.), (Brno), pp. 62–67, 2002.